Le système binaire aluminium-iridium, du diagramme de phases aux surfaces atomiques

Joris Kadok

To cite this version:

Joris Kadok. Le système binaire aluminium-iridium, du diagramme de phases aux surfaces atomiques. Science des matériaux [cond-mat.mtrl-sci]. Université de Lorraine, 2016. Français. NNT : 2016LORR0202 . tel-01527988

HAL Id: tel-01527988
https://theses.hal.science/tel-01527988v1

Submitted on 26 May 2017

THÈSE

pour l'obtention du diplôme de:

Docteur de l'Université de Lorraine

Spécialité: Science des matériaux

Présentée par:

JORIS KADOK

Le système binaire aluminium-iridium, du diagramme de phases aux surfaces atomiques

Thèse défendue le 16 novembre 2016 à Nancy

Composition du jury:

Mme Valérie Demange	Chargée de recherche	Examinatrice
M. Michel Vilasi	Professeur	Examinateur
M. Marc de Boissieu	Directeur de recherche	Rapporteur
M. Franck Gascoin	Maître de conférences	Rapporteur
M. Vincent Fournée	Directeur de recherche	Co-directeur
M. Julian Ledieu	Chargé de recherche	Directeur
M. Juri Grin	Professeur	Invité
M. Yurii Prots	Chercheur	Invité

Equipe 203, métallurgie et surfaces

IJL, UMR CNRS *7198, Université de Lorraine, 54011 Nancy cedex, France*

"In heaven, everything is fine. You've got all your good things and you've got mine"

In Heaven - The Pixies

Acknowledgements

I would like to express my real gratitude to my two supervisors Dr. Julian Ledieu and Dr. Vincent Fournée for their great support of my studies. I learnt within the years that it is not so usual to have supervisors that take so much care of their PhD students. My sincere thanks also go to Marie-Cécile De Weerd who introduced me to the work in lab and helped me a lot with my experiments. I thank also Dr. Pascal Boulet and Dr. Émilie Gaudry for their nice help and explanations about crystallography and theoretical studies.

All my gratitude also goes to my unofficial third supervisor Pr. Juri Grin who gave me the opportunity to work in the Max-Planck Society, opening me the doors of the institute in Dresden and providing me access to the labs and research facilities. Thank you professor for leading my researches about the Al-Ir system. My special thanks go to Dr. Yurii Prots for all his dedication to my work, I will never be grateful enough for all his mentorship. I owe almost all my knowledge in crystallography to you Yurii.

I'm also very thankful to all the researchers, in the IJL or the MPI, with who I had great discussions and who took on their time to give me helpful explanations about their speciality: Lionel Aranda, Ulrich Burckardt, Raul Cardoso, Christine Gendarme, Bernard Malaman, Bernard Rouat, Markus Schmidt, Walter Schnelle, Paul Simon and Julien Zollinger. Thanks also the all the people from the different competence groups who took care of a part of my analysis.

I thank all my other fellow collegaues, everyday or punctual compeers, in the lab or in the office, in the IJL, the MPI or outside: Adel, Alfred, Benoit, Božo, Charles, Dmytro, Erwan, Gary, Jonathan, Julien, Kanika, Luka, Marko, Matthias, Nataliya, Pierre, Riccardo and all the others I may have forgotten. Really thank you for making the working days much more enjoyable. And thanks of course to all the non-scientific staff who helped me going through all the administrative procedures.

And finally I would like to thank my family and my friends for the moral support and the encouragements during all my PhD. Thank you dad, mom, brother and sister, Alicia, Amaury, Kevin, Margaux, Morgane and Yannick for all the support in this work and in my life in general.

Contents

List of Figures

List of Tables

List of Abbreviations

ADP	**A**nisotropic **D**isplacement **P**arameter
BCC	**B**ody **C**entered **C**ubic
BSE	**B**ack-**S**cattered **E**lectron
CCD	**C**harge-**C**oupled **D**evice
CMA	**C**omplex **M**etallic **A**lloy
DFT	**D**ensity **F**unctional **T**heory
DOS	Electronic **D**ensity **O**f **S**tates
DSC	**D**iffential **S**canning **C**alorimetry
DTA	**D**ifferential **T**hermal **A**nalysis
EDS	**E**nergy **D**ispersive **S**pectroscopy
EPMA	**E**lectron **P**robe **M**icro-**A**nalysis
ESRF	**E**uropean **S**ynchrotron **R**adiation **F**acility
FCC	**F**ace **C**entered **C**ubic
HR-PXRD	**H**igh-**R**esolution **P**owder **X**-**R**ay **D**iffraction
ICSD	**I**norganic **C**rystal **S**tructure **D**atabase
LEED	**L**ow **E**nergy **E**lectron **D**iffraction
MLE	**M**ono**L**ayer **E**quivalent
PPA	**P**ush-**P**ull **A**lloy
PXRD	**P**owder **X**-**R**ay **D**iffraction
QC	**Q**uasi**C**rystal
SC-XRD	**S**ingle-**C**rystal **X**-**R**ay **D**iffraction
SE	**S**econdary **E**lectron
SEM	**S**canning **E**lectron **M**icroscopy
STM	**S**canning **T**unneling **M**icroscopy
TEM	**T**ransmission **E**lectron **M**icroscopy
TM	**T**ransition **M**etal
UHV	**U**ltra-**H**igh **V**acuum
UPS	**U**ltra-violet **P**hotoelectron **S**pectroscopy
UV	**U**ltra-**V**iolet
VASP	**V**ienna **A**b initio **S**imulation **P**ackage
VPN	**V**ickers **P**yramid **N**umber
WDS	**W**avelength **D**ispersive **S**pectroscopy
XPS	**X**-ray **P**hotoelectron **S**pectroscopy
XRD	**X**-**R**ay **D**iffraction

Chapter 1

General introduction

1.1 Preamble

The development of always better metallic alloys is an area of study that never cease to find interest in the high-technology industries such as aeronautics, biomedicine, catalysis, etc. An alloy is defined by an homogeneous mixture of two or several metallic elements. The purpose in forming alloys is to provide a new material with physical, mechanical or chemical properties that are different from those of its components. Considering the number of possible combinations of the elements of the Periodic Table in a way to form a metallic alloy, this left to tens of thousand possibilities of conceiving an alloy constituted of two or three elements. The development of such materials and the study of their properties is then an active and wide field of research that is today still extensively explored.

An intermetallic compound is a chemical compound of two or more metallic elements and adopts an - at least partly - ordered crystal structure that differs from those of the constituent metals [1]. A single system of two (binary) or more (ternary, quaternary...) elements can exhibit several intermetallic compounds. The physical, mechanical and chemical properties are arising from the nature of the elements that constitute the alloys but also from their crystal structures. For example in the aluminium-copper binary system, the intermetallic compound Al_2Cu can crystallise in two different atomic structures, one stable tetragonal and one metastable cubic. Because of the different atomic arrangement, the tetragonal phase shows a much better hardness compared to the cubic phase. Thus, the stability of this tetragonal phase relative to the other one is of considerable interest [2].

Some alloys are designed for specific resistance to corrosion, fatigue and temperature. This is the case for example of the stainless steel, combination of iron, chromium and nickel yielding metallic alloys very resistant to corrosion with high tensile strength and fracture toughness. Nickel and cobalt based superalloys present even better properties such as excellent mechanical strength and resistance to thermal creep deformation and corrosion under high temperature environments. Such alloys are employed in the fabrication of reactors in the field of aeronautics for example. Other alloys are made to offer interesting magnetic or electrical properties such as the gallium arsenide which is a semiconductor that is used in electronics or the lanthane-baryum-copper oxide, a superconducting alloy.

When looking into the literature, it can be noticed that interesting properties are oftently found in intermetallic compounds with complex crystal structures. The particular alloys that present such complex crystal structure are called complex metallic alloys or CMAs. The CMAs are the subject of interest of this thesis and will be more precisely described in the following section.

1.2 Complex metallic alloys

1.2.1 Definition and quasicrystals

A complex metallic alloy is an intermetallic compound which is characterised by a large unit cell holding tens to thousands of atoms with the presence of well-defined atomic clusters. These clusters usually exhibit an icosahedral symmetry thus including also the C15 Laves phases in the CMAs, although such phases can have only 12 atoms per unit cell. According to this definition, the quasicrystalline phases are typically CMAs as well. The discovery of the quasicrystals (QCs) is attributed to Dan Shechtman who pointed out ten-fold symmetry in an electron diffraction pattern of a rapidly solidified Al-Mn alloy in 1982 [3]. The particularity of the QCs is that they have an ordered crystal structure but without translational periodicity.

While a periodic crystal can show two, three, four or six-fold rotational symmetry and different translational symmetries, a quasicrystal can present five, seven, eight, ten or twelve-fold rotational symmetry without 3-D translational symmetry [3]. A large majority of the QCs exhibit five (icosahedral phases) or ten-fold symmetry (decagonal phases). Figure 1.1 shows a typical five-fold Penrose tiling, invented by Sir Roger Penrose in 1974. It is built under certain rules with a pair of thin and thick rhomb tiles that can only fit together non-periodically. The diffraction pattern of such tiling and of a QC actually present the same motifs. Like periodic crystals, the aperiodic network of atoms in a QC is also providing an essentially discrete pattern of diffraction. This discovery had the consequence of the modification of the definition of a "crystal" by the International Union of Crystallography. Indeed, while the previous definition mentioned that a crystal should have a periodic structure, the new definition now says that "a material is a crystal if it has essentially a sharp diffraction pattern" [4].

1.2.2 Examples

Quasicrystals are a type of CMA that can be found in various systems. With the exception of Cd-Ca and Cd-Yb compounds, Dubois *et al.* [3] noticed that stable QCs are frequently found in ternary, or multinary alloys of generic composition $A_xB_yC_z$ that are characterised by two important key facts:

- The binary components A–B and A–C form well-defined compounds and the constituents interactions must therefore be attractive (negative formation enthalpy).
- The B–C pair forms no compound, or B and C are immiscible (positive formation enthalpy).

Such alloys are called Push-Pull Alloys (PPAs), a term introduced by J.-M. Dubois *et al.* [3] to categorise metallic systems that form highly complex crystals, including QCs, from simpler binary systems. The A-B and A-C represent the "pull" systems while the B-C is the "push" system.

A known push-pull system that exhibits quasicrystalline phases is the Al-Cu-Fe ternary system. Indeed, while the Al-Cu and Al-Fe binary systems form compounds with different degrees of complexity, the Cu-Fe shows a miscibility gap [5–7]. In the Al-rich corner of the Al-Cu-Fe phase diagram is found the QC phase $Al_{63}Cu_{24}Fe_{13}$, a compound with an icosahedral aperiodic structure. Among

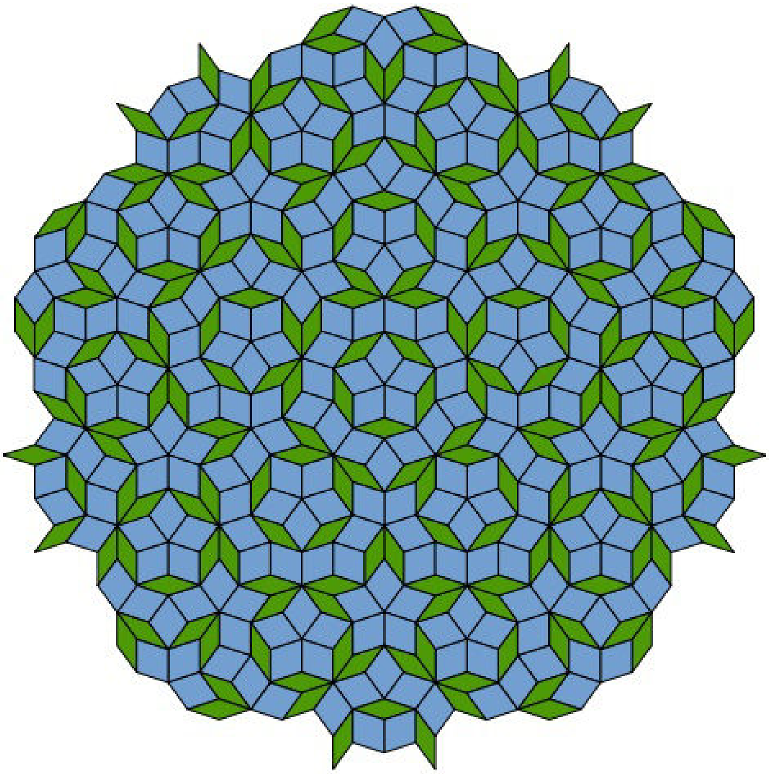

FIGURE 1.1: A five-fold Penrose tiling.

the push-pull alloys, one can also cite the Al-Pd-Mn, Al-Cu-Li, Al-Mg-Zn, Al-Co-Cu or Al-Cu-Ta systems. The latter is remarkable for presenting a very complex periodic CMA with more than 23,000 atoms in the unit cell [8].

Tsai *et al.* demonstrated that QCs with the same structure could be obtained in some cases by substituting a transition metal (TM) by another one from the same column of the Periodic Table at the same composition. For example isostructural icosahedral QCs are found for $Al_{70}Pd_{20}TM_{10}$ where TM = Mn, Tc and Re. The same phenomenon also occurs with $Al_{63}Cu_{25}TM_{12}$ where TM = Fe, Ru and Os [9, 10]. The authors considered that these series of QCs were obtained by following the Hume-Rothery rules. These rules say that the elements of substitution should have a similar atomic radius, valence, electronegativity and crystal structure when alloyed to the same base metals.

All the previously mentioned systems are containing aluminium but quasicrystals can also be found in other systems. Indeed, the Cd-Yb, Ag-In-Yb, Pd-U-Si or Ti-Zr-Ni systems for example also exhibit QC phases and except for the latter, these systems do not enter into the push-pull category. Nevertheless, Dubois *et al.* mentioned that the same major features could be observed in the electronic density of states (DOS) of the icosahedral Al-Cu-Fe (Al-based, push-pull) and Ag-In-Yb (non Al-based, non push-pull) QCs. They estimated that formation of these QCs might be related in part to these characteristic features of the DOS [3]. However, Ishii *et al.* showed that these similar features are determined primarily by a p-d hybridisation rather than the Hume-Rothery mechanism [11].

1.2.3 Properties and applications

Most of the quasicrystalline materials have mechanical properties similar to ceramics: they are hard and brittle with a good thermal resistance. Because of the occurrence of some dislocations due to their particular atomic arrangement, Al-based QCs show also a noticeable ductility above 600°C. Experiments revealed that the surface energy of the QCs is decreasing with the increasing size of the quasi-lattice in which they crystallise. The brittleness of the QCs is the main limiting factor for direct applications as a bulk material but they can be used as coating to benefit from their interesting surface properties or as a precipitate to reinforce materials. For example, non-stick frying pans coated with a quasicrystalline material were developed by the french company Sitram which benefit from the better hardness of the material compared to Teflon [12]. These pans are no longer in use since a problem was encountered in the industrial fabrication process. QCs are also used as a precipitate to harden ductile materials. For example, precipitated nanoparticles of icosahedral QCs are employed to produce maraging steels [13] that were used for Philips razor blades or surgery tools [14]. A composite consisting of a nylon matrix reinforced by Al-based QC powders has been also developed and commercialised for applications in selective laser sintering process [15].

Some QCs are also exhibiting attracting surface properties that find interest for applications in the field of catalysis. Kameoka *et al.* in 2004 for instance studied the catalysis properties of some Al-Cu-Fe QC samples by performing methanol steam reforming to produce H_2. They revealed that all the samples exceeded the performance of a standard commercial catalyst. They suggested that these interesting results are directly arising from the push-pull character of the QCs, i.e. thanks to the fact that Cu and Fe atoms could not mix and therefore formed nanograins that could not coalesce at the surface of the initial coarse-grained material [16]. Armbrüster *et al.* also reported that the $Al_{13}Fe_4$ CMA can be an alternative for palladium in heterogeneous hydrogenation [17]. These interesting results along with the relatively low production cost of these materials compared to the conventional Pd or Pt catalysts can potentially lead to industrial applications in the future.

1.3 Motivations

Despite the great interest of the scientific community in the study of binary or multinary systems to find attractive intermetallic compounds, CMA or not, a lot of systems are still remaining to be fully explored or are lacking a thorough investigation. Even for the systems that were intensively studied, all the existing compounds might not have been identified decades ago. This is the case for example for the Al-Ir binary system. As it will be described in Chapter 3, this system is still a matter of debate. As an example, uncertainties persist in the existence of the $Al_{13}Ir_4$ compound. It is worth noticing that $Al_{13}TM_4$ phases already exist for TM = Co, Fe, Ru, Os. These phases are actually interesting CMAs with respect to their particular chemical bonding and surface properties to name a few [18–20]. Following the Hume-Rothery rules as employed by Tsai *et al.* [9, 10], the $Al_{13}Ir_4$ phase should be actually stable. Generally, the Al-Ir intermetallic compounds exhibit interesting combinatorial properties which could be useful for niche applications.

- They have a high melting point thanks to the presence of iridium which decomposes at 2447°C.

- The iridium-rich compounds exhibit a remarkable hardness, fracture toughness and no brittleness [21].
- The aluminium-rich compounds show good resistance to oxidation at high temperature (1500°C - 1800°C) [22, 23].
- Two CMAs, $Al_{45}Ir_{13}$ [24] and $Al_{28}Ir_9$ [25] have been already reported in this system so far.

Some Al-Ir-TM ternary systems are also known to exhibit CMAs and even QCs for TM = Cu, Pd and Os [26–28]. Again citing Tsai *et al.* [9, 10], substituting one of these TM by another element of the same column of the Periodic Table could lead to compounds with similar structure, i.e. quasiperiodic phases. The Al-Ir-Ni [29] and Al-Ir-Ru [30] systems have already been explored but compounds to those found in the Al-Ir-Pd or Al-Ir-Os were not reported. Following the column n°11 of the Periodic Table, containing Cu, Ag and Au, the Al-Ir-Ag and Al-Ir-Au systems are still remaining to be explored. It is important to note that the binaries Ag-Ir and Au-Ir are immiscible, making the Al-Ir-Ag and Al-Ir-Au two push-pull systems.

For all these reasons, the Al-Ir binary system as well as the Al-Ir-Ag and Al-Ir-Au ternary systems are chosen here for an intensive investigation. The Al-Ir phase diagram will be the subject of a complete reassessment. The phase diagram in the Al-rich side of the Al-Ir-Ag and Al-Ir-Au systems will also be explored. As detailed in the previous section, the surfaces of CMAs sometimes also exhibit interesting properties. Thus, the Al-Ir system will be also the subject of surface investigation under ultra-high vacuum (UHV).

1.4 Structure of the manuscript

After introducing the thesis subject, Chapter 2 starts with the experimental methods that have been used for the preparation and characterisation of bulk metallic alloys. The arc-melting method of preparation is detailed as well as methods of characterisation including X-ray diffraction, scanning electron microscopy and thermal analysis.

Chapter 3 deals with the complete investigation of the Al-Ir binary system as bulk material. After an extensive review of the related literature, the prepared samples are described and the new features brought to the Al-Ir phase diagram are presented. This includes a revision of two known compounds and the discovery of a new phase.

This work continues with the investigation of Al-Ir based ternary systems which are presented in Chapter 4. The Al-rich side of the Al-Au-Ir, Al-Ag-Ir and Al-Si-Ir push-pull systems are explored. From this study, three new phases could be identified. The structures of these new phases are presented and discussed in this Chapter. The reason of the study of the Al-Si-Ir system is explained in its corresponding section.

Chapter 5 is all about the study of the Al-Ir system in terms of surfaces. The growth of Al-Ir single crystals would request several grams of iridium. Since this metal is very expensive, another method of preparation has been considered. For this work, one to few monolayers of iridium were deposited in an Al(100) surface under ultra-high vacuum conditions at different temperatures aiming to form intermetallic compounds. The methods of preparation and the surface characterisation are briefly described. Then, the results of this preparation are presented and the observations are discussed.

This thesis is the result of the cooperation between two institutes of the european consortium C-MAC [31]. The achievements about the Al-Au-Ir, Al-Ag-Ir and the surface investigation of the Al-Ir system has been done in the Jean Lamour Institute in Nancy in France under the supervision of Dr. Julian Ledieu and Dr. Vincent Fournée. The work about the bulk Al-Ir and Al-Ir-Si systems has been carried out in the Max-Planck Institute for Chemical Physics of Solids in Dresden in Germany under the supervision of Pr. Juri Grin and Dr. Yurii Prots.

Chapter 2

Experimental methods

2.1 Introduction

The synthesis and characterisation of intermetallic compounds is a field of research that have been widely explored since the early twentieth century [32, 33]. While today we use the same "techniques" of preparation and characterisation than a century ago, the equipments sensibly evolved. The two most exploited laboratory techniques of preparing a bulk metallic alloy are the arc melting and the induction melting. When the constituents have a low melting point, one can also think about simply melting the elements in a muffle furnace. The technique used for the preparation of all the samples that will be presented in this work was the arc melting. This technique which will be described hereafter involves a rapid cooling of the sample. The latter is then not in a equilibrium state and a heat treatment is often required for each sample after the synthesis. Following this preparation, different techniques of characterisation have been used on our samples in order to determine if one or several intermetallic compounds have been stabilised, along with their chemical composition, their microstructure, their atomic structure etc... Here, the main techniques that were employed were X-ray Diffraction (XRD), Scanning Electron Microscopy (SEM), Energy Dispersive Spectroscopy (EDS), Wavelength Dispersive Spectroscopy (WDS), Differential Thermal Analysis (DTA) and Differential Scanning Calorimetry (DSC). Each steps of preparation and characterisation will be described in the following sections.

2.2 Sample preparation

The first step for preparing a bulk metallic alloy is to define the correct quantity of the constitutive elements. Once the chemical composition of the sample is decided, the highly pure elements (to avoid any contamination) are weighted in order to respect the exact determined mass ratio. The pure elements can be purchased in various shapes, such as platelets, shots, powder, rods, slugs etc... Elements with different shapes were taken for the synthesis of our samples, powder form was avoided as it is too volatile for the selected method of preparation. The constituents are placed in the copper hearth of a laboratory electric arc-melter (see Fig. 2.1) in a strategical order. Thermal exchange between the elements and the hearth plate must be minimised. With respect to that, platelets are not laid at the bottom and elements with high vapor pressure are placed beneath the others so that they melt lastly. An ingot of an easily oxidising element such as titanium can also be placed within the vessel as it will play the role of an oxygen getter during the melting of the elements. The chamber of the arc-melter is then hermetically closed before being pumped ($\sim 10^{-3}$ mbar) and refilled with

FIGURE 2.1: Picture of the chamber of a SA-200 laboratory arc-melter from the Materials Research Furnaces, Inc.

a neutral gas several times. For our preparations, a working atmosphere of 500 mbar of argon was chosen. The principle is to apply a high current between two electrodes in order to ionise the argon gas forming a high temperature plasma. The hearth plays the role of the anode and is water-cooled so as to avoid to be melted with the elements. The cathode is a tungsten tip set above the hearth that can be maneuvered by a handlebar so that the electric arc can be aimed at will. Once the plasma is ignited, the getter is melted first then the elements can be melted together to form an ingot. The obtained sample is overturned and remelted several times to ensure homogeneity. The intense light emitted by the plasma is highly hazardous for the human eyes, it is crucial to place an appropriate filter in front of the observation window. Once the ingot is homogeneous and cooled down, the chamber is then refilled with air and opened to remove the as-cast sample. The chamber must be correctly cleaned after each preparation.

2.3 Heat treatment

As mentioned above, the obtained sample after the arc-melting has been rapidly cooled down on the water-cooled copper hearth bottom and is then not at the thermodynamical equilibrium. Annealing the sample is necessary to correctly recrystallise its constitutive phases. The annealing procedure was the same for each sample synthesised in this work. The as-cast ingot is placed in a crucible, usually made of alumina, which is itself inserted in an one-end closed quartz tube. A piece of glass is also inserted at the bottom of the tube to avoid a direct contact with the crucible. The tube is then connected to a vacuum station, evacuated and refilled with argon three times to avoid oxygen contamination as much as possible. It is filled one last time with 700 mbar of a neutral gas and is then closed. The sealing is performed with an oxyhydrogen torch. The wall of the tube is circularly

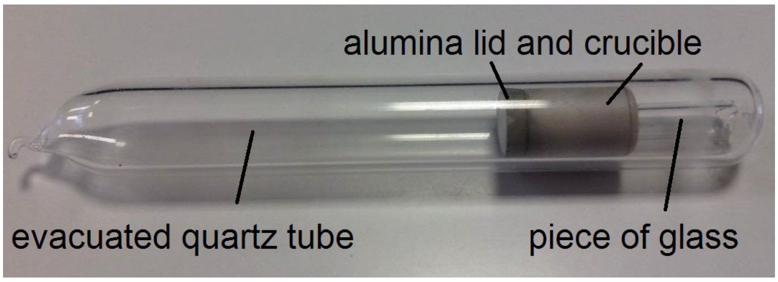

FIGURE 2.2: A sample inside an alumina crucible sealed in an evacuated quartz tube.

heated until it becomes soft. Because of the partial pressure inside, the tube will self-seal itself, hermetically enclosing the crucible. This preparation (shown in Fig. 2.2) is then placed in a muffle furnace where the heat program remains to be determined. The ideal heating rate, cooling rate, dwelling temperature and dwelling time depend on the elements that constitute the sample. The heating rate must not be too fast because the sample is enclosed in an alumina crucible which is itself in a quartz tube, the alloy will take some time to reach the temperature of the furnace. The dwelling temperature must not be above the melting point of the sample and must also not be too low otherwise the equilibrium will be very long to reach. The dwell time is set according to the dwelling temperature; the lower the temperature of the annealing, the longer the treatment. A slow cooling rate favor the crystallisation of bigger grains which is ideal for the characterisation of the phases. For the samples prepared and annealed in our work, a complete heat treatment could last from one to four weeks. The heat programs that were applied will be detailed in Chapter 3. Once the heat treatment is finished, the quartz tube is broken and the sample is retrieved and ready for characterisations.

2.4 Characterisation

The samples obtained with this method of preparation are polycrystalline and rarely contain only a single phase. In order to find the phases present in the samples or to characterise them if they are unknown, different techniques were used in this work. With powder X-ray diffraction data, the phases present in the sample can be identified if they are known. Otherwise, it is also possible to determine the unit cell in which the unknown compound crystallises. Correctly solving single-crystal X-ray diffraction data will lead to the atomic structure of the analysed compound. Scanning electron microscopy gives images of the microstructure of the sample and can be coupled by energy dispersive spectroscopy, technique that yields the chemical composition of precise regions of the sample. Differential thermal analysis and differential scanning calorimetry are similar techniques that can provide the temperature of decomposition of each phases. The following sections introduce these methods of characterisation.

2.5 X-ray crystallography

The determination of the crystal structure of a compound is essential to understand its physical and chemical properties. X-ray crystallography has been widely used for the past century in numerous fields of research and is still the most appropriate experimental technique for this task. In 1912, Max Von Laue demonstrated that X-rays were diffracted by crystals. He reported that interferences are arising in consequence of the lattice structure of the crystals. The reason is because the lattice constants are approximately ten times greater than the conjectured wavelengths of the X-rays. One year later, the Bragg formulation of X-ray diffraction known as Bragg's law was proposed by William Lawrence Bragg and his father William Henry Bragg to explain the angles for coherent and incoherent scattering from a crystal lattice. The following years, diffractometers got modernised and several computational tools were developed. Today, a complete data collection from a laboratory X-ray diffraction experiment can take several minutes to few hours while some weeks were necessary back at the beginning of the technique. This section is dedicated to the general principle of the X-ray diffraction and to the different steps implemented for the data processing. The two techniques of powder and single-crystal X-ray diffraction that were employed in this work will be detailed.

2.5.1 General principle

The X-ray is a form of electromagnetic radiation that have a characteristic wavelength ranging from 0.001 nm to 10 nm, located between the γ-ray and the far-UV. When this kind of radiation interacts with matter and more precisely with atoms, three types of interaction can occur.

- The photoelectric effect. An incoming X-ray ejects an electron from an energy level which will result in an unstable configuration of the atom. To restore equilibrium, an electron from a higher energy falls into the created hole. The energy excess is emitted by a photoelectron.
- The Compton effect. The radiation is inelastically scattered and will transfer a part of its energy to an electron which will be ejected. The scattering of the incident photon is incoherent and will cause a background noise in the diffraction analysis.
- The Rayleigh effect. The radiation is elasticaly scattered so it will rebound to the electron without loosing its energy. Since the wavelength of the radiation has the same order of magnitude as the interatomic distances, if the matter is well organised, this will cause alternatively constructive and destructive interferences. This phenomenon is called diffraction and will be the topic of interest.

As described in Chapter 1, the definition of a crystal has been modified after the discovery of the quasicrystals. The new definition is: "a material is a crystal if it has essentially a sharp diffraction pattern" [4]. In crystallography, the network of the atoms in a crystal is called a lattice and the reciprocal lattice is defined by the Fourier transform of this lattice. Linking three nodes of a lattice constitutes a crystallographic plane. The Miller's indices h, k and l are integers that denotes the family of planes orthogonal to

$$hb_1 + kb_2 + lb_3 \tag{2.1}$$

where b_i are the basis of the reciprocal lattice.

When a X-ray photon hits a crystal, the constructive interferences induced by the Rayleigh effect will be generated only under Bragg's conditions, which is given by the Bragg's law:

$$2d_{hkl} \sin\theta = n\lambda \tag{2.2}$$

where d_{hkl} is the distance in Å between two crystallographic planes from the same family hkl, θ is the diffraction angle, n is an integer and λ is the wavelength of the incoming wave (see Fig. 2.3).

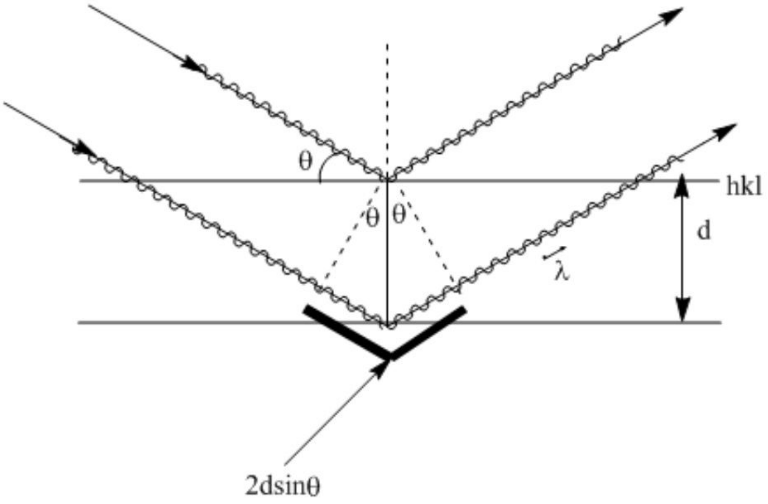

FIGURE 2.3: Schematic drawing of Bragg's law.

Each electron of each atom in a crystal irradiated by a X-ray beam is then providing a scattered wave in a certain direction according to the Bragg's law. As the crystal is a packing of organised atoms, these scattered waves are consequently forming a pattern in a sphere all around the crystal, called the Ewald's sphere. This pattern of scattered waves is directly linked to the reciprocal lattice of the crystal. By resolving it, it will then be possible to determine the atomic structure of the analysed crystal. This is the basic principle of X-ray crystallography.

2.5.2 Single crystal X-ray diffraction

In order to determine the atomic structure of a crystal, several steps of preparation and experiment must be first performed. First of all, a suitable single crystal must be collected for the experiment. Then, this crystal is mounted on the diffractometer and diffraction images of this crystal are collected. The data set is then processed and computed to resolve the atomic structure of the crystal. Finally, this structure is improved by refining the obtained model. After explaining the functioning of a single crystal X-ray diffractometer, we will describe step by step the progress of a Single Crystal X-Ray Diffraction (SC-XRD) experiment.

The most common diffractometer used today for SC-XRD experiments is the four-circle or kappa diffractometer (see Fig. 2.4). The principle of functioning of this device is the following. The crystal (1) is mounted on a goniometer head (2) which is fixed on the diffractometer. The digital camera (3) helps for the centering of the crystal in the middle of the X-ray beam. A high voltage is applied in a X-ray tube (4) that will deliver the X-rays through a monochromator and a collimator (5). The crystal is irradiated by the beam of X-rays and will diffract it so that a bi-dimentionnal charged-couples device (CCD) detector (6) will collect images with the diffracted positions and intensities. A beam-stop (7) is placed between the crystal and the detector so as to keep non-diffracted X-rays from directly hitting the detector. A source of cooling gas (8) can also be added for low temperature measurements. The CCD detector is able to move with a 2θ angle and the crystal can be oriented with three angles ω, ϕ and κ (see Fig. 2.5). In this way, the detector is then able to collect two-dimensional diffraction patterns from all the Ewald's sphere.

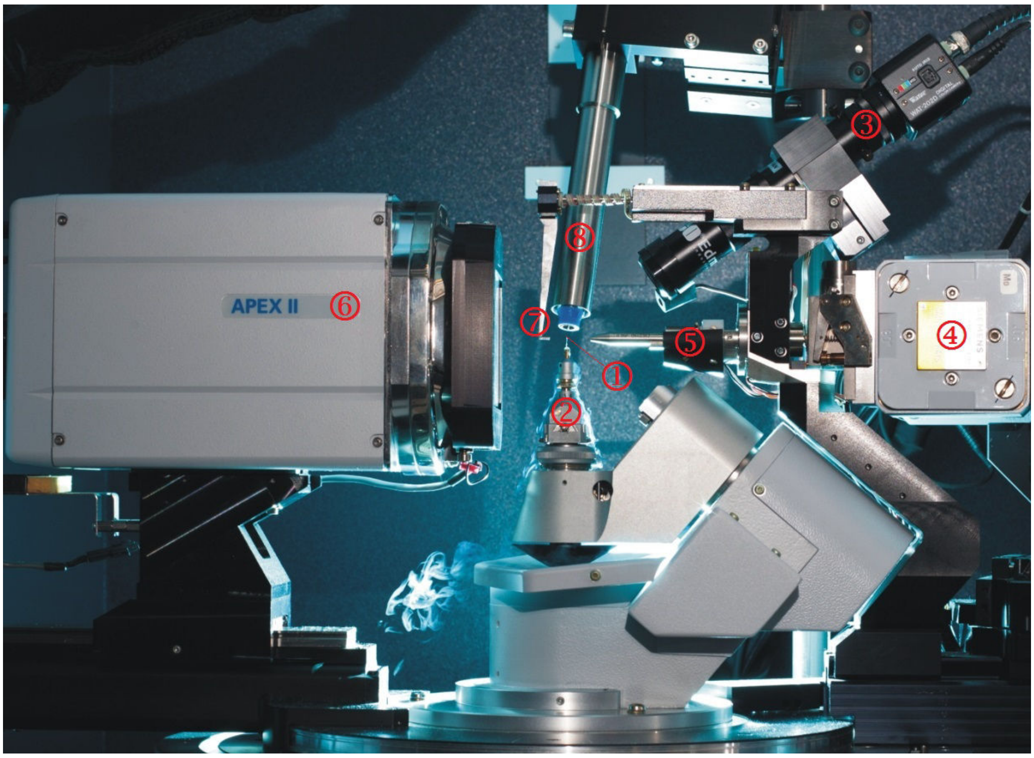

FIGURE 2.4: A four-circle single crystal X-ray diffractometer [34], see text for the description of the elements.

The first step is to select an eligible crystal for the experiment. The specimen must be a single crystal and better not to be twinned. It should be not too small otherwise it will generate low diffraction intensities and not too big so as to avoid an important phenomenon of absorption. Usually, the ideal size is slightly smaller than the size of the X-ray beam. The crystal has to be as much isotropic as possible and should not present cracks. Once an adequate one is selected, it is mounted on the tip of a thin glass fiber with the help of an epoxy resin which is itself attached in a mounting pin. This pin is inserted in the goniometer head and fixed on the diffractometer. The crystal is then centered in the middle of the beam with the help of screws located in the goniometer head that deal with the adjustment of the pin in the three dimensions of space. The crystal is known to be correctly centered when it turns around itself when rotating the three angles ω, ϕ and κ. After that, few images of diffraction patterns are collected by irradiating the crystal and orienting it into few directions. These images are computed in order to determine the orientation of the crystal and the Bravais lattice in which the compound crystallises with no interest for the atomic positions for the moment. Depending on the symmetry of this lattice, it will not be necessary to collect the full Ewald's sphere since the same crystallographic plane will generate several diffracted beams. The more symmetric the system is, the less independent diffracted beams are generated. This step of acquiring few images will then help the program to determine an appropriate data collection strategy [35].

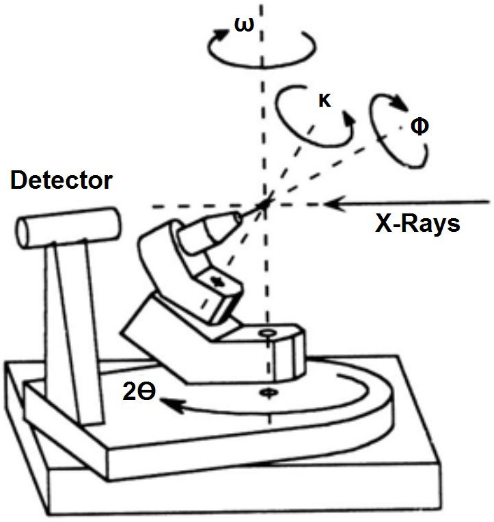

FIGURE 2.5: The possible rotations within the four angles ω, ϕ, κ and 2θ.

Once the complete set of images is collected, all the diffraction peaks are indexed by the Miller's indices. By noticing the systematic extinction conditions given by the symmetry of the system, it will be possible to retrieve the space group in which the compound crystallises and the precise lattice parameters are also determined. All the images obtained from the different orientations of the crystal are then merged, that is, to reconstruct the Ewald's sphere. The same peaks that appear in multiple images will then help to correctly scale their intensities. For the whole dataset, the reflections are then integrated. This step consists of correcting the intensity of the peaks from the background noise in order to maximise the signal/noise ratio. The intensity of the reflections are also corrected from other different factors:

- The Lorentz-polarisation factor. The Lorentz factor is an angular correction applied for each reflections that take into account the speed at which the nodes of the reciprocal space are going through the Ewald's sphere. A lower speed means a higher intensity and that must be corrected. When reflecting on a crystal, the X-ray beam is also partially polarised. The polarisation factor is correcting this effect. Since both corrections depend on the experimental conditions and not on the structural model, they are computed together as a single correction factor.

- The absorption factor. The X-ray beam is partially absorbed by the crystal, this phenomenon is more important for the high-Z elements. Since crystals do not have a perfect spherical shape, the X-ray beam will be differently absorbed depending on how the crystal is oriented. The diffractometry softwares provide good tools to extensively calculate this factor

- The extinction factor. Two types of extinction can occur during a diffraction experiment and must be corrected: (i) the primary extinction, which is responsible for the loss of intensity due to dynamic effect inside every block of a mosaic crystal, (ii) the secondary extinction, occurring when the incident beam crosses a crystal. Each plane of a family satisfying Bragg's law diffracts the incident beam, and thus subtracts part of the intensity to the incident beam. Secondary extinction is equivalent to an increase of the linear absorption factor.

Now the diffracted beams are all indexed, integrated and corrected from different factors, the final dataset obtained has the form of a single file (extension *.hkl) listing all the reflections by their hkl indices, their relative intensity and the error calculated on these intensities. The next step is now to retrieve the atomic structure of the crystallised compound that we analysed. Several softwares have been developed for this task of structural resolution and refinement. In our work, the free package for structural resolution SHELX-2013 [36] is used in the environment of the WinGX software [37] as well as the WinCSD program package [38].

A X-ray wave diffracted from a hkl plane has an amplitude and also a phase that are describing by a mathematical function called the structure factor whose formula is given by the following equation:

$$F_{hkl} = \sum_j f_j \exp\left[2\pi i(hx_j + ky_j + lz_j)\right] \tag{2.3}$$

Where f_j is the amplitude of the wave given by the scatter factor of the j atom, and the terms inside the exponential correspond to the phase which depends on the the atomic positions x_j, y_j and z_j and the Miller's indices hkl.

In a diffraction experiment, the CCD detector is measuring the intensity of the diffracted waves, but the information about the phase of the wave is systematically lost. This knowledge of this phase is crucial for the structure determination so the first step of the resolution is to identify it. There are two main methods to solve this problem.

- The direct methods. The atomicity of compounds and the fact that the electron density cannot be negative at any point of the unit cell dictate certain limitations in the distribution of phases. This method establishes systems of equations that use the intensities of diffracted beams to describe these limitations. The resolution of these systems of equations provides direct information on the distribution of phases. Since the validity of each of these equations is established in terms of probability, it is necessary to have a large number of equations to ascertain the phase values.

- The Patterson method. An electron density map called the Patterson map can be constructed from the inverse Fourier transform of the structure factors of the diffracted waves. This may be interpreted as a map of vectors between the scattering atoms. Vectors in the Patterson space correspond to vectors in the real crystal cell, translated to the Patterson origin. Their weights are proportional to the product of electron densities at the tips of the vectors in the real cell. This method is then useful for the resolution of structures that contain heavy atoms.

The SHELX program works with the hkl reflection file and also with an instruction file (extension *.ins) that will be necessary for the computation of the *.hkl file. Among the multiple instructions that can be employed in the *.ins file (see the SHELX manual for a more exhaustive listing [36]), the main ones that are needed for the resolution of the structure are the following:

- TITL - The title of the project.

- CELL - Lists the wavelength of the X-ray beam and the unit cell parameters of the compound.

- ZERR - Gives the cell formula unit Z and the error on the unit cell parameters given above.

- LATT - The lattice system and an information about whether it is centrosymmetric or not.
- SYMM - The symmetry operations of the space group in which the compound will be handled.
- SFAC - The atomic numbers of the elements. This will give information about their scattering factors.
- UNIT - Number of atoms of each type in one unit cell respecting the SFAC order.
- TREF - Used for direct methods resolution.
- PATT - Used for Patterson method resolution.
- HKLF - Tells the program in which format is written the *.hkl file.
- END - Terminates the program.

After running SHELX with any instruction of resolution, the program gives a list of electronic densities and their coordinates converted from the reciprocal space to the real space. The role of the manipulator is now to assign the correct atoms to these positions. Usually, positions with the highest electronic density value are first assigned to the heaviest atoms present in the compound. The map of the electronic densities deducted from the assigned electronic density of the selected atoms is called the difference Fourier map. The tentative model is then refined in order to recalculate this difference Fourier map. The value of the phases determined during the resolution step are still estimations and remain to be optimised. This is the aim of the refinement step, the difference between the module of the obtained structure factor and the one from the experimental model is minimised by the least square method. For the refinement, some other instructions are usually included in the instruction file:

- MERG - Instruction to sort and merge reflections before refinement, counting Friedel's opposite or not.
- FMAP - Define the way of calculating the Fourier map.
- PLAN - Number of peaks wanted in the Fourier map.
- BOND - Calculating bond length between the assigned atoms.
- L.S. - Instruction for the number of least square cycles wanted.
- WGHT - The weighting scheme used for the least square parameters.
- FVAR - Managing all free variables of the refinement.

Below these new instructions, the assigned atoms are now also taking place in the instruction file as the following:

n x y z Occ DWF

Where n is the atomic number of the element as inputed in the SFAC instruction, x y z are the coordinates of the atom in the unit cell, Occ is its occupancy factor and DWF is its Debye-Waller factor. The Debye-Waller factor, also called the temperature factor, is used to describe the X-ray scattering attenuation caused by thermal motion of the atom.

The complete structure of the compound is determined by a trial and error approach. After each cycle of refinement, the distances between each assigned atoms as well as the Debye-Waller factors are checked. If an interatomic distance is inconsistent with a possible distance or if a temperature factor is too high or too low, this is a sign of a potentially wrong attribution of the atom. This atom is then removed from the list, the difference Fourier map is recalculated and other atoms are assigned to the found electronic densities.

The atomic displacement parameters (ADPs) of the attributed atoms are originally refined as isotropic which does not fully represent the reality. To describe the atom vibrations when refining the ADPs as isotropic, the program generate false peaks of electronic densities in the difference Fourier map around the corresponding atoms. When these atoms seem to be correctly assigned, their ADPs can be refined as anisotropic in order to improve the model. The instruction ANIS is then included for the chosen atoms in the *.ins file that will introduce six more parameters describing the ellipsoids of the anisotropic ADP. This normally makes the noise peaks disappear after another cycle of refinement.

Once no significant peaks are remaining on the difference Fourier map (highest peak and deepest hole not higher than few $e^{-}.\text{Å}^{-3}$ in absolute value in the case of intermetallic compounds) and that the established structural model looks acceptable (interatomic distances, thermal factors, ellipsoids of ADP), the structure determination is done. At the end, as well as after each refinement, the reliability of the established model can be checked with different factors:

- R(int). This factor measures the merging error, namely the precision and the reproducibility of the reflections after data reduction. Thus, this factor does not depend on the structural determination but testify to the quality of the *.hkl file. Its value is given by:

  $$R(int) = \frac{\sum |F_{obs}^2 - F_{obs}^2(mean)|}{\sum F_{obs}^2} \tag{2.4}$$

  With F_{obs} and F_{obs}(mean) the observed and the observed mean structure factors. A good data collection and reduction from a qualitative crystal gives a R(int) value lower than 0.05.

- $R1$. This is the residual factor or R-factor, it quantifies how well the refined structure matches the observed data and is given by the equation:

  $$R1 = \frac{\sum ||F_{obs}| - |F_{calc}||}{\sum |F_{obs}|} \tag{2.5}$$

  With F_{obs} and F_{calc} the observed and calculated structure factors respectively. It has the same magnitude as R(int). Thus, a good refinement of a correct structure determination gives values of $R1$ lower than 0.05. A value between 0.05 and 0.10 is still considered as acceptable.

- $wR2$. The weighted R-factor is directly related to the quantity that is minimised in the least-square refinement. Its changes show whether changes in the structure model are actually meaningful. Its is calculated by:

  $$wR_2 = \sqrt{\frac{\sum w(F_{obs}^2 - F_{calc}^2)^2}{\sum w(F_{obs}^2)^2}} \tag{2.6}$$

  For statistical reasons, refinement against F^2 gives values approximately twice as high than those from the $R1$ factor. A good refinement usually exhibits values for this $wR2$ below 0.10.

- GoF. The Goodness of Fit is another way to calculate how good the established model fits the observed data. Its formula is:

  $$GoF = \sqrt{\frac{\sum w(F_{obs}^2 - F_{calc}^2)^2}{N_{ref} - N_{par}}} \tag{2.7}$$

  Where N$_{ref}$ and N$_{par}$ are the number of independent reflections and the number of the parameters refined respectively. This factor should give values close to 1. A good refinement provides a GoF between 0.9 and 1.2.

At the end of the refinement, if the model shows good values for these factors, the structure can be finally accepted. With a last instruction in the *.ins file, the full informations about data collection, established model, refinement etc... are written in a *.cif file (Crystallographic Information File). The *.cif file is the standard format for presenting crystallographic data and can be opened by structure visualisation programs such as VESTA or DIAMOND for a better 3-D representation of the model.

2.5.3 Powder X-ray diffraction

The structure determination of a compound can also be carried out with the Powder X-Ray Diffraction technique (PXRD). The principle is the same as SC-XRD with the difference that a large quantity of the sample reduced into powder is analysed. Basically, this amounts to measure multiple single-crystals oriented in all the directions at the same time. In our studies, the powder X-ray diffraction was employed for phase identification but not for structural determination. So we will not focus on this aspect here.

The critical part in PXRD is the good preparation of the sample. The quality of the data obtained essentially depends on the quality of the sample. This is based on three essential points:

- The quantity. The larger the quantity of powder is analysed, the stronger the detected signal will be. At least few tens of milligrams are usually required.

- The homogeneity. The powder has to be correctly grinded so as to obtain a fine powder of homogeneous grains. If not correctly grinded, the measurement can suffer from problems of micro-absorption.

- The orientation. The grains have to be randomly oriented. If the grains are platelet-shaped for example, this will cause problems of preferential orientation which will lead to a preferential scattering of certain families of hkl planes.

PXRD diffractometers have the same constitutive parts as SC-XRD diffractometers, i.e. a goniometer, a X-ray tube, a detector etc. . . The main difference is based on the geometry of the apparatus. In the case of a powdered sample, it does not need to be oriented in all the directions so the three angles ω, ϕ and κ of the four-circle diffractometer are not appropriate anymore. Diffractometers from three different geometries are commonly used in laboratories today [39].

- The Bragg-Brentano geometry. The X-ray source can be fixed and the sample and detector can be rotated by θ and 2θ angles respectively (see Fig. 2.6 a). The incoming X-ray beam is defocused and controlled by a divergence slit so as to irradiate the whole sample holder which has a diameter of few centimeters. By reflection on the sample holder, the scattered beam is then refocused on the detector, controlled by a receiving slit. Sideways divergence of either the incident or scattered beam can be controlled using Soller slits inserted in the X-ray beam path. These consist of a set of fine parallel foils which prevent angular divergence of the beam out of the θ-2θ plane. This gives a less asymmetric and narrower peak shape, especially at low scattering angles.

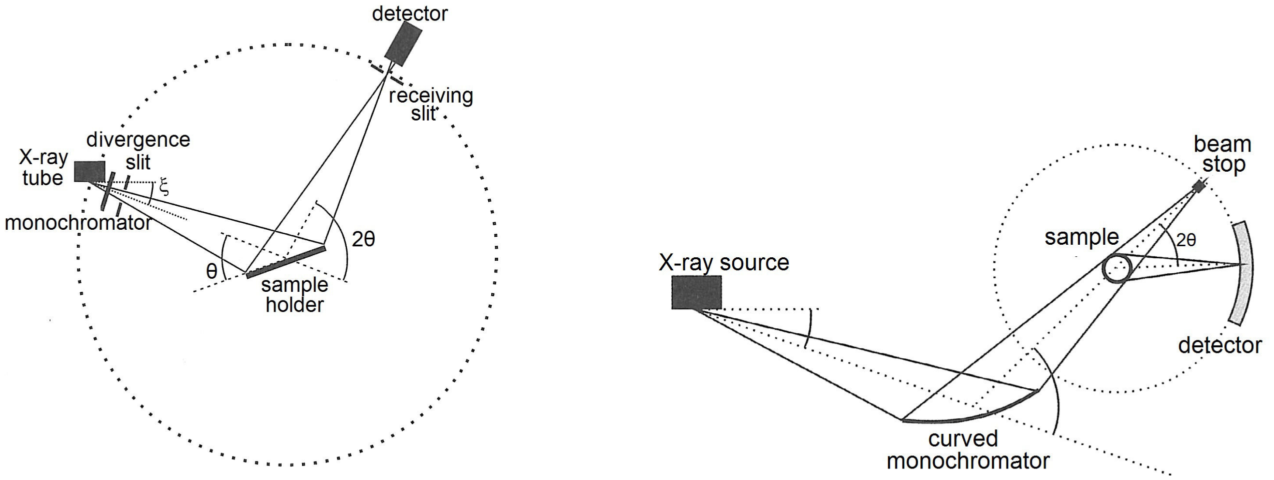

(a) Bragg-Brentano geometry (b) Guinier geometry

FIGURE 2.6: Schematic principle of Bragg-Brentano and Guinier powder X-ray diffractometer geometry

- The Guinier geometry. The X-ray source and the sample are fixed. A polychromatic divergent X-ray beam hits first a curved monochromator so as to focus it on the detector that is able to move along a 2θ angle (see Fig. 2.6 b). Before arriving on the detector, the monochromatised beam irradiates the powder sample which is enclosed in a thin film transparent to X-rays and the diffracted beams are counted. While Bragg-Brentano geometry works in reflection, Guinier works in transmission.

- The Debye-Scherrer geometry. This is the simplest and the oldest concept of diffractometer. The X-ray beam is collimated, monochromatised and then diffracted by the sample in a capillary located in the middle of a circular chamber. Unlike the other methods, all the parts are fixed, the diffracted beams are counted on a film placed all around the chamber (see Fig. 2.7 a). This is the original concept of the Debye-Scherrer chamber, today this method is still exploited but with few different changes. In the synchrotron radiation powder X-ray diffraction for example, the capillary is rotating around its axis and the diffracted beams are counted by a detector rotating around a 2θ axis (see Fig. 2.7 b).

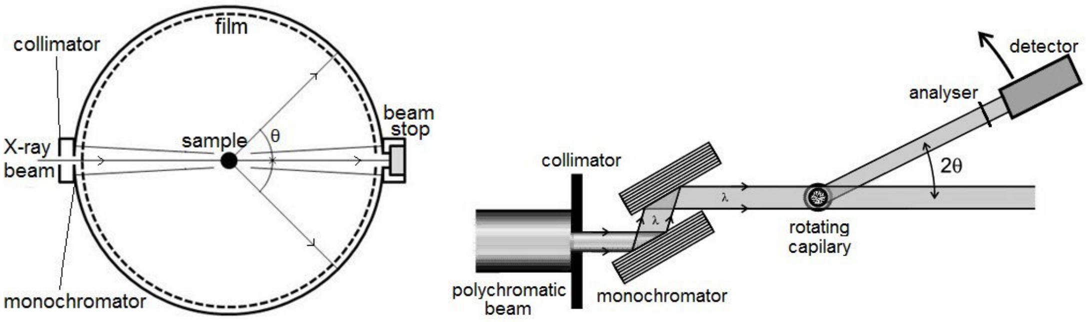

(a) Debye-Scherrer geometry (b) Synchrotron geometry

FIGURE 2.7: Schematic principle of Debye-Scherrer and example of synchrotron powder X-ray diffractometer geometry

The data collection strategy is defined by the user who chooses the angular domain 2θ, the angular step between each measurement and the time of acquisition of each step to obtain an accurate statistic. The data obtained is a diagram with a number of counts on the Y axis as a function of the 2θ angle on the X axis. Once the diffractogram is acquired, the diffraction peaks remain to be indexed. Since the elements that constitute the sample analysed are known, this limits the possibilities of phases. The diagram obtained from the measurement will then be compared to the experimental diagrams reported in the literature. In this work, this step has been handled with the software WinXPow using the Inorganic Crystal Structure Database (ICSD) [40]. An example of a typical indexed powder X-ray diffractogram is presented Fig. 2.8. If it is not possible to index several diffraction peaks with patterns from known compounds, there is potentially an unknown phase present in the sample. In the same way as with SC-XRD, the positions of the diffraction peaks from the unknown phase are indexed in order to retrieve their associated hkl indices. That will lead to the determination of the unit cell in which the compounds crystallises and its lattice parameters. In PXRD, this is a complicated task that increases in difficulty as the unit cell decreases in symmetry. Such task must be solved with the help of algorithms dedicated to it. The WinXPow software provides the possibility to work with three of them, TREOR [41], ITO [42] and DICVOL [43]. The determination of the unit cell will help to confirm whether the compound is known or not. If not, its atomic structure remains to be solved. As mentioned above, this can be accomplished with PXRD but all structure determinations were managed with SC-XRD in this thesis.

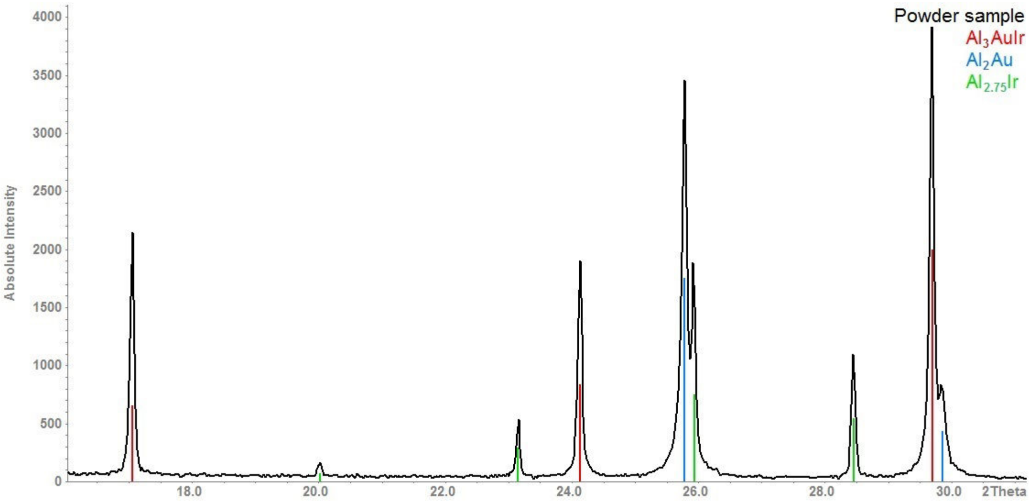

FIGURE 2.8: One section of a PXRD pattern of an Al-Au-Ir alloy, indexed with the three identified phases.

2.6 Scanning electron microscopy and Energy dispersive X-ray spectroscopy

2.6.1 Scanning electron microscopy

The SEM technique of characterisation provides information about the general aspect of the sample topography. Areas ranging from approximately 1 cm to 5 microns in width can be imaged in a scanning mode using conventional SEM techniques (magnification ranging from 20X to approximately 30000X, spatial resolution of 50 nm to 100 nm). This technique is usually coupled with Energy Dispersive Spectroscopy that can provide the chemical composition of the analysed surface. The following paragraphs will describe the general principle of these techniques.

First, the samples have to be correctly prepared for the analysis. In the case of metallic alloys, the samples are usually finely polished for a better observation of their microstructure. Silicon carbide grinding paper is commonly used for this task, finely polished surface is obtained with diamond polishing suspension with grain size down to 0.25 μm. The sample must be perfectly flat in the microscope and is often embedded in a resin with a mould in order to obtain the polished surface exactly parallel to the surface of the sample holder.

Unlike optical microscopes which use light waves, SEM relies on an electron beam to produce the image. As a result, SEM is working under vacuum so that the electron beam does not interact with the ambient air. However, the sample needs to be conductive enough to dissipate the charges. The main advantage to work with an electron beam is that it has a much smaller wavelength than the visible light, thus providing images with a much higher resolution than optical microscopes. Once the sample is placed on the sample holder and the chamber is pumped to reach high vacuum, the SEM works as the following (see Fig. 2.9):

An electron beam is produced within the electron gun where electrons are emitted from a heated tungsten filament. This beam is accelerated by a high voltage created between the wire and the anode. Then, it passes through a combination of electromagnetic lenses and apertures to produce a focused beam of electrons. A mechanism of deflection coils guide the beam so that it scans the surface of the sample in a rectangular frame. As the beam hits the surface of the sample, it produces secondary electrons, backscattered electrons and characteristic X-rays. These signals are collected by appropriate detectors to form images which are then displayed on the computer screen. Each of these three interactions are complementary and provide different useful informations:

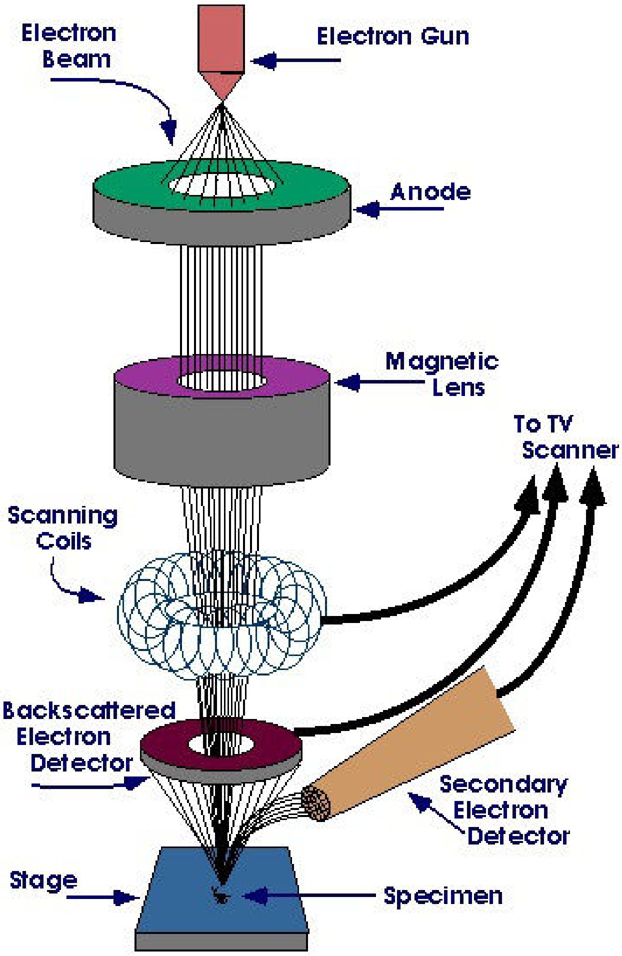

FIGURE 2.9: Schematic principle of functioning of a scanning electron microscope.

- The secondary electrons (SE). The SE are generated by the incident electron beam which loses part of its energy. As a consequence, thousands of SE can be obtained from a single incident electron. This large amount of secondary electrons are able to provide images with a good signal/noise ratio and resolution. Because of their low energy, these secondary electrons mostly represent the topography of the sample. This guaranties a large depth of focus when observing nano-objects but is not very accurate to observe a phase contrast in case of metallic polished samples.

- The back scattered electrons (BSE). These electrons are generated by colliding elastically with the surface of the sample. The higher the atomic number of the element, the more it provides this type of electron. As a result, heavy elements appear usually brighter on the image. This has the advantage of displaying a good phase contrast which is useful in metallography. However, because of their high energy and limited number, back scattered electrons provide images with a lower resolution than when using secondary electrons. A comparison of the same SEM image taken in SE mode and in BSE mode is shown in Fig. 2.10.

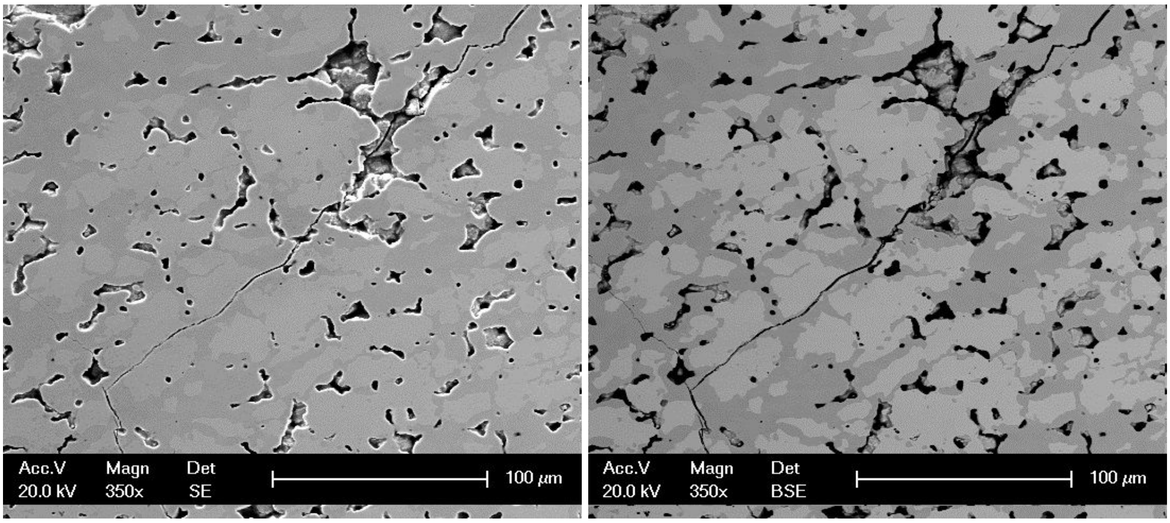

(a) SE mode (b) BSE mode

FIGURE 2.10: SEM micrograph of an Al-Ir alloy. Light and dark gray areas are two different phases while black regions are holes. While the left hand side image exhibits a better depth resolution, the second image shows a more pronounced phase contrast.

- X-rays. An incoming electron "collides" with an inner shell electron. The ejected electron leaves a hole in the inner shell. The latter will be filled by an outer shell electron with simultaneous emission of an X-ray photon. This photon is of equal energy than the difference of energy between the two energy levels. A cascade emission is generated until the last layers of electrons have been replaced hence creating a ray spectrum. Detecting this spectrum gives useful information about the chemical composition of the sample. This is the principle of the EDS technique that will be discussed hereafter.

2.6.2 Energy dispersive X-ray spectroscopy

The EDS detector measures the relative abundance of emitted X-rays versus their energy. The energy is characteristic of the element from which it was emitted, thus by indexing the rays on the spectrum, it is possible to retrieve the elements present in the sample. The total X-ray intensity for a particular electronic transition is divided between several lines (For example Kα and Kβ for the K transition). By measuring and comparing the intensities of all the lines, it is also possible to obtain quantitative data about the chemical composition of the analysed region. The spectrum provided by EDS also exhibits a certain continuous background upon which the characteristic lines resulting from electronic transitions are superimposed . This continuum arises from interactions between incident electrons and atomic nuclei. Its intensity decreases with increasing X-ray energy and is systematically subtracted from the whole spectrum. A typical EDS spectrum is shown in Fig. 2.11

The main problem with EDS is that X-rays can travel important distances in materials. When an incident electron generates a secondary electron deep below the surface, this secondary electron does not have sufficient energy to come out at the surface, which is not the case with X-rays. EDS is then a technique that does not scan only the surface, but also a non negligible quantity of the volume below. The penetration depth of the incident electrons is principally function of the acceleration voltage, the

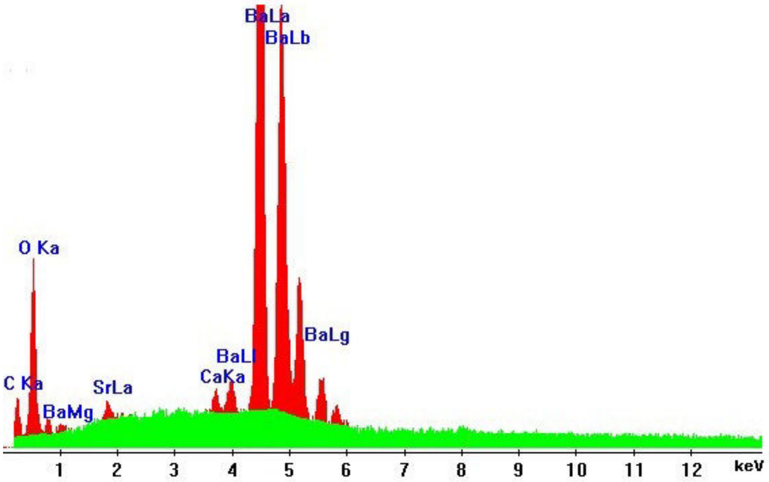

FIGURE 2.11: Typical energy dispersive X-ray spectrum. The background is shown in green while the characteristic peaks are depicted in red and indexed with the corresponding electronic transition of elements.

material atomic number and the angle between the incident beam and the surface. However, lowering the acceleration voltage also decreases the resolution of the measurement. Thus when carrying out an EDS measurement, a compromise must be found between the resolution and the scanning depth.

The chemical composition of a sample region obtained with EDS must be taken with care. If the SEM image shows the surface of the sample, the composition measured with EDS is relative to a volume up to several microns below this surface. In the case of metallic alloys, when measuring the composition of one phase that have typical grains size of about several microns, other phases with different compositions located below those of interest may interfere with the measurements, hence leading to an incorrect stoichiometry. In order to solve this problem, a large quantity of measurements are usually taken to obtain good statistics about the chemical composition. The typical error when acquiring the chemical composition with SEM is about 1 to 2 percent in relative value.

EPMA and WDS

The Electron Probe MicroAnalyser (EPMA) is an analytical tool that works exactly as a SEM with the difference that it is equipped with a different spectrometer. The same way as a SEM is coupled to EDS, an EPMA is coupled to wavelength dispersive X-ray spectroscopy. In WDS, the emitted X-rays are selected using an analytical crystal. When X-rays encounter the analytical crystal at a specific angle, only those which satisfy Bragg's Law are reflected and a single wavelength is passed on to the detector. All the interactions electron-matter as well as the problem with the depth of the scanning that are encountered with EDS are the same with WDS. The advantage to choose WDS is that this particular detection leads to more precise quantitative values of the chemical composition of the sample.

2.7 Thermal analysis

Thermal analysis techniques such as differential thermal analysis or differential scanning calorimetry are also useful characterisation techniques that have been used in our studies. As explained above, the intermetallic phases that constitute the metallic alloys can be identified by their atomic structure with PXRD. This task can also be done with thermal analysis by identifying their characteristic temperatures of transition (melting point, boiling point etc...). DTA is mainly employed for this task of identification but also for establishing phase diagrams by determining the temperature of the liquidus, the solidus and also invariant reactions like eutectic and peritectic transformations. DSC is utilised for more quantitative measurements, namely the determination of enthalpies of transformation (enthalpy of fusion, solidification, etc...) and heat capacities. Both these techniques consist of measuring the difference in temperature between a sample and an inert standard during programmed heating and cooling cycles. As such, the measurements are sensitive to the difference between the enthalpy vs. temperature relation of the sample and the enthalpy vs. temperature relation of the standard. These two techniques of DTA and DSC are detailed in the following sections.

2.7.1 Differential Thermal Analysis

The sample is first placed in a capped alumina crucible designed for the DTA apparatus. If the sample may react with alumina, it is also possible to use zirconia or yttria crucibles. All these crucibles have the advantage to be good thermal conductors and to prevent any transformation reaction until very high temperatures. An inert reference, usually alumina powder, is placed in another crucible in the same proportion as the sample. The two crucibles are placed on a support that contains two thermocouples, one for each crucible, and inserted into the DTA chamber. The chamber is hermetically closed, evacuated and refilled with a neutral gas several times to avoid oxidation when heating. The measurement is carried out under a neutral gas flow for evacuating potential evaporated elements. The heating rate, the maximal temperature of the measurement and the cooling rate are then programmed. Increasing the mass of the sample and the heating speed will result in increasing the measured signal. However, the more important the signal, the less the resolution of the peaks are, i.e. close peaks will be difficult to resolve. The signal difference between the thermocouple related to the sample and the one related to the reference is measured. It is called the heat flow and has a dimension of a voltage (μV). When the sample undergoes a reaction, this results in one peak on the heat flow signal (see Fig. 2.12). If the sample is at the equilibrium during all the measurements, the same peaks should appear on the heating and on the cooling curves. The appropriate value of the temperature (T_{onset}, T_{peak}, T_{offset}) that should be kept to be associated to the reaction depends on the nature of the sample and of the reaction itself [44].

As mentioned above, DTA can be used for phase identification, usually as a confirmation of PXRD. With a knowledge of the constituting elements present in the sample, the peaks obtained on the DTA curve can be related to the reactions and phase formations of the appropriate compounds. Inversely in the case of the establishment of phase diagrams, it is important to know the phase composition of the samples before analysing them by DTA. The thermal conditions of the measurements can affect the sample by stabilising a phase at the expense of an other. In that case, the DTA signal will exhibit a peak on the heating curve that will not appear on the cooling one (vanishing phase)

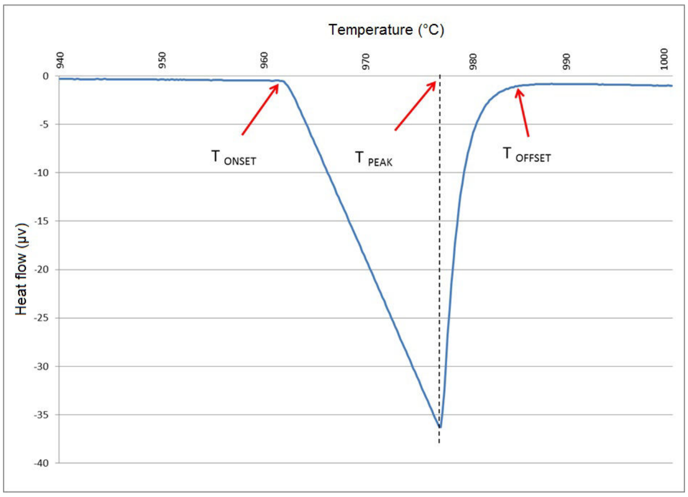

FIGURE 2.12: Typical DTA curve showing the melting of pure silver, T_f = 961.8°C [45].

and inversely, a new peak will appear on the cooling curve while nothing will be observed on the heating curve at the same temperature (stabilised phase). To clarify such situation, it is interesting to know the phase composition of the sample also after the DTA measurement.

If the basic principle of DTA is easy to understand, the full determination of a phase diagram with metallic alloy samples can be a troublesome task. The events appearing on the heat flow signal are governed by several parameters such as the metallurgical state of the sample, the heating and the cooling rate, the type of reactions observed (eutectic reaction, melting, freezing etc...), the stability of the phases etc... Thus, it happens that the temperatures that can be extracted from DTA scans have no "meaning" with regard to the alloy. Sometimes, some of these temperatures are merely an indication of thermal lags within the instrument. Further information about the interpretation of DTA measurements of metallic alloys are detailed in Ref. [44].

2.7.2 Differential Scanning Calorimetry

The DSC technique is very similar to DTA. While DTA measures the heat flow between the sample and a reference, DSC with a proper calibration can directly measure the heat flow of the sample and the reference. In other words, in DSC the difference in the amount of heat required to increase the temperature of the sample and the reference is measured as a function of temperature. In addition, to observe the temperatures of reactions, it is also possible to measure the energies of these reactions. The term differential scanning calorimeter was originally applied to instruments with separate heaters for the reference and the sample. The heat flow signal of a true DSC is the power difference required to keep the temperatures of the reference and sample identical during a defined temperature ramp. This type of instrument is today called a power compensating DSC. Many instruments with a single heater are called a DSC, but are more properly called a heat flux DSC. Although quantitative measurements of heats of transformation can also be evaluated by DTA, there are differences in sensitivity and accuracy comparing to DSC.

DSC calorimeters are usually calibrated using several pure metallic standards. These standards are measured with DSC under given conditions. Knowing their melting point and their melting enthalpy, it is then possible to calibrate the apparatus with the appropriate values. Full explanation about the calibration of DSC calorimeters is given in reference [46]. Once the device is calibrated, the sample is analysed in the same way as for DTA with the difference that the heat flow signal is now given in Watts. With knowledge of the values of the mass of the sample and the heating and cooling rates, the DSC curve can be drawn as normalised heat flow (W.g^{-1}) vs. time (s). By measuring the area under the peaks, it is then possible to directly retrieve the enthalpy of the reaction (J.g^{-1}). In the same way and with an appropriate temperature program, it is also possible to calculate the heat capacity of the sample [47].

Chapter 3

The aluminium-iridium system

3.1 Introduction

For the reasons described in Chapter 1, the study of complex metallic alloys has attracted much interest within the past decades. When looking into the literature, aluminium-based binary or ternary systems, in association with one or two transition metals, have shown to exhibit such complex compounds [48–52].This is well illustrated in the case of the aluminium-iridium system which has been already intensively investigated. As it will be described hereafter, some discrepancies regarding the phase diagram and the structure identifications still remain. The present study has then been carried out with the aim of establishing a new assessment of the aluminium-iridium system. This work begins with an exhaustive chronological review of the literature about this system. The existing Al-Ir binary compounds will be listed and the evolution of the phase diagram through the years will be presented. Then, the complete experimental procedure of the reexamination of the phase diagram will be detailed before presenting the new features brought to the system.

3.2 Review of the literature

3.2.1 Discovering the first Al-Ir compounds

The first compound to be reported in the Al-Ir system is attributed to Esslinger and Schubert who identified the AlIr phase in 1957 in a 50/50 at. % as-cast sample [53]. They were initially studying several compounds of the NiAs-type when they determined the structure of their AlIr sample as a *bcc* packing of the CsCl-type with lattice parameter a = 2.983 Å (Pearson symbol $cP2$). In a 1968 study, when preparing intermetallic phases using base metal oxides reduction, Schulz *et al.* also reported the AlIr phase with the same structure and lattice parameter a equal to 2.978 Å [54]. In 1986, Axler and Roof accidentally produced a single crystal of AlIr and after further examinations, they confirmed the CsCl-type structure with a refined lattice parameter a = 2.9867 Å [55]. Edshammar reported the second compound of the Al-Ir system in 1967 [56]. He prepared a sample of a single phase Al_3Ir by arc-melting and after analysis of single crystals obtained from the crushed melt, he determined the structure to be hexagonal ($P6_3/mmc$ group, Pearson symbol $hP8$) with lattice parameters a = 4.246 Å and c = 7.756 Å. In this work, he also observed a cubic polymorph of this Al_3Ir phase but could not give any more details about its structure. One year later, the same author published a study about the crystal structure of Al_9Rh_2 and Al_9Ir_2, two new phases in the Al-Rh and Al-Ir systems [57]. He prepared the samples by arc melting and obtained single crystals of Al_9Rh_2 but did not find any suitable ones for analysing the Al_9Ir_2 crystal structure. Since these two phases exhibited similar X-ray patterns, Edshammar assumed that they had the same structure, i.e. isomorphous to the Al_9Co_2 compound, crystallising in a monoclinic cell (space group $P2_1/c$, Pearson symbol $mP22$). The lattice parameters found for the Al_9Ir_2 phase were a = 6.378 Å, b = 6.430 Å, c = 8.732 Å and β = 94.77°. In 1968, Ferro *et al.* [58] investigated thoroughly the Al-Ir system by reporting X-ray diffraction and micrographic examinations of 33 Al-Ir samples. The latter were prepared by induction melting and annealed to different temperatures for several days. They confirmed the existence of the cubic AlIr and the hexagonal Al_3Ir compounds but also reported the following compounds: Al_5Ir, $Al_{3.75}Ir$ (both unknown structures) and $Al_{2.75}Ir$, existing over a homogeneity range from 26 to 28 at. % Ir. The $Al_{2.75}Ir$ compound is isomorphous to the $AuZn_3$ cubic compound with the lattice parameter a comprised between 7.660 Å and 7.685 Å. As Axler *et al.* will suggest later [59], the cubic polymorph of Al_3Ir discovered by Edshammar is most probably this $Al_{2.75}Ir$ phase rather than a structural modification of the hexagonal Al_3Ir phase. Ferro *et al.* also specified the structure of this hexagonal Al_3Ir phase to be of Na_3As-type and estimated the composition of an AlIr + Ir eutectic at about 70 at. % Ir.

3.2.2 Establishing the phase diagram

At this point in the late 1960s, several Al-Ir binary compounds were reported and most of their structure were determined. Some partial phase diagrams were attempted but not a single complete experimental phase diagram was established yet. We will now describe authors by authors the main contributions brought to the system that led to the most complete phase diagram we know today.

Axler *et al.*

In 1989, Axler *et al.* [59] reported the first experimental diagram of the Al-Ir system. It was built from X-ray powder diffraction data, electron microprobe examination and differential thermal analysis obtained from 15 samples with compositions covering the whole range of the phase diagram. The samples weighing 2 to 4 grams were synthesised by arc melting, inverted and remelted several times to ensure homogeneity and annealed at different temperatures for several days. They revealed the existence of 5 compounds: Al_9Ir_2, $Al_{13}Ir_4$, Al_3Ir, $Al_{2.75}Ir$ and AlIr. The $Al_{3.75}Ir$ and Al_5Ir phases of Ferro *et al.* were not to be found. It is likely that the Al_5Ir phase corresponds to the Edshammar's Al_9Ir_2 phase which is quite close in composition. It is also worth noticing that unlike the 13:4 phases (i.e. $Al_{13}Co_4$, $Al_{13}Rh_4$, $Al_{13}Ru_4$, $Al_{13}Os_4$…), no 3.75:1 phases (or 15:4) could be found in the literature. Again considering the compositions, the $Al_{13}Ir_4$ phase of Axler *et al.* was probably what Ferro *et al.* [58] reported as $Al_{3.75}Ir$. Axler *et al.* were the first to report this $Al_{13}Ir_4$ compound. However, they could not make any structural determination due to the rather complex X-ray pattern this phase exhibited. For the other already known phases, they reported that:

- The compounds $Al_{2.75}Ir$ and AlIr exist over a homogeneity range of 1.5 at. % and 4 at. %, respectively.
- Only the AlIr phase melts congruently. The other phases melt peritectically.
- Two eutectic reactions occur in the system, at 0.1 at. % Ir (Al + Al_9Ir_2) and 650°C and at 70 at. % Ir (AlIr + Ir) and 2058°C. The remaining phases are leading to a cascade of peritectic reactions.

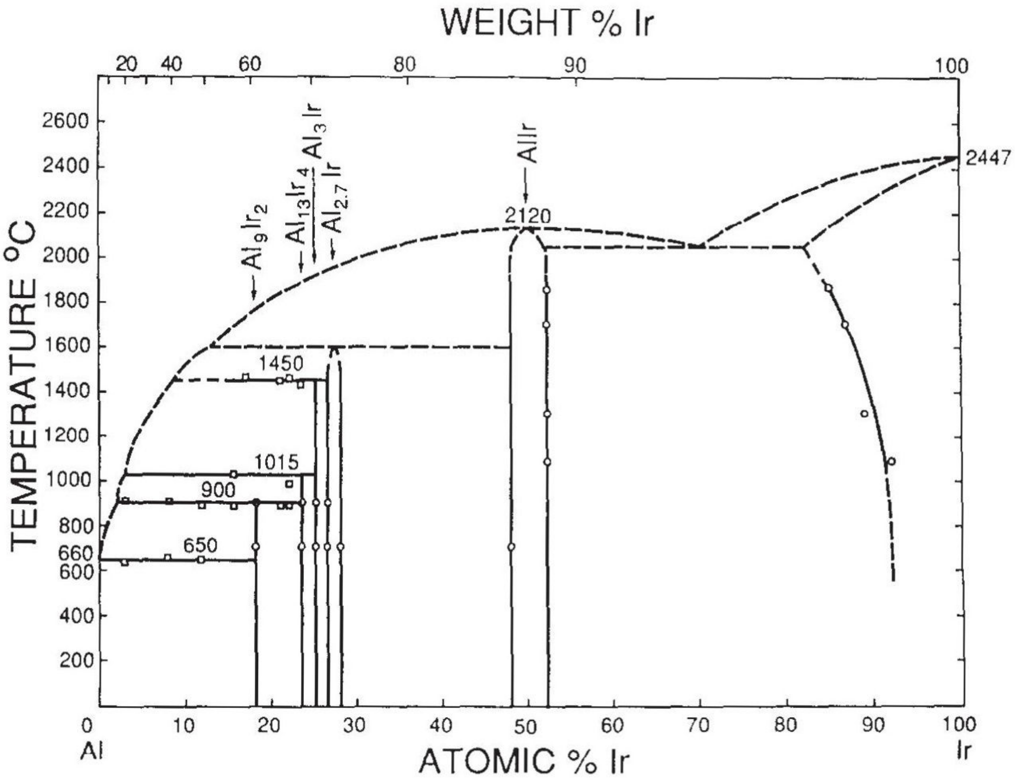

FIGURE 3.1: Al-Ir phase diagram after Axler *et al.* [59].

- The solubility of Al in Ir is calculated to be 15 at. % at 1850°C which extrapolates to a maximum of 18 at. % at 2058°C. The solubility of Ir in Al was determined to be less than 0.1 at. %.
- The Al_9Ir_2, $Al_{13}Ir_4$ and Al_3Ir phases decompose at 900°C, 1015°C and 1450°C respectively.

With all these experimental results, they drew the phase diagram of the Al-Ir system which is presented in Fig. 3.1.

Grin *et al.*

Grin *et al.* in 1997 [60] studied the crystal structure of the $Al_{2.75}Ir$ and $Al_{2.63}Rh$ phases. For the Al-Ir compound, they prepared 3 samples by arc-melting pellets of mixed and pressed pure elemental powder. The compositions of the samples were $Al_{71.5}Ir_{28.5}$, $Al_{73}Ir_{27}$ and $Al_{75}Ir_{25}$. After powder and single-crystal X-ray diffraction analysis, the sample $Al_{73}Ir_{27}$ was found to contain the single phase $Al_{2.75}Ir$. They determined the lattice parameter a to be equal to 7.6789(3) Å and gave more precisions about the crystal structure of this compound. After several trials, they finally successfully solved the structure in the space group $P23$ (Pearson symbol $cP60$). While Ferro *et al.* [58] estimated the structure to be of $AuZn_3$ type, Grin *et al.* described the structure as either a defect and distorted variant of the hypothetic structure of $Al_{13}Ir_4$ ($Al_{13}Os_4$ type) or as a defect variant of the $AuZn_3$ structure with inclusion of additional atoms on the diagonals of the unit cell. This leads to a complex structure with several atomic positions of aluminium partially occupied and with icosahedral environments around some iridium atomic positions. Grin *et al.* discussed a lot about the comparison with the structure

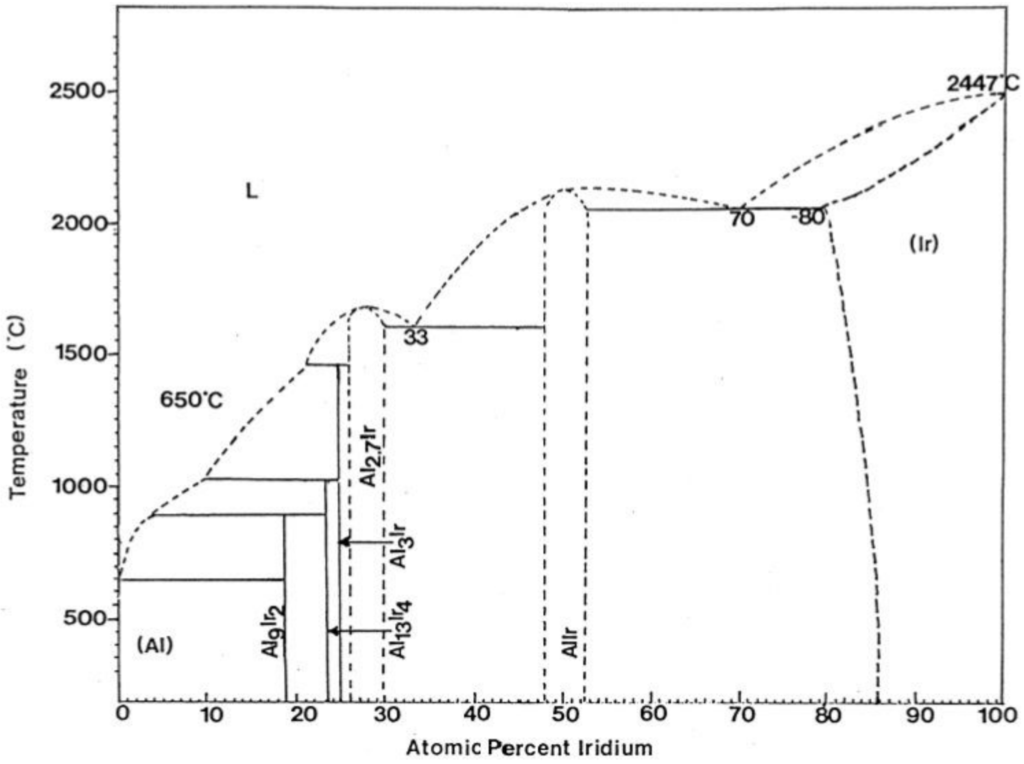

FIGURE 3.2: Al-Ir phase diagram after Hill *et al.* [21].

of $Al_{13}Ir_4$, but this compound remains to be fully identified. They also carried out some WDS measurements on this $Al_{2.75}Ir$ phase that match with the homogeneity range of about 1 at. % previously estimated by Axler *et al.* [59].

Hill *et al.*

In 1998, Hill *et al.* [21] reported the second experimental Al-Ir phase diagram by analysing 13 different Al-Ir alloys with compositions ranging from 2 at. % Ir to 88 at. % Ir. The samples were arc-melted, inverted and remelted several times before undertaking different heat treatments. EDS analysis processed on a scanning electron microscope, X-ray powder diffraction and also Vickers hardness tests were carried out on each sample. In the establishment of the phase diagram, melting points were taken from the DTA analysis of Axler *et al.* The Al-Ir phase diagram that Hill *et al.* reported was in good agreement with the one from Axler *et al.* [59] except for the decomposition of the $Al_{2.75}Ir$ phase which is here estimated to melt congruently rather than peritectically (see Fig. 3.2). Considering this fact, Hill *et al.* deduced the existence of the eutectic $Al_{2.75}Ir$ + AlIr at about 33 at. % Ir since it necessitates that the liquidus temperature decreases on both side of the composition of the phase. Except for this point, Hill *et al.* reported the same phases than Axler *et al.*, i.e. Al_9Ir_2, Al_3Ir, $Al_{2.75}Ir$, AlIr and also $Al_{13}Ir_4$ but did not contribute to the clarification of the crystal structure. The Vickers hardness tests revealed that the presence of the AlIr phase in the samples had a beneficial effect on the hardness of these samples, i.e. the maximum hardnesses measured, 1000 VPN (Vickers Pyramid Number), occurred for alloys which contained the AlIr phase. A similar effect has been observed when there

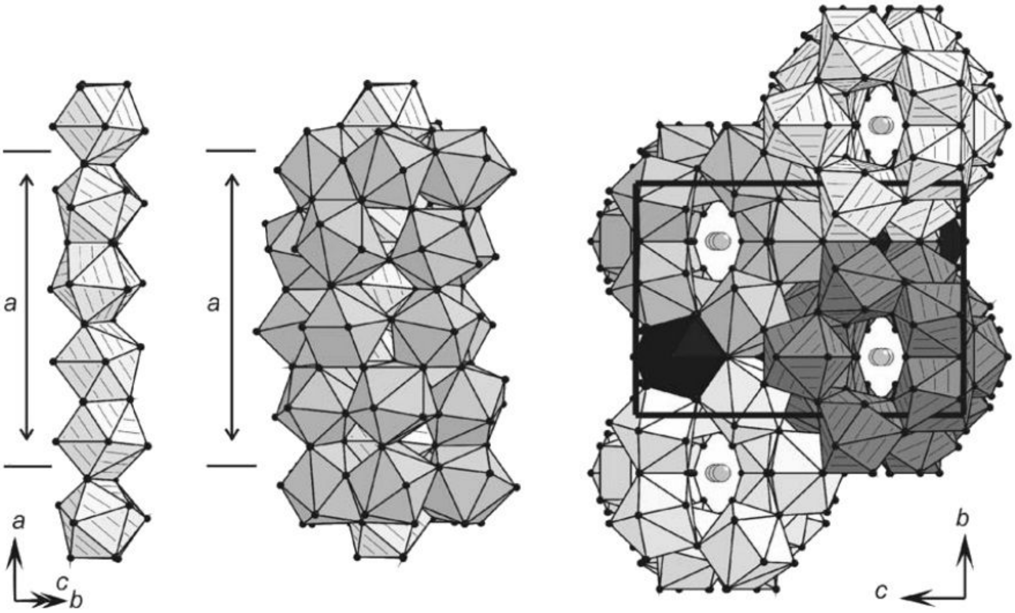

FIGURE 3.3: Polyhedral representation of the crystal structure of $Al_{45}Ir_{13}$ [24].

was an excess of pure iridium in the samples, where not only the hardness increased but also the fracture toughness.

Boström *et al.*

In 2005, Boström *et al.* [24] announced the discovery of a new compound in the Al-rich side of the Al-Ir phase diagram. Boström *et al.* were initially investigating the Al_9Ir_2 compound and after synthesis of single-crystals of this phase, they observed unit cell parameters never reported until then. After SC-XRD analysis, they solved the crystal structure of this new compound. The new phase has a stoichiometry $Al_{45}Ir_{13}$ and was successfully solved in an orthorhombic lattice (space group $Pnma$) with lattice parameters a = 16.760(2) Å, b = 12.321(1) Å and c = 17.425(2) Å (Pearson symbol oP236). The crystal structure determination revealed 38 independent atomic positions, 29 for aluminium and 9 for iridium. The 9 independent iridium atoms are all surrounded by irregularly shaped aluminium coordination polyhedra exclusively. The structure of this $Al_{45}Ir_{13}$ phase can be described as columnar packings of certain of these polyhedra along the a axis. These rods are encircled by other polyhedra building up pseudo-pentagonal columns. These columns are arranged in the structure as a hexagonal packing with the axial direction parallel to the a axis. The projection of this structure on the (100) plane shows characteristic pseudo-decagonal motifs (see Fig. 3.3). Then they performed DTA analysis of a sample containing the two $Al_{45}Ir_{13}$ and Al_9Ir_2 phases in order to determine the melting point of the new phase. It revealed a signal at T_{onset} = 895°C, only 19°C higher than the known melting point of the Al_9Ir_2 phase. They proposed a revision of the Al-Ir phase diagram in the vicinity of $Al_{45}Ir_{13}$ where we can notice that this new phase is close by less than 2 at. % to the $Al_{13}Ir_4$ phase reported by Axler *et al.* (see Fig. 3.4).

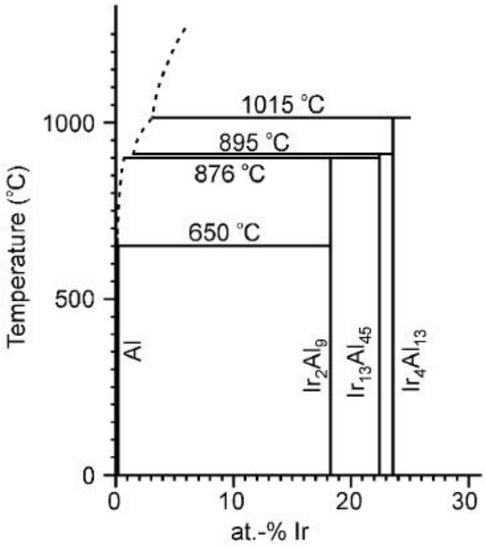

FIGURE 3.4: Part of the Al-Ir phase diagram including the new $Al_{45}Ir_{13}$ phase [24].

Katrych *et al.*

One year later, Katrych *et al.* [25] reported the discovery of a next new compound in the Al-Ir system. At first, they noticed the close compositions of the $Al_{13}Ir_4$ phase ($Al_{76.5}Ir_{23.5}$) reported by Axler *et al.* [59] and the $Al_{3.75}Ir$ phase ($Al_{78.9}Ir_{21.1}$) reported by Ferro *et al.* [58]. Since none of these two phases were ever completely ascertained, they decided to clarify this region of the diagram. Katrych *et al.* prepared 3 samples by arc melting with the only nominal composition $Al_{78}Ir_{22}$, just between the compositions of the two previously mentioned phases. The 3 samples were:

- As cast.
- Reheated to 1200°C then slowly cooled down to 780°C during 18 hours and subsequently annealed at this temperature for 12 hours.
- Remelted then rapidly cooled down to 800°C and annealed at this temperature during 96 hours.

X-ray powder diffraction measurements revealed a new phase in the two first samples along with the known Al_3Ir phase. In the third sample, only $Al_{45}Ir_{13}$ was observed. The structural model of the new compound was determined by solving single-crystal X-ray diffraction data. It resulted in a compound with a new structure type, solved in the space group $P31c$ (Pearson symbol $hP236$). The stoichiometry of the compound is $Al_{28}Ir_9$ and the unit cell dimensions are a = 12.2864(4) Å, b = 12.2864(4) Å and c = 27.341(1) Å. As for the $Al_{45}Ir_{13}$ structure, aluminium atoms are forming different coordination polyhedra around iridium atoms, one different for each independent atomic position of iridium (11 in that case). The arrangement of these polyhedra is close to those in the $Al_{45}Ir_{13}$ structure and rather complex to describe. However, the projections of $Al_{45}Ir_{13}$ and $Al_{28}Ir_9$ upon the (100) plane lead to the same pseudo-decagonal motifs but arranged in a different way (see Fig. 3.5). A DTA analysis of another sample with a nominal composition $Al_{78}Ir_{22}$ annealed for 12 hours at 820°C revealed two features: one at 1450°C and another one at 1443°C. Katrych *et al.* deduced that, since no other feature was observed below this temperature, the real composition of the sample should

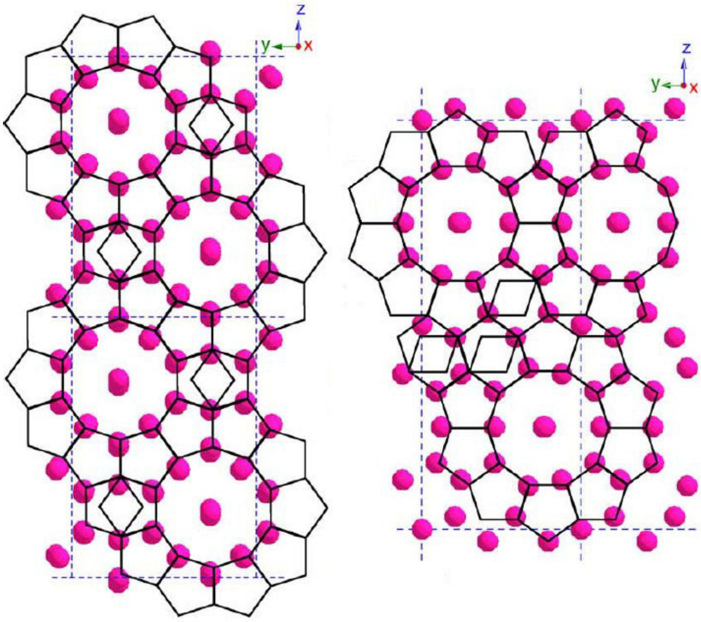

FIGURE 3.5: Projection of the structure of $Al_{45}Ir_{13}$ (left hand picture) and $Al_{28}Ir_9$ (right hand picture) along the [100] direction [25].

be between the Al_3Ir ($Al_{75}Ir_{25}$) and the $Al_{28}Ir_9$ ($Al_{75.7}Ir_{24.3}$) phases. So the temperature of 1450°C matches with the melting point of the Al_3Ir phase, in agreement with the work of Axler *et al.*, and the temperature of 1443°C can be attributed to the melting point of the new $Al_{28}Ir_9$ phase. We can notice that the real composition is 2 to 3 at. % higher in iridium than desired. The reason is probably because of some evaporation of aluminium (T_f = 660°C) due to the large difference with the melting point of iridium (T_f = 2466°C).

Pavlyuchkov *et al.*

As two new compounds were discovered in the Al-Ir system, Pavlyuchkov *et al.* in 2008 [61] reported a study about the Al-Ir system where they built their own revised experimental phase diagram. They prepared 15 alloys by levitation induction melting in the range between 10 and 35 at. % Ir and characterised them with PXRD, SEM, EDS and DTA techniques. They highlighted all the known compounds of the system in this composition range: Al_9Ir_2, $Al_{45}Ir_{13}$, $Al_{28}Ir_9$, Al_3Ir and $Al_{2.75}Ir$. The $Al_{13}Ir_4$ phase was not reported though. Pavlyuchkov *et al.* assumed that it could have been mistaken with one of the two recently discovered phases since no one after Axler *et al.* [59] has ever reported its existence. In this work, the following points were revised:

- The homogeneity range of the $Al_{2.75}Ir$ phase is evaluated to be narrower, between 26.7 and 27.5 at. % Ir.
- The $Al_{2.75}Ir$ + AlIr eutectic composition was found to be at 30 at. % Ir rather than the 33 at. % Ir estimated by Hill *et al.*.
- All the temperatures of the eutectic and peritectic reactions were revised: L = Al + Al_9Ir_2, 657°C; L + $Al_{45}Ir_{13}$ = Al_9Ir_2, 877°C; L + $Al_{28}Ir_9$ = $Al_{45}Ir_{13}$, 993°C; L + Al_3Ir = $Al_{28}Ir_9$, 1446°C; L + $Al_{2.75}Ir$ = Al_3Ir, 1466°C; L = $Al_{2.75}Ir$ + AlIr, 1605°C.

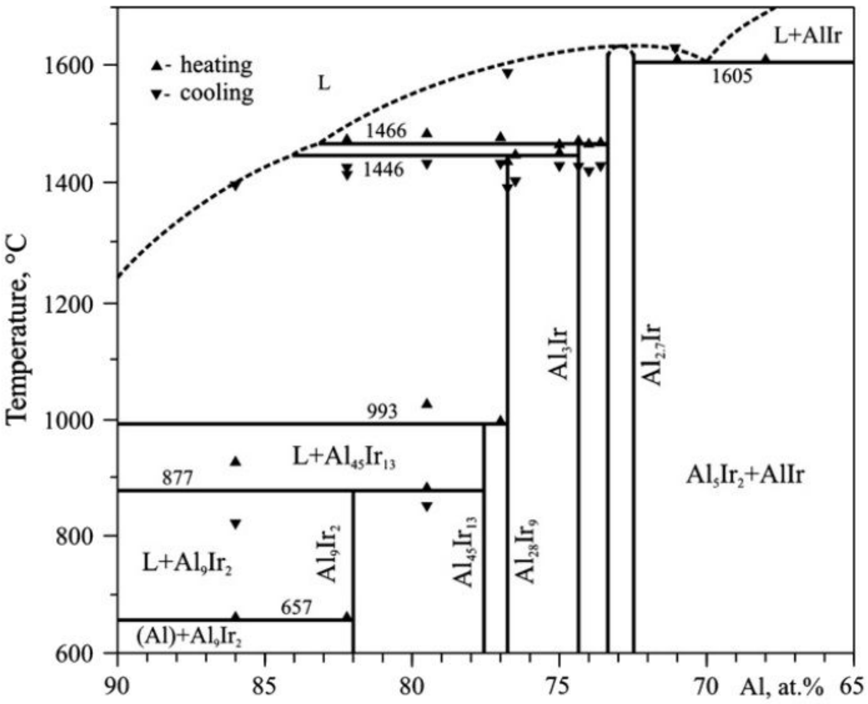

FIGURE 3.6: Al-Ir phase diagram after Pavlyuchkov *et al.* [61].

They also refined the lattice parameters for the two recently discovered phases and found a = 16.771(10) Å, b = 12.327(9) Å and c = 17.437(10) Å for the orthorhombic $Al_{45}Ir_{13}$ compound and a = 12.286(3) Å and c = 27.375(9) Å for the trigonal $Al_{28}Ir_9$ compound. These values are in very good agreement with those from the literature. Their revision of the Al-Ir phase diagram is shown in Fig. 3.6 where the "Al_5Ir_2 + AlIr" phase should be labelled as "$Al_{2.75}Ir$ + AlIr" instead.

Abe *et al.*

In the same year, Abe *et al.* [62] reported a complete study on the Al-Ir system and established a new phase diagram by combining *ab initio* calculations of formation enthalpies, thermodynamic assessment (via CALPHAD [63]) and experimental results of previous studies. While other reports have emerged about thermodynamic assessments of the Al-Ir system [64–66], the one presented by Abe *et al.* remains the most complete. The phases they took into account for their assessment were: Al_9Ir_2, $Al_{45}Ir_{13}$, $Al_{28}Ir_9$, Al_3Ir, $Al_{2.75}Ir$, AlIr and even $Al_{13}Ir_4$. Unlike Pavlyuchkov *et al.* [61], Abe *et al.* did not consider that the $Al_{13}Ir_4$ phase could have been mistaken with another phase. The parameters of their thermodynamic phase diagram were optimised to obtain the best fit to almost all the experimental data of this system reported in the literature within the past twenty years. Thus, the Al-Ir phase diagram established in this work is really complete and is still today the most up to date version (see Fig. 3.7). In this phase diagram, the homogeneity range of the AlIr phase has been revised, taking into account the experimental results of Zhang *et al.* [65]. However, the absence of the homogeneity range of the $Al_{2.75}Ir$ phase is not explained by the authors.

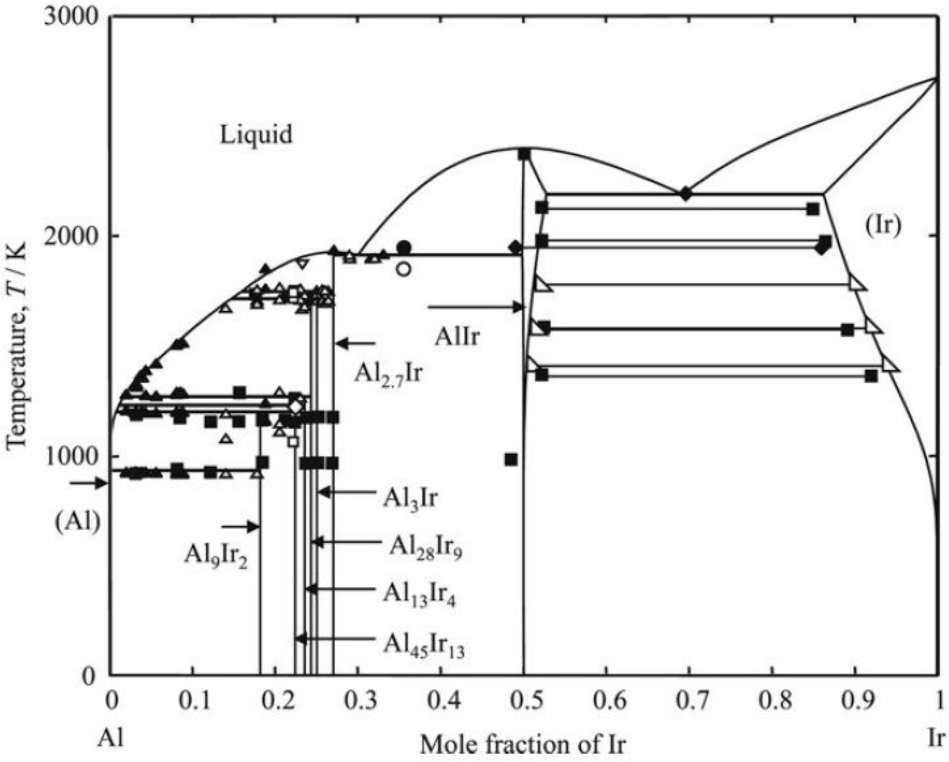

FIGURE 3.7: Al-Ir phase diagram after Abe *et al.* [62].

H. Okamoto

In 2009, Okamoto [67] published a last short review where he briefly summarised the major achievements on the Al-Ir system. He took the phase diagram calculated by Abe *et al.* [62] and simply removed the $Al_{13}Ir_4$ phase. In agreement with Pavlyuchkov *et al.* [61], he estimated that this $Al_{13}Ir_4$ phase has been mistaken for one of the two most recently discovered complex phases $Al_{45}Ir_{13}$ or $Al_{28}Ir_9$. His phase diagram is presented in Fig. 3.8 and will be taken as a reference in the rest of this manuscript.

Oishi *et al.*

The same year, Oishi *et al.* reported a paper about the two $Al_{2.75}Ir$ and $Al_{64.5}Ir_{22}Pd_{13}$ compounds [28]. While the $Al_{2.75}Ir$ compound has always been reported as crystallising in a primitive cubic lattice with parameter a = 7.674 Å, Oishi *et al.* detected reflections that correspond to a doubled unit cell in electron diffraction experiments. They concluded that the $Al_{2.75}Ir$ compound is actually crystallising in a primitive cubic lattice with parameter a = 15.345 Å. Without giving any further insight about the atomic arrangement of this superstructure, they compared the powder X-ray diffraction patterns of the two $Al_{2.75}Ir$ and $Al_{64.5}Ir_{22}Pd_{13}$ phases. By pointing out great similarities between the two patterns, the authors suggested that $Al_{2.75}Ir$ could be of $Al_{64.5}Ir_{22}Pd_{13}$ type. The latter compound is an 1/0 approximant to a quasicrystal and its structure can be regarded as a simple cubic arrangement of icosahedral clusters. The above mentioned reflections in the electron diffraction patterns, evidence of the $Al_{2.75}Ir$ superstructure, are actually very weak. Because the interaction of atoms with electrons

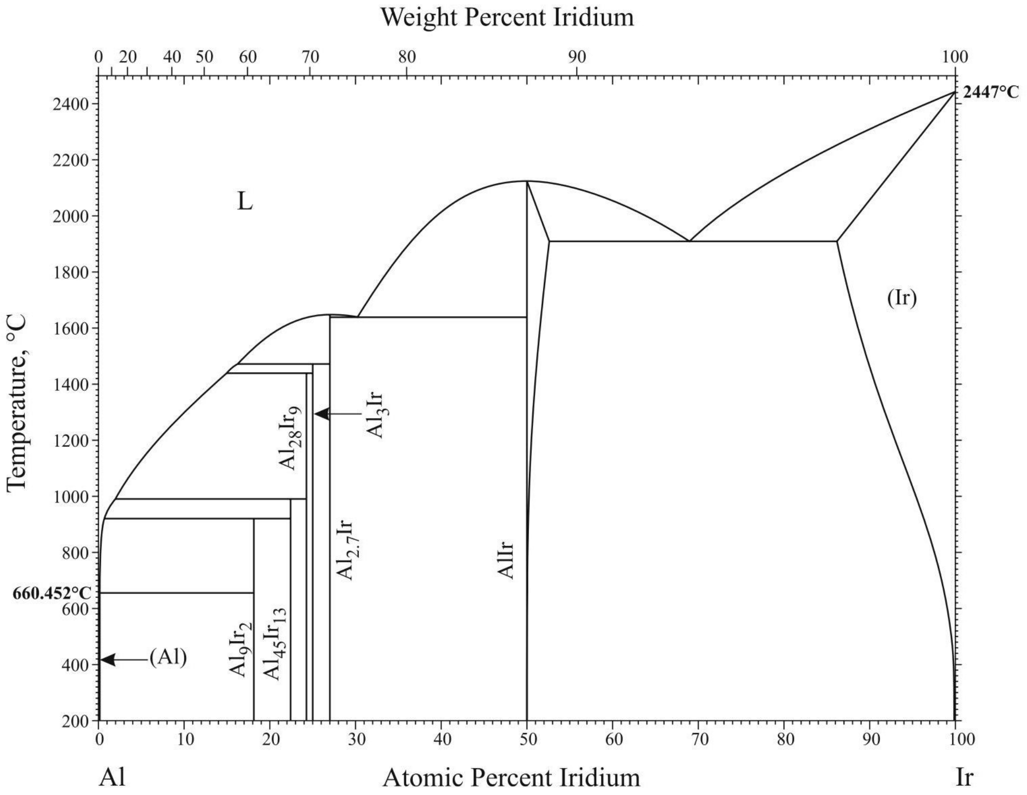

FIGURE 3.8: Al-Ir phase diagram after Okamoto [67].

is stronger than with X-rays, electron diffraction is providing more resolved data than XRD. It is likely that such weak indications of the superstructure could not be observed during the previous studies of this compound.

Mihalkovič *et al.*

In 2013, Mihalkovič *et al.* [68] reported a theoretical study about the $Al_{2.75}Ir$ phase. They predicted the crystal structure of this compound using pair potentials [69] fitted to an *ab initio* database [70], combined with replica-exchange simulated annealing [71–73]. They determined the structure of $Al_{2.75}Ir$ to be a *bcc* packing of iridium icosahedral cages in which the body-centre cage holds an $Al_{12}Ir$ icosahedron while the cell-corner cages hold pseudo-Mackay icosahedra clusters. The description of this structure is in agreement with what was previously predicted by Oishi *et al.* [28]. The two most stable structures occur with a filling of either $Al_{10}Ir$ clusters (called the 10-phase) or an equal mixture of Al_9Ir and $Al_{10}Ir$ clusters (called the 9.5-phase). Each of these structures have ~40 partially occupied sites with a combined occupancy equal to 10. The calculated electronic density of states revealed that the 10-phase is predicted to be a semi-conductor while the 9.5-phase should be strongly metallic, two radically different electronic properties for very similar structures (see Fig. 3.9).

The authors also carried out some calculations about the phase stability in the Al-Ir system. At 0 K and at about 25 at. % Ir, the Al_3Ir phase is predicted to be unstable in favor of an hypothetic $Al_{21}Ir_8$ phase with the structure prototype of $Al_{21}Pt_8$. This $Al_{21}Ir_8$ compound has never been experimentally observed. Considering the existence of the $Al_{21}Pt_8$ and $Al_{21}Pd_8$ compounds, it is also possible that the 21:8 phase exists within the Al-Ir system.

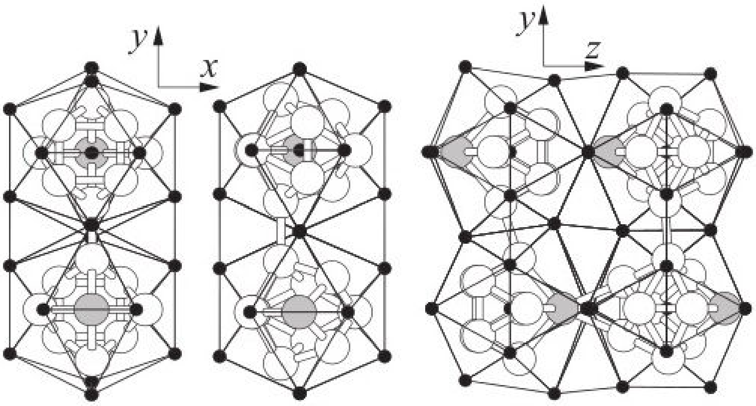

FIGURE 3.9: Orientation of the Al-clusters in the 9-phase (left), the 10-phase (middle) and the 9.5-phase (right). Black atoms are iridium and other atoms are aluminium, the shaded atom indicates the orientation of the cluster [68].

3.2.3 Conclusion

This review of the literature shows that despite of the numerous studies that were performed on the aluminium-iridium system, uncertainties still remain. Indeed, the $Al_{13}Ir_4$ phase is still a matter of debate. The numerous intermetallic phases that exist in this narrow region of the phase diagram (22 at. % - 27 at. %) add to the difficulty of clarifying the situation. The structural model of the $Al_{2.75}Ir$ phase is also open for debate. Recent reports have shown that the structure of this compound could be more complex that what was already determined ; the superstructure of $Al_{2.75}Ir$ still remains to be experimentally established. For the investigation of the Al-Ir phase diagram, a large majority of the samples that were prepared in all these previous reports contain up to 27 at. % Ir. An exploration of the iridium richer side of the phase diagram is still lacking and could potentially reveal new compounds that were not unveiled up to now.

3.3 Experimental investigation

3.3.1 Preparation and characterisation of the alloys

The Al-Ir system has been experimentally revisited with the aim to clarify several uncertainties present in the phase diagram and to potentially discover complex metallic compounds exhibiting new chemical and physical properties. A total of 47 samples covering the aluminium-rich side of the phase diagram were synthesised with a laboratory arc-melter. The compositions are ranging from 12 at. % Ir to 36 at. % Ir. The alloys were all prepared starting from pure aluminium (purity 99.9965 %, Alfa Aesar) and iridium (purity 99.9 %, Evochem). The elements were melted together under a working atmosphere of 500 mbar of argon gas. For the preparation, the samples were melted once then moved upside down and melted again. This was repeated several times in order to ensure the homogeneity of the alloys. The melting point and boiling point of pure aluminium are 660°C and 2519°C respectively and those of iridium are 2466°C and 4428°C [45]. It is worth noticing that when iridium is just melting, aluminium is almost boiling. Consequently, during the arc-melting, the samples underwent each a certain mass loss due to a partial evaporation of aluminium. All samples weighted between 0.3 g and 1.0 g and encountered a loss of about 1 % to 2 % of their initial mass.

The final chemical compositions of the samples were therefore slightly shifted from the desired ones. The alloys were weighted after the arc-melting so that to evaluate this exact loss of mass. The final shifted compositions could then be recalculated by subtracting this mass loss of aluminium to its initial mass.

Most of the samples were then directly prepared for a heat treatment right after the arc-melting, with the preparation method described in Chapter 2. The chosen temperatures of the annealing cycles are ranging from 800°C to 1200°C and the dwell time from 72 h to 552 h. The heating and cooling rates of the heat treatments are between $1K.min^{-1}$ and $2K.min^{-1}$. After annealing, all the alloys were analysed with the following techniques of characterisation:

- PXRD on a Huber Imaging Plate Guinier Camera G670 using the CuKα_1 radiation (λ = 1.54056 Å). For this analysis, a part of the sample was finely pulverised in an agate mortar and deposited on a polymer film transparent to X-rays. The film is then mounted on a sample holder that will be fixed on the apparatus. Because of the softness of pure aluminium, the Al-rich samples could not be pulverised in a mortar. These samples were thus scratched with a fine diamond file until the needed quantity of powder was obtained. This sometimes led to a presence of diamond Bragg reflections in the diffraction patterns but these peaks are easily identified and differentiated from the others.

- Single-crystal XRD on a Rigaku AFC-7 diffraction system equipped with a Saturn 724 CCD detector using the MoKα radiation (λ = 0.71069 Å). A suitable single-crystal (see Chapter 2) is selected from the crushed sample and mounted on a glass tip with the help of a two-components epoxy glue under binoculars. The quality and metric of each single-crystal was firstly checked with a short scan before launching a complete data collection.

- High-Resolution PXRD on the ID22 beamline at the European Synchrotron Radiation Facility (ESRF) in Grenoble. Experiments at the ESRF were carried out on different beam times. Therefore, the wavelength of the radiation was different and will be given when presenting the corresponding results. For the preparation, a part of the sample was pulverised in the same way as described for PXRD. The powder was then sieved with a 32 μm sieve to keep very fine grains. Finally, the powder is enclosed in a thin glass capillary (diameter 0.2 mm) and is ready to be mounted on the device.

- SEM and EDS on a Philips XL30 with a LaB_6 cathode. For SEM observations, the samples were polished down to a 0.25 μm roughness and embedded in a conductive resin as detailed in Chapter 2. Images were taken in SE and BSE modes with an acceleration tension of 20 kV to 25 kV. The chemical compositions are evaluated by averaging the results from 3 to 5 EDS spectra at different regions of the aimed phases.

- EPMA and WDS on a Cameca SX100. As for SEM observations, images were taken in SE and BSE modes with an acceleration tension of 20 kV. The compositions of the phases were precisely calculated from an average of 10 points measured at different regions of the samples.

- DSC on a Netzch 404 C. This technique was employed only for the observation of the phase transitions and formations. The sample is pulverised and placed in an alumina crucible with a lid that are designed for the apparatus. Experiments were carried out with 30 mg to 100 mg of powder up to a temperature of 1600°C. The heating and cooling rates were $10K.min^{-1}$.

3.3.2 Outline of the samples

Table 3.1 lists the initial mass of the elements constituting the samples, the mass lost during the arc-melting, the chemical composition of the samples taking the mass loss into account, the temperature and the time of annealing and the phases found with PXRD in the as-cast and annealed samples. The entries are sorted in increasing order of the atomic percent of iridium. For the best reading of this table, the lector should be informed of the following points:

- The samples n°11, 22 and 32 broke into several pieces during the arc-melting, all the parts could not be gathered thus explaining their important loss of mass. Consequently, the evaporation of aluminium could not be correctly evaluated and the atomic composition has been estimated taking only the initial masses into account.
- The samples n°20, 21, 29, 30, 34, 35, 40, 41, 44 and 45 were not weighted after the arc-melting. The same way as the previously mentioned samples, their composition could then not be recalculated by considering the evaporation of aluminium they underwent.
- The samples n°12, 29 and 35 exhibit the ternary compound $Al_{11}SiIr_6$ after the annealing. The presence of silicon in these samples is due to the absence of a lid on the alumina crucible used for their annealing. Full explanations about this phenomenon and details about the $Al_{11}SiIr_6$ compound are given in Section 4.3.
- The samples n°21 and 41 showed weak Bragg reflections in the PXRD patterns that could not be attributed to any known compound. Like the samples n°12, 29 and 35, they were annealed without a lid on the alumina crucible and a probable addition of silicon could have occurred. It is likely that the unidentified peaks could be attributed to a Si-Ir or another Al-Si-Ir compound.
- The samples n°26, 27 and 28 underwent a heat treatment with two stages. For instance, the sample n°26 was annealed to 900°C during 120 h then slowly cooled down to 600°C and annealed at this temperature for 348 h.
- The samples n°36 and 38 were divided into two and three parts respectively. Each of these parts were taken to a different heat treatment.
- The following binary Al-Ir phases were observed:
  - Al_9Ir_2 [56]
  - $Al_{45}Ir_{13}$ [24]
  - $Al_{28}Ir_9$ [25] (see Section 3.5)
  - Al_3Ir [57]
  - $Al_{2.75}Ir$ [60] (see Section 3.6)
  - $Al_{2.4}Ir$ (new compound, see Section 3.4)
  - AlIr [53]

TABLE 3.1: Experimental information about the prepared Al-Ir samples

Sample n°	Starting composition Al (mg)	Ir (mg)	Loss of mass (mg)	Composition (at. %) Al	Ir	Phase composition of the as-cast sample	Temperature of annealing (°C)	Time of annealing (h)	Phase composition of the annealed sample
1	562.2	545.8	0.0	88.01	11.99	Al + $Al_{28}Ir_9$	800	216	Al_9Ir_2
2	453.5	617.7	2.2	83.88	16.12	Al + $Al_{28}Ir_9$	800	216	Al + Al_9Ir_2
3	370.0	659.3	2.4	79.88	20.12	Al + $Al_{28}Ir_9$	920	216	Al + Al_9Ir_2 + $Al_{45}Ir_{13}$
4	123.8	233.7	2.2	78.75	21.25	No data	1200	84	Al_9Ir_2 + $Al_{45}Ir_{13}$
5	102.7	198.1	1.5	78.45	21.55	$Al_{28}Ir_9$ + Al_3Ir	850	348	$Al_{45}Ir_{13}$
6	114.1	277.7	2.4	77.45	22.55	No data	1200	84	$Al_{28}Ir_9$ + Al_9Ir_2
7	97.1	198.8	0.0	77.50	22.50	$Al_{28}Ir_9$ + Al_3Ir	850	348	$Al_{28}Ir_9$ + $Al_{45}Ir_{13}$
8	88.6	182.8	2.5	77.04	22.96	No data	1200	84	$Al_{28}Ir_9$
9	90.5	195.5	1.9	76.35	23.65	$Al_{28}Ir_9$ + Al_3Ir	850	348	$Al_{28}Ir_9$ + Al_3Ir
10	89.3	189.1	4.1	76.25	23.75	No data	1200	84	$Al_{28}Ir_9$ + Al_3Ir
11	344.7	774.2	19.6	76.03	23.97	$Al_{28}Ir_9$ + Al_3Ir	800	216	$Al_{28}Ir_9$ + Al_3Ir
12	318.8	718.0	0.1	75.98	24.02	Al + $Al_{28}Ir_9$	1200	96	$Al_{2.75}Ir$ + $Al_{11}SiIr_6$
13	93.4	208.7	2.3	75.70	24.30	No data	900	552	$Al_{28}Ir_9$ + Al_3Ir
14	306.2	688.6	5.9	75.65	24.35	$Al_{28}Ir_9$ + Al_3Ir	920	216	Al_3Ir
15	110.5	276.3	2.7	73.54	26.46	No data	900	348	Al_3Ir + $Al_{2.75}Ir$
16	96.4	243.5	2.3	73.36	26.64	No data	900	348	$Al_{2.75}Ir$
17	172.9	441.2	4.4	73.12	26.88	Al_3Ir + $Al_{2.75}Ir$	-	-	-
18	296.9	761.3	9.4	73.07	26.93	$Al_{2.75}Ir$	-	-	-
19	91.9	232.0	3.6	73.06	26.94	No data	900	348	$Al_{2.75}Ir$
20	79.3	208.3	No data	73.06	26.94	No data	950	156	$Al_{2.75}Ir$ + $Al_{2.4}Ir$
21	110.9	292.5	No data	72.98	27.02	No data	1200	84	AlIr + Unidentified
22	272.8	721.6	25.4	72.92	27.08	$Al_{2.75}Ir$	-	-	-
23	118.4	305.3	4.0	72.75	27.25	No data	900	348	$Al_{2.75}Ir$
24	108.6	278.7	4.2	72.74	27.26	No data	950	348	$Al_{2.75}Ir$
25	93.5	245.2	3.0	72.45	27.55	$Al_{2.75}Ir$	-	-	-
26	79.4	209.2	2.2	72.44	27.56	No data	900 then 600	120 then 348	$Al_{2.75}Ir$ + AlIr
27	264.4	731.3	9.2	71.19	28.81	$Al_{2.75}Ir$	1200 then 500	12 then 60	$Al_{2.4}Ir$ + AlIr
28	97.5	261.0	7.8	71.07	28.93	No data	900 then 600	120 then 348	$Al_{2.75}Ir$ + $Al_{2.4}Ir$ + AlIr
29	104.9	305.2	No data	71.00	29.00	No data	1200	84	$Al_{2.4}Ir$ + AlIr + $Al_{11}SiIr_6$
30	73.8	214.8	No data	70.99	29.01	No data	950	156	$Al_{2.75}Ir$ + $Al_{2.4}Ir$
31	82.1	239.3	3.2	70.14	29.86	No data	1200	90	$Al_{2.75}Ir$ + $Al_{2.4}Ir$
32	82.9	253.5	30.0	69.97	30.03	No data	1200	90	$Al_{2.4}Ir$ + AlIr
33	75.5	226.5	1.7	69.89	30.11	No data	1200	84	$Al_{2.4}Ir$ + AlIr
34	75.6	241.3	No data	69.06	30.94	No data	950	156	$Al_{2.4}Ir$ + AlIr
35	96.1	307.8	No data	68.98	31.02	No data	1200	84	$Al_{2.4}Ir$ + AlIr + $Al_{11}SiIr_6$
36	83.7	266.7	1.7	68.66	31.34	No data	900 900	348 72	$Al_{2.4}Ir$ + AlIr $Al_{2.4}Ir$ + AlIr
37	77.7	249.2	2.2	68.34	31.66	No data	1200	90	$Al_{2.4}Ir$ + AlIr
38	83.8	270.2	2.1	68.30	31.70	No data	900 1200 900	348 84 552	$Al_{2.75}Ir$ + $Al_{2.4}Ir$ + AlIr $Al_{2.4}Ir$ + AlIr $Al_{2.75}Ir$ + $Al_{2.4}Ir$ + AlIr
39	77.9	237.7	6.6	68.10	31.90	No data	1200	84	$Al_{2.4}Ir$ + AlIr
40	79.5	279.4	No data	66.96	33.04	No data	950	156	$Al_{2.4}Ir$ + AlIr
41	98.6	347.2	No data	66.92	33.08	No data	1200	84	AlIr + Unidentified
42	85.8	305.1	1.5	66.31	33.69	No data	1400	8	$Al_{2.75}Ir$ + $Al_{2.4}Ir$ + AlIr
43	85.9	306.0	1.7	66.22	33.78	$Al_{2.75}Ir$ + AlIr	-	-	-
44	73.5	281.5	No data	65.04	34.96	No data	950	156	$Al_{2.4}Ir$ + AlIr
45	92.7	355.8	No data	64.99	35.01	No data	1200	41	$Al_{2.4}Ir$ + AlIr
46	78.2	275.1	7.9	64.55	35.45	No data	1200	84	$Al_{2.4}Ir$ + AlIr
47	80.4	308.2	3.0	64.15	35.85	No data	1200	84	$Al_{2.4}Ir$ + AlIr

3.4 The new $Al_{2.4}Ir$ compound

3.4.1 Experimental details

As seen in the Table 3.1, a lot of samples contain the $Al_{2.4}Ir$ phase after the different heat treatments which was never observed in the as-cast samples. This new compound was first observed as unidentified Bragg's reflections in the X-ray diffraction patterns of the samples n°27 to 29. At the time, the $Al_{11}SiIr_6$ phase also present in the sample n°29 was still not known and the peaks from the AlIr phase were very weak. Since the X-ray pattern of this sample n°29 exhibited a large quantity of highly intense peaks that could not be identified, the alloy was directly crushed and single-crystals were collected for SC-XRD measurements before any other characterisation. The structure of a new compound was approached and revealed several disordered atomic positions. The stoichiometry of the new compound is estimated around $Al_{72}Ir_{30}$. The theoretical powder pattern arising from the established structural model corresponds to the unidentified peaks found in the patterns of the samples n°27 and 28. The samples n°30 to 34 were subsequently synthesised and annealed for different conditions in order to obtain this new compound as pure. Although these samples still showed the two other $Al_{2.75}Ir$ and AlIr phases as impurities, they were still used for further characterisations of the $Al_{2.4}Ir$ compound.

3.4.2 Powder X-ray diffraction

The four PXRD patterns of the samples n°30, 31, 33 and 34 are presented in Fig. 3.10. Despite the different temperatures and annealing sequences, they are rather comparable. In addition to the $Al_{2.75}Ir$ phase in samples n°30/31 and the AlIr phase in samples n°33/34, the PXRD patterns reveal the presence of intense peaks from the new phase in all four samples. It can be noticed that when looking at these four samples, the $Al_{2.75}Ir$ phase is present in sample compositions over 70.1% at. Al but not below 69.9% at. Al. Inversely, the AlIr phase is present for compositions below 69.9% at. Al but not above 70.1% at. Al. The more the composition of the sample approaches the 70% at. Al, the less intense are the peaks of the second phase ($Al_{2.75}Ir$ or AlIr). These facts suggest that the new compound should have a composition at the exact value $Al_{70}Ir_{30}$ but SC-XRD revealed a real composition of $Al_{72}Ir_{30}$.

3.4.3 Crystal structure

As explained above, the structure of the new $Al_{2.4}Ir$ compound has been first analysed using SC-XRD. The structure solution has been initially performed in the space group $R32$ and the final lattice parameters were a = 7.6089(3) Å and c = 30.177(1) Å. The positions of the heavy iridium atoms have been obtained by direct methods and the positions of the aluminium atoms have been determined using difference Fourier synthesis. Full crystallographic data about the structure resolution is detailed in Table 3.2 and the atomic positions with their isotropic displacement parameters are listed in Table 3.3.

The final refinement of the structure shows good reliability factors but they are not optimum. The value of the R(int) factor indicates a probable low quality of the data caused probably by a significant phenomenon of absorption of the investigated crystal. Also, some atoms show slightly high values

TABLE 3.2: Crystallographic and data collection information for $Al_{2.4}Ir$.

Composition	$Al_{72}Ir_{30}$
Formula weight (g.mol^{-1})	7708.56
Temperature (K)	295
Wavelength (Å)	0.71073
Crystal system	Trigonal
Space group	$R32$ (No. 155)
Unit cell dimensions (Å)	a = 7.6089(3)
	c = 30.177(1)
Volume (Å^3)	1513.04(13)
Z	1
Calculated density (g.cm^{-3})	8.46
Absorption coefficient (mm^{-1})	66.72
$F(000)$	3246.0
θ range (deg)	2.0 to 33.6
Index ranges	$-10 \leq h \leq 11$
	$-11 \leq k \leq 5$
	$-44 \leq l \leq 40$
Refined in the $R32$ space group	
Collected and independent reflections	4225, 1240
Goodness of fit	1.135
R indices	R(int) = 0.0637
	$R1$ (all) = 0.0641
	$R1$ ($I \geq 4\sigma$) = 0.0516
	$wR2$ (all) = 0.1087
	$wR2$ ($I \geq 4\sigma$) = 0.0944
No. of parameters refined	39
$\Delta\rho_{max}$, $\Delta\rho_{min}$ (e.Å^{-3})	4.55, -6.33
Refined in the $R3$ space group	
Collected and independent reflections	4225, 2275
Goodness of fit	1.089
R indices	R(int) = 0.0578
	$R1$ (all) = 0.0667
	$R1$ ($I \geq 4\sigma$) = 0.0522
	$wR2$ (all) = 0.1310
	$wR2$ ($I \geq 4\sigma$) = 0.1073
No. of parameters refined	63
$\Delta\rho_{max}$, $\Delta\rho_{min}$ (e.Å^{-3})	7.09, -6.37

TABLE 3.3: Atomic coordinates and isotropic displacement parameters for $Al_{2.4}Ir$ refined in the $R32$ and $R3$ space groups.

Space group $R32$							Space group $R3$						
Atom	Site	x	y	z	U_{eq} (Å^2)	Occ.	Atom	Site	x	y	z	U_{eq} (Å^2)	Occ.
Ir1	3a	0	0	0	0.0121(4)	1	Ir1	3a	0	0	0.7198(2)	0.0097(4)	1
Ir2	3b	0	0	1/2	0.0109(4)	1	Ir2	3a	0	0	0.2218(2)	0.0081(4)	1
Ir3	18f	0.2679(2)	0.13927(14)	0.21736(3)	0.0136(2)	1	Ir3A	9b	0.0641(1)	0.5287(5)	0.17021(5)	0.0109(7)	1
							Ir3B	9b	0.5287(5)	0.0669(10)	0.27169(5)	0.0124(7)	1
Ir4	6c	0	0	0.35957(5)	0.0190(3)	1	Ir4A	3a	0	0	0.0845(16)	0.0140(13)	1
							Ir4B	3a	0	0	0.36125(17)	0.0168(14)	1
Al1	18f	0.1103(11)	0.2414(18)	0.4289(2)	0.0139(14)	1	Al1A	9b	0.143(2)	0.250(3)	0.1467(5)	0.0027(17)	1
							Al1B	9b	0.234(4)	0.116(2)	0.2891(5)	0.0027(17)	1
Al2	18f	0.1281(10)	0.264(2)	0.1517(2)	0.0123(12)	1	Al2A	9b	0.393(3)	0.194(5)	0.2040(7)	0.0101(18)	1
							Al2B	9b	0.211(5)	0.410(3)	0.2238(7)	0.0101(18)	1
Al3	6c	0	0	0.2765(4)	0.015(2)	1	Al3A	3a	0	0	0	0.012(3)	1
							Al3B	3a	0	0	0.4477(10)	0.012(3)	1
Al4	9d	0.363(3)	0	0	0.035(4)	1	Al4	9d	0.309(3)	0.328(5)	0.491(9)	0.022(4)	1
Al5	18f	0.319(5)	0.283(5)	0.0302(11)	0.048(7)	1/2	Al5A	9b	0.356(6)	0.046(5)	0.0218(11)	0.071(9)	1
Al6	18f	0.094(7)	0.247(7)	0.0611(13)	0.074(11)	1/2	Al6A	9b	0.431(4)	0.178(4)	0.1160(7)	0.042(6)	1
Al7	6c	0	0	0.0842(15)	0.052(10)	1/2	Al7A	3a	0	0	0.6380(13)	0.064(11)	1

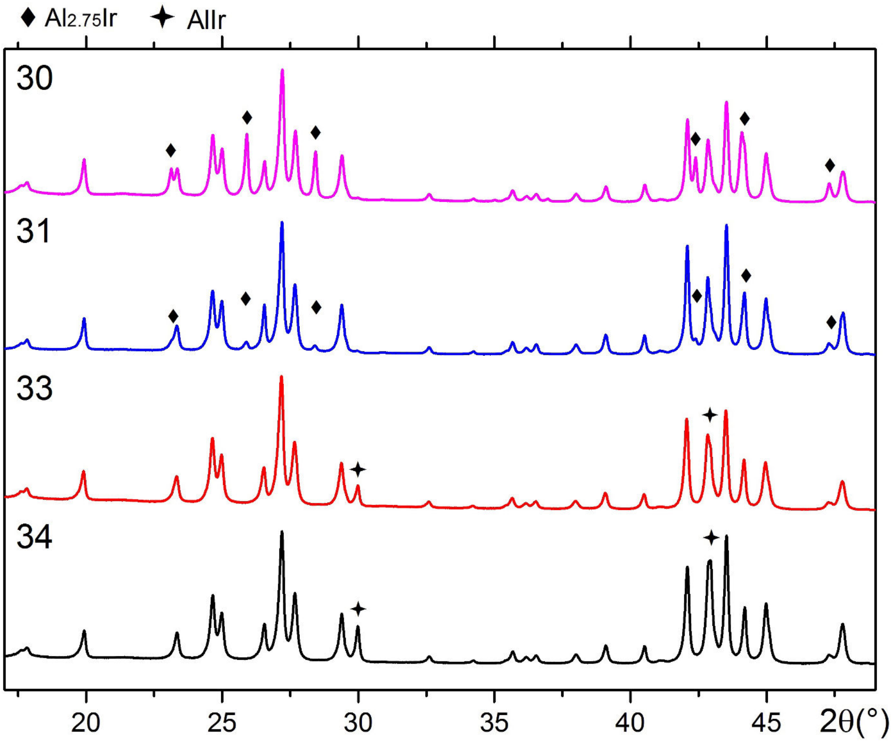

FIGURE 3.10: Powder X-ray diffraction patterns of samples n°30, 31, 33 and 34. Additionally to the major $Al_{2.4}Ir$ phase, $Al_{2.75}Ir$ (rhombuses) or AlIr (stars) was also observed.

of isotropic displacement parameters. Even so, the structural model is still acceptable. The discrepancies probably originate from the assignment of the atomic positions to aluminium that are partially occupied. Indeed, unrealistic short interatomic distances are also found between these disordered Al atoms. The improvement of the structural model will certainly emerge from a better description of these atoms. As seen in Table 3.2, the final chemical composition found after the complete structure determination is $Al_{72}Ir_{30}$ ($Al_{70.6}Ir_{29.4}$) which differ slightly from $Al_{70}Ir_{30}$ as previously suggested.

When looking at the structure model, it can be noticed that the Ir1 position has a very disordered environment, containing all the partially occupied atoms. Indeed, it is surrounded by a polyhedron of aluminium built with 3 Al4 atoms (fully occupied), 6 Al5, 6 Al6 and 2 Al7 atoms (partially occupied) (see Fig. 3.11, upper pannel). The occupancy of each of the disordered positions is $^1/_2$. Thus, the Ir1 position is actually coordinated with 10 atoms. Some of the absolute interatomic distances between the partially occupied Al atoms are too short (typically 1.7 Å). It can be noticed that the Ir1 atoms is located on the two-fold axis of the $R32$ space group. Out of this disordered polyhedron, two well-ordered 10-coordination polyhedra can be distinguished. As seen on Fig. 3.11, middle and lower panels, these two polyhedra are identical but inverted to each other. This is the result of the rotation around the two-fold axis of the $R32$ space group. They are both built with the same fully occupied 3 Al4 atoms and with half and half of the remaining partially occupied atoms, 3 Al5, 3 Al6 and 1 Al7. In each of these two polyhedra, the interatomic distances are no longer too short. Two possible cases can explain this feature:

- The Al environment around the Ir1 position has two different orientations within one unit cell of $Al_{2.4}Ir$.

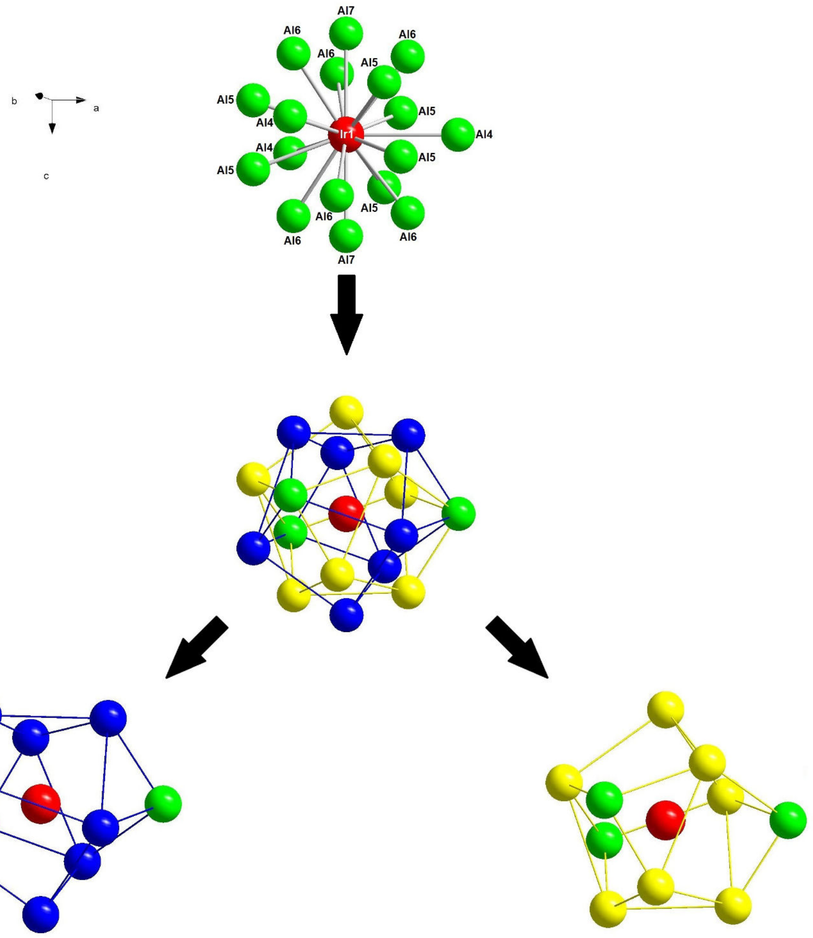

FIGURE 3.11: Coordination sphere of the Ir1 atomic position. Out of the disordered Al polyhedron, two identical ordered Al polyhedra can be distinguished.

- The Al environment around the Ir1 position is always the same in the unit cell, but two different orientations of this polyhedron exist throughout the structure, locally breaking the two-fold symmetry. Thus, an ordered model can be described in the $R3$ space group, but the real structure with the two different orientations can be described by using a twinning approach .

In any case, it results in a disordered Al polyhedron we observe in the SC-XRD data. The ordered model has been refined in the $R3$ space group. The Laue class of the crystal is then decreasing from $\overline{3}m$ to $\overline{3}$ but no particular matrix links the two space groups. Due to this reduced symmetry, some atomic positions will be evidently splitted. The results of the refinement of the crystal structure of $Al_{2.4}Ir$ in the $R3$ space group is presented in Table 3.2 and the atomic positions with their corresponding atomic displacement parameters are listed in Table 3.3. The three partially occupied positions in the $R32$ model (Al5 Al6 and Al7) are each splitted into two other positions. In the $R3$ model, only one over these two splitted positions were kept to form the ordered Al polyhedron (Al5A, Al6A and Al7A). The other orientation of this polyhedron is considered with the twinning parameter.

Figure 3.12 shows the polyhedra representation of the $Al_{2.4}Ir$ crystal structure in the two $R32$ and $R3$ models. As explained above, the Ir1 position is coordinated with a polyhedron of 10 Al atoms (represented in yellow). When looking at the coordination sphere of this polyhedron, it can be noticed that it is actually enclosed in a Ir icosahedron built with the Ir3 and Ir4 position in the

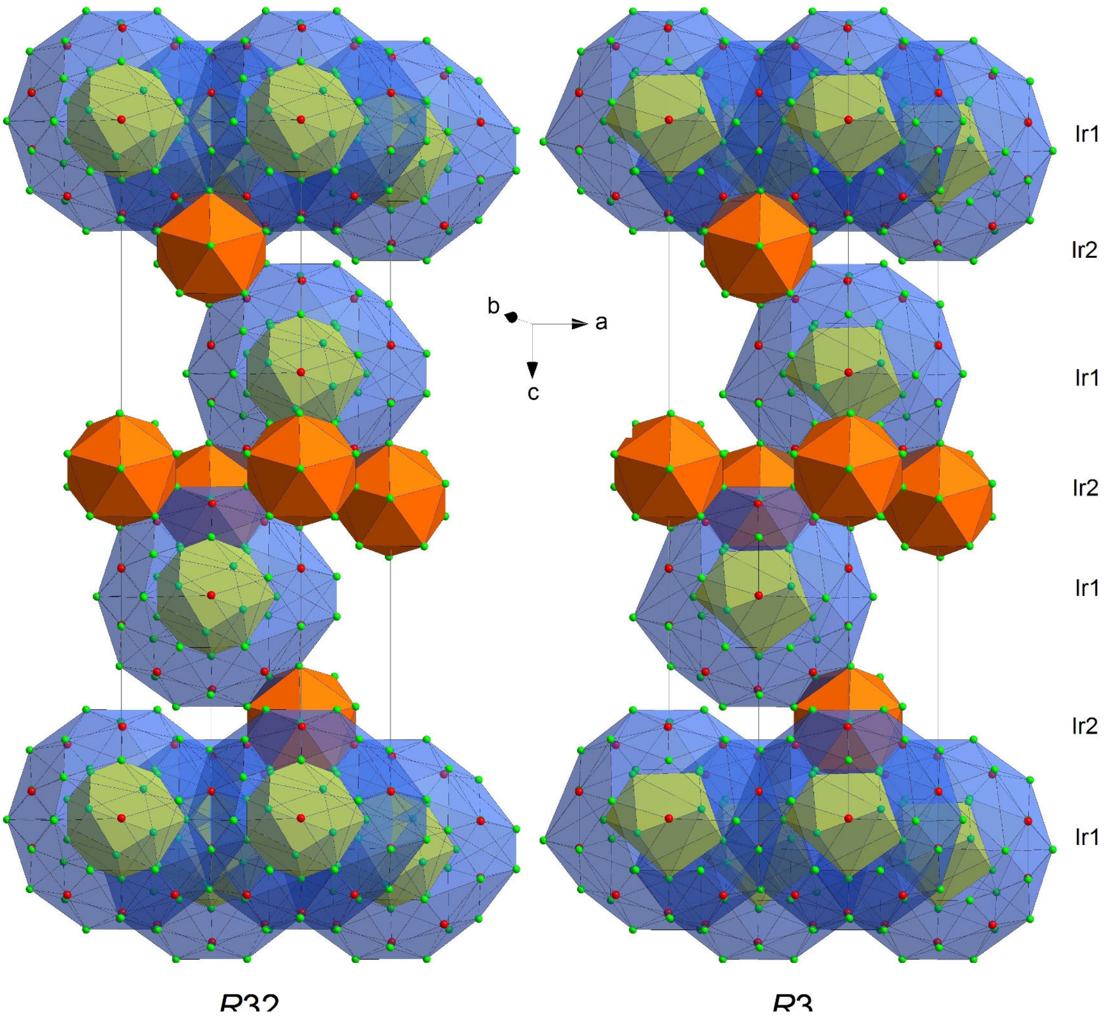

FIGURE 3.12: Representation of the Al$_{2.4}$Ir crystal structure in the $R32$ and $R3$ models as polyhedra packing.

$R32$ model (or with the Ir3A, Ir3B, Ir4A and Ir4B positions in the $R3$ model). Now considering the first Al environment of this Ir icosahedron, the second shell around Ir1 can be described as a pseudo-Mackay icosahedron (represented in blue). In the crystal structure, slabs constituted of interpenetrating pseudo-Mackay icosahedra are formed perpendicular to the c axis. The first coordination shell of the Ir2 position is also a icosahedron (represented in orange) built with the Al1 and Al2 positions in the $R32$ model (Al1A, Al1B, Al2A and Al2B in the $R3$ model). These icosahedra are filling the interspace of the slabs of pseudo-Mackay icosahedra. The twofold axis found in the $R32$ space group has no influence on the description of the pseudo-Mackay icosahedron. Indeed, this particular environment is found to be similar in the $R3$ model. However, this axis has influence on the first coordination shell of the Ir1 position, breaking locally the symmetry by creating the disordered polyhedron we observe. This particular environment is then more properly described in the $R3$ model, where the twofold axis is missing.

Regarding the results of the refinements, the reliability factors still do not show optimum values. This can be caused by serious problems of absorption. For the data collection, it is then crucial to select a single crystal that have an ideal size (not too big) and shape (isotropic). The absorption correction must also be carried out with a particular care. In the case of this work, it is possible that the selected single-crystal was not ideal.

The refinement of the structure in both the $R32$ and $R3$ space groups show similar results. It is not surprising since the difference between the two models is minor. The $R3$ model is ordered but local disorientation around the Ir1 position actually exists.To obtain the best fit of the $R3$ model with the experimental data we are using a twinning approach. This model is then more convenient for a clear description of the crystal structure.

3.4.4 Other characterisations

The sample n°34 has been analysed with SEM. A typical image obtained in BSE mode is presented in Fig. 3.13. Three areas can be described:

- A white phase in minor quantity with an eutectic microstructure. Considering the very low intensity of the diffraction peaks from the AlIr phase in the PXRD pattern, this minor phase can be attributed to this compound.
- A wide gray area that corresponds to the new $Al_{2.4}Ir$ phase. As detailed in Section 2.6, the heavier the elements, the brighter they appear in SEM. The AlIr phase is richer in iridium than $Al_{2.4}Ir$ which corroborates well with the contrasts of these two phases in the SEM image.
- Black regions mark porosities and holes.

EDS measurements recorded at different points within the gray phase reveal an average composition of $Al_{71.0(1.2)}Ir_{29.0(1.8)}$ which is in good agreement with the expected composition of $Al_{72}Ir_{30}$ given by the crystal structure.

Differential scanning calorimetry has been carried out up to 1500°C on the samples n°28, 29, 33 and 45. All measurements lead to similar results. Typical heating and cooling curves of sample n°33 are presented in Fig. 3.14. One small signal is systematically observed at 1384°C on the heating curve. The sample n°33 contains both the new $Al_{2.4}Ir$ phase and the AlIr phase. The latter is known to melt around 2200°C [53]. The melting peak of this phase would then be far out of our experimental range. The feature at 1384°C can be attributed to the decomposition of the new $Al_{2.4}Ir$ phase. PXRD experiments carried out on the samples n°28, 29 and 45 after DSC analysis reveal the absence of the $Al_{2.4}Ir$ phase. This explains the reason why the feature observed at 1384°C in the heating curve is never present on the cooling curves of the DSC.

To identify possible twinning in the structure, the sample n°34 has been taken for Transmission Electron Microscopy (TEM) and electron diffraction observations. The analysis of $Al_{2.4}Ir$ crystals by *in situ* SEM confirms a composition close to $Al_{71.2}Ir_{28.8}$. However, the two previously cited possible cases would generate very slight intensity differences in the electron diffraction patterns. Taking into account the dynamical effect of electron diffraction, it would not be possible to detect such weak differences. As seen in TEM images presented in Fig. 3.15, evidences of local dislocations and stacking faults could be observed. However, no sign of twinning could be observed among the acquired images. It is then concluded that the Al polyhedron around the Ir1 position is more likely to have different orientations resulting in the distortion of the long-range ordering. Even if twinning is not real in this compound, it is a tool that can be kept to describe the well-ordered $R3$ model.

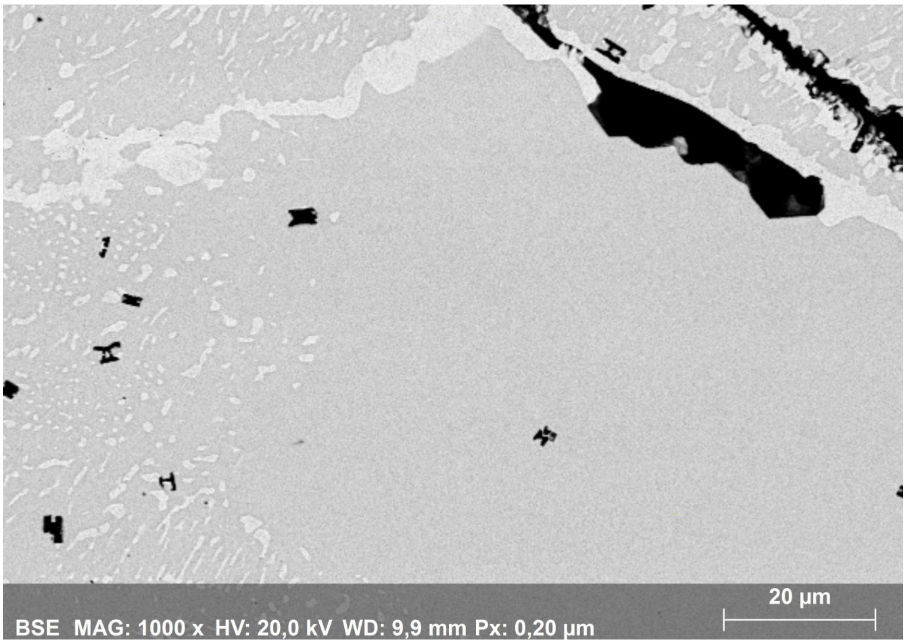

FIGURE 3.13: SEM image of the sample n°34 obtained in BSE mode. The light gray phase (minority) corresponds to the AlIr compound, the darker gray phase (majority) is the new $Al_{2.4}Ir$ compound and the black regions are holes.

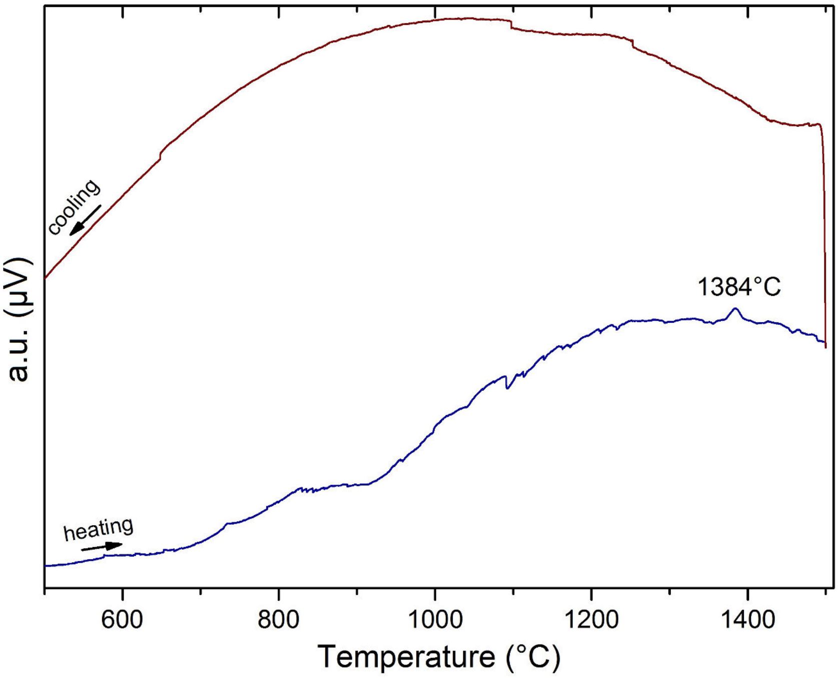

FIGURE 3.14: DSC heating and cooling curves of the sample n°33. The signal at 1384°C corresponds to decomposition of the $Al_{2.4}Ir$ compound.

3.4.5 Discussion

When looking in the literature, Al_7Rh_3 [74], a compound of similar stoichiometry as $Al_{2.4}Ir$ has been already reported. The authors determined the unit cell of Al_7Rh_3 to be monoclinic with lattice parameters $a = 10.309(5)$ Å, $b = 3.808(2)$ Å, $c = 6.595(3)$ Å and β = 102.42(3)°. Information about the space group or the structural model is still lacking. The PXRD pattern of this compound can be found in a study of the Al-Cu-Rh system reported by the same authors [75]. A comparison between this PXRD pattern and the one of sample n°33 is presented in Fig. 3.16. Beside the two peaks of AlIr in sample n°33 and few slightly different intensities, the two patterns look very similar. Moreover, it is worth mentioning that the unit cell reported for Al_7Rh_3 is actually linked to the unit cell of $Al_{2.4}Ir$ by the matrix: 0 -1 -1, 0 -1 -1, -3 0 -1. Since rhodium stands just above iridium in the Periodic Table of elements, it is very likely that Al_7Rh_3 (more probably $Al_{2.4}Rh$) would be actually of the $Al_{2.4}Ir$ type. Further investigations on this Al-Rh compound will be needed to confirm this hypothesis.

The quality of the specimens that were used of SC-XRD experiments was not excellent. The collected crystals showed evidences of polycrystallinity, indicating that the grains of the $Al_{2.4}Ir$ phase in the samples are probably very small. The problem of absorption is crucial in the treatment of SC-XRD data where elements have very different scattering factor. The collection of a homogeneous small single-crystal along with a thorough absorption correction could certainly improve the dataset and the results of the refinements of the crystal structure. The data collection with the AgKα_1 radiation can also help to reduce the phenomenon of absorption. Concerning the crystal structure, the first two shells of the coordination sphere of the Ir1 atomic position (pseudo-Mackay icosahedron) is an environment that can also be found in another Al-Ir CMA. Indeed, authors reported the exact same clusters in the structure model of $Al_{28}Ir_9$ [25]. This compound is discussed in the next section.

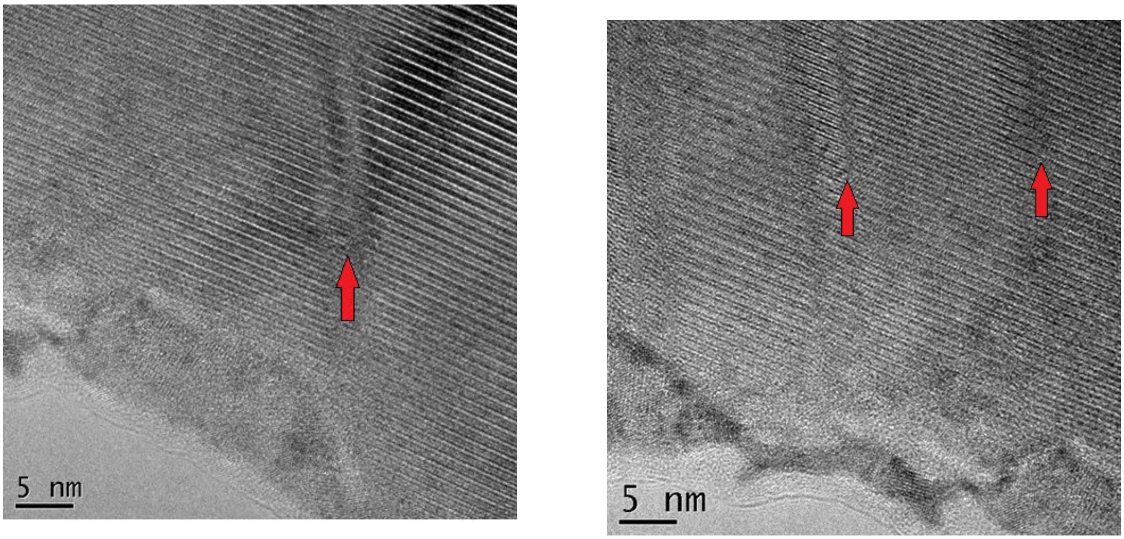

(a) Indication of edge dislocation in the crystal.

(b) Stacking faults in the arrays of the atoms.

FIGURE 3.15: Typical TEM images of the sample n°34.

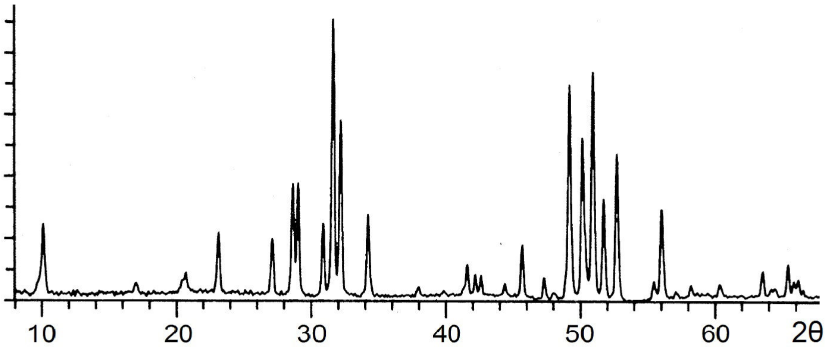

(a) PXRD pattern of the Al_7Rh_3 compound taken with the $CoK\alpha_1$ radiation [75].

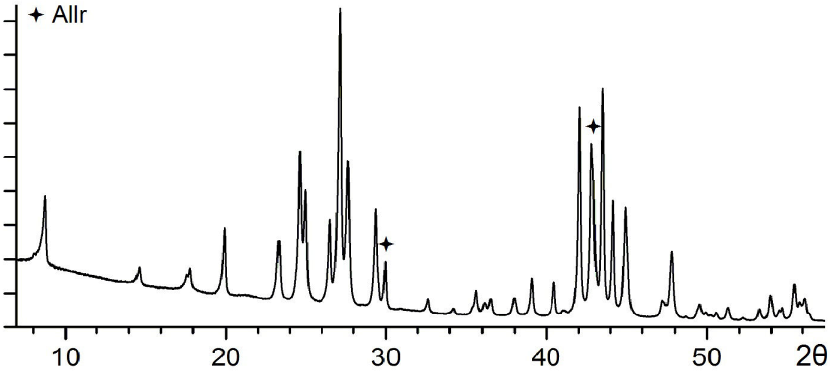

(b) PXRD pattern of the sample n°33 taken with the $CuK\alpha_1$ radiation. Beside the peaks from the major $Al_{2.4}Ir$ phase, few reflections of the AlIr phase are also present.

FIGURE 3.16: Comparison between the PXRD patterns of the $Al_{2.4}Ir$ and Al_7Rh_3 phases.

3.5 Revising the $Al_{28}Ir_9$ compound

3.5.1 Introduction

The $Al_{28}Ir_9$ compound is the last Al-Ir binary phase that was reported by Katrych *et al.* [25] in 2006. It crystallises in a trigonal unit cell with lattice parameters a = 12.2864(4) Å and c = 27.341(1) Å (space group $P31c$). This compound has the most complex crystal structure of the system with 222 atoms in the unit cell and can be described either as a stacking sequence of six atomic layers along the [100] direction or as a packing of pseudo-Mackay icosahedra. However, the structural model reported for this compound shows some discrepancies. Indeed, the model is partially disordered and some displacement parameters are too high. Moreover, the reliability factors obtained from the structure refinement are also rather high: R(int) = 0.175, $R1$ (all) = 0.172 and wR (all) = 0.166. For these reasons, the $Al_{28}Ir_9$ compound will be thoroughly reinvestigated. This chapter will present new PXRD, HR-PXRD, SC-XRD and DSC results carried out on the sample n°8 that contains only the $Al_{28}Ir_9$ phase.

3.5.2 Powder X-ray diffraction

The Guinier PXRD (λ = 1.540598 Å) pattern of the sample n°8 is shown in Fig. 3.17 (upper panel). This experimental pattern can be correctly indexed, in terms of position and intensity of the Bragg reflections, by the previously reported model of $Al_{28}Ir_9$ [25]. However, the shape of the reflections appear unusually broad and asymmetric. This can be a hint of a close splitting of the reflections and thus, a reduced symmetry of the reported model, which could explain the above mentioned discrepancies. To confirm this hypothesis, this sample has been taken to HR-PXRD characterisation.

3.5.3 High-resolution powder X-ray diffraction

The HR-PXRD (λ = 0.400737 Å) pattern of the sample n°8 is shown in Fig. 3.17 (lower panel). Because of the different wavelength compared to the PXRD experiment, the patterns are compared in terms of 1/D for convenience (see Bragg's law in Chapter 2). From the synchrotron pattern, we can confirm some systematic splitting of the reflections compared to those of the Guinier pattern. Because of the lower angular resolution of the Guinier technique, this splitting could not be detected since the splitted peaks are very close and hidden in broad reflections. If the Guinier PXRD pattern can be correctly indexed with the known structural model of $Al_{28}Ir_9$, it is evidently not the case for the synchrotron radiation PXRD pattern. This is the evidence that the atomic structure of the $Al_{28}Ir_9$ compound probably crystallises in a distorted variant of the known model. Such features have never been reported before for this compound.

In Fig. 3.17, the PXRD pattern of the sample n°8 is indexed with the Bragg indices corresponding to the reported known model of $Al_{28}Ir_9$. Compared to HR-PXRD patterns, the hkl reflection (300) is splitted in two other reflections while the (008) one is not. This means that the derived model actually keeps the same c parameter as the previously reported model but the a and b parameters are changing. The peaks in the HR-PXRD pattern have been indexed to determine the unit cell of the structure variant. The indexation of the peaks pointed toward an orthorhombic C-centered lattice with a volume of the unit cell twice that of the trigonal unit cell.

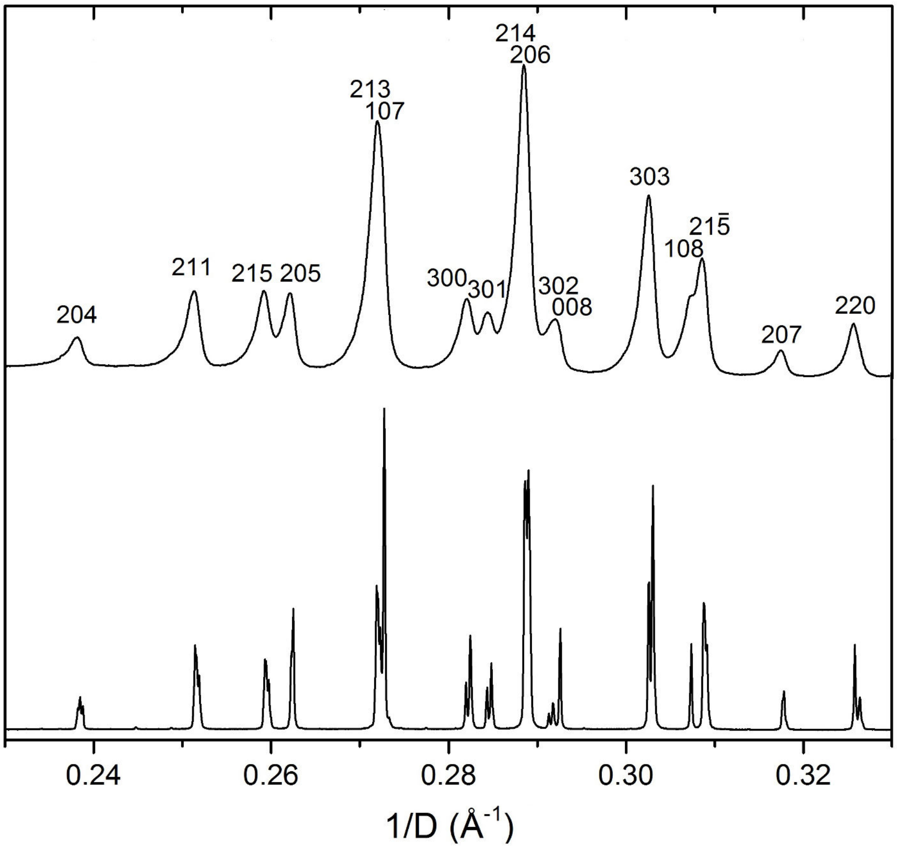

FIGURE 3.17: PXRD patterns of the sample n°8 taken with a Huber Guinier camera, λ = 1.540598 Å, indexed with the available model of $Al_{28}Ir_9$ (upper panel) and HR-PXRD pattern λ = 0.400737 Å of the same sample (lower panel).

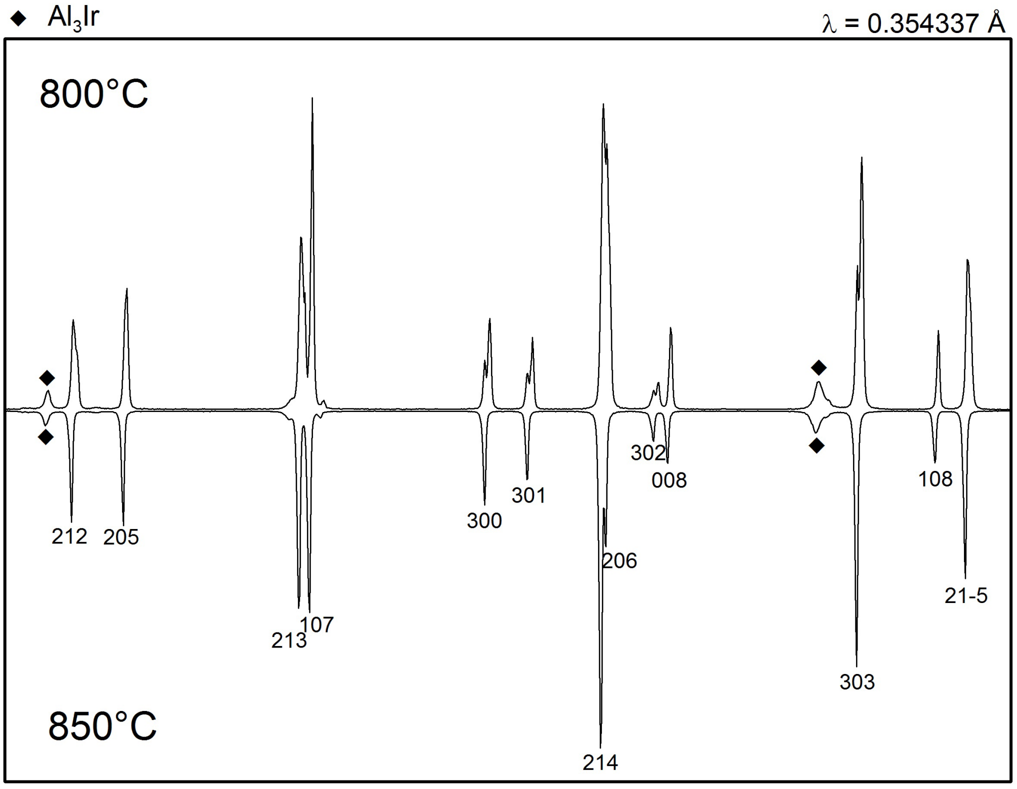

FIGURE 3.18: HR-PXRD patterns of the sample n°8 heated *in situ*. The pattern taken at 850°C is indexed with the model reported by Katrych *et. al* [25].

The lattice parameters of this orthorhombic unit cell were refined with the help of the WinCSD program. The precise obtained values are a = 12.2567(3) Å, b = 21.2785(5) Å and c = 27.3445(7) Å at room-temperature. At first, the b parameter appears to be $\sqrt{3}$ times larger than the a parameter, hence suggesting that the derivative unit cell is similar to the trigonal one. In our case, the precise ratio between the a and b parameters is:

$$\left(\frac{21.2785}{12.2567}\right)^2 \simeq 3.014 \tag{3.1}$$

Here, the ratio deviates from the exact value 3, meaning that the unit cell of the model deviates very slightly from a hexagonal unit cell, thus resulting on the orthorhombic unit cell and explaining the very closely splitted reflections.

The sample n°8 was also heated *in situ* while acquiring other HR-PXRD data (λ = 0.354337 Å). Different patterns were taken incrementally every 100°C from 100°C to 900°C and every 25°C from 775°C to 925°C. Up to 800°C, the HR-PXRD patterns show all the splitted reflections and are correctly indexed with the C-centered orthorhombic lattice. However, the patterns taken from 825°C and higher do not show this splitting anymore. In these patterns, the reflections are correctly indexed with the hexagonal metric of the literature model. The values of the hexagonal lattice parameters are a = 12.38377(2) Å and c = 27.60979(6) Å at 900°C. Figure 3.18 shows a comparison between the HR-PXRD patterns taken at 800°C and at 850°C. The splitted reflections can be observed on the 800°C pattern but are absent on the 850°C one. In this figure, it can also be noticed that some additional Bragg reflections can be observed. These peaks actually correspond to the Al_3Ir phase that started to grow at 700°C. The appearance of this contaminating phase is likely to be the result of the annealing effect of the experiment. In conclusion, the $Al_{28}Ir_9$ compound crystallises in a slightly different structure as a function of the temperature. The "low-temperature" orthorhombic variant being a derivation of the "high-temperature" known hexagonal model.

3.5.4 Differential scanning calorimetry

In order to assess more precisely the transition temperature of this lattice derivation, the sample n°8 was analysed with DSC from 100°C to 950°C with 3 different heating and cooling rates: $5K.min^{-1}$, $10K.min^{-1}$ and $20K.min^{-1}$. The resulting curves are presented in Fig. 3.19 where a small event is systematically observed at 790°C. When looking into the Al-Ir phase diagram, this feature at 790°C cannot be related to any known reaction. The temperature at which this peak appears matches with the previously discussed high-temperature HR-PXRD data. It could correspond to the transition between the two atomic structures of the $Al_{28}Ir_9$ compound. However, we could have expected this peak to appear around 800°C as suggested by the HR-PXRD observations. This temperature shift could be explained by the short dwell time used for each temperature step when collecting the synchrotron PXRD patterns (longer for the DSC technique). It is also important to note that an external heater was used for the HR-PXRD experiments. The slight difference in temperature can also arise from the different calibrations of the equipments.

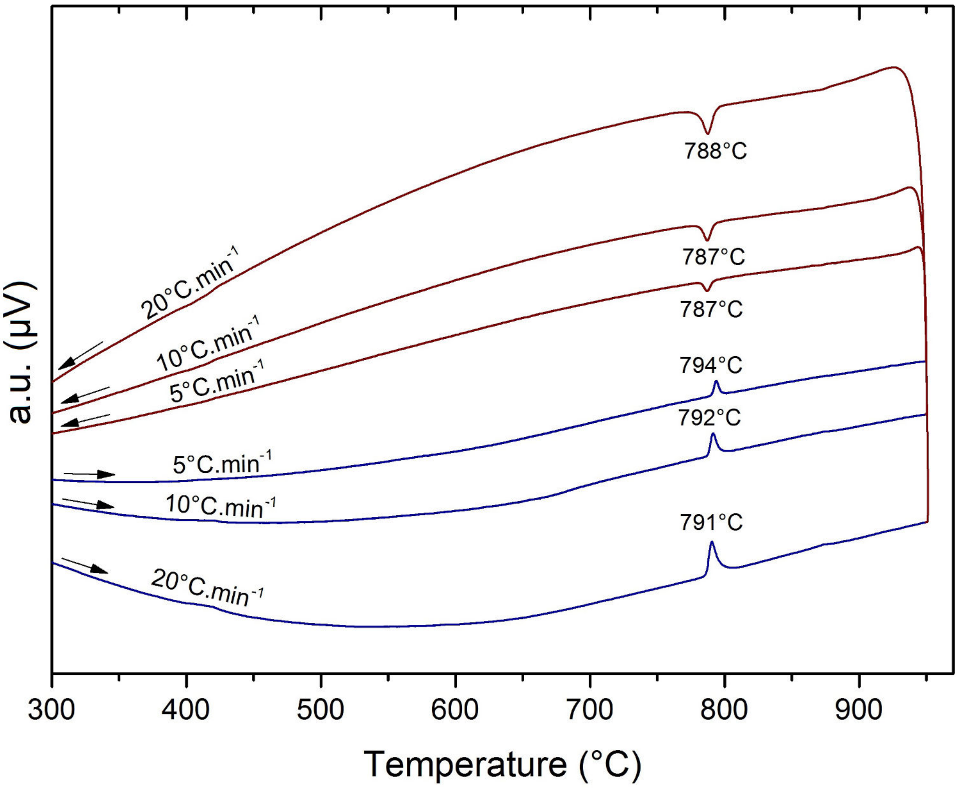

FIGURE 3.19: DSC heating (blue) and cooling (red) curves of the sample n°8 taken with 3 different temperature ramps.

3.5.5 Single-crystal X-ray diffraction

In order to determine the crystal structure of the orthorhombic variant of the $Al_{28}Ir_9$ compound, the sample n°8 has been analysed by SC-XRD at room-temperature. The indexation of the reflections leads to a trigonal unit cell with the known hexagonal lattice parameters of the literature model. As explained above, the unit cell of the orthorhombic variant deviates very slightly from the trigonal unit cell. It is then not surprising that the orthorhombic unit cell could not be properly indexed because it is impossible to resolve such small lattice parameters differences from SC-XRD data. However, the comparison of the R(int) values does not give any preference. For the hexagonal settings, the R(int) value is equal to 0.0797. The three different possible transformations in the C-centered orthorhombic settings lead to the following R(int) values: $\vec{a}_1 = \vec{a}_h$, $\vec{b}_1 = \vec{a}_h + 2\vec{b}_h$, $\vec{c}_1 = \vec{c}_h$, R(int) = 0.077; $\vec{a}_2 = \vec{a}_h + \vec{b}_h$, $\vec{b}_2 = - \vec{a}_h + \vec{b}_h$, $\vec{c}_2 = \vec{c}_h$, R(int) = 0.079; $\vec{a}_3 = \vec{b}_h$, $\vec{b}_3 = 2\vec{a}_h - \vec{b}_h$, $\vec{c}_3 = \vec{c}_h$, R(int) = 0.079. The reason could be the occurrence of twinning due to the formation of the orthorhombic variant from the trigonal high temperature modification. In this case, there are three possible directions for the distortion of the hexagonal cell. This particular twinning is also called "drilling".

To check the accuracy of the reported trigonal model, it was used as starting data for the structure refinement of $Al_{28}Ir_9$. This model does not fit completely with our observed data (see Ref. [25] for full details about the literature model). Some small changes were brought to the reported model. Among the 6 partially occupied Al atomic positions of the model, two were removed and the four other were considered as fully occupied. This leads to a fully ordered model with reasonable interatomic distances in all the structure. Crystallographic data and details about the refinement are listed in Table

3.4. The Table of the atomic coordinates is given in Appendix A. Reliability factors are improved comparing to the initially reported model [25]. While our revised model is not significantly different, the improved refinement is probably the result of a better quality of the single-crystal analysed. Indeed, the authors mentioned that " The rather large internal R-value, $R(\text{int}) = 0.175$, can be explained with the presence of a large majority of weak reflections and the rather low quality of the crystals available " [25]. Our revised model of $Al_{28}Ir_9$ has however 2 extra atoms in the unit cell (224 in total) comparing to the literature, point which will be discussed later.

Nevertheless, this revised trigonal model still disagrees with our room-temperature powder diffraction data which present split reflections. Another refinement has then been carried out to establish a C-centered orthorhombic model as suggested by the indexation of these reflections. Because of the high complexity of the structure (the orthorhombic model has a unit cell twice as large as the trigonal unit cell) and due to the probable existence of drilling in the structure, it is very difficult to obtain a model from this structure solution trial. Another possibility would be to develop a model from our trigonal revised model by group-subgroup relations. However, when looking into the International Tables for Crystallography, group-subgroup relations can be found linking the $P31c$ space group with a monoclinic one but not with any orthorhombic one. In the PXRD patterns, we do not observe additional splitting of the reflections, typical for the orthorhombic -> monoclinic or trigonal -> monoclinic distortion. Thus, for a rigorous description of the orthorhombic variant, the trigonal model must be first described in an intermediate space group that can link the $P31c$ space group with a C-centered orthorhombic one. Again according to the International Tables for Crystallography, the $P6_3mc$ space group appears to be the minimal supergroup that has a direct relation with the $P31c$ and with C-centered orthorhombic space groups. Thus, our revised $P31c$ model of $Al_{28}Ir_9$ has been first described in the higher symmetric $P6_3mc$ space group, which was then splitted to describe the orthorhombic variant in the $Cmc2_1$ space group. Figure 3.20 summarises this scheme and gives the atomic position relationship between these three space groups.

The intermediate model has been established and refined by group-subgroup transformation from our ordered $P31c$ model to the $P6_3mc$ space group. Most of the atomic positions are correctly described in this model but two of them must have been generated with a partial occupancy (see the Table of atomic coordinates of this model in Appendix A). From this $P6_3mc$ model, the crystal structure of the C-centered orthorhombic variant of $Al_{28}Ir_9$ has been established by direct group-subgroup transformation to the $Cmc2_1$ space group. The refinement of this model has been performed by taking into account the drilling factor. The results of the refinement of the $Cmc2_1$ model are presented in Table 3.5. The atomic coordinates are given in Appendix A.

3.5.6 Discussion

The trigonal model of $Al_{28}Ir_9$ has been revised. This structural model is well-ordered and correctly fits the observed HR-PXRD data taken above 800°C. Below this temperature, the patterns show evidences of a C-centered orthorhombic distortion of the trigonal lattice. The trigonal model is then in disagreement with these low-temperature observed data. Thus, the $Cmc2_1$ model has been established and agrees well with the observed data. Indeed, this model correctly describes the systematic splitting of the reflections observed in the HR-PXRD patterns. However, it presents two partially occupied atomic positions so it is not a completely ordered model. The reliability factors obtained after

TABLE 3.4: Crystallographic and data collection information for $Al_{28}Ir_9$ refined in the $P31c$ space group.

Chemical formula	$Al_{28}Ir_9$
Formula weight (g.mol^{-1})	2485.4
Temperature (K)	295
Wavelength (Å)	0.71073
Crystal system	Trigonal
Space group	$P31c$ (No. 159)
Unit cell dimensions (Å)	a = 12.275(2)
	c = 27.351(3)
Volume (Å^3)	3569.0(1)
Z	6
Calculated density (g.cm^{-3})	6.94
Absorption coefficient (mm^{-1})	51.159
$F(000)$	6342.0
Index ranges	$-18 \leq h \leq 12$
	$-17 \leq k \leq 18$
	$-30 \leq l \leq 42$
Collected and independent reflections	42234, 8164
Goodness of fit	1.110
R indices	R(int) = 0.0726
	$R1$ (all) = 0.0695
	$R1$ ($I \geq 4\sigma$) = 0.0603
	$wR2$ (all) = 0.1352
No. of parameters refined	204
$\Delta\rho_{max}$, $\Delta\rho_{min}$ (eÅ^{-3})	5.48, -3.99

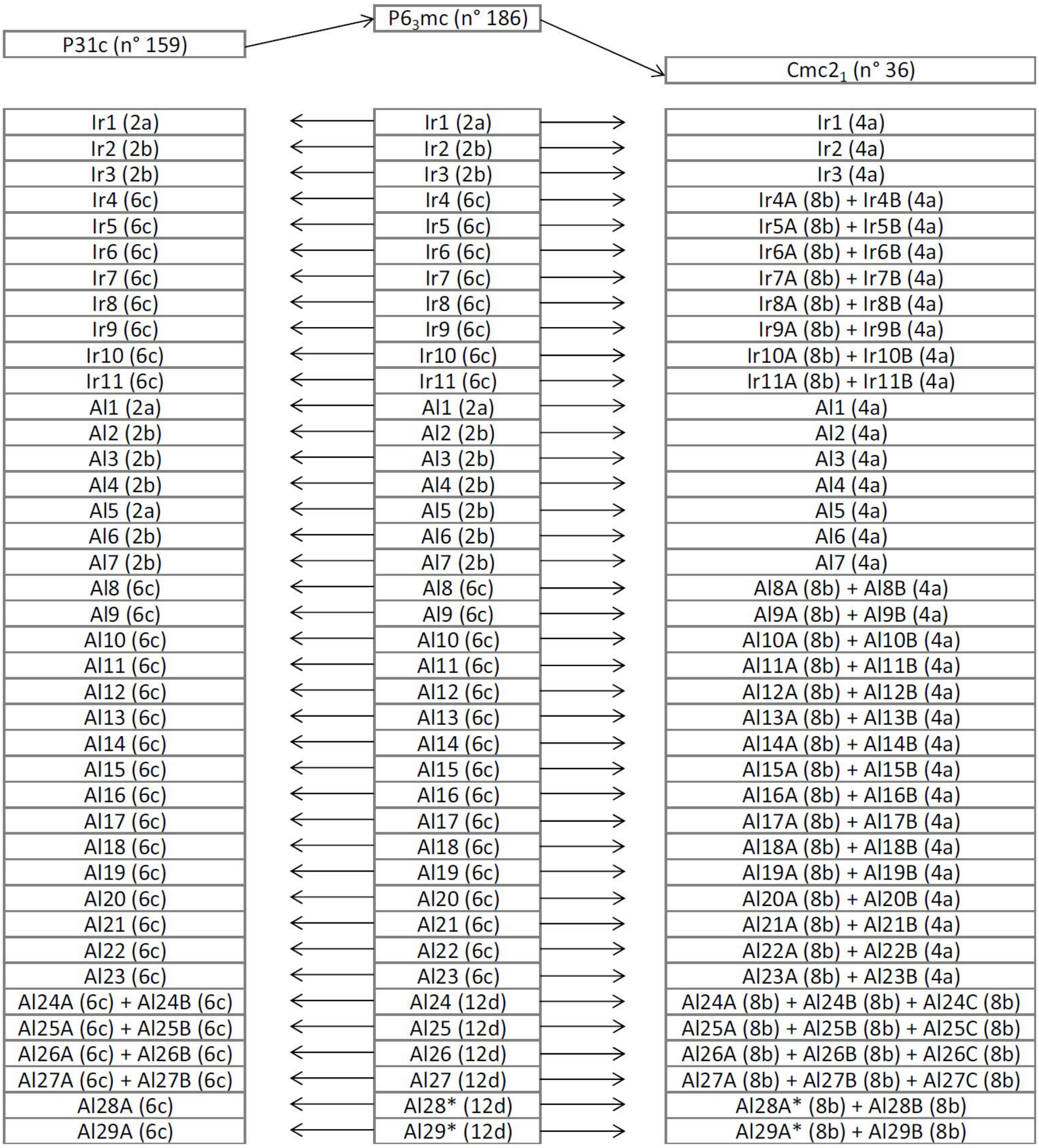

P31c (n° 159)	$P6_3mc$ (n° 186)	$Cmc2_1$ (n° 36)
Ir1 (2a)	Ir1 (2a)	Ir1 (4a)
Ir2 (2b)	Ir2 (2b)	Ir2 (4a)
Ir3 (2b)	Ir3 (2b)	Ir3 (4a)
Ir4 (6c)	Ir4 (6c)	Ir4A (8b) + Ir4B (4a)
Ir5 (6c)	Ir5 (6c)	Ir5A (8b) + Ir5B (4a)
Ir6 (6c)	Ir6 (6c)	Ir6A (8b) + Ir6B (4a)
Ir7 (6c)	Ir7 (6c)	Ir7A (8b) + Ir7B (4a)
Ir8 (6c)	Ir8 (6c)	Ir8A (8b) + Ir8B (4a)
Ir9 (6c)	Ir9 (6c)	Ir9A (8b) + Ir9B (4a)
Ir10 (6c)	Ir10 (6c)	Ir10A (8b) + Ir10B (4a)
Ir11 (6c)	Ir11 (6c)	Ir11A (8b) + Ir11B (4a)
Al1 (2a)	Al1 (2a)	Al1 (4a)
Al2 (2b)	Al2 (2b)	Al2 (4a)
Al3 (2b)	Al3 (2b)	Al3 (4a)
Al4 (2b)	Al4 (2b)	Al4 (4a)
Al5 (2a)	Al5 (2b)	Al5 (4a)
Al6 (2b)	Al6 (2b)	Al6 (4a)
Al7 (2b)	Al7 (2b)	Al7 (4a)
Al8 (6c)	Al8 (6c)	Al8A (8b) + Al8B (4a)
Al9 (6c)	Al9 (6c)	Al9A (8b) + Al9B (4a)
Al10 (6c)	Al10 (6c)	Al10A (8b) + Al10B (4a)
Al11 (6c)	Al11 (6c)	Al11A (8b) + Al11B (4a)
Al12 (6c)	Al12 (6c)	Al12A (8b) + Al12B (4a)
Al13 (6c)	Al13 (6c)	Al13A (8b) + Al13B (4a)
Al14 (6c)	Al14 (6c)	Al14A (8b) + Al14B (4a)
Al15 (6c)	Al15 (6c)	Al15A (8b) + Al15B (4a)
Al16 (6c)	Al16 (6c)	Al16A (8b) + Al16B (4a)
Al17 (6c)	Al17 (6c)	Al17A (8b) + Al17B (4a)
Al18 (6c)	Al18 (6c)	Al18A (8b) + Al18B (4a)
Al19 (6c)	Al19 (6c)	Al19A (8b) + Al19B (4a)
Al20 (6c)	Al20 (6c)	Al20A (8b) + Al20B (4a)
Al21 (6c)	Al21 (6c)	Al21A (8b) + Al21B (4a)
Al22 (6c)	Al22 (6c)	Al22A (8b) + Al22B (4a)
Al23 (6c)	Al23 (6c)	Al23A (8b) + Al23B (4a)
Al24A (6c) + Al24B (6c)	Al24 (12d)	Al24A (8b) + Al24B (8b) + Al24C (8b)
Al25A (6c) + Al25B (6c)	Al25 (12d)	Al25A (8b) + Al25B (8b) + Al25C (8b)
Al26A (6c) + Al26B (6c)	Al26 (12d)	Al26A (8b) + Al26B (8b) + Al26C (8b)
Al27A (6c) + Al27B (6c)	Al27 (12d)	Al27A (8b) + Al27B (8b) + Al27C (8b)
Al28A (6c)	Al28* (12d)	Al28A* (8b) + Al28B (8b)
Al29A (6c)	Al29* (12d)	Al29A* (8b) + Al29B (8b)

FIGURE 3.20: Atomic and Wyckoff positions generated after splitting the $P6_3mc$ space group into the $P31c$ and $Cmc2_1$ space groups. The positions marked by a star (*) are half occupied.

TABLE 3.5: Crystallographic and data collection information for the variant of $Al_{28}Ir_9$ refined in the $Cmc2_1$ space group.

Chemical formula	$Al_{28}Ir_9$
Formula weight (g.mol^{-1})	4970.9
Temperature (K)	295
Wavelength (Å)	0.71073
Crystal system	Orthorhombic
Space group	$Cmc2_1$ (No. 36)
Unit cell dimensions (Å)	a = 12.2567(3) b = 21.2785(5) c = 27.3445(7)
Volume (Å^3)	7131.6(3)
Z	12
Calculated density (g.cm^{-3})	6.94
Absorption coefficient (mm^{-1})	51.205
F(000)	12684.0
θ range for data collection (deg)	1.9 to 33.7
Index ranges	$-18 \leq h \leq 18$ $-32 \leq k \leq 32$ $-42 \leq l \leq 42$
Collected and ($I \geq 4\sigma$) reflections	42190, 26417
Goodness of fit	1.159
R indices	R(int) = 0.077 $R1$ (all) = 0.1159 $R1$ ($I \geq 4\sigma$) = 0.0765 $wR2$ (all) = 0.1851 $wR2$ ($I \geq 4\sigma$) = 0.1491
No. of parameters refined	342
$\Delta\rho_{max}$, $\Delta\rho_{min}$ (eÅ^{-3})	8.49, -6.31

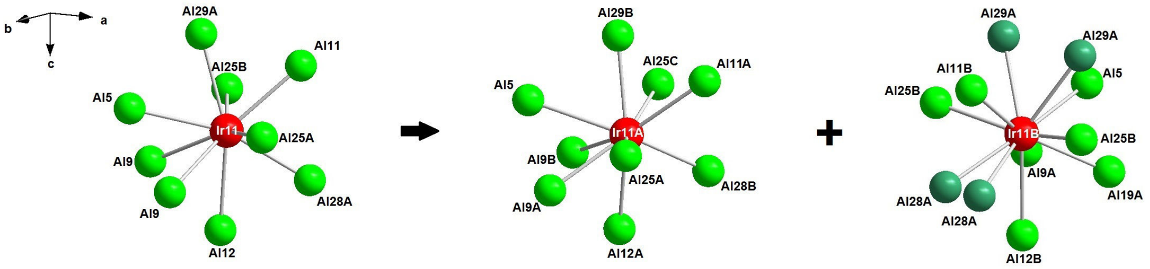

FIGURE 3.21: Coordination spheres of the Ir11 position of the $P31c$ model and of the Ir11A and Ir11B in the $Cmc2_1$ model.

the refinement of this derived model are also rather high. In this derivative model, all the disorder takes place around the Ir11B position. Figure 3.21 shows the coordination sphere of the Ir11 position in the $P31c$ model and of the two resulting Ir11A and Ir11B positions in the $Cmc2_1$ model. While the Ir11A position has a similar ordered environment than Ir11, the Ir11B environment is different where the disorder emerges from the splitting of the Al28A and Al29A positions.

The establishment of a complete and fully ordered orthorhombic model can be a difficult task. Indeed, most of the atoms can be described in the higher symmetry $P6_3mc$ model. Only a few of the aluminium atoms are breaking this overall symmetry. Because of the significantly lower scattering power of Al comparing to Ir, these few aluminium atoms have a low influence of the diffraction patterns. The breaking of the symmetry is really localised on these Al atoms. Thus, they do not present a long range ordering. The twinning is a tool that has been used for the description of this local disorder but it is still not proven that such phenomenon is really present in the investigated single-crystal. Also, the SC-XRD investigation using the MoKα radiation frequently exhibits problems of absorption. The absorption correction is then probably not optimal. Such problem can be settled by collecting another dataset with the AgKα_1 radiation. For all these reasons, the reliability factors obtained after the refinement of the orthorhombic variant are rather high. However, when compared to previously reported R-factors (see introduction), these values are fairly acceptable.

Our revised $P31c$ and $Cmc2_1$ models have both extra Al atoms compared to the $Al_{28}Ir_9$ expected stoichiometry (2 for the $P31c$ model and 4 in the case of the $Cmc2_1$ model since it has a doubled unit cell). As there are no experimental evidence for a partially occupied Al position, it is possible that the two models proposed here are indeed correct, hence leading to a real stoichiometry of $Al_{85}Ir_{27}$ for the compound, i.e. slightly richer in Al compared to the literature data.

As mentioned earlier, the Ir1 environment in $Al_{28}Ir_9$ can be compared to the one described previously for the $Al_{2.4}Ir$ phase. The Ir1 position in these two compounds is surrounded by similar 10-Al atom coordination polyhedron. The second shell around this polyhedron can be described as a second-shell of a pseudo-Mackay icosahedron. While these pseudo-Mackay environments are closely packed in the structure of $Al_{2.4}Ir$, they are differently arranged in the unit cell of $Al_{28}Ir_9$. Beside this environment, no remarkable highly-symmetric polyhedra can be built around the other Ir positions. Figure 3.22 shows a representation of the distribution of the pseudo-Mackay environments in the $Cmc2_1$ model.

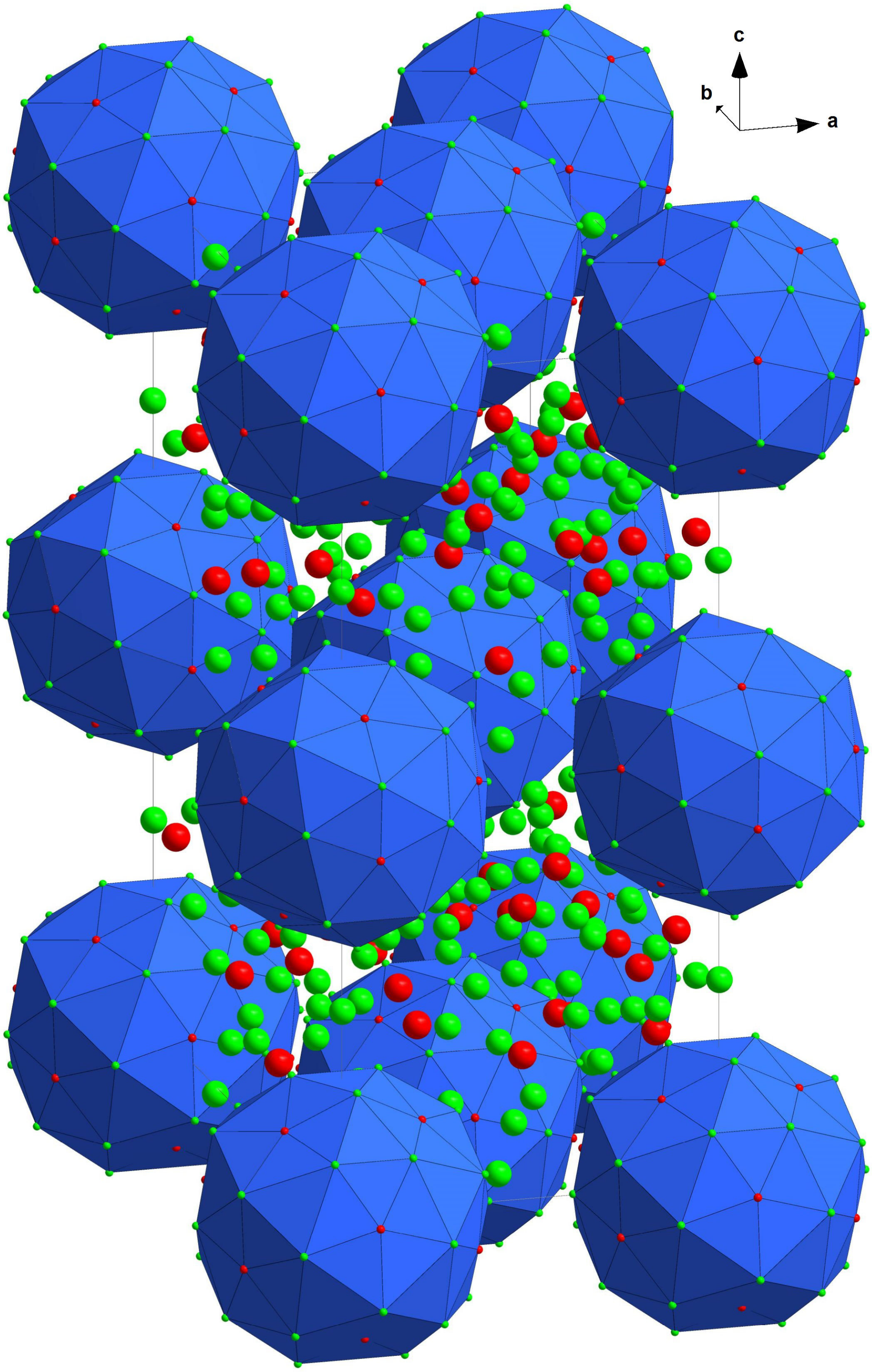

FIGURE 3.22: Representation of the $Cmc2_1$ structure model where pseudo-Mackay clusters around Ir1 positions are depicted.

3.6 New features in the crystal structure of the $Al_{2.75}Ir$ compound

3.6.1 Observations

The $Al_{2.75}Ir$ phase was found pure in the as-cast samples n°18, 22 and 25 and in the annealed samples n°16, 19, 23 and 24. The PXRD patterns of each of these samples could be correctly indexed with the well-known structural model of $Al_{2.75}Ir$ [60] with a lattice parameter a = 7.666 Å. Nevertheless, several weak Bragg reflections have been also systematically observed on every diagram. Figure 3.23a presents the PXRD pattern of the sample n°25 and shows these additional reflections. The known peaks of the $Al_{2.75}Ir$ phase (rhombuses) and the most intense additional peaks (stars) can be indexed together as a face-centered cubic lattice with a doubled lattice parameter a = 15.3313(2) Å. When looking even closer on this PXRD pattern, there are evidences for even weaker peaks (labelled as suns in Figure 3.23b). Indexing these weak Bragg reflections with all the other ones leads to a primitive cubic unit cell with the same doubled lattice parameter a = 15.3313(2) Å. These observations obtained using PXRD are in agreement with the work reported by Oishi *et al.* [28]. Indeed, the latter have also observed these superlattice reflections using electron diffraction. They indexed their pattern as a primitive lattice with a double lattice parameter $a \simeq 15.33$ Å.

The sample n°25 was also analysed with HR-PXRD at a wavelength λ = 0.4007371 Å. The pattern indicated the $Al_{2.75}Ir$ as the major phase along with a small amount of $Al_{28}Ir_9$ and AlIr in the sample. The reflections from the two latter phases are very weak and could not be observed in the previous PXRD pattern due to the much lower resolution of the laboratory powder X-ray diffractometer. All the superlattice reflections of the $Al_{2.75}Ir$ phase have been indexed and the lattice parameter has been precisely refined with the help of the WinCSD program [38]. The resulting value is a = 15.3313(2) Å given previously.

In order to get further insight into the formation of the superstructure of the $Al_{2.75}Ir$ phase, several X-ray diffraction patterns of the sample n°25 have been collected with HR-PXRD while it was annealed *in situ*. At first, some reflections seem to disappear at a temperature between 600°C and 650°C. Patterns have then been collected with a finer increment within the same temperature range. These X-ray diffraction patterns are superimposed and presented in Figure 3.24. Up to a temperature of 630°C, few reflections that correspond to the superlattice are still visible on the patterns. Upon heating the sample above this temperature, these reflections (and only these) are disappearing. Inversely, these reflections appear again when cooling the sample. The X-ray diffraction patterns taken at temperatures above 630°C are correctly indexed with the known primitive cubic lattice with the parameter a = 7.666 Å. Considering that these weak reflections are the only differences between the PXRD patterns of the two modifications of the $Al_{2.75}Ir$ phase, the two structures should not be drastically different. The $Al_{2.75}Ir$ phase is known to have some disorder among its Al positions. Hence, the difference is probably arising from a slightly different organisation of these atoms. As Mihalkovič *et al.* suggested [68], the reason could be related to a different orientation of the aluminium clusters found in the structure.

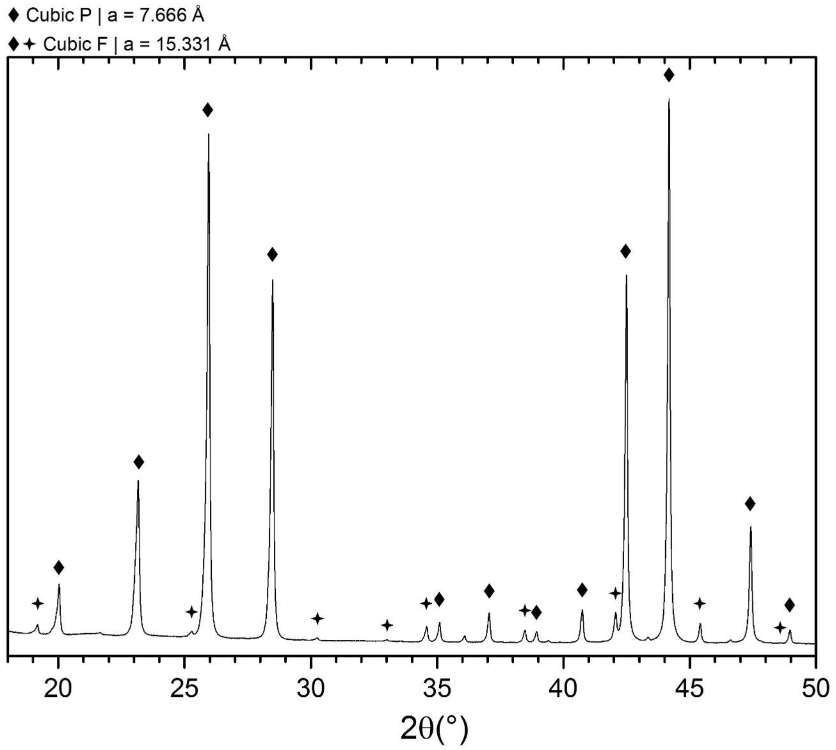

(a) PXRD pattern of the sample n°25 showing the reflections from the reported structural model of $Al_{2.75}Ir$ (rhombuses) and some additional reflections (stars).

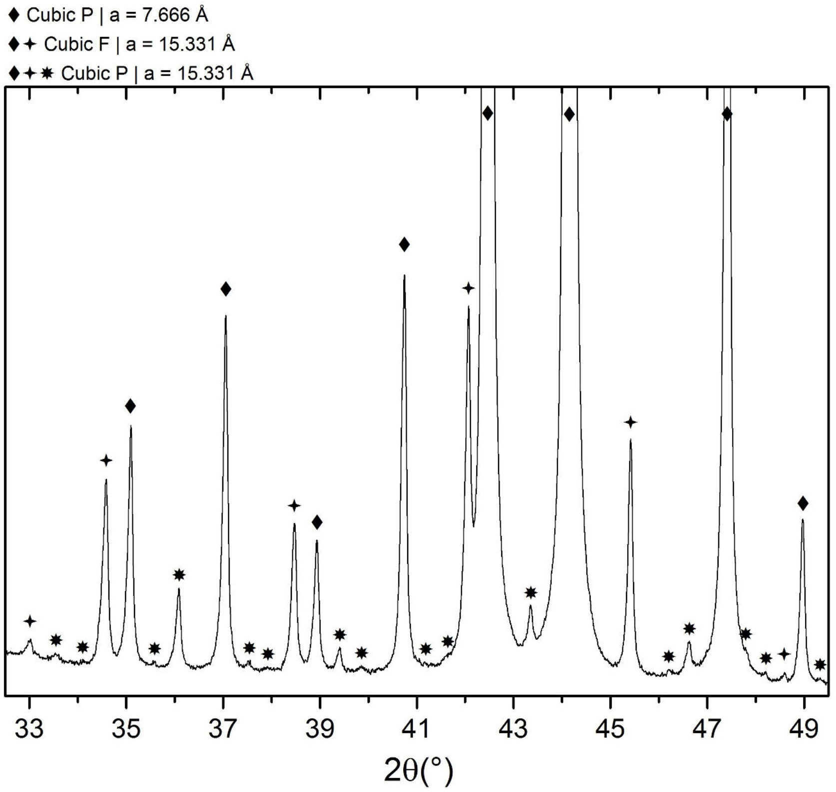

(b) Close-up view of a region of the PXRD pattern of the sample n°25 revealing even weaker additional reflections (suns).

FIGURE 3.23: PXRD pattern of the sample n°25 and its indexation.

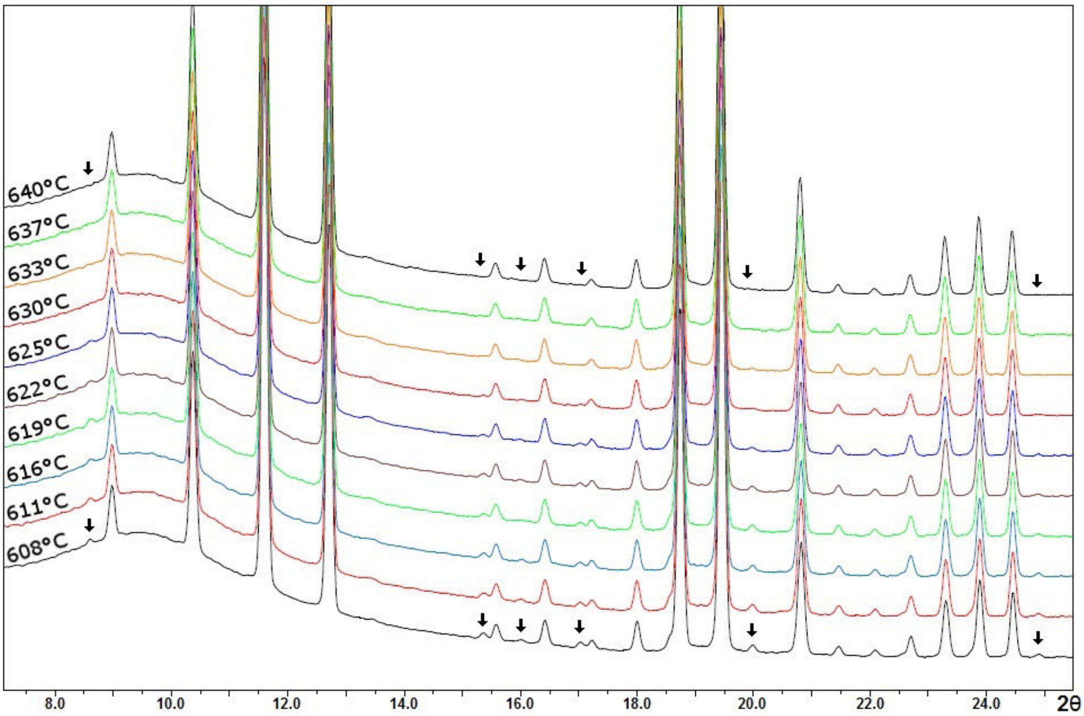

FIGURE 3.24: HR-PXRD patterns (λ = 0.69748 Å) of the sample n°25 annealed *in situ*. Arrows indicate the position of the superstructure reflections.

3.6.2 Superstructure determination

The determination of the atomic arrangement of the $Al_{2.75}Ir$ phase crystallising in the cubic superlattice was undertaken with the WinCSD program using collected SC-XRD data. Figure 3.25 shows a SC-XRD diffraction pattern along the a-axis. Beside the strong reflections of the sublattice, weak peaks indicating the presence of the superlattice are clearly visible. A preliminary almost ordered superstructure model could be established out of the resolution of these data. The structure refinement has been performed in the $F23$ space group. Data collection and structure refinement informations are available in Table 3.6. Atomic coordinates are shown in Table 3.7. This model shows a splitted 48-fold position of Ir into the two Ir5 and Ir6, less than 1 Å apart from each other and with a total occupancy of 48.

The superstructure model can be described as a fcc packing of aluminium polyhedra centered by iridium. Figure 3.26 shows a polyhedra representation of the structure and Fig. 3.27 illustrates the different polyhedra built around each independent Ir atomic position:

- The Ir1 position is the centre of a tetrahedron of 4 Al1 and is located at the vertices and at the centre of the unit cell faces. The Ir1-Al1 distance is the shortest interatomic distance found in the unit cell with $d_{Ir1-Al1}$ = 2.317(7) Å.
- The Ir2 position is coordinated with a cuboctahedron of aluminium built from the Al2, Al3 and Al6 positions. It decorates the centre of the cell and the cell edges.
- The Ir3 and Ir4 positions are the centers of two identical icosahedra built with the Al4 and Al5 atomic positions. They are located in the tetrahedral sites of the cubic cell.

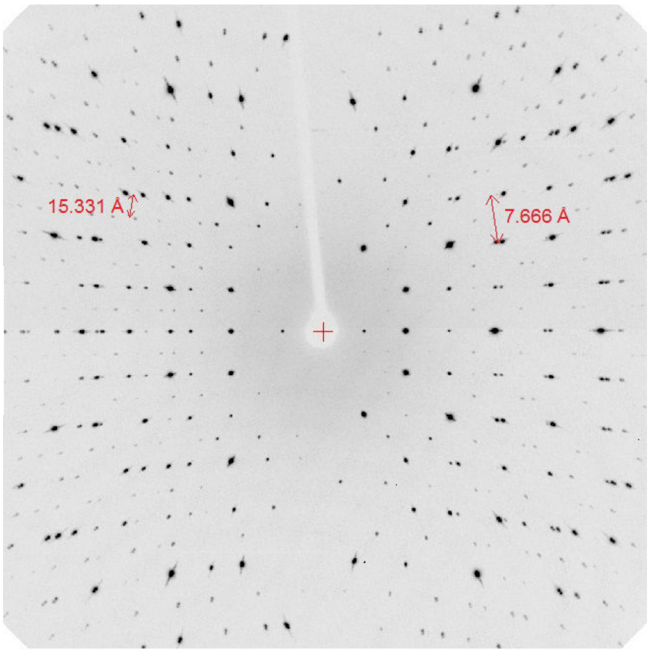

FIGURE 3.25: Rotation image of the SC-XRD data around the [100] direction of the sample n°25. The arrays of weak spots correspond to the superstructure reflections.

TABLE 3.6: Crystallographic and data collection information for $Al_{2.75}Ir$ refined in its superlattice.

Chemical formula	$Al_{42}Ir_{16}$
Formula weight (g.mol^{-1})	16833.43
Temperature (K)	293
Wavelength (Å)	0.71073
Crystal system	Cubic
Space group	$F23$ (No. 196)
Unit cell dimensions (Å)	a = 15.3312(2)
Volume (Å^3)	3603.5(2)
Z	4
Calculated density (g.cm^{-3})	7.743
Absorption coefficient (mm^{-1})	63.31
F(000)	7112.0
θ range for data collection (deg)	2.0 to 34.6
Index ranges	$-23 \leq h \leq 10$
	$-22 \leq k \leq 24$
	$-24 \leq l \leq 24$
Collected and $I \geq 4\sigma$ reflections	8124, 698
Goodness of fit	1.13
R indices	R(int) = 0.1141
	$R1$ ($I \geq 4\sigma$) = 0.0929
	$wR2$ ($I \geq 4\sigma$) = 0.0973

TABLE 3.7: Atomic coordinates and temperature parameters for the superstructure of $Al_{2.75}Ir$ (Space group $F32$).

Atom	Site	x	y	z	B (iso)	Occupancy
Ir1	4a	0	0	0	0.66(5)	1
Ir2	4b	1/2	1/2	1/2	0.64(5)	1
Ir3	4c	1/4	1/4	1/4	0.56(5)	1
Ir4	4d	3/4	3/4	3/4	0.56(5)	1
Ir5	48h	0.0035(1)	0.2392(2)	0.1416(2)	0.55(4)	1/2
Ir6	48h	0.0017(4)	0.2592(2)	0.1490(2)	0.55(5)	1/2
Al1	16e	0.0872(8)	x	x	0.8(2)	1
Al2	16e	0.5983(8)	x	x	0.60(14)	1
Al3	16e	0.4037(7)	x	x	1.5(4)	1
Al4	24f	0.3230(1)	0	0	0.9(2)	1
Al5	48h	0.1056(10)	0.1642(8)	0.2430(8)	1.0(3)	1
Al6	48h	0.1575(10)	0.2540(7)	0.5950(7)	0.42(13)	1

- The two disordered Ir5 and Ir6 positions have similar environment of 10-coordination distorted polyhedra. These polyhedra are constructed with all the 6 different atomic positions of Al and occupy the remaining space in the cell.

Despite the relatively high values of the reliability factors after the refinement, the theoretical PXRD pattern generated by this model is in good agreement with the experimental data. Nevertheless, this superstructure model is still incomplete. Indeed, it consists of 64 Ir and 168 Al atoms in the unit cell, thus lacking 8 Al atoms compared to the reported stoichiometry of $Al_{2.75}Ir$. The difference Fourier map created after the refinement of this superstructure model did not show any suitable possible location of additional atoms. A careful analysis of the atomic distribution in the unit cell indicates that there are non-negligible empty spaces around the Al tetrahedron environment of the Ir1 position. Adding two aluminium atomic position around this environment could generate a similar cuboctahedron environment as for the Ir2 position without creating any short interatomic distance in the whole unit cell. These two additional positions would be 16-fold and 24-fold and thus be automatically partially occupied to respect the 176 needed Al atoms. Such model has been established but the results of the refinement did not show a real improvement. Moreover, it has been noticed that placing the 8 missing atoms anywhere in the unit cell did not change anything to the refinement results and to the theoretical PXRD pattern generated by the model. Generally, the position of the Al atoms have practically no direct incidence on these results in this structure. The position of the iridium atoms, because of their much larger scattering power, are dictating essentially all the intensities of the Braggs peaks. The position of the Al atoms can have nevertheless an indirect influence by moving the position of the Ir atoms. It is then a hard task to determine the position of these 8 remaining atoms. The available Wyckoff positions that are remaining in the model presented here are at least 16-fold (the 4-fold positions being already occupied by Ir atoms). If the $F23$ space group is preserved for the determination of a more complete model, the additional Al position will then be

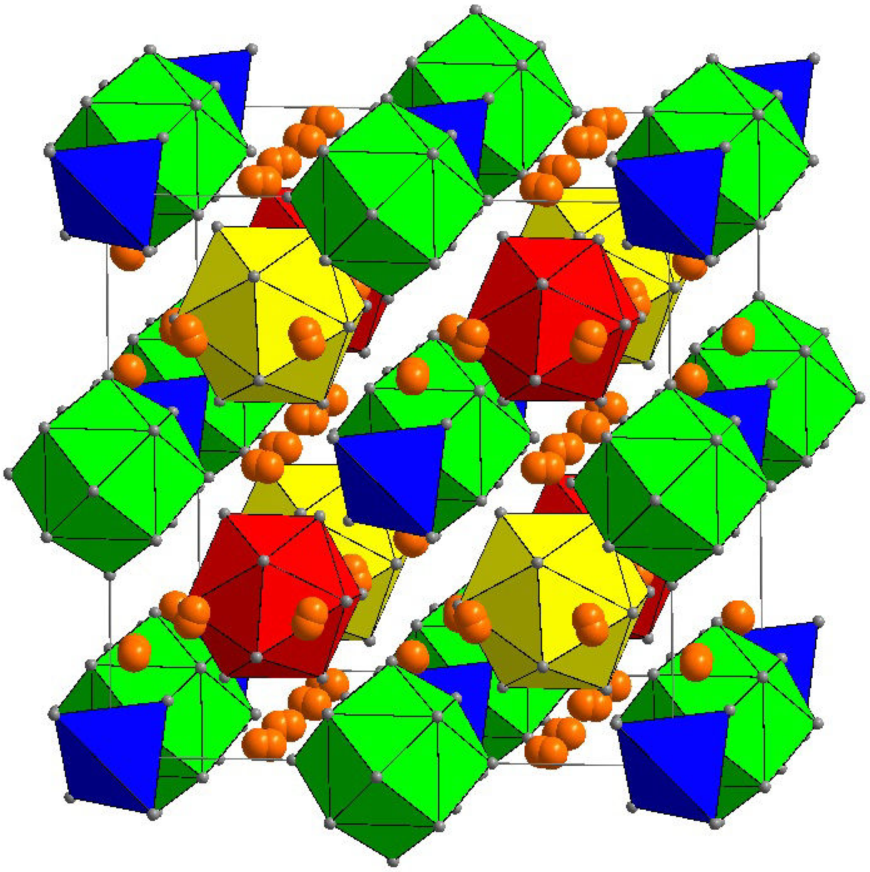

FIGURE 3.26: Polyhedra representation of the $Al_{2.75}Ir$ superstructure. The unbonded atoms are all Ir5 and Ir6 for which the polyhedra are not drawn for clarity.

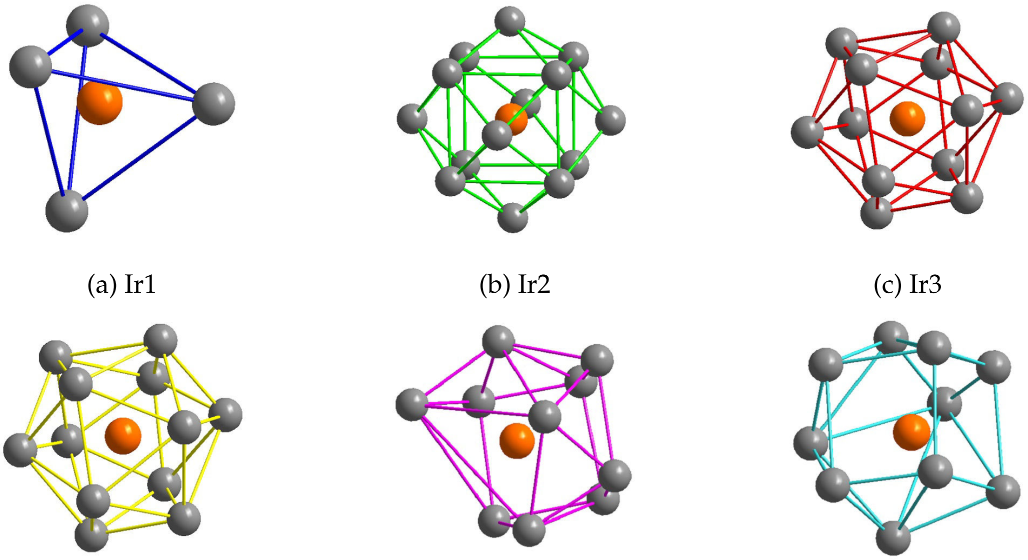

(a) Ir1 (b) Ir2 (c) Ir3 (d) Ir4 (e) Ir5 (f) Ir6

FIGURE 3.27: The different polyhedra of Al found around each independent Ir position.

automatically partially occupied. The structure model presented here has been considered in a face-centered space group, but evidences of primitive reflections were observed on the PXRD patterns. These primitive reflections are very weak and are likely to be absent in the SC-XRD patterns. Also, the dataset presented in this section suffers from strong absorption problems (μ = 66.31 mm^{-1}). Another data collection, taken with the silver radiation for example, could help to improve the dataset and to refine a more complete structural model in a primitive cubic space group.

3.6.3 Conclusion

The presence of a superstructure of the $Al_{2.75}Ir$ compound was already observed using electron diffraction [28]. Here we confirm the existence of such a superstructure using PXRD and SC-XRD experiments. While the initial reports consider the $Al_{2.75}Ir$ phase crystallising only in one modification, we have demonstrated by HR-PXRD that this compound is actually polymorphic. From room-temperature to 630°C, the $Al_{2.75}Ir$ phase crystallises in a primitive cubic superlattice with a doubled lattice parameter a = 15.3312(2) Å. Above 630°C, only subcell reflections are detectable with the simple lattice parameter a = 7.6656(2) Å. The superstructure model of $Al_{2.75}Ir$ has been approached in a face-centered space group and agrees well with the observed data. This model has the advantage to correctly describe the observed 2x2x2 enlargement of the unit cell. However it does not seem to completely describe the structure as it leaves too much empty space around the Ir1-4Al_1 tetrahedra. The determination of the position of the 8 missing Al atoms is not trivial. Future works will concentrate in the establishment of a more complete model, handled in a primitive cubic space group and refined with a better data collection.

3.7 The other phases

The new $Al_{2.4}Ir$ and the two already known $Al_{28}Ir_9$ and $Al_{2.75}Ir$ compounds have been discussed. Unlike them, the Al_9Ir_2, $Al_{45}Ir_{13}$ and Al_3Ir phases did not present any new features during their respective analysis. Their PXRD, SEM and DSC observations are presented in the following sections.

3.7.1 The Al_9Ir_2 phase

PXRD

According to the PXRD analysis, the Al_9Ir_2 phase was found as the only phase present in the sample n°1. However, as seen on the pattern presented in Fig. 3.28, the diffraction peaks at low angles show a strong asymmetry and some of them also exhibit a slight shoulder on the left. The same sample has been analysed with HR-PXRD but these kinks were not observable anymore. Their apparition is probably due to a flawed sample preparation or to an artifact of the laboratory diffractometer. Apart from these features, the pattern (black curve) is perfectly indexed with the theoretical pattern available for the well-known structural model of this compound (red lines). However, the chemical composition of this sample is $Al_{88.0}Ir_{12.0}$ (see Table 3.1) while the Al_9Ir_2 phase is expected at $Al_{81.8}Ir_{18.2}$. According to the phase diagram, the sample n°1 should exhibit a contamination of pure aluminium. Since the sample looks very heterogeneous, it is possible that the pure aluminium is actually present in the sample but somehow separated from the Al_9Ir_2 phase. It is likely that the scratched region of the sample when collecting powder for PXRD experiment contained only the Al_9Ir_2 phase, thus explaining the absence of the Bragg reflections of pure aluminium on the PXRD pattern.

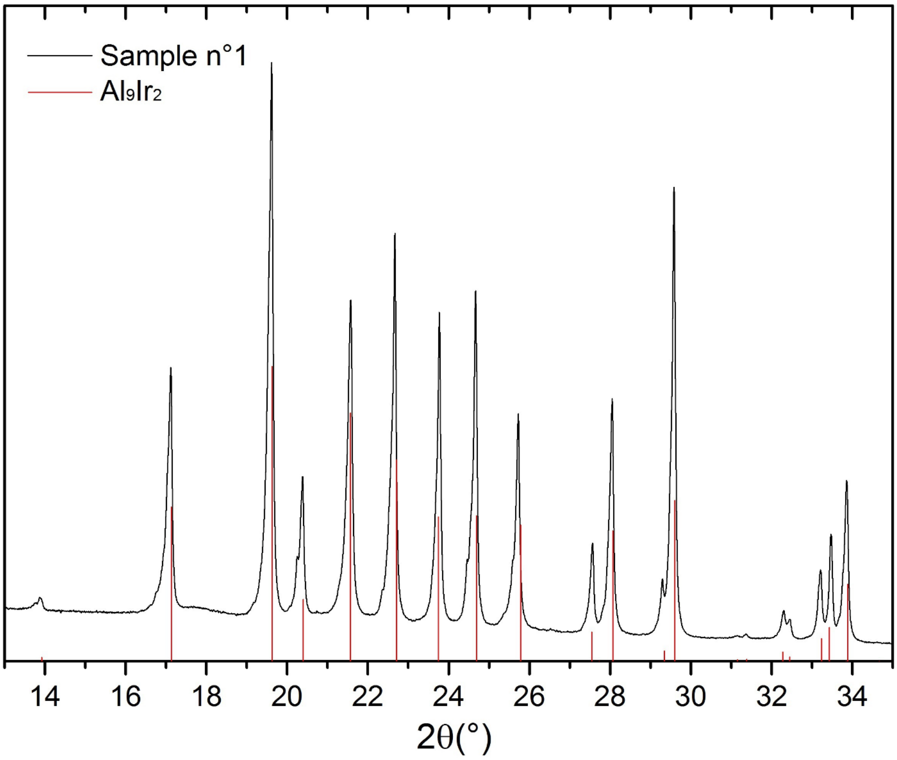

FIGURE 3.28: PXRD pattern of the sample n°1 indexed with the Al_9Ir_2 phase.

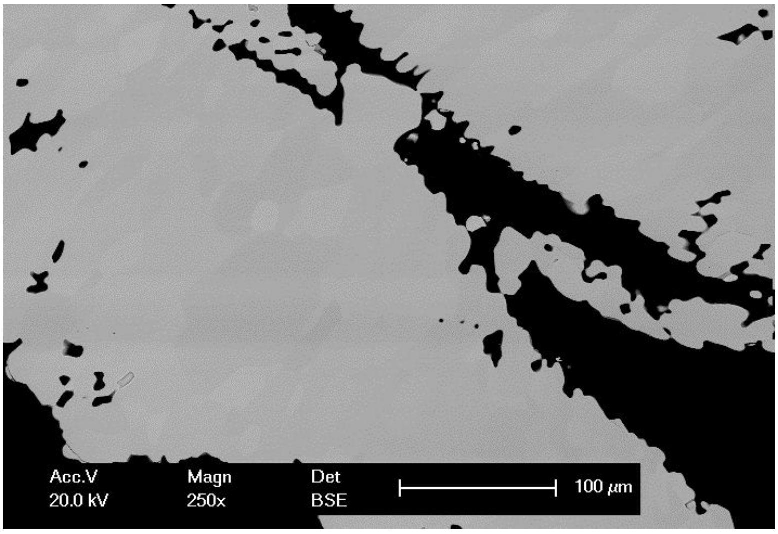

FIGURE 3.29: SEM image of the sample n°1 taken in BSE mode.

SEM

Figure 3.29 shows a SEM image of the sample n°1 taken in BSE mode at a magnification of 250x. The black regions are holes and a slightly different contrast can be observed within the differently oriented grains. EDS measurements have been carried out on four different grains. The chemical composition obtained is $Al_{82.8}Ir_{17.2}$ with a standard deviation of 0.5 for both values. The error on these values is 1.8 and 1.6 at. % for Al and Ir respectively. These results are in good agreement with the known chemical composition of Al_9Ir_2 given above.

DSC

The DSC heating (blue) and cooling (red) curves of the sample n°1 are presented in Fig. 3.30a. On the heating curve, two clear peaks can be observed at 912°C and 1032°C. These two peaks can be associated with the two peritectic reactions of the Al_9Ir_2 and $Al_{45}Ir_{13}$ phases (Fig. 3.30b is recalling the phase diagram in this region). Another broad feature identified around 1400°C corresponds to the two other close peritectic reaction of $Al_{28}Ir_9$ and Al_3Ir but also of the crossing of the liquidus at this compositional region. On the cooling curve, three sharp peaks appear at 1449°C, 1354°C and 651°C which correspond to the temperature of recrystallisation of the Al_3Ir and $Al_{28}Ir_9$ compounds and pure aluminium respectively. The formation of these 3 phases and not of Al_9Ir_2 and $Al_{45}Ir_{13}$ can be explained by the fact that the sample is out of the equilibrium due the rather high cooling rate of the experiment.

3.7.2 The $Al_{45}Ir_{13}$ phase

PXRD

The PXRD pattern of the sample n°5 shows only the $Al_{45}Ir_{13}$ phase (see Fig. 3.31). As for the sample n°1 and the Al_9Ir_2 phase, the sample n°5 has a composition slightly richer in aluminium than the pure $Al_{45}Ir_{13}$ compound which suggests that this sample also contains a few amount of the Al_9Ir_2 phase. Beside that, the PXRD pattern is in full agreement with the structural model of $Al_{45}Ir_{13}$ established

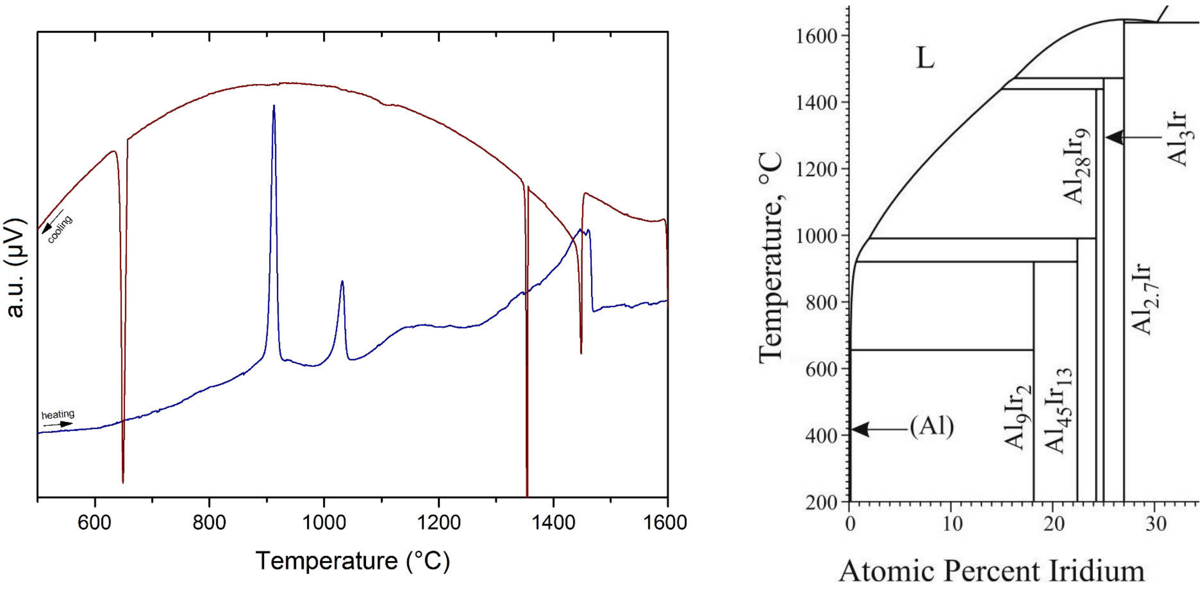

(a) DSC heating and cooling curves of the sample n°1

(b) Al-rich side of the Al-Ir phase diagram [67]

FIGURE 3.30: DSC curves of the sample n°1 and Al-rich side of the Al-Ir phase diagram.

by Boström *et al.* [24]. Even with the HR-PXRD experiment (λ = 0.4007371 Å), no additional feature such as splitted peaks, additional peaks or intensity discrepancies could be highlighted.

SEM

The presence of the undesired Al_9Ir_2 phase in the sample n°5 was confirmed with SEM observations. Figure 3.32 shows a SEM image taken in BSE mode for a Al_9Ir_2 rich region. In agreement with the phase contrast, EDS analysis reveals that the brighter/darker regions are $Al_{45}Ir_{13}$ and Al_9Ir_2 respectively. The black areas are holes and cracks. The average composition of the $Al_{45}Ir_{13}$ phase was measured to be $Al_{78.6}Ir_{21.4}$ with a standard deviation of 0.4 for both values. The error on the measurements are 1.5 and 1.8 at. % for Al and Ir respectively. This composition is slightly richer in aluminium than expected for the $Al_{45}Ir_{13}$ phase but it is still in agreement considering the error values. Since EDS is known to scan a certain depth of the sample, it is possible that it also measures grains of the Al_9Ir_2 phase located beneath grains of the $Al_{45}Ir_{13}$ phase.

3.7.3 The Al_3Ir phase

PXRD

The PXRD pattern of the sample n°14 exhibits only peaks from the Al_3Ir phase (see Fig. 3.33). However, HR-PXRD measurements reveal also the presence of the $Al_{2.75}Ir$ phase. Considering that the sample has a composition of $Al_{75.7}Ir_{24.3}$ and that the two Al_3Ir and $Al_{2.75}Ir$ phases are richer in iridium, it is possible that we underestimate the evaporation of Al for this sample. The lattice parameters of Al_3Ir obtained after the least square refinement of the HR-PXRD data (λ = 0.4007371 Å) are a = 4.24996(3) Å and c = 7.76205(5) Å.

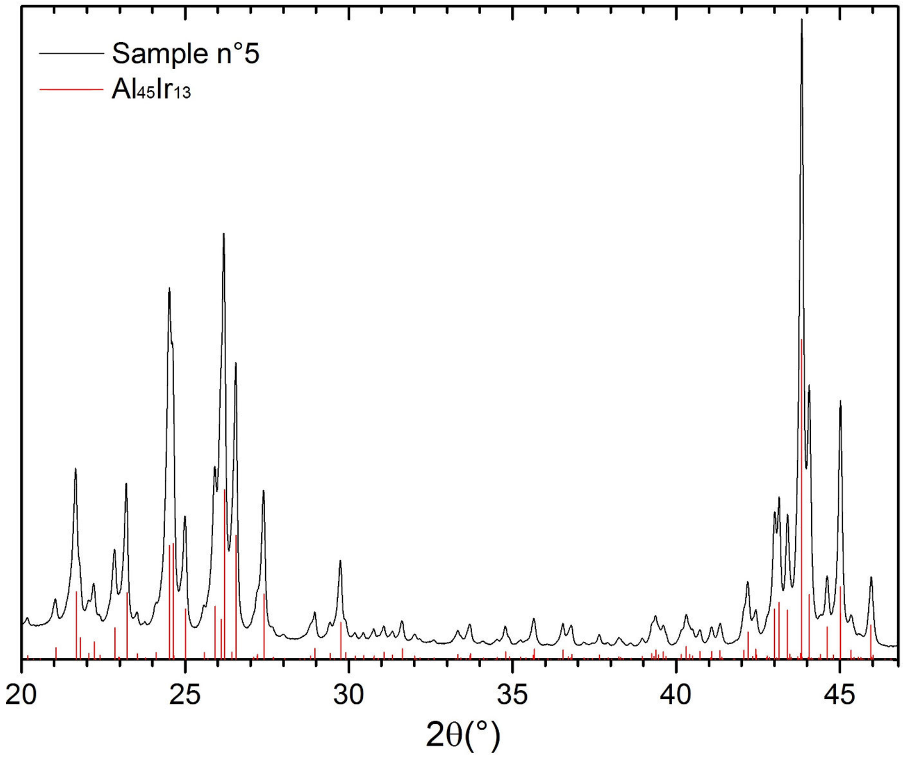

FIGURE 3.31: PXRD pattern of the sample n°5.

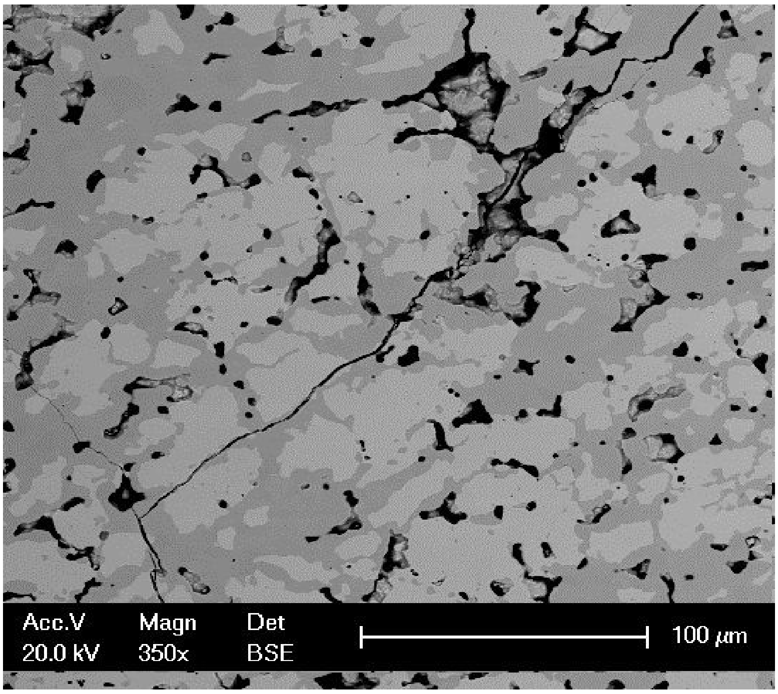

FIGURE 3.32: SEM image of the sample n°5 taken in BSE mode.

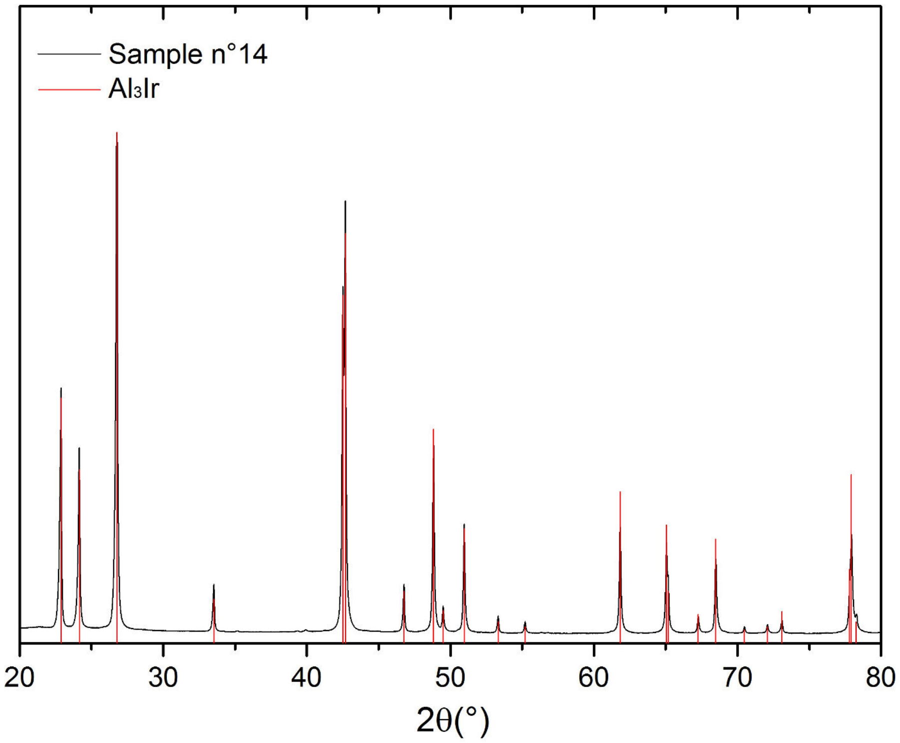

FIGURE 3.33: PXRD pattern of the sample n°14.

WDS

Figure 3.34 shows an image of the sample n°14 obtained using an EPMA. The composition of the Al_3Ir phase present in this sample n°14 has been precisely determined with WDS analysis. An average of ten points of measurements gives a chemical composition of $Al_{74.47}Ir_{25.53}$ with a deviation of 0.04 for both values. This is in full agreement with the composition of the sample n°14. However, the Al_3Ir phase appears to have a higher content in iridium than expected. The WDS technique is much more precise than EDS so this phenomenon should be considered to be real. This is the evidence of a probable small homogeneity range of the Al_3Ir phase which has not been reported before.

DSC

DSC was carried out on the sample n°14. One clear peak is observed at 1461°C on the heating curve and another sharp peak appears at 1412°C on the cooling curve (see Fig. 3.35). This temperature of 1461°C is in full agreement with the known melting point of the Al_3Ir phase [67]. The peak at 1412°C on the cooling curve corresponds to the recrystallisation of the same phase. The shift in temperature could be explained by a supercooling phenomenon [76].

3.8 Conclusion

The aluminium-iridium system has been intensively reinvestigated on the Al-rich side of the phase diagram. From this study, a new compound $Al_{2.4}Ir$ has been reported and fully characterised. Its crystal structure has been solved and similar building blocks than in the $Al_{28}Ir_9$ compound have

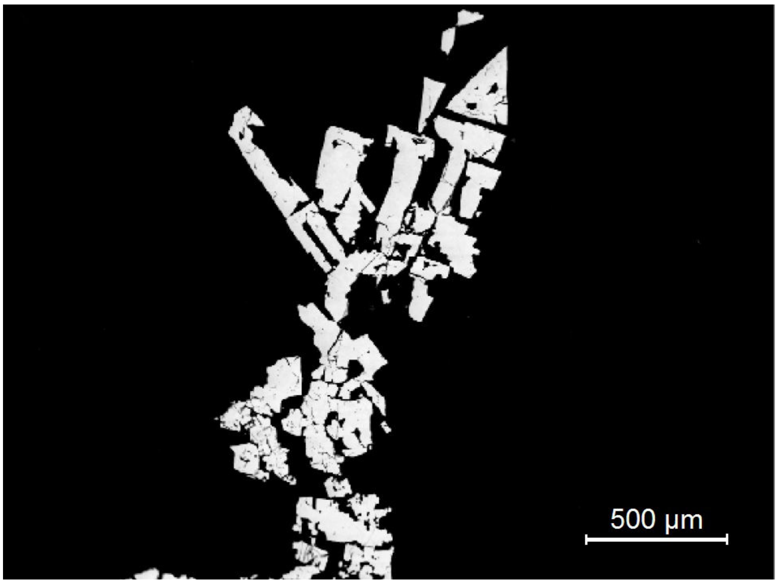

FIGURE 3.34: EPMA image of the sample n°14 taken in BSE mode at 20kV.

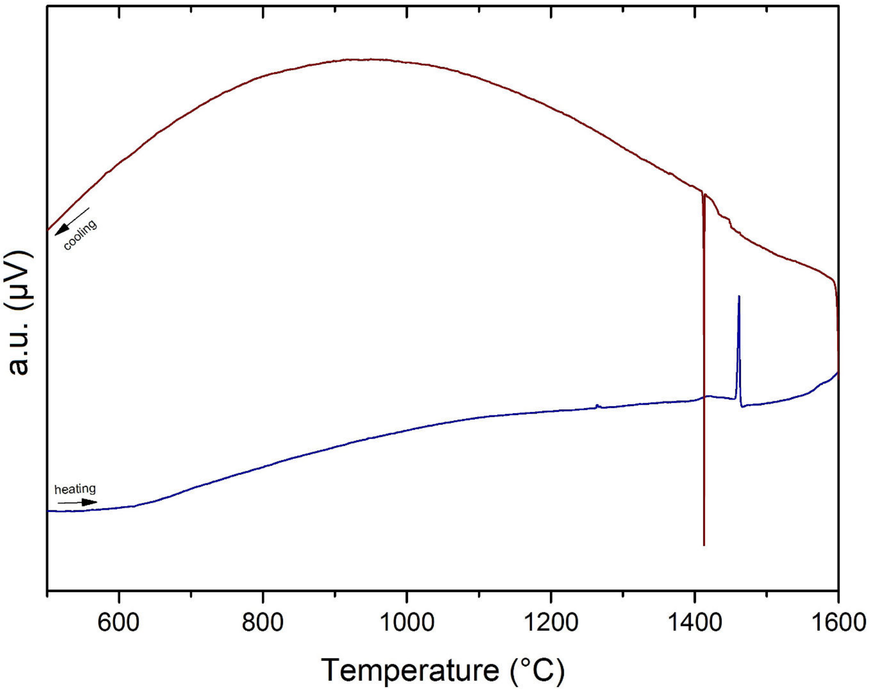

FIGURE 3.35: DSC heating and cooling curves of the sample n°14.

been identified. Concerning this latter phase, it can adopt two structural models as demonstrated by HR-PXRD analysis. While the previously reported model for this compound agrees well with its high temperature structure, a new model has been established for its low temperature variant. The evidences of a superstructure for the $Al_{2.75}Ir$ compound has been confirmed with PXRD. A preliminary superstructure model has been established and the temperature of the transition between the two structures has been also determined. The other Al_9Ir_2, $Al_{45}Ir_{13}$ and Al_3Ir phases did not show any new notable features. They have been studied and the results are in good agreement with the literature data. Among the different works carried out on the Al-rich side of the Al-Ir phase diagram, the $Al_{13}Ir_4$ remained a matter of debate among several authors. In our study, the questionable $Al_{13}Ir_4$ phase has never been observed. The numerous samples that have been prepared in its compositional region never showed any hint of such compound. The hypothesis given by Pavlyuchkov *et al.* by which the $Al_{13}Ir_4$ phase has most probably been mistaken with $Al_{28}Ir_9$ or $Al_{45}Ir_{13}$ is probably the best explanation. All these new results concerning the Al-Ir system will help to establish a new phase diagram. The system is currently the subject of a thermodynamic reassessment. For this task, the database of the latest Al-Ir assessment has been taken (courtesy of Abe *et al.* [62]), including the experimental results presented in this Chapter. An updated Al-Ir phase diagram should be available soon.

Chapter 4

Aluminium-iridium-based ternary systems

4.1 Introduction

As explained in Chapter 1, within a given ternary system, substituting transition metal by elements of the same column in the Periodic Table can lead to compounds that share similar physical and chemical properties. This was demonstrated by Tsai *et al.* [9], who found stable icosahedral quasicrystals by replacing Fe with either Ru or Os in Al-Cu-Fe, hence suggesting that Al-based quasicrystals are electronically stabilised (Hume-Rothery phases). For Al-Ir-TM systems, several stable quasicrystalline or approximant phases have also been discovered. For instance, a decagonal quasicrystal with a nominal composition of $Al_{73}Ir_{14.5}Os_{12.5}$ has been reported in the Al rich part of the Al-Ir-Os phase diagram [27]. Its structure along the 10-fold axis can be described as a periodic stacking of eight quasiperiodic layers of atoms, leading to a 16.8 Å periodicity [27]. Similarly, stable decagonal $Al_{65}Ir_{15}Cu_{20}$ (for other compositions, see refs [77] and [26]) and icosahedral $Al_{60}Ir_{20}Cu_{20}$ [78] phases and recently a cluster-based cubic phase [26] with a composition of $Al_{63.3}Ir_{24.4}Cu_{12.3}$ have been identified in the Al-Ir-Cu system. The structure of the $Al_{63.3}Ir_{24.4}Cu_{12.3}$ intermetallic compound consists of a packing of endohedral clusters. The latter is considered as a (2 x 2 x 2)- fold superstructure of a 1/0 approximant of a Mackay cluster-based icosahedral quasicrystal [26]. This type of structure (comparable unit cell dimensions and space group) has also been observed in a $Al_{64.5}Ir_{13.5}Pd_{22}$ sample [28] although the latter structure remains to be fully determined. As explained above, complex intermetallic phases exist in the Al-Ir-(Os, Cu, Pd) systems. In the framework of this thesis, new phases have been explored in the Al-Ir-Au, Al-Ir-Si and Al-Ir-Ag systems, systems for which nothing has been reported yet.

4.2 The Al-Au-Ir system

4.2.1 Introduction

With the aim of finding compounds with similar atomic structure to the interesting quasicrystals found in the Al-Cu-Ir system, we have replaced Cu by Au and have explored the Al-Au-Ir ternary system, starting with a composition similar to what has already been selected in previous studies, i.e. in the Al-rich part of the phase diagram (65-70 at. % Al). Nine samples were synthesised in total, annealed and characterised with the standard metallographic techniques. From this investigation,

TABLE 4.1: Considered atomic compositions of the Al-Au-Ir samples and the thermal conditions of their annealing treatments.

Sample n°	Considered Atomic composition Al	Au	Ir	Temperature of annealing (°C)	Duration of annealing (h)
1	62.2	16.2	21.6	950	72
2	67.5	16.3	16.2	600	168
3	79.4	10.3	10.3	940	30
4	78.1	18.7	3.3	900	102
5	34.6	14.8	50.6	900	128
6	62.3	24.8	12.9	900	252
7	67.7	29.7	2.9	-	-
8	68.3	28.7	3.0	900	336
9	59.7	15.3	25.0	900	336

two new intermetallic compounds, Al_3AuIr and $Al_{72}Au_{2.5}Ir_{29.5}$ were revealed. This part will be about the identification and the full description of these new phases.

4.2.2 Experimental details

Ingots of 0.3 g to 0.5 g mass were synthesised from high-purity Al, Au and Ir elements. The samples were prepared by arc melting under a partial argon atmosphere. As for the Al-Ir alloys, the samples underwent a mass loss of about 1 % to 2 % because of a partial evaporation of aluminium. The ingots were each wrapped in tantalum foils, sealed in evacuated quartz tubes filled with a partial He/H_2 10 % atmosphere, and annealed to various temperatures for different times. Full details about the composition of the samples and their annealing conditions are presented Table 4.1. A small fraction of the sample was sometimes found evaporated on the Ta foil after the annealing treatment. The as-cast and annealed samples were studied by powder XRD (using Cu $K\alpha_1$ radiation), optical microscopy, and scanning electron microscopy. The local phase compositions were obtained by SEM with energy dispersive X-ray spectroscopy analysis, and the melting points of the different phases were determined using differential thermal analysis with heating and cooling rates of $10K.min^{-1}$. Single crystals were obtained from crushed part of the samples. The XRD data were collected on a Bruker Kappa Apex II diffractometer equipped with a mirror monochromator and a Mo $K\alpha$ IμS (λ = 0.71073 Å). The Apex 2 program package was used for the cell refinements and data reductions. The structures were solved using direct methods and refined with the SHELXL-2013 and WinCSD programs. Semi-empirical absorption correction (SADABS) was applied to the data. Structural relaxation and DOS calculations were performed for the new compound Al_3AuIr by Dr. Émilie Gaudry from the Metallurgy and Surfaces team of the Institut Jean Lamour in Nancy. Analysis of the chemical bonding was also performed for this compound by Pr. Juri Grin from the Chemical Metals Science of the Max-Planck institute of Dresden.

4.2.3 Overview on the samples

The first ternary compound Al_3AuIr was discovered directly following the characterisation of the sample n°1 which was prepared by selecting a composition similar to Al-Cu-Ir quasicrystals. Since this first compound is finally not quasicrystalline, the samples n°2, 3, and 4 were synthesised for further explorations of this region of the phase diagram. However, there was no sign of an additional ternary compound. The composition of sample n°5 was inspired by the $Al_{34}Au_{51}Yb_{15}$ quasicrystal [79]. The authors reported that this quasicrystalline phase was observed in their as-cast sample. Our as-cast and annealed samples n°5 did not show any evidence of a ternary compound however. The composition of sample n°6 was chosen for the exploration of the Ir-richer side of the phase diagram. PXRD pattern of this alloy showed hints of a compound that could not be attributed to any known binary Al-Ir or Al-Au phases. Further investigation on this specimen led to the preparation of the samples n°7 and 8. The new ternary compound $Al_{69.2}Au_{2.4}Ir_{28.4}$ was finally identified and fully characterised out of the sample n°8. A recent report about a new quasicrystal $Al_{58}Cu_{26}Ir_{16}$ [80], i.e. with a composition richer in gold than the previous ones, influenced the preparation of the sample n°9. The same thermal treatment as reported by Seki *et al.* [80] were applied to this sample. Unfortunately, no new ternary phase could be identified. The characterisation of the Al_3AuIr compound was carried out with only the sample n°1. The sample n°8 was used for the study of the $Al_{69.2}Au_{2.4}Ir_{28.4}$ phase.

4.2.4 The Al_3AuIr compound

Composition and Thermal Behaviour

Figure 4.1 exhibits typical optical microscopy images collected on polished as-cast and annealed samples. For the as-cast sample shown in Fig. 4.1a, three phases have been identified. They are referred to as the dark, gray, and bright phases, appearing gray, orange, and nearly white in true color, respectively. Prior to polishing the sample, the dark phase can be described by a distribution of well-faceted cubes (edge length $\leq 50\ \mu$m) surrounded by the gray and bright phases. The dark phase seems to have solidified first, followed by the other two phases that would have solidified simultaneously. The EDS measurements have revealed the dark phase to be $Al_{2.75}Ir$, the gray one to be Al_2Au, and the bright one to be a Al-Au-Ir ternary phase. Although the Al_2Au compound has a orange/reddish tint here (similar color to that in Ref. [81]), it is a well-known phase referred to as the "purple plague" in integrated electronics [82]. From optical microscopy observations (see Fig. 4.1b), the annealed sample appears to be almost entirely single-phase with the presence of porosities. This ternary phase can have slightly different color contrasts, and extensive EDS measurements revealed different compositions ranging from $Al_{56}Au_{23}Ir_{21}$ to $Al_{64}Au_{18}Ir_{18}$, indicating a certain homogeneity range. Some material evaporation, which is inherent to the arc-melting technique, has occurred during the specimen preparation. The PXRD patterns of the as-cast and annealed samples are depicted in Fig. 4.2. The diffractogram of the as-cast sample in Fig. 4.2 (a) is indexed using the two well-known Al_2Au [83] and $Al_{2.75}Ir$ phases [60] as impurities. The material for PXRD measurements of the annealed sample has been taken from a homogeneous region. The annealed sample diffractogram in Fig. 4.2 (b) displays sharp and intense peaks, indicative of large crystallites. The peaks present on this diffractogram correspond to those not indexed in Fig. 4.2 (a). They are associated with the peaks of the

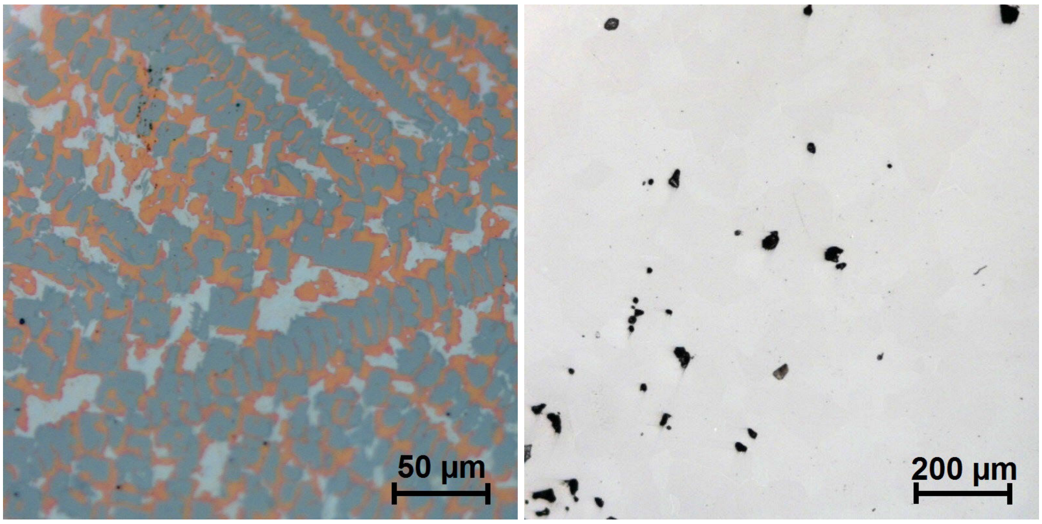

(a) As-cast (b) Annealed

FIGURE 4.1: Optical microscopy images of the as-cast and annealed samples. The gray phase is $Al_{2.75}Ir$, the orange one is Al_2Au and the white one is the new ternary compound.

ternary phase revealed by EDS. DTA analysis was carried out on the as-cast sample between 600°C and 1200°C (with heating and cooling rates of $10K.min^{-1}$). The DTA curve in this region (see Fig. 4.3) seems to bear at least two thermal effects: decomposition of the Al_2Au phase (known to take place at 1060°C [84]) and decomposition of the ternary phase at 990°C. This would explain the appearance of the single crystals used hereafter. Because of the temperature range used, the feature associated with the decomposition of the $Al_{2.75}Ir$ phase could not be observed because it occurs around 1640°C. [66] These values are consistent with the optical microscopy observations regarding the order of the solidification of the different phases.

Crystal Structure

A single crystal was obtained from a single-phase region of the annealed sample and was analysed by single-crystal XRD using the Mo Kα radiation. Reconstructed sections of the reciprocal space are not included because no additional information could be gained from the different planes measured. The final trigonal unit cell parameters are a = 4.2584(5) Å and c = 5.1991(7) Å and the crystal structure was successfully solved in the centrosymmetric space group $P\bar{3}m1$. The three atomic positions have been obtained by direct methods. This ternary phase has a total composition of Al_3AuIr and corresponds to the Ni_2Al_3 structure type (see Fig. 4.4a). The EDS measurements performed on the same single crystal indicate equal content of Ir and Au within the accuracy of the measurements ($Al_{59}Ir_{19.5}Au_{21.5}$). This results in the occupation of one atomic position 2d by a mixture of Au-Ir (respectively 0.5/0.5). To validate the composition measured by EDS, the structure refinement has been performed on the fractional occupancy of the 2d position of the Au/Ir site. The results did not lead to significant changes or to improvement of the reliability factor. The complete crystallographic data are available in Table 4.2, the atomic coordinates and isotropic displacement parameters for this ideal model are shown in Table 4.3, and the anisotropic displacement parameters are given in Table 4.4.

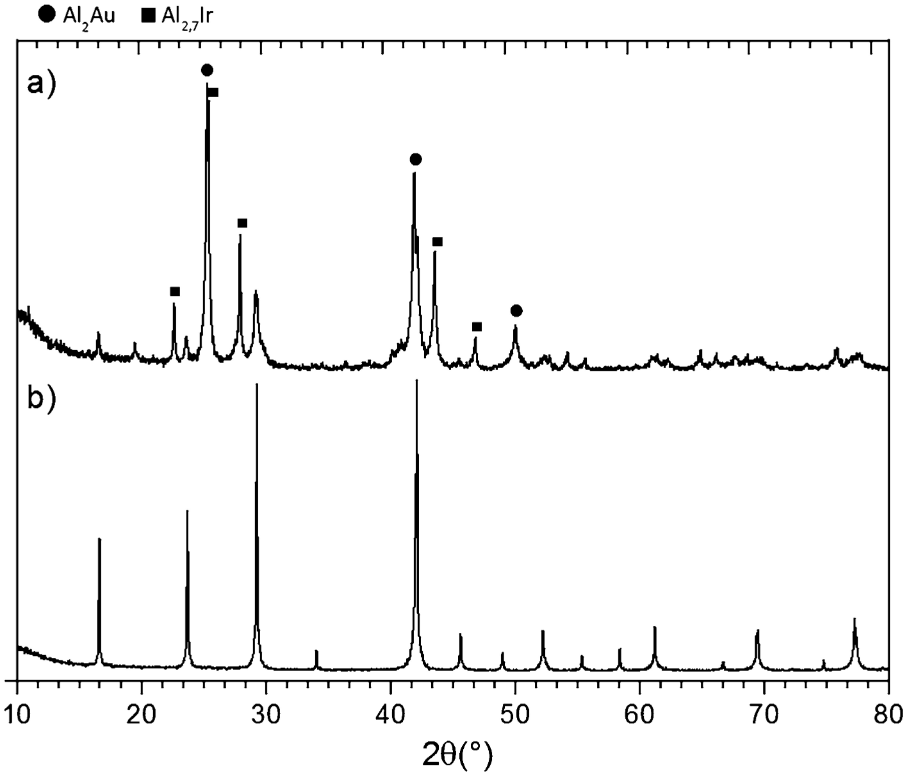

FIGURE 4.2: Powder XRD patterns of the (a) as-cast and (b) annealed samples.

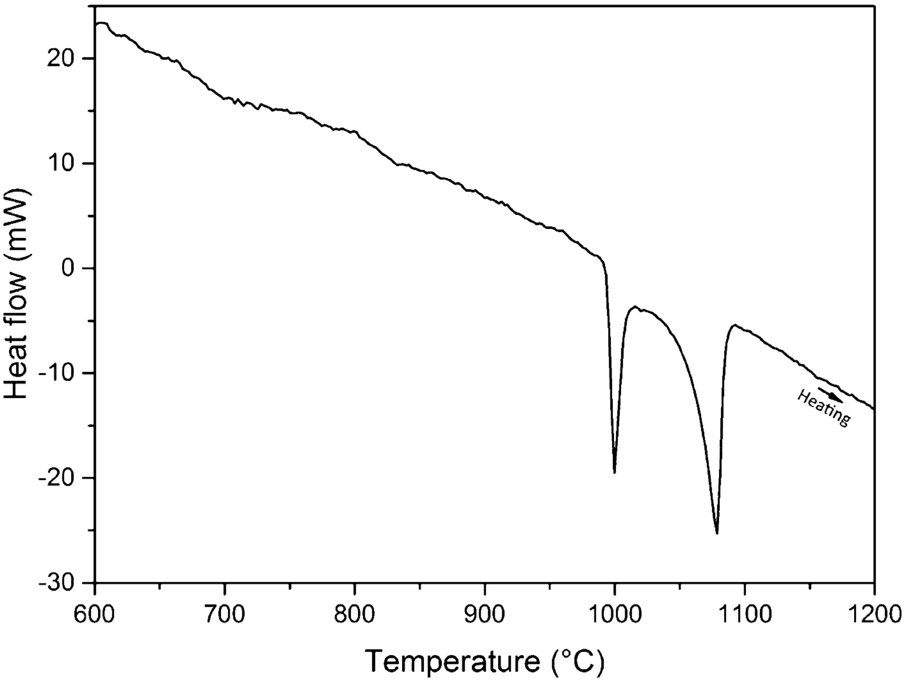

FIGURE 4.3: Differential Thermal Analysis of the as-cast sample.

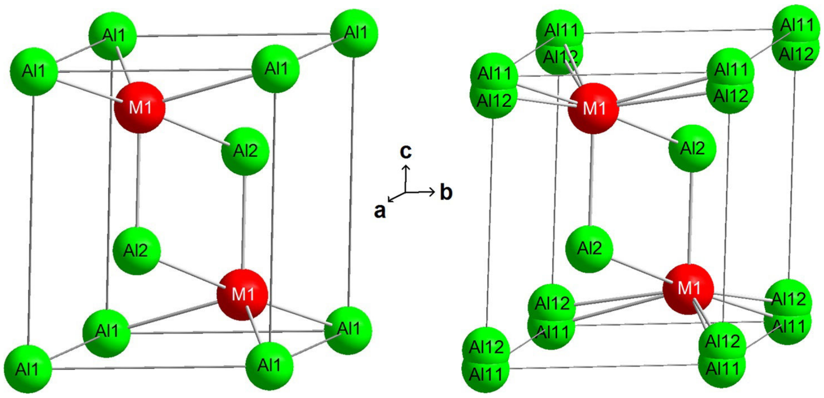

(a) The ideal model (b) The split model

FIGURE 4.4: Unit cells of the ideal and the split model. M1 is either a Au or a Ir atom.

TABLE 4.2: Crystallographic data for Al_3AuIr.

Chemical formula	Al_3AuIr
Formula weight (g.mol^{-1})	470.11
Temperature (K)	296(2)
Wavelength (Å)	0.71073
Crystal size (μm)	22 x 22 x 22
Crystal system	Trigonal
Space group	$P\bar{3}m1$
Unit cell dimensions (Å) (hexagonal setting)	a = 4.2584(5), c = 5.1991(7)
Volume (Å^3)	81.65(2)
Z	1
Calculated density (g.cm^{-3})	9.561
Absorption coefficient (mm^{-1})	86.084
F(000)	195
θ range for data collection (deg)	3.92 to 35.60
Index ranges	$-6 \leq h \leq 5, -6 \leq k \leq 6, -8 \leq l \leq 8$
Collected and independent reflections	1377, 161
Coverage of independent reflections (%)	95.3
GOF	1.323
R indices (all data)	R(int) = 0.0495, $R1$ = 0.0177, $wR2$ = 0.0397
Extinction coefficient	0.130(8)
No. of parameters refined	10
$\Delta\rho_{max}$, $\Delta\rho_{min}$ (eÅ^{-3})	2.78, -2.62

TABLE 4.3: Atomic coordinates and isotropic displacement parameters for Al_3AuIr (ideal model).

Atom	Site	x	y	z	U_{eq} (Å^2)	Occupancy
Al1	1a	0	0	0	0.033(2)	1
Al2	2d	1/3	2/3	0.6459(7)	0.0133(8)	1
Au1/Ir1	2d	1/3	2/3	0.16360(6)	0.00677(17)	0.5/0.5

TABLE 4.4: Anisotropic atomic displacement parameters (Å^2) for Al_3AuIr (ideal model).

Atom	U_{11}	U_{22}	U_{33}	U_{12}	U_{13}	U_{23}
Al1	0.0085(15)	U_{11}	0.082(7)	0.0042(8)	0	0
Al2	0.0161(12)	U_{11}	0.0075(15)	0.0081(6)	0	0
Au1/Ir1	0.00765(19)	U_{11}	0.0050(2)	0.00383(10)	0	0

Split Model

In order to understand the unusually strong displacement anisotropy of the Al1 position calculated with z = 0 (hereafter Al11), the difference density map was calculated without any atoms at this place. Figure 4.5 represents the distribution of the difference electron density in the (010) plane in the vicinity of the Al1 position: (top panel) calculated without any atoms in the Al1 position; (upper middle panel) calculated with Al in the Al12 position; (lower middle panel) calculated with Al in the Al11 position; (bottom panel) calculated with Al in equal amounts in the Al11 and Al12 positions. In the upper three panels, the isolines are drawn with a step of 4 e Å^{-3}, and in the bottom panel, with a step of 0.4 e Å^{-3}. Positive values of the difference density are shown with solid lines, zero values with dashed lines, and negative values with dashdotted lines. The scale ticks on the axes are shown with a step of 0.5 Å. The so-obtained difference density distribution reveals marked elongation in the [001] direction (Fig. 4.5, top). Such a distribution cannot be described completely either by locating Al atoms in the off-centre position (the coordinate z = 0.063 resulted from the final refinement) with an isotropic displacement parameter (u = 0.0119, Al12 position) or by positioning the Al in the ideal position with z = 0.0 (Al11 position). In both cases, a non-negligible part of the density remains undescribed (Fig. 4.5, middle panel). Only after location of Al in equal amounts in both positions does the final difference electron density map show only very weak features in the vicinity of the Al1 position (Fig. 4.5, bottom). The results of the final refinement are shown in Tables 4.2, 4.5, and 4.6; the interatomic distances are listed in Table 4.7. The appearance of Al in different positions in this part of the crystal structure (see Fig. 4.4) correlates with the locally different coordination of this site by Ir and Au atoms having different sizes. In the case of a symmetrical environment (with either Ir or Au coordinating this position), Al occupies the Al11 position, and in the case of a nonsymmetrical environment (Ir and Au in equal amounts coordinate Al1), the Al12 atoms are shifted from the ideal

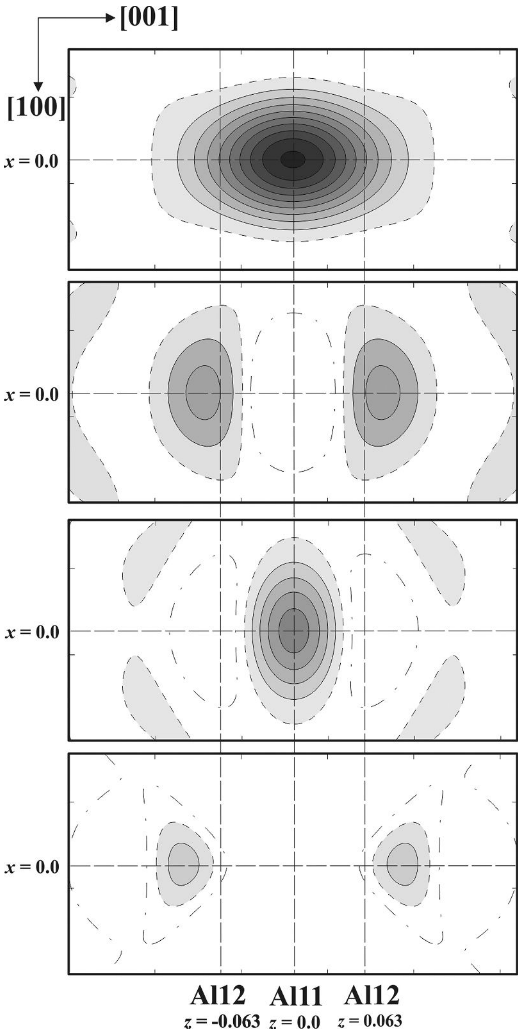

FIGURE 4.5: Difference Fourier maps at the Al1 position (see text for conditions).

position at z = 0.0. The intermediate variants of occupation may cause smaller shifts.

Electronic Structure

To investigate how the interatomic distances evolve with the TM decoration inside the structure, the fictitious Al_6Au_3Ir and Al_6AuIr_3 compounds have been considered and will be compared later to the Al_6Co_3Ir and Al_6CoIr_3 compounds later. They are built by doubling the periodicity along the c axis. Electronic structure calculations and structural relaxations were performed for the three ordered models Al_3AuIr (i.e. $Al_{60}Au_{20}Ir_{20}$), Al_6Au_3Ir (i.e. $Al_{60}Au_{30}Ir_{10}$), and Al_6AuIr_3 (i.e. $Al_{60}Au_{10}Ir_{30}$). The Al_3AuIr crystal structure was built using the cell parameters of Table 4.2 and the atomic positions of Table 4.3 with one Ir atom in one of the two 2d sites ($^1/_3$, $^2/_3$, 0.1636) and one Au atom in the other one ($^2/_3$, $^1/_3$, -0.1636). The crystal structures of Al_6Au_3Ir and Al_6AuIr_3 were built by doubling the periodicity along the c axis. The resulting cells contain then four TM atoms: three Au (respectively three Ir) and one Ir (respectively one Au) atoms in the case of the Al_6Au_3Ir (respectively Al_6AuIr_3) phase. The Vienna Ab initio Simulation Package (VASP) [70, 85–87] was used for calculations based on the density functional theory (DFT). VASP performs a variational solution of the Kohn-Sham equations in a plane-wave basis. We used the projector-augmented wave method [88, 89] and the

Table 4.5: Atomic coordinates and isotropic displacement parameters for Al_3AuIr (split model).

Atom	Site	x	y	z	U_{eq} (Å^2)	Occupancy
Al11	1a	0	0	0	0.0122(8)	0.5
Al12	2c	0	0	0.0624)	0.00119(8)	0.25
Al2	2d	$^1/_3$	$^2/_3$	0.645(1)	0.0167(12)	1
Au1/Ir1	2d	$^1/_3$	$^2/_3$	0.16357(9)	0.0091(2)	0.5/0.5

Table 4.6: Anisotropic atomic displacement parameters (Å^2) for Al_3AuIr (split model).

Atom	U_{11}	U_{22}	U_{33}	U_{12}	U_{13}	U_{23}
Al2	0.017(2)	U_{11}	0.010(2)	0.0086(8)	0	0
Au1/Ir1	0.0089(3)	U_{11}	0.0067(3)	0.0044(1)	0	0

Table 4.7: Main interatomic distances (Å) for Al_3AuIr.

Atom	Distance
Au1/Ir1 - 6Al11	2.6015(3)
Au1/Ir1 - 3Al12	2.514(4)
Au1/Ir1 - 3Al12	2.726(8)
Au1/Ir1 - Al2	2.507(5)
Au1/Ir1 - 3Al2	2.651(2)
Au1/Ir1 - Al2	2.692(5)
Au1/Ir1 - 3Au1/Ir1	2.9896(5)
Al12 - Al12	0.65(3)
Al2 - 6Al11	3.072(3)
Al2 - 3Al12	2.888(10)
Al2 -3Al12	3.277(13)
Al2 - 3Al2	2.889(4)

generalised gradient approximation of Perdew-Burke-Ernzerhof [90, 91] to describe the interactions. The following cutoff and k-points grid were used for the calculations (Al_3AuIr model): E_{cut} = 500 eV; 29 × 29 × 13 k-points grid. The calculation of the Hellmann-Feynman forces on the atoms allows us to perform a full optimisation of the atomic positions in the unit cell and of the lattice parameters. The total energies and density of states were calculated using the relaxed structures. The formation enthalpies are given with reference to pure Al, Au, and Ir (a face-centered-cubic system).

The DFT structural relaxations obtained on Al_3AuIr are consistent with the cell parameters deduced from XRD analysis (a = 4.28 Å and c = 5.26 Å) and with the atomic displacement proposed in the split model. For the noncentrosymmetric Al_3AuIr structure, a displacement of Al1 atoms by z = 0.069 is observed, while the mean positions of the Al2 and TM atoms remain roughly unchanged ($z_{Al2}{}^{mean}$ = 0.647 and $z_{TM}{}^{mean}$ = 0.166). The Al1-Au distance $d_{Al1-Au}{}^{Au,Ir}$ is increased in a mixed environment (Au and Ir) compared to the one ($d_{Al1-Au}{}^{Au}$) obtained in a Au-rich environment ($d_{Al1-Au}{}^{Au,Ir}$ - $_{Al1-Au}{}^{Au}$ $\simeq$ 0.30 Å). In the same way, the Al1-Ir distance $d_{Al1-Ir}{}^{Au,Ir}$ in a mixed environment is smaller than the one ($d_{Al1-Ir}{}^{Ir}$) found in an Ir-rich environment ($d_{Al1-Ir}{}^{Ir}$ - $_{Al1-Ir}{}^{Au,Ir}$ $\simeq$ 0.22 Å). These observations are consistent with the results presented in the next section based on the electron localiisingbility approach.

The structure of this new compound Al_3AuIr belongs to the structure type Ni_2Al_3 [92] and is related to that of the $Al_3Cu_{1.5}Co_{0.5}$ phase (i.e. $Al_{60}Cu_{30}Ir_{10}$), a compound crystallising in the same trigonal crystal system (space group $P\overline{3}m1$) with parameters close to the here-reported ternary alloy: a = 4.116 Å and c = 4.938 Å [93, 94]. The close relationship between these two phases may be explained by the replacement of Co and Cu with Ir and Au atoms, elements of the same group in the Periodic Table. The $Al_3Cu_{1.5}Co_{0.5}$ phase has a nominal composition slightly different from that of the new ternary alloy Al_3AuIr (richer in elements of the VIII-B group). According to Grushko *et al.* [93] the $Al_3Cu_{1.5}Co_{0.5}$ phase exists in a quite wide region, between 58 and 62 atom % Al and 12-20 atom % Co. However, electronic structure calculations using the tight-binding linear muffin-tin orbital method performed by Sabiryanov *et al.* [95] concluded that the $Al_3Cu_{1.5}Co_{0.5}$ phase is thermodynamically stable while the Al_3CuCo phase is not. The cohesive energy of the $Al_3Cu_{1.5}Co_{0.5}$ compound is found to be slightly larger than that of the Al_3CuCo compound. The calculated electronic DOS exhibits a small minimum (pseudogap) at the Fermi level in the case of the $Al_3Cu_{1.5}Co_{0.5}$ compound but not for the Al_3CuCo phase. Authors concluded that the latter is not stabilised by a Hume-Rothery mechanism, while the Fermi surface-Brillouin zone interaction contributes to stabilisation of the former [95].

In the present study, it appears that a Au to Ir ratio equal to 1 is favorable in the Al-Au-Ir system, and it results in a stable phase. We note that the Al_3Ni_2 structure type is common to Al_3Pd_2 and Al_3Pt_2, i.e. for all TM elements of the same column of the Periodic Table [96, 97]. Therefore, the formation of stable Al_3TM_2 compounds (with TM = Ni, Pd, or Pt) is equivalent to an isoelectronic substitution because elements of the same column have similar chemistry. The formation of the Al_3AuIr compound can also be viewed as an isoelectronic substitution of Pt atoms, with adjacent TM elements Ir and Au having similar Pauling electronegativities. This strongly suggests a Hume-Rothery stabilisation mechanism for the Al_3AuIr phase, contrary to the Al_3CuCo case. This mechanism is based on a Fermi sphere-Brillouin zone interaction, where a reduction of the DOS at the Fermi level contributes to stabilisation of the crystal (for a review, see refs [98] and [99]). The electronic DOSs of the three Al_3TM_2 phases (TM = Ni, Pd, or Pt) have been calculated using a full potential linear muffin-tin orbital method. In each case, a marked pseudogap at the Fermi level is observed in agreement with the Hume-Rothery picture [100, 101]. We can further estimate if the Hume-Rothery condition $2k_F = K_{hkl}$ is satisfied for some intense Bragg reflections. Assuming a negative valence of -0.6 for the (Au, Ir) pair inferred from Raynor's value for Ni and a valence of 3+ for Al, the Fermi wave vector is approximated using a free electron model, which leads to $2k_F = 2.8$ Å^{-1}, a value close to that of the K_{110}, K_{102}, and K_{012} Bragg planes (2.95 Å^{-1}) associated with the most intense diffraction peak in Fig. 4.2. This again suggests a Hume-Rothery stabilisation mechanism.

Figure 4.6 presents the electronic DOSs calculated for the Al_6Au_3Ir, Al_6AuIr_3, and Al_3AuIr phases. The DOSs of both Al_6Au_3Ir and Al_3AuIr systems show a broad local minimum in the vicinity of the Fermi level. The overall shape of the Al_3AuIr DOS is similar to that of the Al_3Pt_2 system [100, 101]. In addition, ΔH_f is located within a broad minimum of the DOS. To analyse the stability of the Al-Au-Ir phases, total energy calculations have been carried out and lead to a formation enthalpy of -0.681 eV atom^{-1} for the Al_3AuIr compound, while it is -0.517 and -0.730 eV atom^{-1} for the Al_6Au_3Ir and Al_6AuIr_3 compounds, respectively. These results clearly demonstrate a higher stability of the Al_3AuIr phase compared to the Al_6Au_3Ir composition, i.e. consistent with the absence of the Al_6Au_3Ir phase in the samples characterised. Contrary to the Al-Cu-Co system, here a Au to Ir ratio equal to 1 is favored. As demonstrated by the Al_6AuIr_3 compound, other chemical variants may lead to more favorable formation enthalpies. Here, the formation enthalpy of -0.730 eV atom^{-1} obtained for the Al_6AuIr_3 compound would suggest at first an even higher stability. However, this hypothetical composition has not been observed experimentally and has been considered only to complete our systematic approach. Hence, it is suggested that a configurational entropy contribution (higher for the 1:1 than for the 1:3 Au/Ir ratio) may counterbalance the formation enthalpy difference of 49 meV atom^{-1} between both phases, then resulting in a greater stability of the Al_3AuIr phase.

Chemical Bonding

Analysis of the chemical bonding was performed for the ordered Al_3AuIr model using the lattice parameters and atomic coordinates from the crystal structure refinement of single-crystal XRD data and changing of the occupation of the TM position. These criteria chosen to generate the Al_3AuIr model led locally to a completely ordered structure. For Al_3AuIr, the symmetry was reduced from $P\overline{3}m1$ to $P3m1$. The z coordinates for the two, in this space group, independent atoms Al21 and Al22 representing the Al2 position in the structure refinement were fixed at values reflecting their positions in the experimental structure. So, the calculations were performed for different positions of Al1 with z = 0.0 (Al11), 0.063, and -0.063 (Al12). The TB-LMTO-ASA program package [102] was employed using the von Barth-Hedin exchange potential [103] for the local-density approximation calculations. The radial scalar-relativistic Dirac equation was solved to obtain the partial waves [104]. The addition of empty spheres was not necessary because the calculation within the atomic sphere approximation (ASA) includes corrections for the neglect of interstitial regions and partial waves of higher order [105]. The following radii of the atomic spheres were applied for calculations on Al_3AuIr: r(Ir) = 1.638 Å, r(Au) = 1.593 Å, r(Al1) = 1.606 Å, r(Al21) = 1.530 Å, and r(Al22) = 1.489 Å. A basis set containing Au(6s,6p,5d), Ir(6s,6p,5d), and Al(3s,3p) orbitals was employed, with Au(5f), Ir(5f), and Al(3d) functions being downfolded. The electron localiisingbility indicator (ELI, Y) was

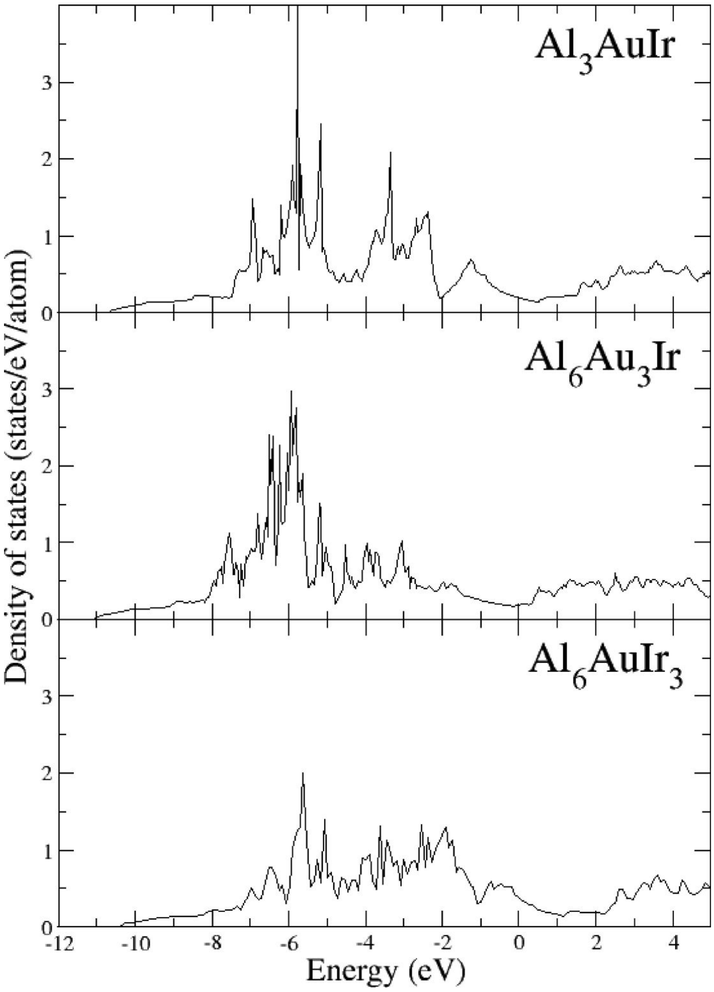

FIGURE 4.6: Electronic DOSs calculated for the Al_3AuIr, Al_6Au_3Ir and Al_6AuIr_3 models.

evaluated in the ELI-D (distribution of the ELI) representation [106–108] with an ELI-module within the TB-LMTO-ASA program package. Estimation of the shapes, volumes, and charges of the atoms after Bader (quantum theory of atoms in molecules, QTAIM [107]) and topological analysis of the ELI, e.g., localisation of the ELI maxima as indicators of the direct atomic interactions, estimation of their basins, as well as calculations of the QTAIM/ELI-D intersection [108], were performed with the program DGrid [109].

To gain further insight into the bonding present within the Al-Au-Ir compound, quantum chemical calculations have been performed for the Al_3AuIr composition. For this ternary model, the non-centrosymmetric space group $P3m1$ was used with three different values for the z coordinate of the Al1 position. The lowest total energy was calculated for the ordered Al_3AuIr structure with Al at the Al12 site and z = -0.063, being slightly larger for z = 0.0 and the largest one for z = 0.063. The Au/Ir distribution is presented in Fig. 4.7a. This model is in well-agreement with the atomic radii of Au and Ir (1.44 and 1.35 Å, respectively), showing longer Au-Al12 distances compared to the Ir-Al12 ones.

The shapes and effective charges of the QTAIM atoms (see Fig. 4.7a) are in good agreement with the electronegativity values of the components. Au and Ir show negative effective charges playing the role of electron acceptors but revealing different charges independently on the position of Al1. Al atoms show different positive charges depending on their environment. The lower difference between the charges of different Al atoms is observed with Al1 in the off-centre position Al12. For the Al12 position, the lowest difference between Au and Ir effective charges is observed for z = 0.063, thus revealing this model as one with the most regular distributions of atomic charges. In general, taking into account large effective charges, charge transfer makes a large contribution to stabilisation of the structural pattern of Al_3IrAu.

Figure 4.7 shows the chemical bonding in three models of Al_3AuIr with different positions of the Al1 atoms. The ELI-D in the vicinity of the atom nuclei in Al_3AuIr reveals strong deviations from the spherical shape characteristic for the isolated atoms (see Fig. 4.7b). The deviations are stronger in the valence region (i.e. in the last atomic shells), but also the penultimate shells of Ir and Au show clear nonsphericity, indicating participation of the electrons of these shells in the bonding interactions [110, 111]. Independently of the z coordinate for Al1, there are six different types of ELI-D maxima (attractors) in the unit cell. Their functions in the bonding pattern are different depending on the value of z(Al1). For the model with z = 0.0, the three symmetrically equivalent ELI-D attractors around each Au-Al21 contact reflect well the ring attractor of the two-centre (2c) interaction between d metals or between a d metal and a p element, similarly to those reported for Sc-Ge, $(Sc\text{-}Sc)^{2+}$ [110, 111], and Cu-Cu [112]. The basin of the ELI-D maximum located in the vicinity of the Au-Al1 contact is intersecting only the basins of these two atoms, thus indicating also here a 2c bonding. A similar topological situation is found for the Ir-Al1 interaction, which also has 2c character. The next type of ELI-D maxima is located close to the Al21-Al22 contacts and may suggest a direct Al-Al bonding. Nevertheless, intersection analysis reveals that the largest part of the basin for this attractor is located within the QTAIM atom of Ir and its basin has a contribution from Au, revealing the four-centre (4c) bonding in this part of the crystal structure being in agreement with the relatively large Al-Al distance of 2.89 Å, which is compatible with the distance of 2.86 Å in elemental Al, where a picture of a multicentre interaction is often applied to understand the bonding. Even more complex

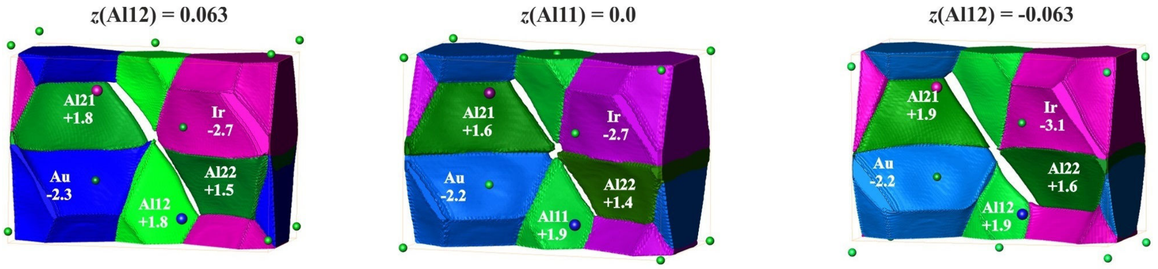

(a) Shapes and effective charges of the QTAIM atoms

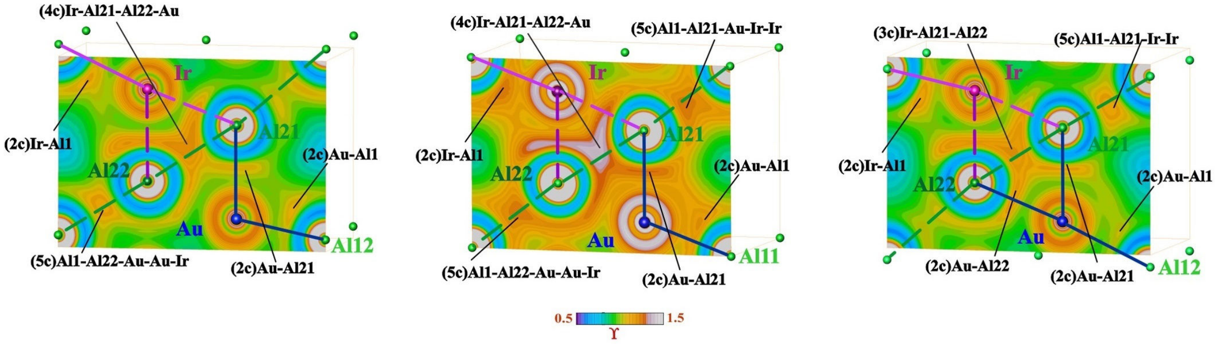

(b) ELI-D in the (110) plane with assignment of the ELI-D attractors to the two-centre and multicentre interactions according to the intersection technique

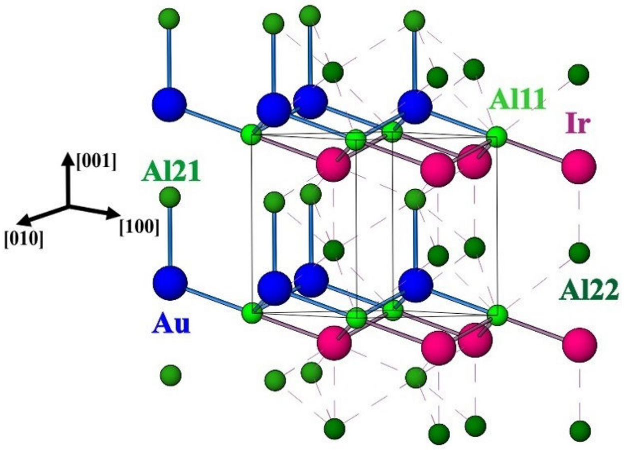

(c) Distribution of the two-centre and multicentre bonds in the ordered model of Al_3AuIr

FIGURE 4.7: Chemical bonding in the three models of Al_3AuIr. Two-centre interactions are shown with solid lines, and multicentre ones are represented with dashed lines.

topological situations are represented by the ELI-D between Al1 and Al21 as well as between Al1 and Al22, respectively. The according maxima are located close to the direct lines between the nuclei. Nevertheless, intersection analysis shows that in each case five atoms contribute to these interactions, both Al and three TM atoms, i.e. revealing the five-centre (5c) bonding in this region of the crystal structure.

The character of the bonding attractors for the model with z = 0.063 is similar to that with z = 0.0. All two- and three-centre (3c) interactions remain unchanged. One of the 5c interactions observed for z = 0.0 disappears for z = 0.063. The picture for z = -0.063 is more different. A new 2c bond Au-Al22 appears, and the former (4c) interaction now becomes a 3c one. This leads to a seven-coordinated Au atom counting only 2c bonds, which is remarkably different from the two other configurations, where each Au atom forms only four 2c bonds. Together with the largest energy for this model, this makes it less probable for the crystal structure of Al_3AuIr.

In the crystal structure of Al_5Co_2, the 2c and multicentre interactions are distributed in a way that allows for interpretation as 2c-bonded zero-dimensional clusters separated by the regions with multicentre bonds [113]. The 2c and multicentre interactions in Al_3AuIr are distributed in layers perpendicular to the [001] direction (see Fig. 4.7c); a similar topology of bond distribution was observed in $Al_{13}Co_4$ [114, 115]. Ir and Au atoms are interconnected via Al, forming puckered layers. The Au atoms on the outer side of such layers are additionally "protected" by 2c bonds to the Al21 atoms, whereby the Ir-Al22 interaction is mainly of multicentre character. The layers of 2c bonds are separated by 4c and 5c bonds. Assuming that the strength of the 2c bonds is larger than those for the multicentre bonds (this is known, for instance, for the B compounds), the region of 4c and 5c interactions is intuitively more suitable for cleaving of the material and formation of the more stable surface with Ir atoms on the outer side.

4.2.5 The $Al_{72}Au_{2.5}Ir_{29.5}$ compound

A new phase identified

As explained in Section 4.2.3, this new ternary compound was first identified in the sample n°6. PXRD measurements carried out on this as-cast sample revealed the presence of the two well-known compounds $Al_{2.75}Ir$ and AlIr and of the recently discovered Al_3AuIr compound. No evidence of another phase could be identified in this sample. After the heat treatment, this sample was again analysed with PXRD. The pattern still showed the peaks corresponding to the AlIr and Al_3AuIr phases but the Bragg reflections from to the $Al_{2.75}Ir$ phase disappeared and were replaced by peaks that could not be attributed to the usual known compounds. This sample was polished and observed using scanning electron microscopy. Three phases could be clearly identified and EDS measurements confirmed the presence of the Al_3AuIr and AlIr phases. The third phase exhibited a ternary composition with a very low content of gold. Six regions of this third phase were measured with EDS and gave an average composition of $Al_{68.5(7)}Au_{2.4(1)}Ir_{29.1(7)}$ in atomic percent. This value was then used as the nominal composition for the samples n°7 and 8. After technical problems with sample n°7, only the sample n°8 was retained for characterisation of the new phase. This alloy was directly annealed to 900°C for 336 h after its preparation.

The PXRD pattern of the annealed sample is shown in Fig. 4.8. Again, the two Al_3AuIr and AlIr phases and the unknown one are clearly identified. The Bragg reflections of the unknown phase are this time relatively intense, testifying to its large amount in the sample. SEM observations of this sample after polishing confirm this hypothesis. The AlIr phase is found to be packed in a concentrated region of the observed surface. As seen in Fig. 4.9, the rest of the sample exhibits roughly 10 % of the Al_3AuIr phase while 90 % of the remaining area is attributed of the new ternary compound.

Crystal structure

Since the annealed sample exhibits the unknown phase in a large majority, it was partially crushed so as to collect single crystals. A suitable specimen was then analysed by SC-XRD using the Mo Kα radiation. The resolution of the data after collection and reduction lead to a tetragonal unit cell with parameters a = 8.6339(2) Å and c = 21.8874(7) Å. The crystal structure was successfully solved in the most symmetric tetragonal space group $I4_1/acd$. The structure has 104 atoms in its unit cell and has the structure prototype of $BaMg_2[VO_4]_2$ [116] (Pearson symbol $tI104$). As for the Al_3AuIr compound, the Au and Ir atoms are probably statistically distributed among the same atomic positions. Extensive WDS measurements were carried out on the annealed sample in order to obtain the precise amount of gold in the unit cell. An average of 200 points revealed a composition of $Al_{68.53}Au_{2.42}Ir_{29.05}$ with a dispersion of 0.17 %, 0.18 % and 0.23 % respectively. An amount of 2.42 % of gold among 104 atoms is equal to an average of 2.5 Au atoms per unit cell. This strongly corroborates with the hypothesis of a statistical distribution of the Au atoms among the Ir positions or at least a partially occupied atomic site since a definite location of these atoms would have shown an integer number of atom per unit cell. The atomic structure was then refined counting these 2.5 Au atoms distributed among the two atomic positions of Ir of the model, leading to a final chemical formula of $Al_{72}Au_{2.5}Ir_{29.5}$ or $Al_9(Au,Ir)_4$. The complete crystallographic data are available in Table 4.8, the atomic coordinates

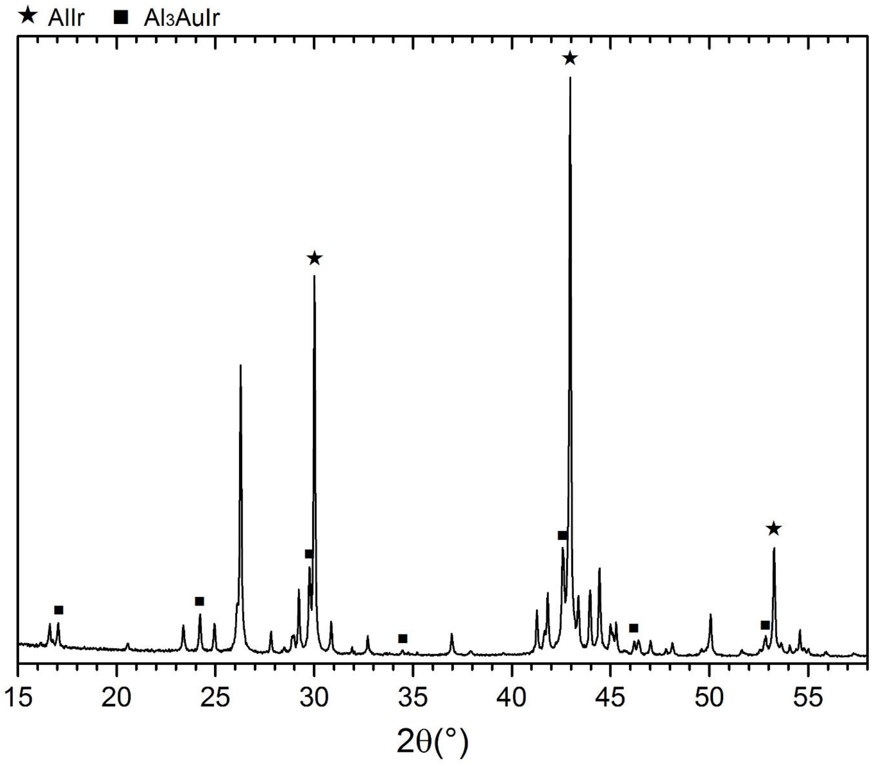

FIGURE 4.8: PXRD pattern of the annealed sample n°8. Beside the peaks from the known AlIr and Al_3AuIr compounds, a new phase can be identified.

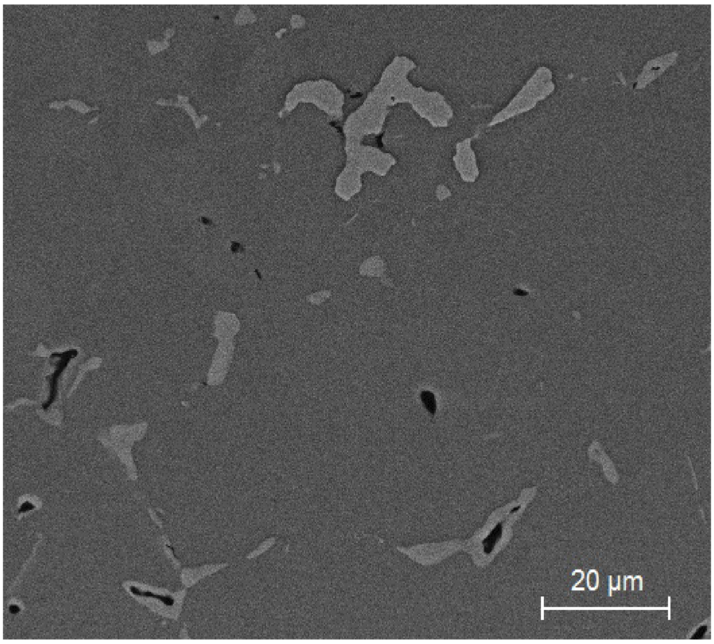

FIGURE 4.9: SEM image of the polished surface of the sample n°8 taken in BSE mode with a 2000x magnification. The light gray phase is Al_3AuIr and the dark gray phase is the new ternary compound. The AlIr phase is present in another region of the sample.

TABLE 4.8: Crystallographic data for $Al_{72}Au_{2.5}Ir_{29.5}$.

Chemical formula	$Al_{72}Au_{2.5}Ir_{29.5}$
Formula weight (g.mol^{-1})	8104.9
Temperature (K)	296(2)
Wavelength (Å)	0.71073
Crystal size (μm)	45 x 45 x 10
Crystal system	Tetragonal
Space group	$I4_1/acd$
Unit cell dimensions (Å) (tetragonal setting)	a = 8.6339(2), c = 21.8874(7)
Volume (Å^3)	1631.58(9)
Z	1
Calculated density (g.cm^{-3})	8.249
Absorption coefficient (mm^{-1})	66.450
F(000)	3405
θ range for data collection (deg)	3.8 to 44.3
Index ranges	$-16 \leq h \leq 16$, $-16 \leq k \leq 16$, $-42 \leq l \leq 42$
Collected and unique reflections	44132, 1629
GOF	1.127
R indices	R(int) = 0.0644 $R1$ (all) = 0.0250 $R1$ ($I \geq 4\sigma$) = 0.0165 $wR2$ (all) = 0.0432 $wR2$ ($I \geq 4\sigma$) = 0.0388
Extinction coefficient	0.00013(1)
No. of parameters refined	35
$\Delta\rho_{max}$, $\Delta\rho_{min}$ (eÅ^{-3})	4.05, -1.85

and isotropic displacement parameters are shown in Table 4.9, and the anisotropic displacement parameters are given in Table 4.10.

Comparing the new $Al_{72}Au_{2.5}Ir_{29.5}$ to the $BaMg_2[VO_4]_2$ compound, the Al atoms are located at the Ba and O positions while the Ir atoms are decorating the Mg and V sites. The two Au/Ir positions are each coordinated with a 9-Al polyhedron which are both comparable capped quadratic prisms (see Fig. 4.10). 4 Al1, 4 Al2 and 1 Al3 are coordinating each of the two Au/Ir positions. A representation of the crystal structure is shown in Fig. 4.11. Among the other known Al_9TM_4 compounds, none can be found with a similar structure.

TABLE 4.9: Atomic coordinates and isotropic displacement parameters for $Al_{72}Au_{2.5}Ir_{29.5}$.

Atom	Site	x	y	z	U_{eq} (Å^2)	Occupancy
Al1	32g	0.04687(12)	0.03071(12)	0.31109(4)	0.0063(2)	1
Al2	32g	0.27779(12)	0.19958(12)	0.19068(5)	0.068(2)	1
Al3	8b	0	$1/4$	$1/8$	0.0060(3)	1
Au1/Ir1	16d	0	$1/4$	0.01467(2)	0.00316(4)	0.08/0.92
Au2/Ir2	16f	0.19858(2)	0.44858(2)	$1/8$	0.00368(3)	0.08/0.92

TABLE 4.10: Anisotropic atomic displacement parameters (Å^2) for $Al_{72}Au_{2.5}Ir_{29.5}$.

Atom	U_{11}	U_{22}	U_{33}	U_{12}	U_{13}	U_{23}
Al1	0.0084(4)	0.0049(4)	0.0057(4)	0.0003(3)	0.0004(3)	0.0012(3)
Al2	0.0049(3)	0.0091(4)	0.0064(4)	0.0003(3)	-0.0010(3)	-0.0015(3)
Al3	0.0080(4)	U_{11}	0.0020(6)	-0.0043(5)	0	0
Au1/Ir1	0.00365(14)	U_{11}	0.00224(5)	0.00039(3)	0	0
Au2/Ir2	0.00358(4)	U_{11}	0.00390(5)	0.00009(3)	0	0

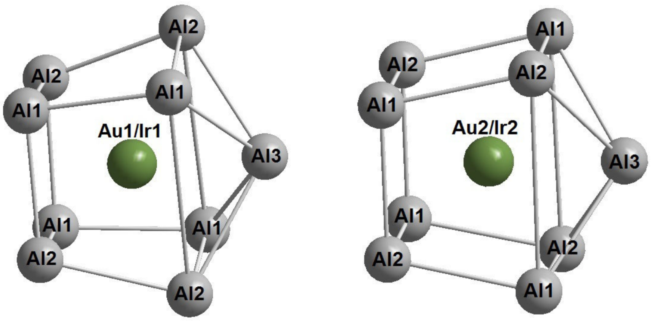

(a) Au1/Ir1 (b) Au2/Ir2

FIGURE 4.10: Coordination polyhedra around the Au1/Ir1 and Au2/Ir2 positions in the crystal structure of $Al_{72}Au_{2.5}Ir_{29.5}$.

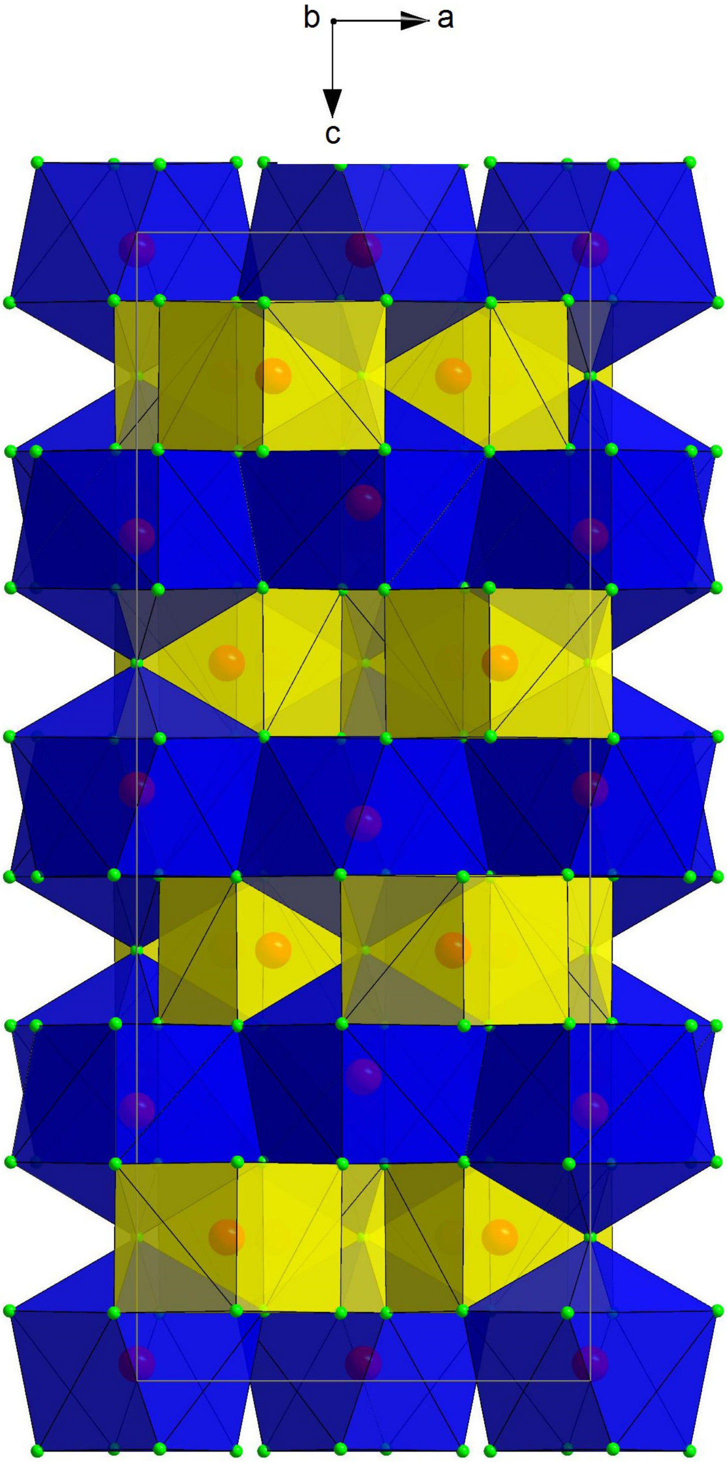

FIGURE 4.11: Representation of the crystal structure of $Al_{72}Au_{2.5}Ir_{29.5}$ in terms of polyhedra packing (Au/Ir positions in red, Al positions in green). Blue and yellow polyhedra are Al environments around the Au1/Ir1 and Au2/Ir2 positions, respectively.

4.3 The Al-Si-Ir system

4.3.1 Introduction

While aluminium and silicon are immiscible and do not form any compounds [117], the iridium-silicon system exhibits a rich variety of intermetallic compounds with structures containing up to 64 atoms per unit cell [118]. As explained in Chapter 1, intermetallic compounds stemming from systems that contain two immiscible elements such as in the Al-Si-Ir system are called "push-pull" alloys and are known to exhibit sometimes complex structures. Although the Al-Si-TM ternary systems have been widely investigated, there is no reported phases for the Al-Si-Ir system up to now. During the thorough examination of the Al-Ir phase diagram detailed in Chapter 3, a new ternary compound stabilised by silicon has been fortuitously obtained. At first, an arc-melted sample with composition $Al_{76}Ir_{24}$ was placed in an alumina crucible without a lid and sealed into a quartz tube under a partial pressure of argon before being annealed at 1200°C during 96 hours. Under this high temperature annealing condition, the quartz tube partially recrystallised and few particles of SiO_2 may have fallen into the open crucible, stabilising the ternary phase. EDS analysis revealed the presence of the aluminium, iridium and silicon elements but no oxygen was detected (except for the environmental background). To our knowledge, this is the first reported phase in the ternary system Al-Ir-Si, leading us to willingly synthesise it again. Since the Al-Si-Ir system was not the aim of this thesis, only this new ternary compound was investigated for this system.

4.3.2 Experimental details

Ingots of 5 compositions weighing about 0.3g each were prepared starting from aluminium (Alfa Aesar, 99.9965 %) iridium (Evochem, 99.9 %) and silicon (Alfa Aesar, 99.999 %). The samples were arc-melted under a partial pressure of argon, inverted and remelted several times on a water-cooled copper hearth pad using titanium sponge as a getter. Each alloy was then placed in a capped alumina crucible and sealed in an evacuated quartz tube filled with 0.5 bars of argon. All samples were annealed at 1200°C for 84 hours with a heating and cooling rate of $0.8 K.min^{-1}$. The resulting samples were analysed by PXRD with a laboratory diffractometer (Huber imaging plate Guinier Camera 670) and also at the European Synchrotron Radiation Facility in Grenoble at the ED22 beamline. SEM measurements (Philips XL30 with a LaB_6 cathode) were also carried out and the local phase compositions were determined in SEM with EDS and WDS under an Electron Probe Micro Analyser (Cameca SX100) . The melting point of the phases were obtained with DTA (Setaram Setsys 16/18). Single crystals were obtained from the crushed samples and SC-XRD data were collected on a Bruker Kappa Apex II diffractometer equipped with a mirror monochromator and a Mo $K\alpha$ IμS (λ = 0.71073 Å). The Apex 2 program package was used for the cell refinements and data reductions. Semi-empirical absorption correction (SADABS) was applied to the data. The crystal structure was solved by direct methods and was then refined using the SHELXL-2013 program. To determine the compound stability, *ab initio*-based calculations have been performed for several compounds by Dr. Émilie Gaudry from the Metallurgy and Surfaces team of the Institut Jean Lamour in Nancy. The DFT calculations were performed using the VASP package [70, 85, 86]. The interaction between the valence electrons and the ionic core was described using the projector-augmented wave (PAW) method [88, 89] and

TABLE 4.11: Nominal compositions of the prepared samples and phases found with PXRD after the annealing treatment.

Sample n°	Composition (at. %)			Phases found
	Al	Si	Ir	
1	61.18	6.07	32.75	$Al_xSi_yIr_z$ + AlIr
2	61.38	4.73	33.89	$Al_xSi_yIr_z$ + AlIr
3	64.30	4.22	31.48	$Al_xSi_yIr_z$ + $Al_{2.75}Ir$
4	63.81	3.87	32.33	$Al_xSi_yIr_z$ + $Al_{2.75}Ir$
5	64.18	3.38	32.44	$Al_xSi_yIr_z$ + $Al_{2.75}Ir$

the calculations were performed within the generalised gradient approximation (GGA-PBE) [90, 91]. A plane wave basis set for electron wave function with cutoff energy of 600 eV was used.

4.3.3 General observations

Table 4.11 indicates the nominal composition of the 5 samples prepared and the phases found after the annealing treatment. Final compositions of the samples after the arc-melting may deviate from the nominal ones due to the known difference between the melting points of Al (660°C) and Ir (2466 °C). The total loss of mass due to the potential evaporation of Al is about 2 % for each sample. Beside the occurrence of the AlIr and the $Al_{2.75}Ir$ phases, PXRD analysis reveals the presence of another unknown phase in each sample that corresponds to neither Al-Ir nor Ir-Si known compounds, thus suggesting the stabilisation of a Al-Si-Ir ternary phase. Unfortunately, no sample exhibits this ternary phase as pure.

Figure 4.12 shows a typical SEM image obtained in the BSE mode for the sample n°1. Two phases can be distinguished: AlIr in white and the unidentified phase in gray. The different contrasts of gray mark the different orientation of the grains. The proportion of the AlIr impurity is estimated to be less that 5% for this sample. EDS measurements on this unknown phase confirmed a ternary composition around $Al_{61.7}Si_{4.4}Ir_{33.9}$, leading us to choose this composition for the synthesis of the sample n°2. WDS experiment was carried out on this second sample and an average of ten points focused on the ternary phase gave a more precise composition $Al_{61.53\pm0.27}Si_{5.64\pm0.08}Ir_{32.83\pm0.26}$.

Figure 4.13 shows the PXRD patterns of the samples n°2 and n°5. The peaks of the AlIr and $Al_{2.75}Ir$ phases are labelled by rhombuses and stars respectively and the remaining peaks correspond to the ternary phase. The peaks associated with this new ternary phase do not significantly shift among the patterns of all the samples. Considering this fact and the low dispersion value of the composition obtained with WDS, this compound should have a narrow homogeneity range at 1200°C.

DTA was carried out on the samples n°4 and n°5 from 100°C to 1600°C with heating and cooling rates of $10K.min^{-1}$. The two curves obtained are similar and the one of the sample n°4 is presented in Fig. 4.14. This sample is known to contain the new ternary and the $Al_{2.75}Ir$ phases. PXRD analysis carried out after the DTA experiment still revealed the presence of these two phases. In addition, the AlIr phase and another additional phase, that could not be determined, are observed. On the heating curve, the peak at 1470°C most probably corresponds to the peritectic decomposition of the

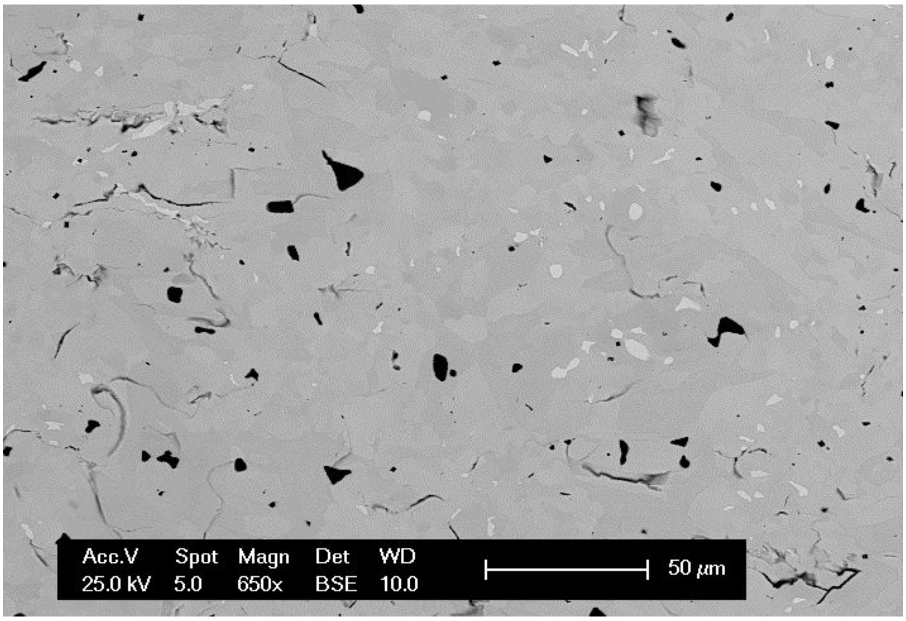

FIGURE 4.12: SEM image of the sample n°1 in BSE mode. White phase marks AlIr while the two shades of gray phase correspond to the new ternary phase with a composition given by EDS around $Al_{61.7}Si_{4.4}Ir_{33.9}$. Black areas are holes.

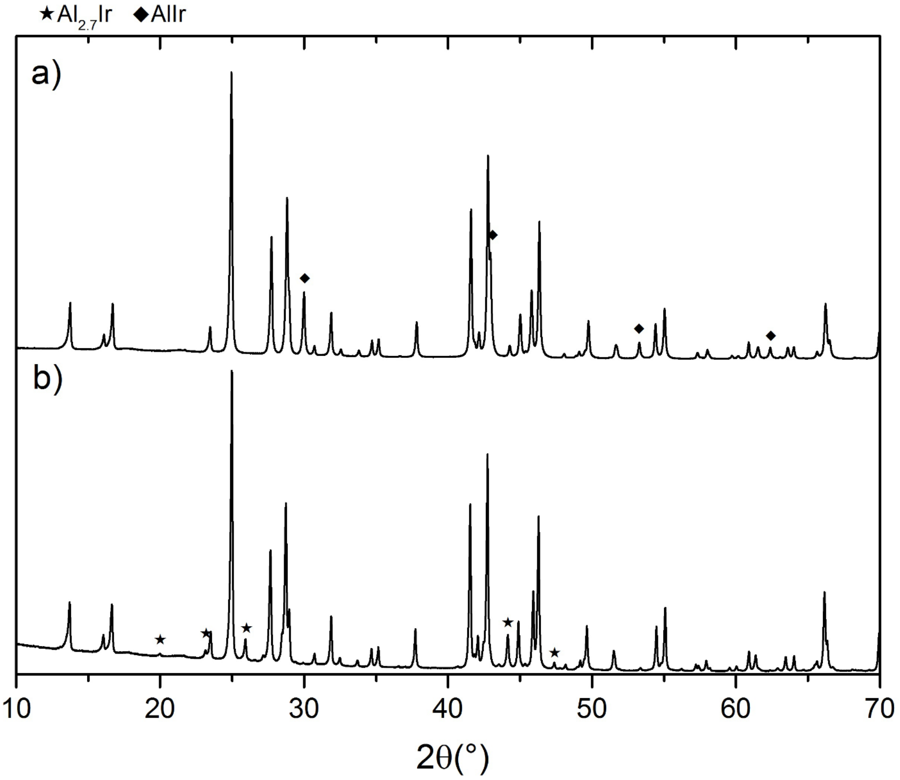

FIGURE 4.13: PXRD patterns of samples a) n°2 and b) n°5. Beside the $Al_{2.7}Ir$ and AlIr phases marked as stars and rhombuses respectively, the remaining peaks correspond to the new ternary phase $Al_{61.7}Si_{4.4}Ir_{33.9}$.

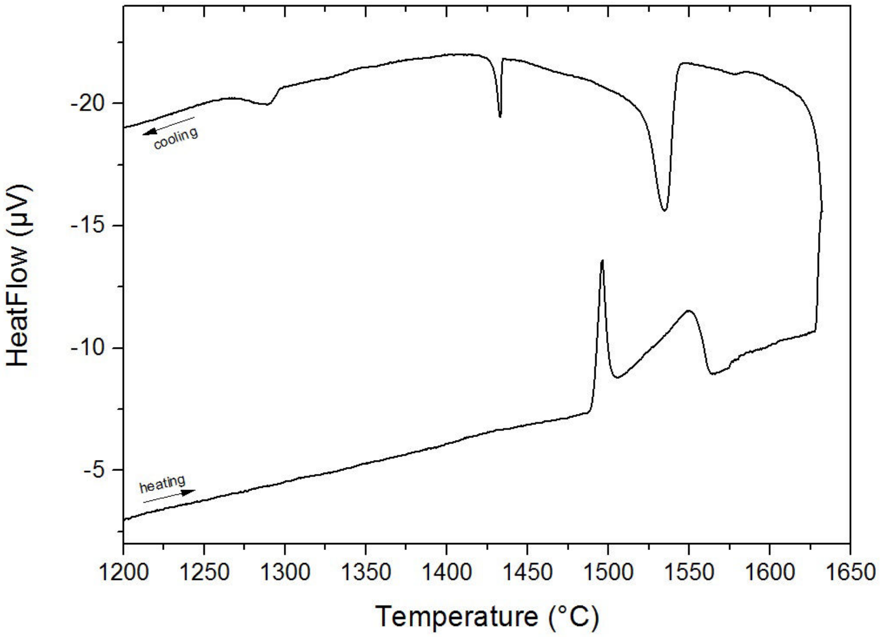

FIGURE 4.14: DSC heating and cooling curves of sample n°4. The peak at 1470°C is attributed to the peritectic decomposition of $Al_{11}SiIr_6$.

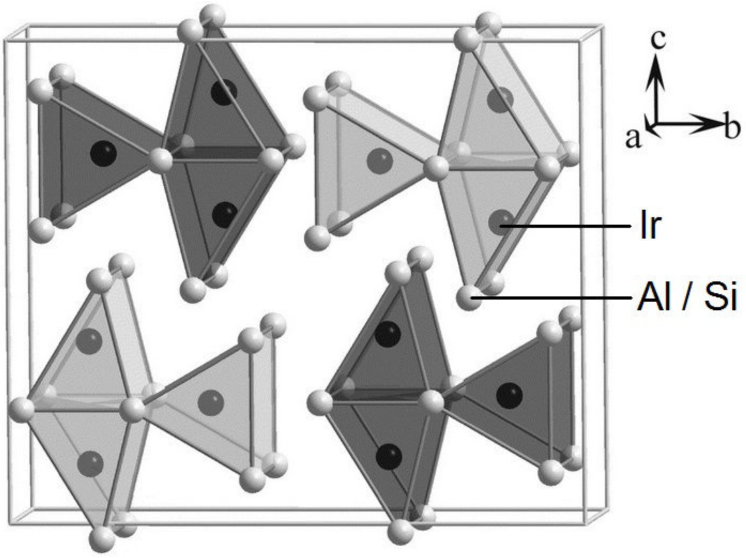

FIGURE 4.15: Structural representation of the new Al-Si-Ir ternary compound using the representation of Ga_2Ir taken from Ref. [119].

ternary phase. The following peak at 1550°C should correspond to the melting of the $Al_{2.75}Ir$ phase known to happen around 1600°C. Because of the broad shape of this second peak, it is likely that the composition of the sample is moving along the liquidus line. On the cooling curve, the same feature is observed also at 1550°C. This corresponds to the crystallisation of the $Al_{2.75}Ir$ phase. The smallest peak at 1425 °C should be the peritectic reformation of the ternary phase. Since the composition of the sample slightly changed during this experiment, this could explain the formation at 1300°C, possibly peritectic, of a neighboring phase that could not be identified.

4.3.4 Crystal structure

Several single crystals were analysed by SC-XRD. The indexation of the reflections leads systematically to an orthorhombic C-centered unit cell with lattice parameters around a = 3.96 Å, b = 12.85 Å and c = 10.58 Å, a cell very close to the one of the Ga_2Ir compound [119]. Considering that Al and Ga belong to the same column of the Periodic Table of elements and that WDS revealed a composition close to $(Al,Si)_2Ir$, it would not be too surprising that our ternary compound is actually isostructural to Ga_2Ir. However, because of the close scattering factor of aluminium and silicon, these two atoms could not be differentiated when resolving the structure. Only aluminium and iridium atoms were then taken into account during the refinement. Distinguishing two atoms with only one electron difference is a hard task for single crystal X-ray diffraction. An alternative would be neutron diffraction but this would require one more step of single crystal growth since much bigger specimens are needed for this characterisation method.

Full crystallographic and data collection information are presented in Table 4.12, atomic coordinates and isotropic displacement parameters in Table 4.13, anisotropic displacement parameters in Table 4.14 and interatomic distances in Table 4.15. As expected, the final structure is exactly the same as the Ga_2Ir one (Pearson symbol $oC36$) with the exception that our ternary compound has a slightly smaller unit cell considering the lower size of aluminium atoms compared to gallium atoms. The discussion about the atomic arrangement remains the same as for Ga_2Ir. The structure can be described in terms of trigonal-prismatic coordination polyhedra of aluminium centered by iridium (see Fig. 4.15). The Ir1 position is surrounded by 9 Al atoms forming a trigonal prism with capped rectangular faces. Another strongly distorted trigonal prism is built around the Ir2 position. Two of the three rectangular faces are capped by one atom while the third one is capped by two atoms, forming a 10-coordination polyhedra [119]. Figure 4.16 depicts these two Ir1 and Ir2 environments. Such structure can also be found in the Al-Si-Fe ternary system but for a different stoichiometry $Al_2Si_4Fe_3$ [120]. In this compound, the heavy Fe atoms replace the Ir atoms while the remaining Al/Si atoms are located at the same positions as the Al atoms in our model.

Considering the composition $Al_{61.53}Si_{5.64}Ir_{32.83}$ obtained by WDS experiment, some silicon atoms should replace part of the aluminium atoms in the refined model Al_2Ir, given the stoichiometry of our ternary compound being $Al_{11}SiIr_6$. This formula gives a theoretical composition of $Al_{61.11}Si_{5.56}Ir_{33.33}$ which is in full agreement with the average composition obtained by WDS. This means that among the 24 aluminium atoms of the structure, 2 of them must be replaced by silicon. However, these aluminium atoms are distributed only between 4-fold and 8-fold Wyckoff positions, the substitution of 2 aluminium by 2 silicon will automatically split one of these positions, leading to a reduced symmetry. According to the International Tables for Crystallography, the splitting of the 4c position

TABLE 4.12: Crystallographic and data collection information for $Al_{11}SiIr_6$ refined as Al_2Ir.

Chemical formula	Al_2Ir
Formula weight ($g.mol^{-1}$)	246.2
Temperature (K)	296(2)
Wavelength (Å)	0.71073
Crystal system	Orthorhombic
Space group	$Cmcm$ (63)
Unit cell dimensions (Å)	a = 3.9573(1) b = 12.8574(6) c = 10.5989(9)
Volume ($Å^3$)	539.28(5)
Z	12
Calculated density ($g.cm^{-3}$)	9.096
Crystal form	Irregular
Crystal size (mm^3)	0.007 x 0.007 x 0.015
Absorption coefficient (mm^{-1})	74.673
F(000)	1236
θ range for data collection	3.17° to 27.27°
Index ranges	$-5 \leq h \leq 4$ $-16 \leq k \leq 16$ $-12 \leq l \leq 13$
Collected and independent reflections	5093, 368
No. of parameters refined	32
Goodness of fit	1.110
R indices	R(int) = 0.0442 $R1$ (all) = 0.0190 $R1$ ($I \geq 4\sigma$) = 0.0154 $wR2$ (all) = 0.0350 $wR2$ ($I \geq 4\sigma$) = 0.0339
Extinction coefficient	0.00178(8)
$\Delta\rho_{max}$, $\Delta\rho_{min}$ ($eÅ^{-3}$)	1.109, -1.809

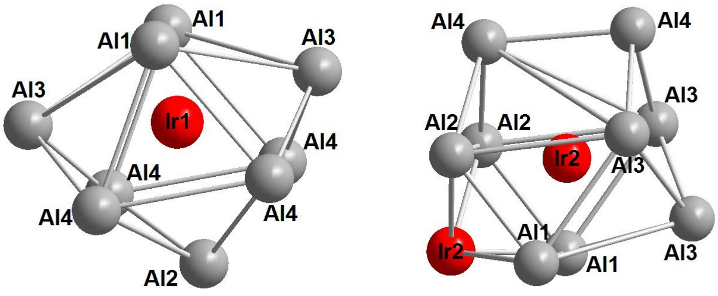

(a) Ir1 (b) Ir2

FIGURE 4.16: Coordination polyhedra around the Ir1 and Ir2 positions.

TABLE 4.13: Standardised atomic coordinates and isotropic displacement parameters for $Al_{11}SiIr_6$ refined as Al_2Ir.

Atom	Site	x	y	z	U_{eq} (Å^2)	Occupancy
Ir1	4c	0	0.85451(3)	1/4	0.00372(14)	1
Ir2	8f	0	0.64272(2)	0.12108(3)	0.00449(13)	1
Al1	4c	0	0.2404(3)	1/4	0.0060(7)	1
Al2	4c	0	0.0439(3)	1/4	0.0098(8)	1
Al3	8f	0	0.82136(19)	0.0147(2)	0.0042(4)	1
Al4	8f	0	0.44067(19)	0.1082(2)	0.0066(5)	1

TABLE 4.14: Anisotropic atomic displacement parameters (Å^2) for $Al_{11}SiIr_6$ refined as Al_2Ir.

Atom	U_{11}	U_{22}	U_{33}	U_{12}	U_{13}	U_{23}
Ir1	0.0037(2)	0.0039(2)	0.0036(2)	0	0	0
Ir2	0.00681(19)	0.00432(19)	0.00233(19)	-0.00035(12)	0	0
Al1	0.0026(16)	0.0081(17)	0.0072(19)	0	0	0
Al2	0.0094(18)	0.0024(17)	0.018(2)	0	0	0
Al3	0.0029(10)	0.0046(11)	0.0050(12)	0.0019(11)	0	0
Al4	0.0080(12)	0.0048(13)	0.0068(12)	-0.0010(9)	0	0

TABLE 4.15: Interatomic distances for $Al_{11}SiIr_6$ refined as Al_2Ir.

Atoms	Distance (Å)
Ir1 - 2 Al1	2.464(2)
Ir1 - 1 Al2	2.435(3)
Ir1 - 2 Al3	2.530(2)
Ir1 - 4 Al4	2.7207(17)
Ir1 - 2 Ir2	3.0467(5)
Ir2 - 2 Al1	2.7126(15)
Ir2 - 2 Al2	2.7198(16)
Ir2 - 2 Al3	2.4897(15)
Ir2 - 1 Al3	2.559(2)
Ir2 - 1 Al4	2.601(2)
Ir2 - 1 Al4	2.656(3)
Ir2 - 1 Ir2	2.7327(7)
Al1 - 2 Al3	2.915(3)
Al1 - 1 Al4	2.982(4)
Al1 - 2 Ir1	2.464(2)
Al1 - 4 Ir2	2.7126(15)
Al2 - 1 Al1	2.526(5)
Al2 - 4 Al4	2.817(2)
Al2 - 1 Ir1	2.435(3)
Al2 - 4 Ir2	2.7198(16)
Al3 - 1 Al1	2.915(3)
Al3 - 2 Al3	2.717(3)
Al3 - 2 Al4	2.693(2)
Al3 - 2 Ir2	2.4897(15)
Al4 - 1 Al1	2.982(4)
Al4 - 2 Al2	2.817(2)
Al4 - 2 Al3	2.693(2)
Al4 - 1 Al4	2.754(5)
Al4 - 2 Ir1	2.7207(17)
Al4 - 1 Ir2	2.656(3)

TABLE 4.16: Wyckoff positions generated after the group-subgroup transformation from *Cmcm* to *Amm*2.

Cmcm		*Amm*2	
At. pos.	Wyck. pos.	At. pos.	Wyck. pos.
Ir1	4c	Ir1a	2a
		Ir1b	2b
Ir2	8f	Ir2a	4c
		Ir2b	4c
Al1	4c	Al1a	2a
		Al1b	2b
Al2	4c	Al2a	2a
		Al2b	2b
Al3	8f	Al3a	4c
		Al3b	4c
Al4	8f	Al4a	4c
		Al4b	4c

in the space group *Cmcm* is possible when transforming to the subgroups *Pmmn*, *Pmma* or *Amm*2 and lead each time to two different twofold positions. In the case of our data collection, we can notice that primitive reflexions are missing in both PXRD and SC-PXRD patterns, thus excluding the subgroups *Pmmn* and *Pmma*. The space group *Amm*2 was then retained for the group-subgroup transformation (matrix: 0 1 0, 0 0 1, 1 0 0). The R(int) factor subsequently dropped to 0.0430.

To get insight on the possible Si location, DFT calculations have been performed for two configurations differing by their Si-Si interatomic distances. The interaction energies are evaluated by the estimation of the total energy difference in the system. Total energy calculations are realised using a cut-off energy (E_{cut}) equal to 500 eV and a k-points grid set to 23x7x9. Two configurations based on the *Cmcm* model are compared: a model with two silicon atoms distant from 5.84 Å in the unit cell (not taking into account the repetition of the unit cell of 3.95 Å) and a model with two silicon atoms distant from 2.56 Å. The energy difference between these two systems was found to be ΔE = 0.45 eV in favor to the model with the largest Si-Si distance. Such difference is significant enough to expect the two silicon atoms to be located far from each other when establishing the *Amm*2 model.

The two 4c atomic position Al1 and Al2 in the *Cmcm* model generated two 2a Wyckoff position Al1a and Al2a and two 2b Wyckoff positions Al1b and Al2b in the *Amm*2 model (see Table 4.16). Among these four twofold atomic positions, one can now be attributed to a silicon position. By choosing any of these four positions for the attribution of the Si atoms, the resulting Si-Si distance is invariably 6.726 Å. Such distance is in full agreement with the conclusions given by DFT calculations. Regarding the interatomic distances in the *Cmcm* model in Table 4.15, the shortest distance is found between Ir1 and Al2 (2.435 Å). Considering that the covalent radius of the Si atom is shorter than for Al, it can be suggested that the Si atoms are actually located at a position generated by this Al2 position. This hypothesis is supported by the inconsistent anisotropic displacement parameters observed at the Al2 position. Refinement of the *Amm*2 model was tested by taking into account a silicon atom either at the Al2a or Al2b positions, hence renamed as Si2a or Si2b. In each case, the reliability factors $R1$ (all data) and wR_2 (all data) rose to 0.0310 and 0.0611 respectively. In the first case, the Ir1-Si2a and Ir1-Al2a distances were 2.426 Å and 2.440 Å respectively, while in the second case, the Ir1-Si2b and Ir1-Al2a distances were 2.440 Å and 2.426 Å. Because of the shortest distance, the most favorable case would be with a Si atom at the Si2a position. However in this model, the isotropic U_{eq} factors in the whole structure are unrealistic, especially at this Si2a position. Trying to refine the atoms as anisotropic leads to several non-positive definite U_{ij} factors, even when processing with only the heavy iridium atoms. In crystallographic structure refinement, this usually means a probable incorrect scattering factor at the considered atomic positions or even a wrong symmetry for the whole structure. Nevertheless, the splitting of the model along with the reducing of the symmetry has the consequence of increasing the number of refined parameters while keeping the same number of reflections. This could be also the explanation of the rising of the reliability factors.

Regarding the positions of the atoms and the interatomic distances and despite the increased refinement factors, the $Amm2$ model remains the most appropriate. Still, the above mentioned evidences of a potential faulty model do not allow us to conclude for this model to be fully acceptable. Another possibility would be for the silicon atoms to be statistically distributed among the aluminium positions in the $Cmcm$ model. This could explain why the splitted model is not optimum. In the case of a statistical distribution, the Si atoms would be located at any of the Al positions. In the $Cmcm$ model, the shortest distances are found to be Ir1-Al1 and Ir1-Al2. Thus, these two Al1 and Al2 positions could be more preferable than Al3 and Al4 for the location of the Si atoms.

4.3.5 Stability

To get a better understanding of the stability of this new compound, the formation enthalpies (ΔH_f) and DOS have been calculated for 10 compounds in the Al_2TM - Si_2TM (TM = Fe,Ir) range:

- The Si_2Ir, Al_2Fe and Si_2Fe binary compounds. The two Ga_2Ir and Si_2Fe structure types have been considered for all compounds. The Si_2Fe structure type is a simple tetragonal lattice with 3 atoms in the unit cell [121].
- Our real ternary compound $Al_{11}SiIr_6$ and a hypothetical isostructural $Al_{11}SiFe_6$ compound.
- The real ternary compound $Al_2Si_4Fe_3$ and a hypothetical isostructural $Al_2Si_4Ir_3$ compound.

For structural relaxations, integrations in the Brillouin zone were performed using special k-points generated with 23×7×9 for the Ga_2Ir-type structures. For DOS calculations, finer $k - points$ meshes were used (up to 39×12×17). The unit cell parameters were calculated for all these compounds and are presented in Table 4.17 and 4.18. For real compounds, the values are in good agreement with the experimental ones.

Figure 4.17 summarises the calculated values of the formation enthalpies as a function of the Al/Si content of the considered compounds. The values were obtained using the following formula:

$$\Delta H_f(Al_{2(1-x)}Si_{2x}M) = E_{coh}(Al_{2(1-x)}Si_{2x}M) - 2(1-x)E_{coh}(Al) - 2xE_{coh}(Si) - E_{coh}(M) \quad (4.1)$$

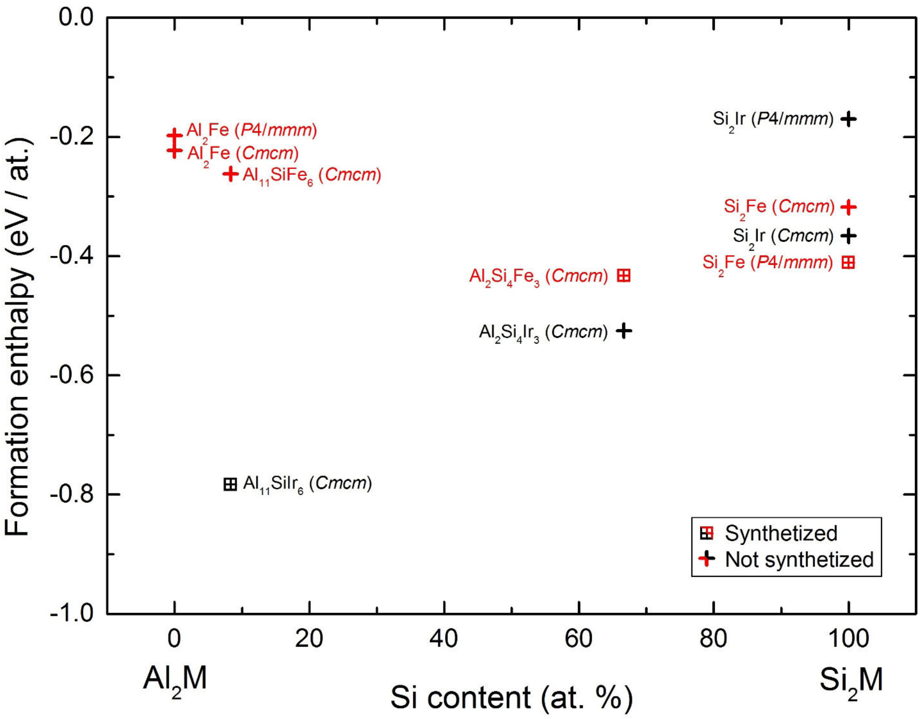

FIGURE 4.17: Stability of the Al-Si-Ir (black) and Al-Si-Fe (red) compounds considered either as crystallising in the Ga_2Ir ($Cmcm$) or Si_2Fe ($P4/mmm$) structure type.

TABLE 4.17: Lattice parameters (Å) calculated for Al-Si-Ir compounds. For the real compound, the experimental values are given in parenthesis for comparison.

Lattice parameter	Al_2Ir	$Al_{11}SiIr_6$	$Al_2Si_4Ir_3$	Si_2Ir	Al_2Ir	Si_2Ir
	Ga$_2$Ir type				Si$_2$Fe type	
a	3.95	3.98 (3.96)[a]	3.76	3.34	2.92	2.95
b	13.04	12.89 (12.86)[a]	13.37	16.71	a	a
c	10.76	10.73 (10.60)[a]	10.53	9.76	5.75	5.27

[a] This work

TABLE 4.18: Lattice parameters (Å) calculated for Al-Si-Fe compounds. For real compounds, the experimental values are given in parenthesis for comparison.

Lattice parameter	Al_2Fe	$Al_{11}SiFe_6$	$Al_2Si_4Fe_3$	Si_2Fe	Al_2Fe	Si_2Fe
	Ga$_2$Ir type				Si$_2$Fe type	
a	3.89	3.28	3.65 (3.67)[a]	3.55	2.75	2.70 (2.69)[b]
b	12.75	13.63	12.21 (12.39)[a]	12.35	a	a (a)[b]
c	10.15	10.99	10.08 (10.15)[a]	9.94	5.87	5.14 (5.13)[b]

[a] See Ref. [122]

[b] See Ref. [120]

In the case of the Al-Si-Fe compounds, ΔH_f increases with the decrease of the Si concentration. For these compounds, the values are in agreement with the existing compounds. Indeed, the lowest formation enthalpies are found for the two real compounds $Al_2Si_4Fe_3$ (Ga_2Ir type), -0.433 eV.at^{-1} and Si_2Fe (Si_2Fe type), -0.411 eV.at^{-1}. As a comparison, the real compound Ga_2Ir has an equivalent value (ΔH_f = -0.426 eV.at^{-1}).

Inversely for the Al-Si-Ir compounds, ΔH_f decreases with decreasing Si concentration. The $Al_{11}SiIr_6$ compound has the lowest formation enthalpy (ΔH_f = -0.783 eV.at^{-1}). The value for the hypothetical $Al_2Si_4Ir_3$ compound is found to be higher (ΔH_f = -0.525 eV.at^{-1}). Also, the hypothetical Si_2Ir compounds in the two considered crystal structures have the highest formation enthalpies (ΔH_f = -0.170 eV.at^{-1} and -0.366 eV.at^{-1} for the Si_2Fe and Ga_2Ir types respectively).

To gain insight into the calculated structural stabilities, we calculated the electronic structure of the considered $(Al_{1-x}Si_x)_2TM$ compounds (see Fig. 4.18). For Al-rich compounds, at low energy, the DOS is nearly free electron like. These states are mainly sp states of the aluminium atoms. For $Al_2Si_4Ir_3$ and $Al_2Si_4Fe_3$, the s states of Si are the main contributions at low energy. In all compounds, the d states of TM atoms (TM = Ir, Fe) are observed in the middle of the sp band (between -6 and 0 eV approximatively). The Fermi level E_F is found near a valley in the DOS that splits the band between bounding and anti-bounding states. This valley is called the pseudo-gap and is attributed to a combined effect including the electron diffraction by the Bragg planes of a prominent Brillouin zone and a strong Al(sp)-TM(d) hybridisation [99]. The presence of the pseudo-gap in the DOS of the considered compounds suggests that they may be included in the so-called "electron compounds", i.e. that the stable crystal structures may be mainly controlled by the number of valence electrons per atom.

According to the electron theory of metallic alloys, the electronic energy is more effectively lowered when a pseudo gap is formed at the Fermi level. Both the depth and the width of the pseudogap contributes to energy stabilisation. In the case of $Al_{11}SiIr_6$, the width of the pseudogap is larger than the one calculated for $Al_{11}SiFe_6$ or $Al_2Si_4Ir_3$, leading to a larger energy stabilisation.

When rationalising compositions and structures, the average number of valence electrons per atom (e/a), introduced by Hume-Rothery, is proved to be a relevant parameter. The determination of the e/a value for TM elements, however, has been controversial for many decades. Very recently, first-principles calculations with subsequent Fourier analyses have been performed to determine the effective electrons per atom ratio (e/a) [123, 124]. Using the values deduced from such calculations for Fe and Ir ($(e/a)_{Ir}$ = 1.58, $(e/a)_{Fe}$ = 1.05), we found that the e/a ratio increases when the Si concentration increases. For the new compound $Al_{11}SiIr_6$, we calculated $(e/a)_{Al_{11}SiIr_6}$ = 2.58, close to the one of $Al_2Si_4Fe_3$ ($(e/a)_{Al_2Si_4Fe_3}$ = 2.79). The value calculated for the hypothetical compound $Al_{11}SiFe_6$ is lower ($(e/a)_{Al_{11}SiFe_6}$ = 2.40) and the one for the hypothetical compound $Al_2Si_4Ir_3$ is larger ($(e/a)_{Al_2Si_4Ir_3}$ = 2.97).

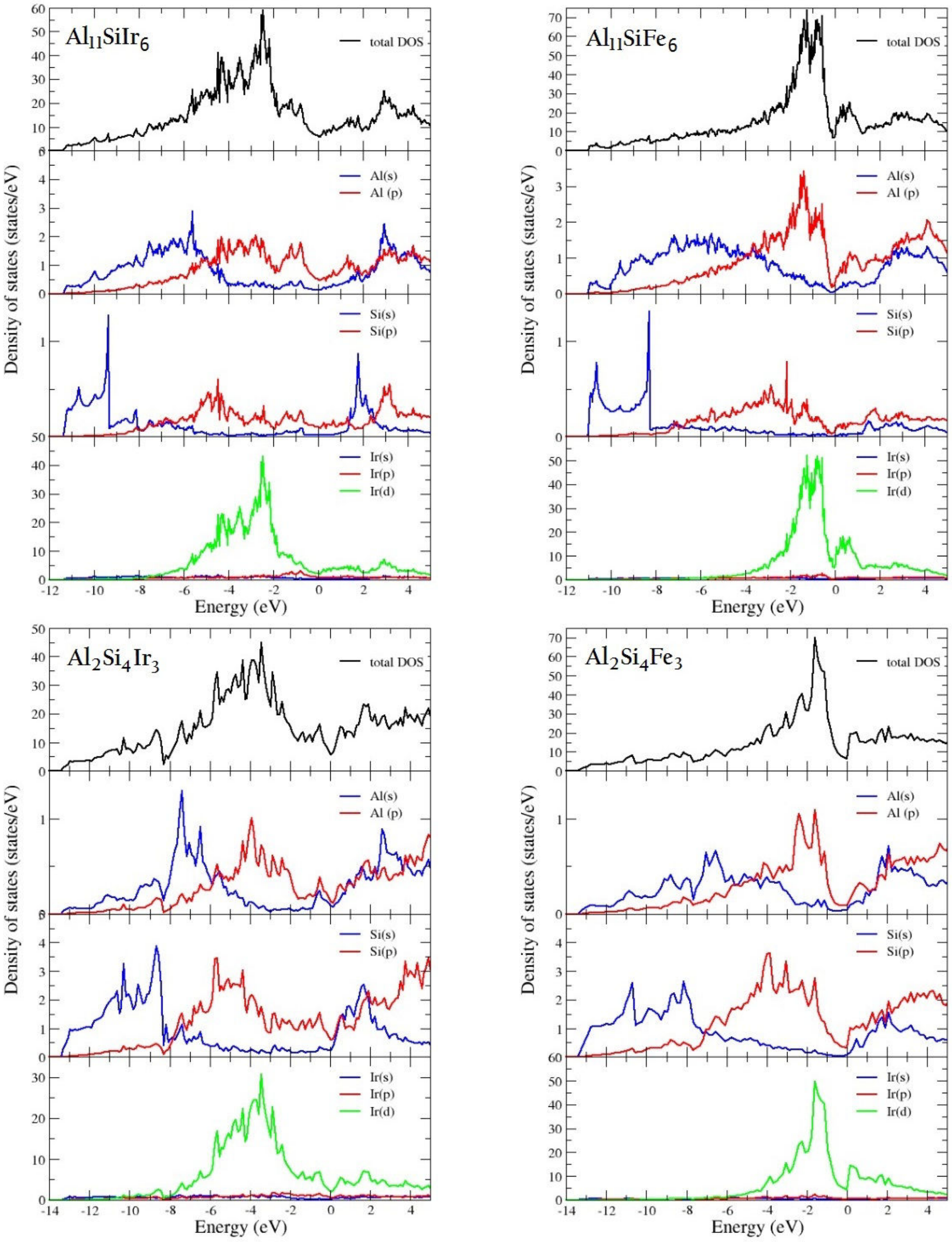

FIGURE 4.18: DOS for the considered Al-Si-Fe and Al-Si-Ir compounds. The DOS of Ga_2Ir is given for comparison.

4.4 The Al-Ag-Ir system

4.4.1 Introduction

The three elements Cu, Ag and Au belong to the same column of the Periodic Table. Following the strategy of Tsai *et al.* [9] (as explained in the Chapter 1) and after the investigation of the Al-Au-Ir system, we have replaced Cu by Ag in the Al-Cu-Ir system with the hope to find compounds with similar quasicrystalline structure in the Al-Ag-Ir system. The Al-Ag system has been extensively investigated and is known to exhibit three silver-rich intermetallic compounds although some metastable phases were also pointed out [125]. On the contrary, the Ag-Ir system shows a wide miscibility gap in almost all the width of the phase diagram and no intermetallic compounds [126]. The Al-Ag-Ir system is then a so-called "push-pull" system, thus being interesting to study.

4.4.2 Experimental details

Four samples have been synthesised and characterised with the same experimental techniques as for the Al-Au-Ir compounds. Pure silver has a higher melting point than pure aluminium, 961.8°C vs 660.3°C respectively. However, the boiling point of silver (2162°C) as well as its heat of vaporisation (254 kJ.mol^{-1}) are lower than those of aluminium (2470°C and 284 kJ.mol^{-1}). Consequently, during the melting of the alloys with an arc-melter, the samples underwent not only the usual evaporation of aluminium, but also a huge mass loss due to a very consequent evaporation of silver. As a result, the chemical compositions that were initially aimed were notably shifted. Knowing the mass loss after melting the specimen, the compositions of each four samples are roughly estimated by considering an evaporation of few mg of Al (as usually observed with Al-Ir compounds, see Chapter 3) and the rest of the mass loss caused by evaporation of Ag. An excess of Ag was then added in the samples n°2, 3 and 4 in order to counterbalance this evaporation. Moreover when preparing these samples, Al and Ir were first melted before adding Ag. With Al-Ir compounds formed first (lower melting point than pure Ir), it allows us to melt Ag with a decreased power of the arc. Only the sample n°4 was annealed to 650°C during 672 hours. All as-cast and annealed alloys were characterised with PXRD and optical microscopy techniques.

4.4.3 Results and discussion

Table 4.19 shows the estimated compositions and the phases found in the samples using PXRD after the arc-melting. All the as-cast samples look very heterogeneous (see the sample n°2 presented in Fig. 4.19), the elements are not completely mixed together. PXRD patterns confirmed the presence of pure silver in the samples n°1 and 2 but also Al-Ir and Al-Ag binary phases. All peaks can be indexed by known phases on these patterns. The samples n°3 and 4 were prepared with a large excess of silver and aluminium respectively. Again, the PXRD patterns can be correctly indexed by the known binary compounds detailed in Table 4.19. Unlike the two previous alloys, elemental silver cannot be detected in samples n°3 and 4. However, sample n°4 shows a small amount of aluminium. Because of its high Al content, the sample n°4 was annealed to 650°C to avoid the possible melting of aluminium. The duration of the heat treatment is consequently chosen to be rather long (672 hours).

TABLE 4.19: Estimated compositions of the prepared as-cast samples.

Sample n°	Composition (at. %)			Phases found
	Al	Ir	Ag	
1	65	22	13	$Al_{2.75}Ir + Ag + Ag_2Al$
2	50	23	27	$Al_{2.75}Ir + Ag + AlIr$
3	38	14	48	$Al_{2.75}Ir + AlIr + Ag_3Al$
4	73	7	20	$Al_{28}Ir_9 + Ag_2Al + Al$

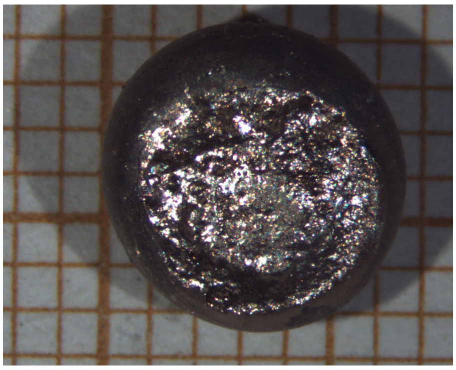

FIGURE 4.19: Optical microscope image of the as-cast sample n°2

Even after melting the sample, its shape is still inhomogeneous. The PXRD pattern of the annealed sample exhibits peaks from the Al_9Ir_2 and Ag_2Al phases and still pure aluminium. Figure 4.20 shows an optical microscopy image of the polished annealed sample. Three phases can be observed on this image:

- Large round shaped crystallites, measuring from one to several tens of microns.
- Smaller elongated grains, with 1 μm to 10 μm width and 10 μm to 20 μm length.
- A very porous phase, surrounding all the crystallites.

When analysing the mutual arrangement of these three phases, the large crystallites seem to have solidified first. Considering the phases that were identified using PXRD, this can be attributed to the Al_9Ir_2 compound. Indeed, this compound has the highest melting point of the three identified phases (T_f = 970°C). The smaller crystallites were most probably solidified in a second step and should correspond to the Ag_2Al phase (T_f = 736°C). The last phase that has certainly melted corresponds to pure aluminium (T_f = 660°C).

The exploration of the Al-Ag-Ir system is still in its infancy. Four samples with different compositions covering the aluminium-rich side of the phase diagram have been prepared. There is no evidence for a hypothetical stable ternary compound at this stage. When preparing the Al-Ag-Ir specimens with the arc-melting method, the samples underwent everytime a huge mass loss due to the evaporation of either silver or/and aluminium. Consequently, the final compositions of the samples differ from what was initially targeted. For preparation of future Al-Ag-Ir alloys, one should think

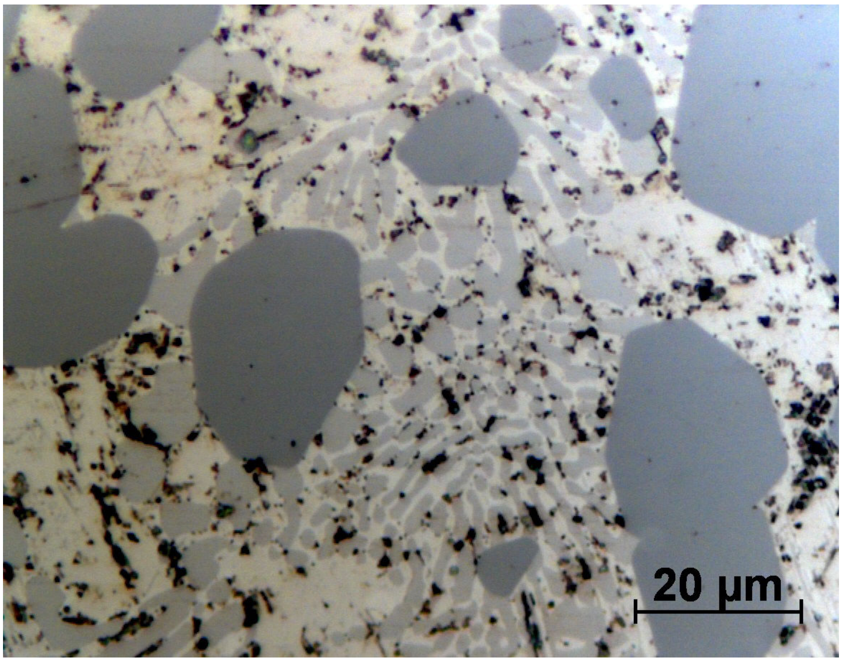

FIGURE 4.20: Optical microscope image of the annealed sample n°4.

of a more delicate method of synthesis (for instance induction melting) in order to limit as much as possible this phenomenon of evaporation.

4.5 Conclusion

From the investigation of the three Al-Au-Ir, Al-Si-Ir and Al-Ag-Ir push-pull systems, three new ternary compounds could be revealed. Despite its simple structure, the Al_3AuIr compound revealed interesting features. Indeed, the Au/Ir mixed position in the structure has the consequence to split one of an Al position, thus resulting in a slightly disordered structure. The $Al_{72}Au_{2.5}Ir_{29.5}$ phase is the only CMA that could be found. Its structure, from the $BaMg_2[VO_4]_2$ type (Pearson symbol $tI104$), is for the first time observed for an intermetallic compound. The $Al_{11}SiIr_6$ compound has been identified and is of the Ga_2Ir type. No QC phases could be identified in these three push-pull systems yet but their investigation is still incomplete, especially for the Al-Ag-Ir system where difficulties were encountered with the preparation of the samples. Future works will continue the exploration of these systems to complete the corresponding ternary phase diagrams.

Chapter 5

Al-Ir surfaces

5.1 Introduction

Bulk materials have particular mechanical, physical and chemical properties arising from their different atomic structures and their different chemical compositions. At the surface of a bulk material, the breaking of the periodicity of the three-dimensional solid leads to structural changes which may differ from a single bulk truncation [14]. These structural differences may lead to properties intrinsic to the surface. As mentioned in Chapter 1, this is the case for several CMA surfaces which have been reported as potential candidates in the field of heterogeneous catalysis. Following the bulk investigation of the Al-Ir system presented in Chapter 3, the surface investigation of the $Al_{28}Ir_9$, $Al_{45}Ir_{13}$, $Al_{2.75}Ir$ or $Al_{2.4}Ir$ compounds would be of interest from a structural point of view but also to determine their associated physical and chemical surface properties. To study the surface of such complex compounds, centimeter-size single-crystals are necessary. However, the growth of a single-crystal of an Al-Ir phase with the Bridgman or Czochralski method would have been very challenging. Indeed, according to the phase diagram, the majority of the Al-Ir phases lie in a small concentration window and require peritectic reaction to be stabilised. The few tens of grams of highly pure iridium for this preparation can also be an obstacle since it is a very expensive metal. For these reasons, an alternative approach of synthesis has been considered. Aiming to form Al-Ir intermetallic phases at the surface, the adsorption of Ir atoms has been carried out on a clean Al(100) surface under ultra high vacuum conditions (UHV). The deposition of Ir atoms has been studied for different substrate temperatures and for several dosing conditions. Prior and following Ir adsorption, the surface has been characterised under UHV using Low Energy Electron Diffraction (LEED), X-ray Photoelectron Spectroscopy (XPS) and Scanning Tunneling Microscopy (STM). Full details about the experimental procedure are given in Section 5.2. To our knowledge, this is the first experimental and theoretical works performed on the Ir/Al(100) system. However, some authors have reported different works about the deposition of aluminium on the Ir(111) surface. Gall' *et al.* [127] reported that at 300K, an aluminium film grows in a layer-by-layer fashion in coherent relation to the Ir(111) substrate. For higher temperature depositions (1100K - 1300K), they observed the formation of a surface aluminide Ir_4Al. In their theoretical study and for 0.25 ML coverage, Zhang *et al.* [128] have determined that it is more energetically favorable for Al atoms to adsorb at hcp-hollow sites of the Ir(111) surface. Buchanan *et al.* reported a study about the intermixing of Al-TM bilayers [129]. They determined that Al deposited on Ir at room-temperature mainly stays at the top surface (intermixing length of 2 Å) while Ir on Al have the propensity to diffuse deep in the bulk of the substrate (intermixing length of 54 Å). After describing the experimental details, the results concerning the Ir deposition on the Al(100) surface at 20°C and 420°C will be presented and discussed.

5.2 Experimental details

5.2.1 Techniques of characterisation used

LEED

LEED is a technique that gives information about the periodicity and the symmetry at the surface of a sample. First, a correct preparation of a very flat sample oriented perpendicularly to the desired crystallographic axis must be achieved (see Subsec. 5.2.2 for details about the sample preparation). The sample is then placed under the electron gun of LEED which will produce a monochromatic electron beam, focused on the sample the same way as for the SEM technique. The electrons of low energy (typically 1 - 400 eV) interact with the sample the same way as for reflection XRD. However, LEED is dominated by multiple scattering while XRD is dominated by single scattering. In addition, the probing depth is much smaller in the case of the LEED because low-energy electrons interact strongly with the solid (see Chap. 2 for details about SEM and XRD). This leads to a high surface sensitivity of the LEED technique. A two-dimensional fluorescent screen collects the diffracted electrons after the latter have passed through a set of grids. These grids play the role of filters suppressing any inelastic back-scattered electrons and accelerating the remaining elastic electrons towards a fluorescent screen held usually at 5-6 keV. The collected data can be used either qualitatively or quantitatively:

- As LEED is a diffraction technique, the diffracted spots that are collected with the detector form the reciprocal lattice. The analysis of the spot position gives direct information on the symmetry at the sample surface and the unit cell dimensions. In the case of adsorbate deposition (like in our study) and if this adsorbate is organised, the relative unit cell size of the overlayer deposited and its rotation with respect to the substrate can also be determined.

- The intensity variations of the diffracted spots as a function of the energy of the incident electrons can be extracted to give I(V) curves. Their comparison with calculated I(V) curves from theoretical trial models can provide the atomic arrangement at the surface of the sample. The model is modified iteratively to optimise the agreement between the experimental and calculated I(V) curves.

XPS

X-ray Photoelectron Spectroscopy is a technique that can provide the composition at the surface of a sample. It consists of irradiating the surface with a monochromatic source of radiation. In XPS, the incident photon (200 - 2000 eV) is absorbed by an atom, leading to ionisation and the emission of an inner shell electron. The kinetic energies of the emitted photoelectrons can be measured using any appropriate analyser and a photoelectron spectrum can thus be recorded [130].

The elements at the surface of the analysed sample will give rise to a characteristic set of peaks in the photoelectron spectrum. These peaks appear at characteristic kinetic energies determined by the photon incident energy, the respective binding energies and the analyser workfunction. The presence of peaks at particular energies therefore indicates the presence of a specific element in the sample. The intensity of the peaks is also related to the concentration of the element present at the surface. Thus, XPS is also a technique that provides quantitative data of the surface composition. Due to the short inelastic mean free path of the photoelectrons, the probing depth of XPS is on the order of 1 to 3 nm depending on the incident photon energy and the take-off angle of the photoelectrons.

STM

Scanning Tunneling Microscopy is a technique of characterisation that provides three-dimensional images of surfaces with an atomic resolution. At first, an atomically sharp tip is approached a few Ångströms away from the surface. A voltage difference (typically ± 1 V) is applied between the tip and the sample surface allowing electrons to tunnel across the gap between the two electrodes (metallic tip and sample surface). This results in a tunneling current that is measured and compared to a reference value (constant current mode). If the tunneling current is larger than the reference, the voltage applied to the piezodrive controlling the tip tends to withdraw the tip away from the surface and inversely, so as to reach the current set point. As the tip rasters the xy plane, a 2D map of z equilibrium positions can be obtained, thus displaying the topography of the surface sample [131]. For this technique to provide atomic resolution images, flat, clean and stable surfaces under UHV as well as excellent vibration damping system are required. Aside from the images, the local density of states of the surface can also be retrieved. Such information is obtained by sweeping the voltage bias and measuring the resulting current with loop-gain off. This type of measurement is called Scanning Tunneling Spectroscopy (STS).

5.2.2 Preparation and characterisation of the sample

The Al(100) surface has been used as a template for iridium deposition. This specimen was obtained from a home-made Al single-crystal, oriented using back reflection Laue X-ray diffraction and cut perpendicular to its (100) direction. The surface of this sample has been polished with diamond polishing suspension with grain size down to 0.25 μm. The experiments were then carried out in a UHV chamber where the base pressure is typically around the 5.10^{-11} mbar. The sample was cleaned before each new deposition by few cycles of Ar^+ sputtering at 2.5 keV followed by 30 min annealing to 510°C. The iridium (Goodfellow, 99.9 %) deposition was carried out with an Omicron EFM3 electron beam evaporator with integrated flux monitor. The pressure of the chamber was kept in the low 10^{-10} mbar during the deposition. Iridium deposition was performed under different conditions of temperature and coverage. The sample was characterised by LEED, XPS and STM measurements. The surface diffraction patterns have been obtained using a 4-grid Omicron LEED instrument. To monitor the cleanliness of the sample and the surface composition, XPS measurements have been carried out using an Omicron photoelectron spectrometer with a non-monochromatised MgKα source. STM images were recorded using a commercial Omicron VT-STM operating in constant current mode. All STM measurements have been carried out at room-temperature. The images were processed using the WSxM freeware [132]. The amount of Ir deposited on the surface of the Al(100) sample is given

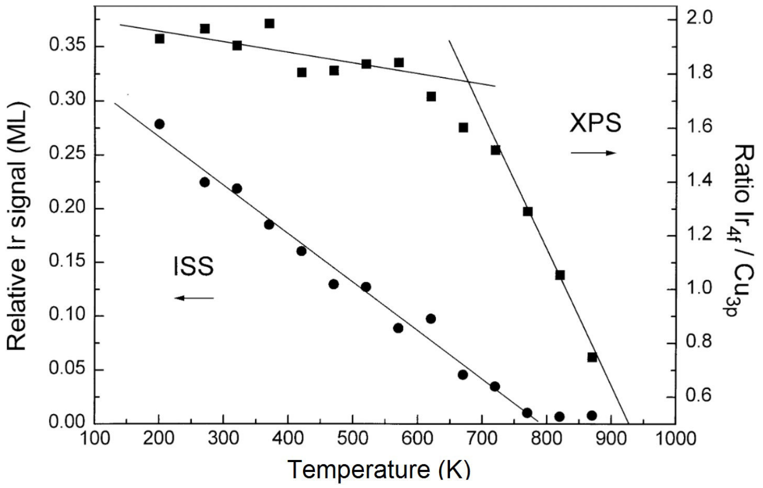

FIGURE 5.1: Amount of Ir as a function of the annealing temperature calculated from XPS and Ion Scattering Spectroscopy (ISS) experiments taken from Ref. [133] (we consider only the XPS curve here). This graph is given for an initial nominal Ir coverage of 1.5 ML.

in monolayer equivalent (MLE). The latter is defined as the Ir exposure needed to obtain a full monolayer on a Cu(110) surface at room-temperature [133] (see the following section for more calibration details). Experiments were carried out up to a coverage of about 2 MLE. As Ir and Ag element are immiscible in the bulk and do not form surface compounds [134], Ir adsorption has been carried out on a Ag(111) surface held at 420 °C to cross-check the deposition rate.

XPS

The adsorption of Ir on a Cu(100) surface has been previously characterised by Gilarowski *et al.* [133] using STM, LEED, XPS and low-energy ion scattering spectroscopy. In this study, the evaporation rate was calibrated with the help of a 20 MHz quartz crystal microbalance. It has been reported that a Ir_{4f}/Cu_{3p} ratio equal to 1.9 corresponds to a nominal Ir coverage of 1.5 ML at room-temperature (see Fig. 5.1). A strong Ir/Cu intermixing has been also reported where iridium tends to stay in the near-surface region [133]. As no Cu(100) sample was available during our experiment, a similar adsorption experiment has been performed on a Cu(110) surface at room-temperature. It has been found that a similar Ir_{4f}/Cu_{3p} ratio equal to 1.9 was obtained for a flux of 60.0 nA of iridium maintained over a Cu(110) surface for 90 min at room-temperature. Here, we assume that the growth mode is similar for both Cu surfaces as a first approximation. However, as the atomic surface density differs between (100) and (110) surfaces by $\sqrt{2}$, the corresponding coverage is equal to 2.1 MLE (named after as 2 MLE). This flux has been fixed for all the experiments and the time is the parameter that has been varied to adjust the quantity of Ir dosage (for example 30 min for a deposition of 0.7 MLE).

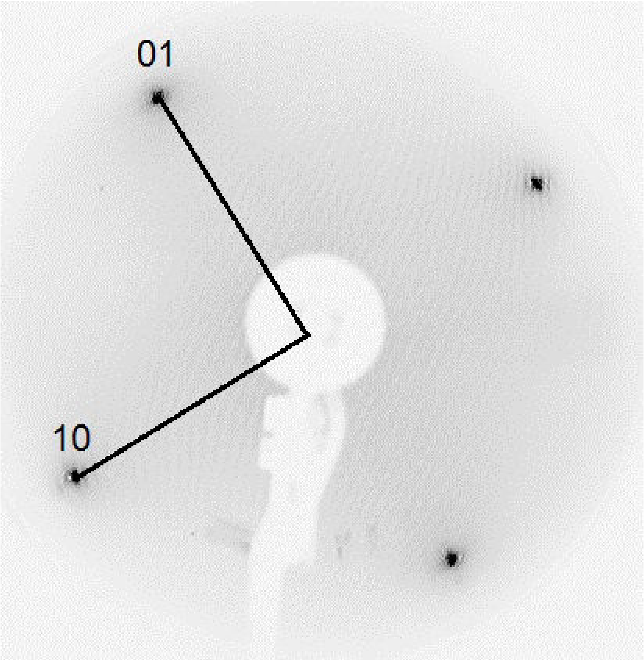

FIGURE 5.2: LEED pattern (50 eV) recorded on the clean Al(100) surface.

5.3 Results

5.3.1 Deposition at room-temperature

LEED

Following the surface preparation described above, a typical LEED pattern obtained from the Al(100) surface is presented in Fig. 5.2. As expected, the surface exhibits a square surface unit cell. The unit mesh dimension determined from the LEED pattern is equal to a = 2.86 Å. Indeed, elemental aluminium is known to crystallise in a fcc structure with a lattice parameter a = 4.05 Å [135]. At the surface, the surface unit cell is defined by the centered faces of the cube. Hence, the two-dimensional lattice parameter is $\sqrt{2}$ times smaller than the known lattice parameter of aluminium:

$$4.05/\sqrt{2} \simeq 2.86 \tag{5.1}$$

The dimension of the square surface unit cell of Al(100) is a = 2.86 Å.

Upon adsorption of Ir atoms (up to 2 MLE) on the Al(100) substrate at room-temperature, we observe the same LEED pattern but with an increase in background. However, there is no evidence for the growth of an additional structure, except for the initial Ir deposition (0.7MLE) where very broad and faint spots around 20 eV can be hardly distinguished. From these results, 5 hypotheses can emerge :

- Iridium did not stick on the surface but this should not cause a change in the background.
- Iridium diffused completely into the bulk forming a diluted solid solution but again, the background should not have changed.

- Iridium landed on the surface without organisation but the 2 MLE deposited should have hidden the LEED of Al(100) except in the case of a 3-D growth of Ir.
- Iridium landed on the surface with the same organisation as Al(100) (i.e. a pseudomorphic growth).
- Intermixing in the near-surface with fcc structure happened, producing a near-surface disorder.

The background increase in the LEED patterns would favor the scenario where Ir atoms adsorb in a disordered manner at the Al(100) surface. To gain more insight into the Ir growth mode, STM measurements have been performed on the dosed surface.

STM

The STM images shown in Fig. 5.3 have been obtained for different regions of the sample after 2 MLE Ir deposition. As it can be seen, the coverage is not homogeneous across the sample which could be explained by the relatively large size of the Al single crystal and the initial alignment of the Ir source (optimised hereafter). Nevertheless, this allows us to investigate the Ir growth behaviour for different coverages under the same preparation. The overall stoichiometry of the surface determined by XPS measurements after a deposition of 2 MLE on Al(100) at room-temperature is equal to $Al_{80.7}Ir_{19.3}$.

Figure 5.3 (a-b) shows STM images obtained for a low Ir covered region (coverage of 20% of the total image area). The adsorption of Ir atoms leads to a preferential decoration of the Al(100) step edges. At this stage it is not clear if the bright protrusions are indeed Ir adatoms, Al atoms originating from a place exchange mechanism (Ir replacing Al atoms in the first surface layer) or both. Regardless of the mechanism, these observations imply a diffusion at room-temperature of Ir adatoms across terraces prior to nucleation at step edges. A plot profile across several terraces (see Fig. 5.4) reveals an islands nucleation (Al or Ir) on the upper side of the step edges. At the step edges, the atoms have less neighbours than atoms in a terrace. There is an additional energy for an adatom to diffuse downward a step edge (called the Ehrlich-Schwoebel barrier [136, 137]) which could explain why the diffusion of the iridium atoms stopped at the step edges.

In addition to this preferential decoration, irregularly shaped three-dimensional islands start to grow on the Al(100) terraces. As shown in Fig. 5.3(c) where bright protrusions cover about 40% of the total image area, their respective density is increasing with increasing Ir dosing. The characteristic heights (h) of these islands with respect to the Al(100) terrace are $1\ \text{Å} < h < 3\ \text{Å}$. The disordered islands consisting of few atoms appear randomly orientated. For higher exposed regions, the lateral size of the individual island increases without coalescence, resulting in a rough surface (see Fig. 5.3d)). Considering the disordered structure observed in Fig. 5.3d), a LEED pattern is not expected if this area was representative of the entire sample surface. However, the spots of Al(100) are still experimentally observed across the sample. This can be explained by the fact that the differently covered terraces shown here can be found within the same region of the sample. The probing area of the LEED is large enough to encompass the differently covered regions, thus explaining why the LEED of Al(100) has experimentally never disappeared under the dosing conditions used in our study.

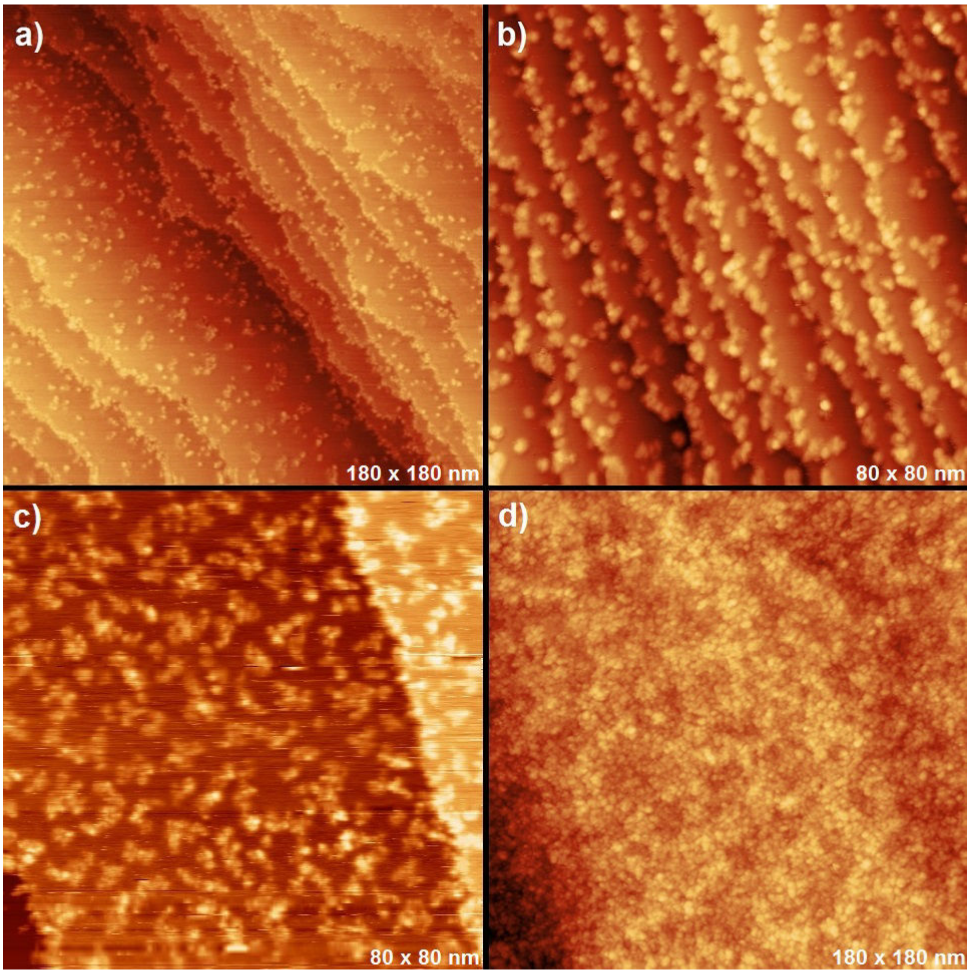

FIGURE 5.3: STM images obtained after deposition of 2 MLE Ir on Al(100). As the deposition is not homogeneous (see text for explanations) and considering possible intermixing phenomenon at room-temperature, the bright protrusions are not necessarily representative of the Ir amount deposited. Hence, the estimated coverage for each image is given as the percentage of surface area covered by the islands for each STM image: a-b) 20% and c) 40%. Image d) corresponds to the highest dosed area of the sample and it is therefore associated with a 2 MLE Ir dosage.

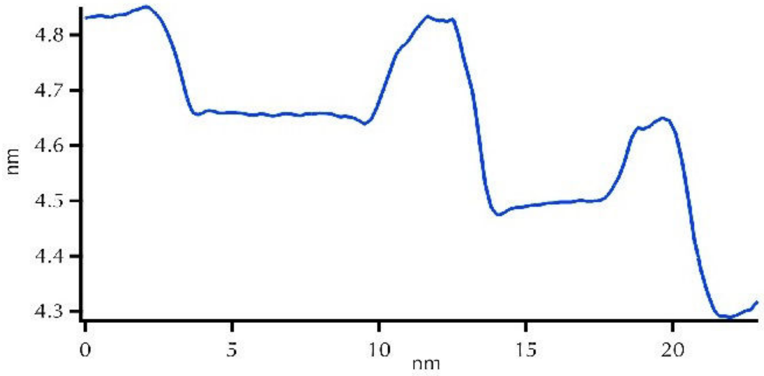

FIGURE 5.4: Plot profile across several terraces from the STM image in 5.3 b).

Considering the intermixing length of Ir in Al at room-temperature determined experimentally [129] and the elemental surface energies of Ir compared to Al [138], it would be probably more energetically favorable to have Ir embedded in the Al surface. Such growth mode has already been observed when adsorbing Ir on a Cu(100) surface, substrate surface energy being higher ($\gamma_{Cu(100)}$ = 0.906 eV.atom^{-1}) than Al(100) surface ($\gamma_{Al(100)}$ = 0.689 eV.atom^{-1}) [138]. Hence, from the LEED pattern, the STM analysis and the associated energetics of the system, Ir adatoms adsorb in a disordered manner at room-temperature on the Al(100) surface with a preference for step edge decoration and most likely embedded in the subsurface region.

5.3.2 Deposition at 420°C

LEED

The Ir adsorption on the Al(100) surface has also been carried out at higher temperatures. Figure 5.5a reveals the LEED pattern obtained after 2 MLE Ir deposition with the sample held at 420°C. A qualitative similar LEED pattern is obtained after room-temperature deposition followed by annealing at 320°C or by directly dosing at 350°C. As seen in Fig. 5.5a, the most intense diffraction spots are associated with the square unit mesh of the Al(100) surface. In addition, sharper and less intense diffraction spots testifies of another atomic arrangement at the surface. The new structure can be understood as two square domains commensurate with the Al(100) substrate. The two domains have a lattice parameter equal to $\sqrt{5}$ times the parameter of Al(100). They are each rotated by +/- 26.6° with respect to the *a* axes of the surface unit cell. Figure 5.5b shows the indexation of the presented LEED pattern. The respective intensities of the diffraction spots for both domains appear similar. Hence, an equal amount of the two domains is expected at the surface. Figure 5.5c indicates the labeling of the diffraction spots that have been used for dynamical LEED analysis (see Section 5.3.3. This results in 8 averaged curves: 4 for Al(100) (index of the spots (10), (11), (20), (21)) and 4 for the two domains (index (2/5 1/5), (1/5 3/5), (2/5 4/5), (4/5 3/5)).

STM

Figure 5.6 presents STM images after Ir deposition under different conditions. Prior to exposure to Ir adatoms, atomically resolved STM images have been obtained on the clean Al(100) surface (see Fig. 5.6(a)), hence confirming both the unit cell dimensions and orientation of our sample with respect to the clean LEED pattern. Figures 5.6(b-c) are typical STM images obtained after 2 MLE deposition at 420°C. They both exhibit a square unit mesh with a measured lattice parameter a = 6.4 ±0.3 Å, i.e. $\sqrt{5}$ times larger than the unit cell parameter of Al(100). Protrusions (bright features) and depressions are always present on such images. Both images correspond to the two possible domain orientations identified with the LEED pattern shown in Fig. 5.5b. They are oriented respectively at ±26±2° with respect to the [011] direction of the Al sample (i.e. the *a* axis of the surface unit cell). These results are in agreement with the analysis of the LEED patterns.

On several parts of the surface, overlayers have been identified on top of the ($\sqrt{5}$x$\sqrt{5}$)R 26.6° phase (see Fig. 5.6(d)). The layers grow in a pseudomorphic manner (i.e. a lattice parameter a = 6.4 ±0.3 Å) and exhibit a step height equal to 2.1 ±0.1 Å. Consequently, the overlayer to overlayer

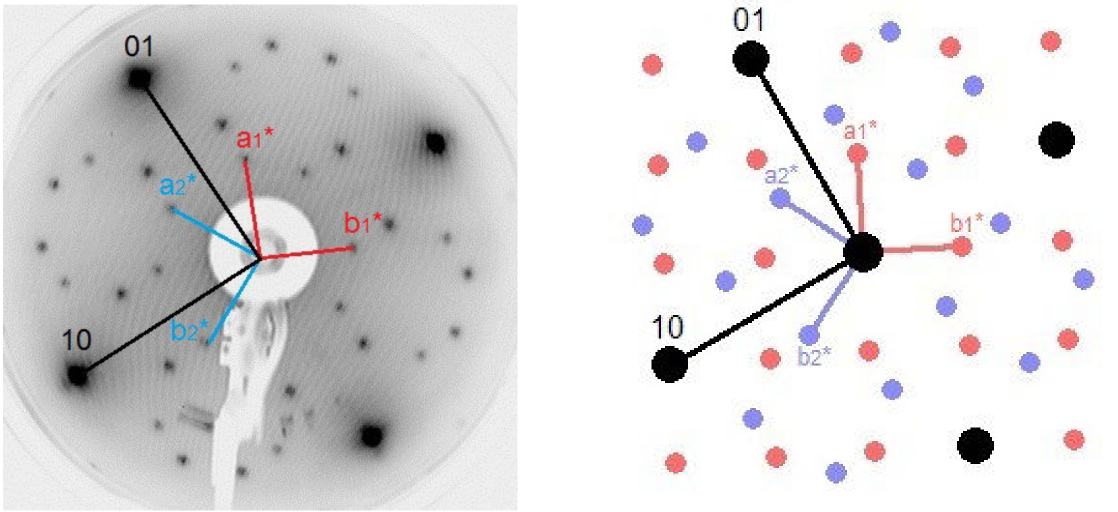

(a) LEED (50 eV) recorded on the Al(100) surface dosed with 2 MLE Ir at 420°C.

(b) Indexation of the LEED pattern with the square unit mesh of Al(100) (black) and two square domains (blue and red) with their corresponding bases.

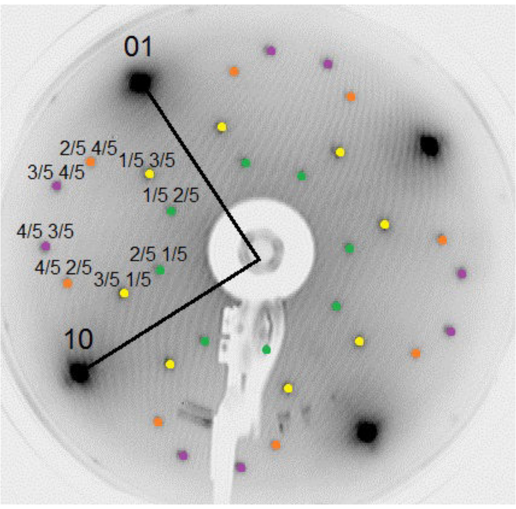

(c) Indexation of the diffraction spots as used for the LEED I(V) measurements presented in Section 5.3.3. The four different colors represent the four different sets of equivalent spots from the two domains.

FIGURE 5.5: A typical LEED pattern with its indexation.

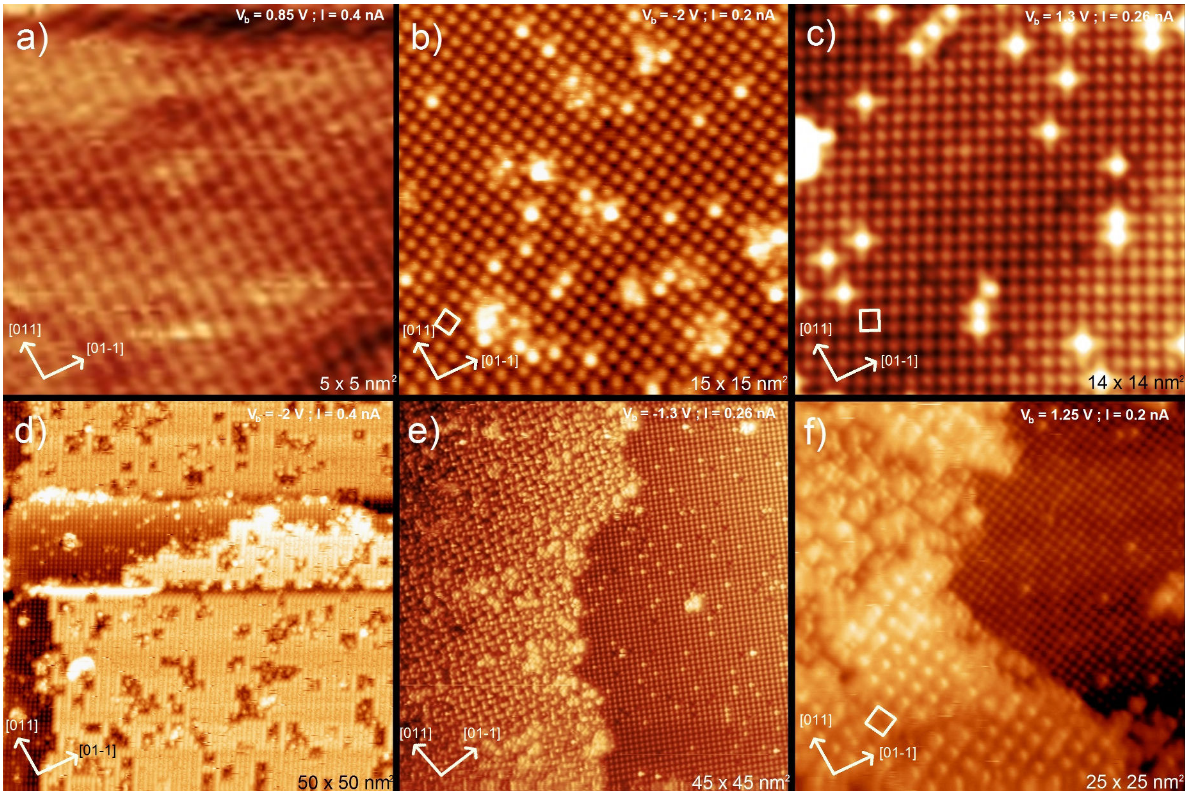

FIGURE 5.6: STM images of a) clean Al(100), b-d) after 2 MLE Ir deposition, and e-f) after 0.7 MLE Ir deposition. The bias voltage and the tunneling current are given for each image along with the axes of the Al(100) substrate.

step height is measured at 4.3 ±0.2 Å. Within these overlayers, several patches of missing atoms (vacancies) are always present.

In addition to the $(\sqrt{5}\text{x}\sqrt{5})$R 26.6° phase, additional phases have been identified for lower Ir deposition. In Fig. 5.6(e), one can recognise a $(\sqrt{5}\text{x}\sqrt{5})$R 26.6° domain coexisting with an apparent new structure. As it will be explained in Section 5.3.3, this structure with a square surface unit mesh of 14.3 Å can be related to both the $(\sqrt{5}\text{x}\sqrt{5})$R 26.6° phase and the overlayers presented in Fig. 5.6(d).

Similarly, Fig. 5.6(f) demonstrates that $(\sqrt{5}\text{x}\sqrt{5})$R 26.6° domain coexists also with a structure with a unit cell measured at a = 12.8(2) Å. Due the orientation and dimension of this superstructure, it corresponds to a (2x2) reconstruction if the reference substrate is considered as the $(\sqrt{5}\text{x}\sqrt{5})$R 26.6° domain.

XPS

We now turn into the XPS analysis carried out on the Al(100) sample for several Ir deposition at 420°C. As a comparison, the concentration of Ir found at the surface for 2 MLE deposition at room-temperature is around 19 at. %. Here, the amount of Ir at the surface is typically between 5.9 at. % and 6.6 at. % for the same quantity deposited (2 MLE) at 420°C. This amount is comparable to the composition obtained after 0.7 MLE Ir deposition on Cu(110) at room-temperature. It is also similar to the amount found (6.1 at. %) for 0.7 MLE Ir deposited on the Ag(111) sample held at 420°C. In this case, hexagonal shaped island of various height and lateral dimensions are observed by STM. While Ir adatoms remain at the Ag(111) surface (even at 420°C), a strong intermixing occurs after

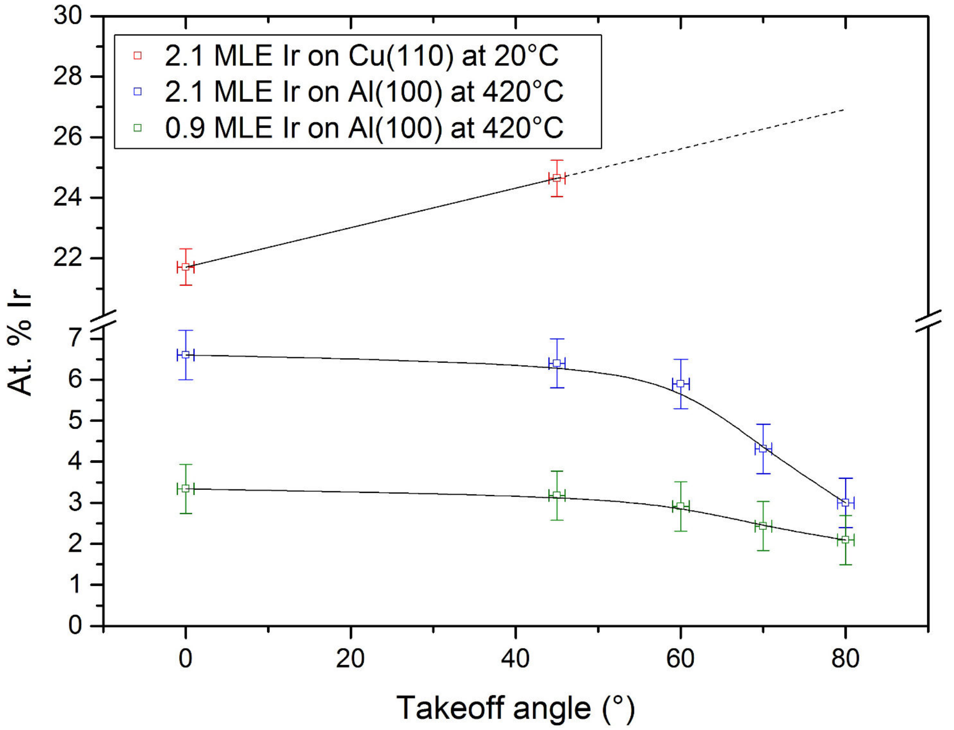

FIGURE 5.7: At. % of Ir calculated as a function of the XPS takeoff angle for different exposures. The horizontal and vertical error bars represent the uncertainty originating from the measurement and the fit of the XPS spectra respectively.

Ir deposition on the Cu(100) surface [133]. Despite the different growth mechanisms between both systems, the same amount of Ir is measured by XPS. This is due to the probing depth of the technique being of the order of few nanometers.

Regarding the adsorption on the Al(100) surface, a similar concentration of Ir is measured by XPS for a 2 MLE Ir deposition at 420°C, i.e. 2/3 of the Ir is missing within the near-surface region. A study reporting the intermixing of Al-TM bilayers [129] revealed that Al deposited on Ir has an intermixing length of 2 Å at room-temperature while Ir deposited on Al has a strong tendency to diffuse in the bulk with a length of 54 Å. Hence, Ir deposition at 420°C leads to an even greater diffusion of Ir into the bulk.

For a comparison, XPS measurements have also been carried out for different takeoff angles on Cu(110) and Al(100) after exposure to Ir adatoms (see Fig. 5.7). The higher the takeoff angle, the more surface sensitive is the measurement. At room-temperature and as expected, Ir adatoms tend to remain at the Cu(110) surface selvedge. For the Ir/Al(100) system at 420°C, the behaviour is different. The Ir concentration is decreasing as the measurements get more surface sensitive which suggests that most of the Ir adatoms diffuse into the Al(100) subsurface.

The position and the shape of the XPS core level spectra can also provide information about the local bonding environment of the elements. The electronic states of pure elements are always found at the same binding energy. In a compound, different types of bonds may affect the core level binding energies, creating a chemical shift. Figure 5.8a reveals the binding energies of the Al 2*p* and Ir 4*f* core levels for 2MLE Ir exposure at different temperatures. The Al 2*p* core level of the clean Al(100) surface (binding energy of ∼72.9 eV) has been measured prior to any Ir deposition. In comparison, the Al

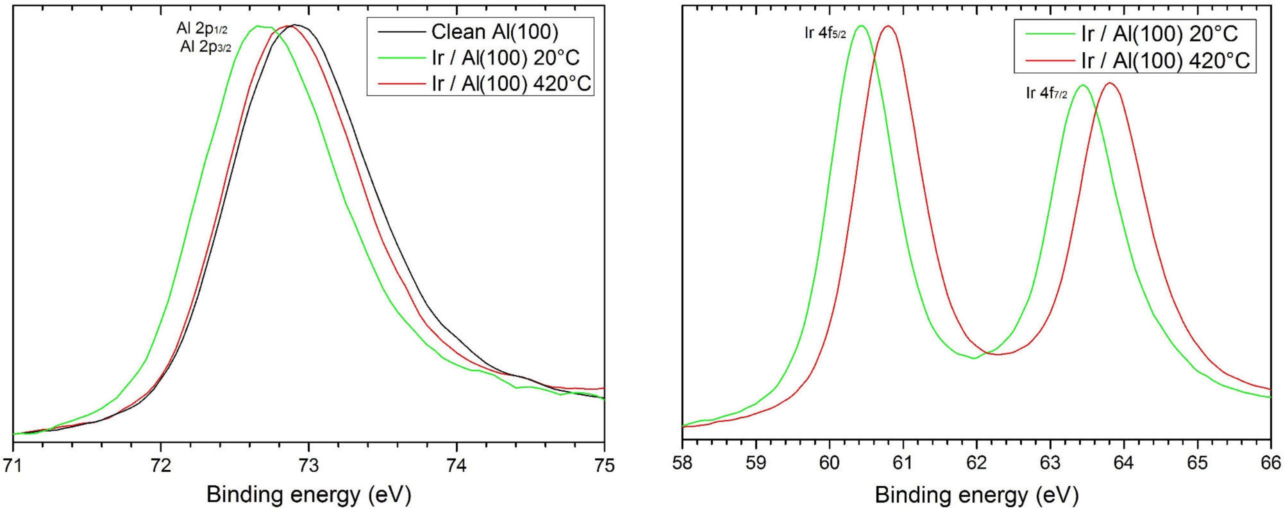

(a) Shift between the Al $2p$ peaks.

(b) Shift between the Ir $4f$ peaks.

FIGURE 5.8: Comparison between the Al $2p$ and Ir $4f$ core level spectra between the clean Al(100) sample and after 2MLE Ir deposition at room-temperature and 420°C.

$2p$ peak of the sample after Ir deposition at 420°C is measured at an energy of 72.8 eV. Within the accuracy of the measurements (±0.05 eV), this is very close to the binding energy measured on the clean surface.

However, the Al $2p$ peak of the sample obtained after Ir deposition at room-temperature exhibits a clearer chemical shift (binding energy of ~72.7 eV). This shift of 0.2 eV - 0.3 eV compared to the clean Al(100) peak indicate a different Al environment at the surface (bonding with Ir, place exchange mechanism...). It suggests that the Ir content in the near-surface region after dosing at room-temperature is probably larger than that after 420°C dosing. The peak shift towards higher binding energy upon alloying indicated an electron transfer between Al and Ir. Figure 5.8b compares the position of the Ir $4f$ peaks after an Ir deposition at room-temperature and at 420°C. A clear shift of approximately 0.4 eV is observed between the peaks of the two experiments. As for the Al $2p$ peaks, the peak obtained after room-temperature deposition is found at a lower binding energy than the peak obtained after deposition at 420°C. This is in full agreement with the STM observations showing a different atomic arrangement (different Al/Ir interactions) for the two temperature regimes.

5.3.3 Discussion

From the previous observations, iridium deposition on Al(100) at room-temperature does not yield any surface reconstruction. However, for adsorption at higher temperature, different atomic arrangements have been identified. The $(\sqrt{5}\mathrm{x}\sqrt{5})\mathrm{R}\ 26.6^\circ$ phase, observed systematically, has been found to be stable between 320°C and 510°C (temperature used to prepare the Al(100) clean surface). Regarding the (2×2) reconstruction and the 14.3 Å unit cell structure, the situation is different. As mentioned before, due to the dosing configuration (size of the sample and source alignment), Ir exposure is considered to be inhomogeneous, i.e. the highest Ir concentration is observed in the middle of the sample while the sample borders are practically uncovered. This effect has been confirmed by STM measurements, where almost clean Al(100) regions have been observed at the sample edges after adsorption.

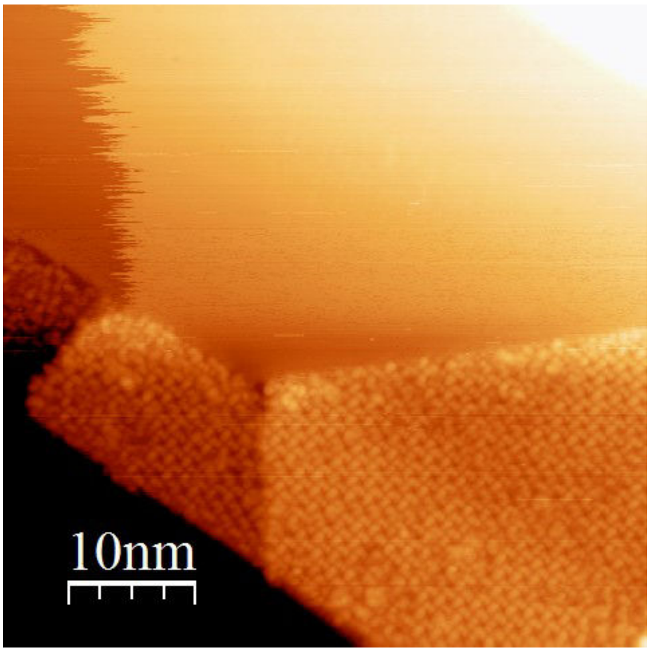

FIGURE 5.9: STM image showing a "clean" Al(100) terrace next to a domain of the "14.3 Å" phase.

Similar "clean" Al(100) surface have been also identified next to domains of the "14.3 Å" phase (see Fig. 5.9, i.e. coexistence of the two structures for a dosed area). These two structures ((2×2) and "14.3 Å" phases) have not been observed routinely and consequently seem to be area dependent. It is likely that their formation occurs for a precise Ir concentration. Their occurrence and amount across the surface are then not sufficient to manifest themselves as additional diffraction spots in the LEED patterns. For these reasons mentioned above, the values of the chemical composition determined by XPS must be taken with care.

In the known Al-Ir binary phases, the lattice parameters of the Al_9Ir_2 compound (Pearson symbol $mP22$) are a = 6.378(1) Å, b = 6.430(1) Å, c = 8.732(2) Å and β = 94.77(2)°. The a and b parameters are matching with the observed square lattice of 6.4 Å. Al_9Ir_2 is the most Al-rich compound of all the Al-Ir binaries. The growth of this compound would then be in good agreement with the experiments since a few amount of Ir is deposited on a large excess of Al. As depicted in Fig. 5.10, the Al_9Ir_2 compound can be described as a periodic stacking of flat and puckered atomic layer along the [001] direction.

- The layers a and a′ can be described as a square arrangement of only Al atoms. The atoms are actually not forming a perfect square unit cell but the interatomic Al-Al distances are between 2.7748(4) Å and 2.8559(4) Å. This type of pure Al layer is very similar to the Al(100) surface termination (square unit cell of 2.86 Å). Due to the symmetry of the crystal structure ($P2_1/c$ space group), a and a' planes related to each other by a 2_1 screw axis along b or by a glide operation along the c axis. The Al squares are rotated by ±26.5 ± 0.5° from the [100] direction. While dubbed “flat layer", the roughness of the Al pure layer is still greater than the Al(100) surface plane.
- The puckered layers b and b′ contain both Al and Ir atoms. The planes can be described by

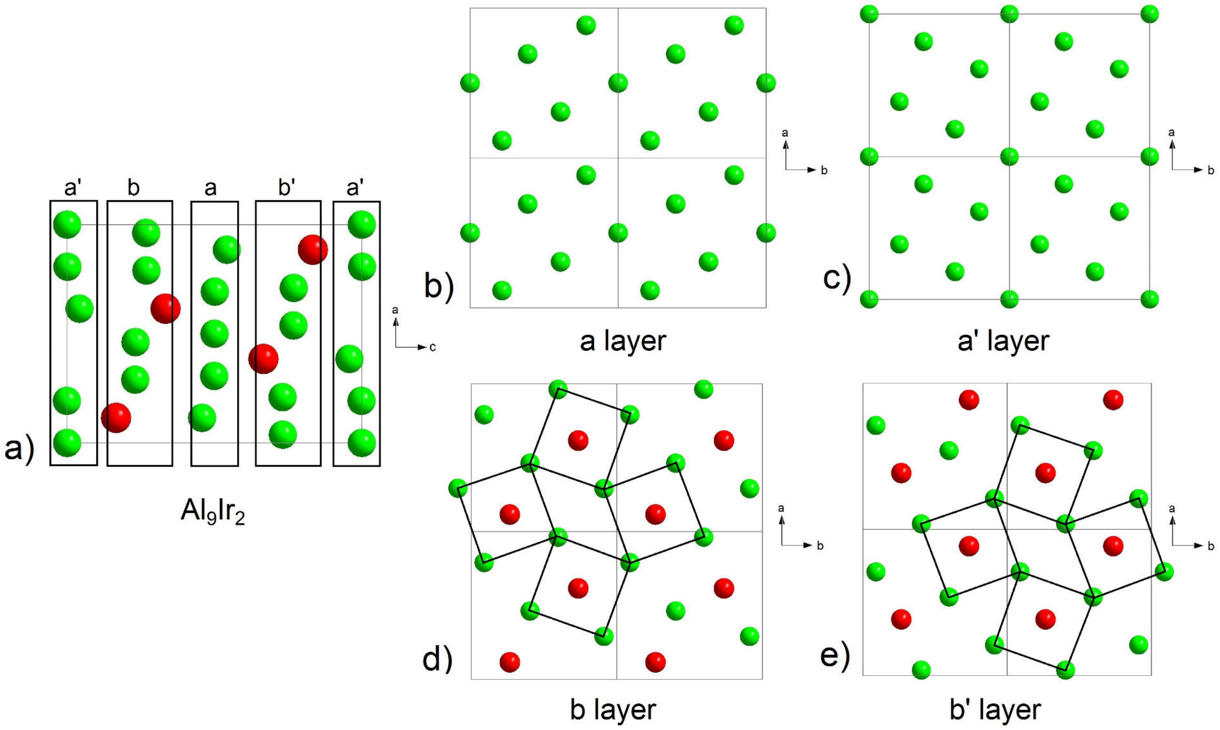

FIGURE 5.10: (a) Visualisation of the Al_9Ir_2 unit cell in terms of periodic stacking layers along the [001] direction. (b) For a better representation, each layer almost perpendicular to the [001] direction is presented in four unit cells.

irregular rhombi and Al squares centered by protruding and buried Ir atoms. These motifs point in two different directions on each plane. The Al square edges length (and *a fortiori* the rhombi edges) range from 3.33 to 3.46 Å, i.e. motifs much larger than on plane *a* and *a*′.

Considering the Al-Ir phase diagram, the unit mesh dimensions, the orientations of the two domains, the step height between alike planes, and the intermixing length of Ir in Al bulk, we believe that the $(\sqrt{5}x\sqrt{5})R$ 26.6° phase corresponds to the onset of the formation of Al_9Ir_2 compound. The alignment of the Al square motifs shown in Fig. 5.10(b-c) with the Al(100) surface unit cell leads to two Al_9Ir_2 domains orientated at 26.6° from the substrate [011] direction. From the Al_9Ir_2 unit cell dimensions (a = 6.378(1) Å, b = 6.430(1) Å), this results in an apparent $(\sqrt{5}x\sqrt{5})R$ 26.6° phase in the LEED pattern. The step height of about half the c^* lattice parameter (where $c^* = c\cos(4.77°)$) is in agreement with surface studies on intermetallic compounds [139]. Indeed, the investigation of the $Al_9Co_2(001)$ surface, compound isostructural to the Al_9Ir_2 intermetallic, has demonstrated that pure Al layers are preferentially selected as surface terminations. This specific plane selection leads to a single step height across terraces equal to $c^*/2$ [140]. Hence, the $(\sqrt{5}x\sqrt{5})R$ 26.6° phase should be regarded as Al_9Ir_2 domains of various thickness coexisting with clean Al(100) patches.

Questions arise on how to explain the remaining observed structures. The formation of the 12.8 Å (2x2) reconstruction observed in Fig. 5.6 can be understood as a superstructure on top of an Al_9Ir_2-like layer. This phase has been observed for low Ir exposure.

The square structure with a unit cell of 14.3 Å can be associated to an incomplete Al_9Ir_2 bulk layer. The dimension of this structure is $\sqrt{5}$ larger than the Al_9Ir_2 surface unit cell, i.e. it is five times

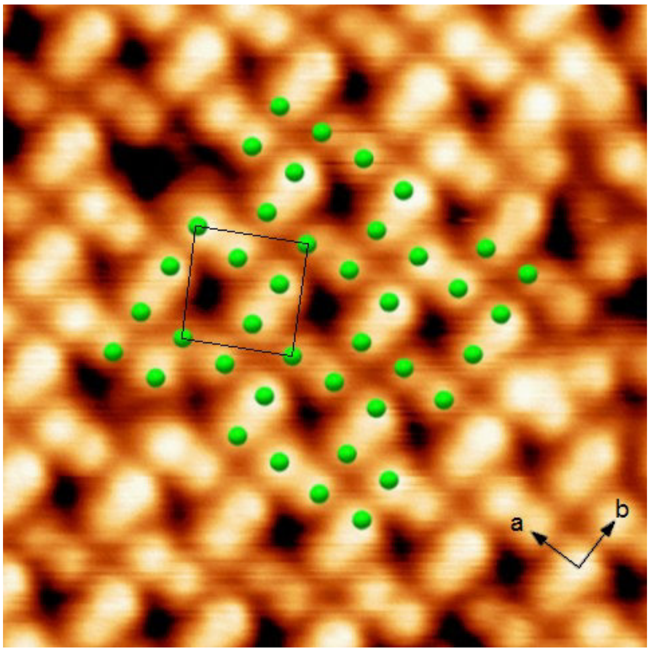

FIGURE 5.11: A model consisting of an incomplete Al layer (a complete layer is shown in Fig. 5.10(b)) has been superimposed on the 14.3 Å phase. The a and b axis correspond to the unit cell axes of the ($\sqrt{5}$x$\sqrt{5}$)R 26.6° phase.

the size of the Al(100) surface unit mesh. As shown in Fig. 5.11, it can be described as an incomplete flat layer of the Al_9Ir_2 compound. There are different ways to generate such an incomplete plane depending on which Al atoms remain within the plane. Here, we have considered Al atoms located above Ir atoms present in the underneath puckered layer. These incomplete pure Al layers have been observed for both domain orientations. It is possible that once complete, this layer will transform into the overlayers identified on top of the ($\sqrt{5}$x$\sqrt{5}$)R 26.6° phase and presented in Fig. 5.6(d)).

Finally, it has to be mentioned that after repetitive preparations of Ir deposition on Al(100), one or two cycles of sputtering/annealing was not sufficient anymore for completely cleaning the surface. Indeed, LEED patterns acquired after two cycles of cleaning still exhibited spots from the ($\sqrt{5}$x$\sqrt{5}$)R 26.6° reconstruction. The spots were less intense and observable in a narrower range of energy but still present. In accordance with intermixing length of Ir in Al, the adatoms diffuse deep in the Al bulk for temperature above 320°C. An experiment of a very high coverage of Ir has also been performed at 420°C. After such preparation, the formation of cross-shaped micrometer-size precipitates could be observed at the surface of the sample. Figure 5.12 shows an optical microscopy image of the corresponding microstructure. Because of their relatively large size, the precipitates could not be removed by simple sputtering/annealing cycles. TEM experiments are pending to determine the nature of these precipitates.

LEED I(V)

To complete these observations, i.e. that Ir deposition on Al(100) at high temperature leads to the formation of Al_9Ir_2 compound, dynamical LEED analysis has been carried out on the sample after a deposition of 2 MLE of Ir at 420°C. LEED patterns were acquired for the energy range 1-300 eV at 120 K. The intensities of 16 Al(100) spots were extracted as a function of the energy as well as 28

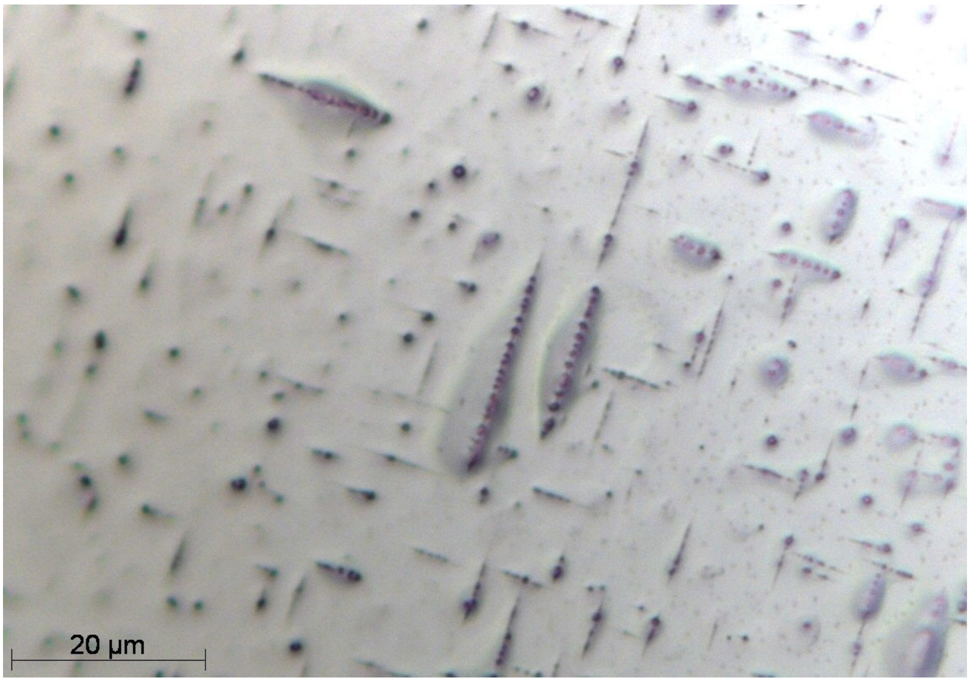

FIGURE 5.12: Precipitates formed at the surface of Al(100) after an excessive coverage of iridium (undetermined).

spots from the two ($\sqrt{5}$x$\sqrt{5}$)R 26.6° domains. As a first observation, spots from the two different reconstructed domains lead to the exact same I(V) curves, confirming that these two domains are totally equivalent. All the equivalent curves were summed, averaged and normalised. This resulted in 8 averaged curves, 4 for Al(100) (index of the spots (10), (11), (20), (21)) and 4 for the two domains (index ($^2/_5$ $^1/_5$), ($^1/_5$ $^3/_5$), ($^2/_5$ $^4/_5$), ($^4/_5$ $^3/_5$)).

The dynamical LEED calculations were performed courtesy of Katariina Pussi from the Lappeenranta University of Technology in Finland. For this task, the Tensor-LEED program [141] was used. The relativistic phase shifts were calculated using the phase shift program [142] that is packaged with Tensor-LEED. The agreement between the theory and the experiment was tested using the Pendry R-factor [143]. A wide range of different model structures have been considered.

The first set of model structures was based on Al(100); Ir on top, hollow and bridge sites was calculated. Substituting one or more Al atoms with Ir was considered on top, second, third and fourth layers and also different combinations of these substitutions were tried. Disordered Ir on different layers / combinations of layers using "average transfer matrix approximation" (ATA) was also considered. The best Al(100) based structure is Ir substitution into second layer, giving Rp = 0.26. Comparison between the 8 experimental and calculated I(V) curves for this model is shown in Fig. 5.13a.

The second set of model structures was based on Al_9Ir_2 alloy. Different thickness and terminations of the slab, both supported by Al(100) and pure alloy structure were considered. The best structure from these models was 6 layers (atoms) Al_9Ir_2 on top of Al(100) giving Rp = 0.29. The graph comparing the I(V) curves for this model is given in Fig. 5.13c. While individual models lead to acceptable Rp values and a reasonable agreement with the experimental I(V) curve, mixing both models gives Rp = 0.23. This reduced Pendry R-factor has been obtained for a 40:60 mixture of both

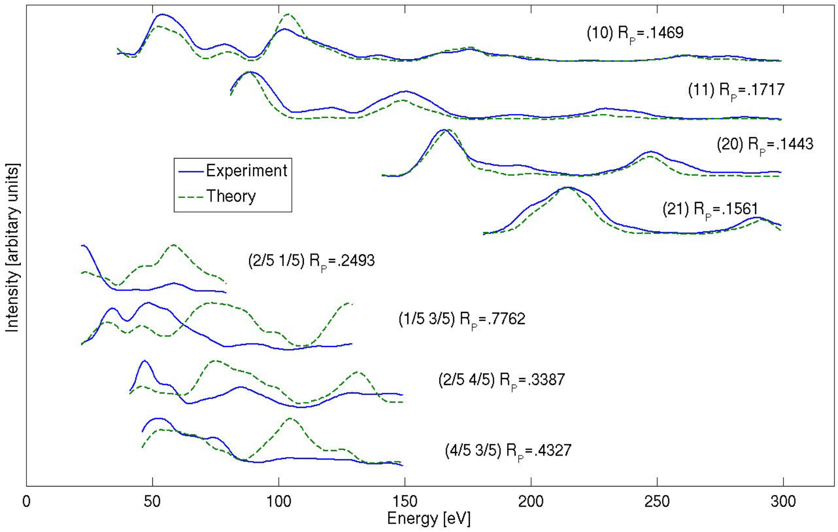

(a) Model 1 based on Ir substitution into second layer.

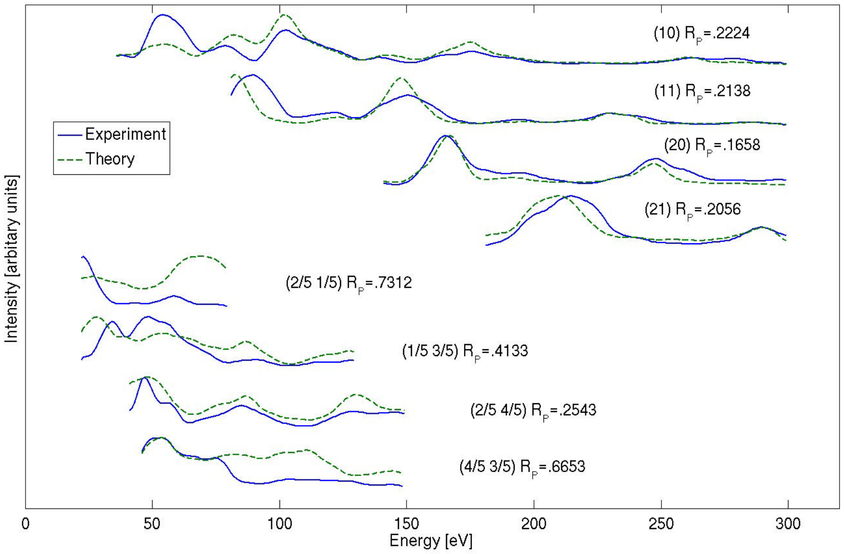

(b) Model 2 based on an Al_9Ir_2 alloy.

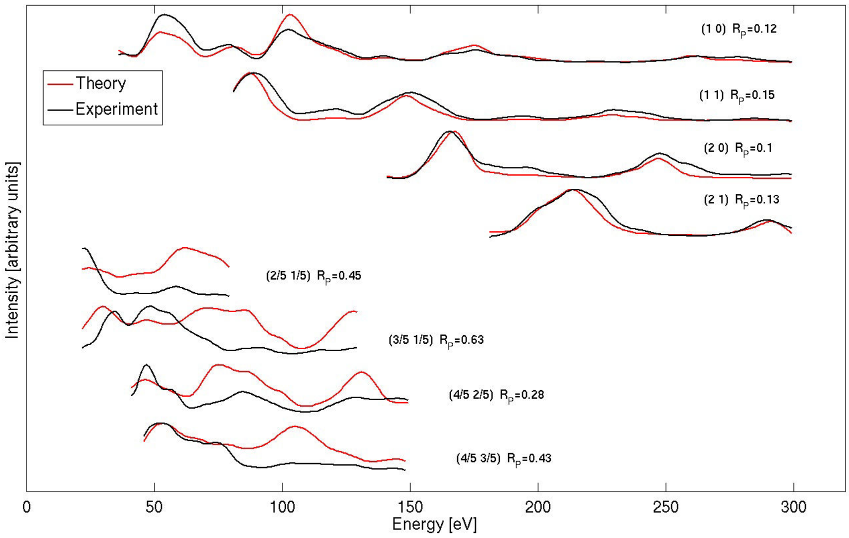

(c) Model 3 resulting from mixing of the above presented models.

FIGURE 5.13: Comparison between experimental and calculated I(V) curves for the considered models.

models (model1:model2). This suggests that the LEED I(V) measurements should be considered as a snapshot representing different stages towards the formation of Al_9Ir_2 compound.

Structural relaxation

In order to get further insight into the previously described observations, calculations based on the DFT were carried out on the Ir segregation and the formation of Al_9Ir_2 in Al(100) by Dr. Émilie Gaudry from the Metallurgy and Surfaces team of the Institut Jean Lamour in Nancy. These calculations are performed with the VASP package [70, 85, 86] within the generalised gradient approximation (GGA-PBE) [90, 91]. The interaction between the valence electrons and the ionic core is described using the PAW method [88, 89]. Spin polarisation is considered. A plane wave basis set for the electron wave function with cutoff energy of 450 eV is used. Integrations in the Brillouin zone are performed using a 13x13x1 k-grid generated according to the Monkhorst-Pack scheme. The segregation of Ir in Al(100) was studied systematically by 1 Ir atom in substitution of an Al into an Al(100) crystal. The considered asymmetric slabs consist of 19 layers : 7 layers fixed at the bottom and 12 layers allowed to relax. The surface unit cell is a square of size 6.38 Å, corresponding to a ($\sqrt{5}$x$\sqrt{5}$)R 26.6° reconstruction. Structures are relaxed using a conjugate-gradient algorithm until the atomic forces are less than 0.02 eV/Å. Relaxations are evaluated using the following quantity ζ:

$$\zeta = \sqrt{\sum_{atoms} (x_r - x_u)^2 + (y_r - y_u)^2 + (z_r - z_u)^2} \tag{5.2}$$

where the index u refers to the initial position (unrelaxed) and the index r refers to the corresponding relaxed position.

The presence of a surface Ir atom is not likely. Indeed, the relaxations of the slab containing a surface Ir atom are large (ζ = 12.75 Å), leading to the displacement of the Ir atom well below the surface Al plane (1.16 Å below). The relaxations are much smaller when the Ir atom is positioned in the subsurface layer. However, even in this case, the transition metal atom lies after relaxation below the subsurface Al layer (0.28 Å). Structural relaxations become negligible when the Ir atom is located in the subsurface layer, or deeper in the crystal (see Fig. 5.14). In this case, the smallest Al-Ir distances are equal to 2.77 Å, i.e. they are roughly equal to the sum of the atomic radii of the elements (r_{Al} = 143 pm and r_{Ir} = 136 pm). The right panel of Fig. 5.14 shows the difference between the z coordinate of the Ir atom and the Al plane in the considered slab. It shows that, already at the layer S-2, the Ir atom tends to take place in the plane.

Since the atomic relaxations do not necessary keep the layer-by-layer structure, we evaluate the non-relaxed segregation energy (atoms fixed at their initial position). Results are plotted in Fig. 5.15. Again, it shows that the presence of surface Ir atoms are very unlikely. Energy differences for slab containing Ir atoms at subsurface planes, or deeper in the crystal are quite similar. The energy difference between a slab containing a surface or subsurface Ir atoms is 1.48 eV.

Experimentally, small amounts of Ir have been deposited on Al(100). The formation of surface alloys is expected. The Al-Ir intermetallic compound which contains the lowest Ir amount is Al_9Ir_2. We will now investigate the possibility to grow the Al_9Ir_2 surface alloy on Al(100). As mentioned above, the Al_9Ir_2 intermetallic compound can be described as a layered compound. Its structure is built by the stacking of two atomic layers that alternates roughly perpendicular to the z-axis : a pure

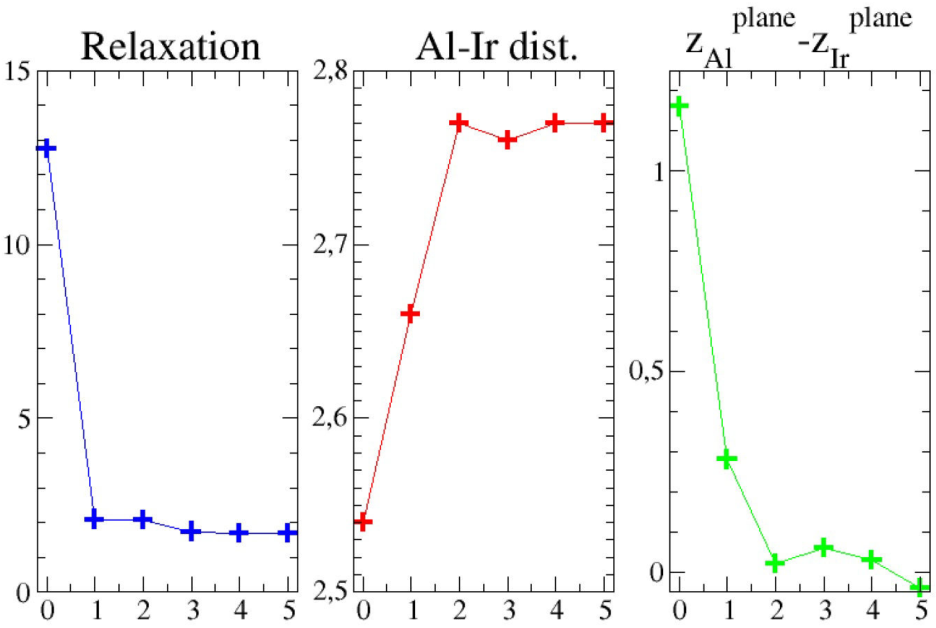

FIGURE 5.14: Structural relaxations obtained by burying an iridium atom into an Al(100) crystal. Relaxations (in Å) are given by the ζ quantity. The smallest Al-Ir distances and the quantity ($z_{Al^{plane}}$ - $z_{Ir^{plane}}$) are given in Å. The x-coordinate shows the Ir position in the slab : 0 for surface layer (S), 1 for subsurface layer (S-1), etc.

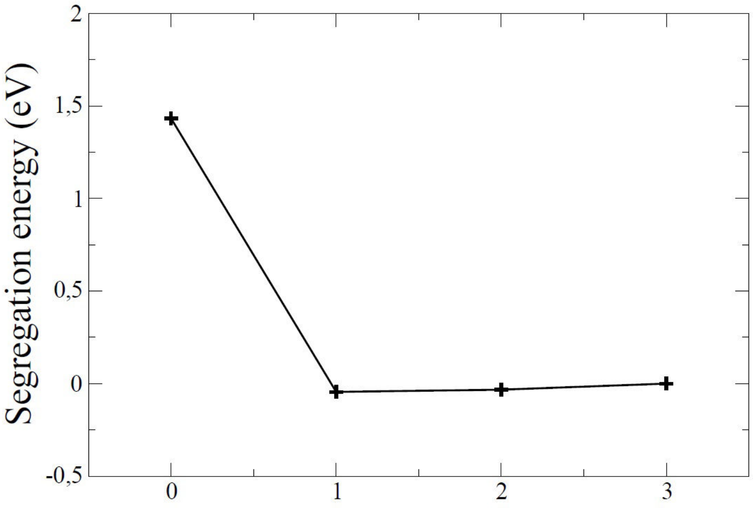

FIGURE 5.15: Segregation energy (eV) evaluated for non-relaxed slabs. The x-coordinate shows the Ir position in the slab : 0 for surface layer (S), 1 for subsurface layer (S-1), etc. The value is obtained with the formula: E = E_{slab}(Ir=i) - E_{slab}(Ir=3).

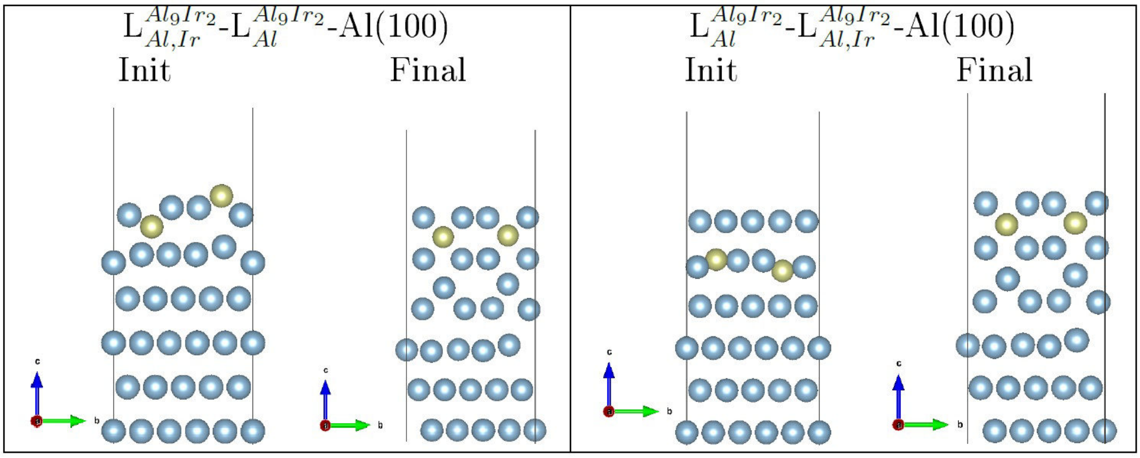

FIGURE 5.16: Structural relaxations of the considered surface alloys.

Al atomic layer ($L^{Al_9Ir_2}{}_{Al}$), made of 5 Al atoms, and a highly corrugated layer ($L^{Al_9Ir_2}{}_{Al,Ir}$), made of 4 Al and 2 Ir atoms. In the following, we consider that the interface plane corresponds either to the $L^{Al_9Ir_2}{}_{Al}$ or $L^{Al_9Ir_2}{}_{Al,Ir}$ atomic layers.

In order to build a structural model, the bulk phases Al_9Ir_2(001) and Al(100) have to be commensurate. The Al_9Ir_2 compound crystallises in the $P2_1/c$ space group, with the following parameters: a = 6.378(1) Å, b = 6.430(1) Å, c = 8.732(2) Å, β = 94.77(2)°. The cell parameter of fcc-Al is 4.04 Å. Then the previous slab, presenting a square surface cell of size 6.38 Å, fits quite well the dimensions of Al_9Ir_2. In the following, two different configurations are considered (see Fig. 5.16). The first structural model, called $L^{Al_9Ir_2}{}_{Al,Ir}$ - $L^{Al_9Ir_2}{}_{Al}$ - Al(100), presents the $L^{Al_9Ir_2}{}_{Al,Ir}$ atomic layer as termination plane and the $L^{Al_9Ir_2}{}_{Al}$ atomic layer as subsurface plane, both planes being deposited on the ($\sqrt{5}$x$\sqrt{5}$)R 26.6° Al(100) substrate. The second structural model, called $L^{Al_9Ir_2}{}_{Al}$ - $L^{Al_9Ir_2}{}_{Al,Ir}$ - Al(100), presents the $L^{Al_9Ir_2}{}_{Al}$ atomic layer as termination plane and the $L^{Al_9Ir_2}{}_{Al,Ir}$ atomic layer as subsurface plane, both being deposited on the ($\sqrt{5}$x$\sqrt{5}$)R 26.6° Al(100) substrate. In this case, the corrugation of the Al_9Ir_2 planes was decreased, in order to allow full convergence of the calculations.

As seen in Fig. 5.16, these two models relax to the same structure. The top layer of this structure is constituted of an Al pure plane where iridium atoms stand just below. This is in full agreement with the previously given results about the segregation of Ir in Al(100) and also with LEED I(V) analysis. Indeed, for the two best models that could be obtained with LEED I(V), iridium is also positioned below the top surface.

5.4 Conclusion

Following the bulk investigations of the Al-Ir system, the adsorption of Ir adatoms on Al(100) surface has been characterised aiming to form surface Al-Ir compound. At room-temperature, a preferential atomic decoration of the terrace step edges has been observed. Then, the growth proceed with the formation of irregularly shaped islands resulting in a rough and disordered overlayer for the highest coverage analysed. From the intermixing length of Ir in bulk Al expected at room-temperature, it is likely that the islands are formed by Al due to a place exchange mechanism between both elements. This is also in agreement with *ab initio* calculations indicating that it is energetically favored to have

Ir adatoms located in subsurface layers. Adsorption of Ir adatoms with the sample held between 320°C and 420°C leads to the formation several surface phases. Only one phase can be identified using LEED. The LEED pattern consists of two domains interpreted as a $(\sqrt{5}\mathrm{x}\sqrt{5})\mathrm{R}\ 26.6^\circ$ phase. STM analysis confirms both the orientations and the 6.4 Å surface unit cell of each domain. The dimensions on the domains match with those of the Al_9Ir_2 compound. This compound should be the first one to grow starting from the Al-rich side of the Al-Ir phase diagram. It is also the only reported Al-Ir compound matching the 6.4 Å unit cell dimensions determined by STM and LEED techniques. The orientation of the Al_9Ir_2 domains with respect to the Al(100) surface is dictated by the alignment of the Al square motif present in Al_9Ir_2 layers with the square surface unit mesh of Al(100). On top of these domains, STM measurements reveal the presence of overlayers referred as a (2×2) reconstruction of the $(\sqrt{5}\mathrm{x}\sqrt{5})\mathrm{R}\ 26.6^\circ$ phase and "14.3 Å" structure. The latter can be associated with an incomplete Al layer present in the Al_9Ir_2 compound. A thorough LEED I(V) analysis points toward the simultaneous presence of Ir adatoms in the subsurface layer of Al(100) and the presence of Al_9Ir_2 domains. In other words, the different stages towards the growth of the Al_9Ir_2 compound coexist under our dosing conditions. This is consistent with *ab initio* calculations which favor Ir in the subsurface layers. Indeed, the latter demonstrate that regardless of the (001) plane selected at the Al_9Ir_2 surface (pure Al or Al-Ir plane), the relaxed structure is identical but deviates from a perfect Al_9Ir_2 structure within the thickness considered for the calculations. The top surface layer is a pure Al termination and Ir atoms remains in the subsurface planes. Now that (001) layers of the Al_9Ir_2 compound could be experimentally synthesised, it would be interesting to study their associated physical and chemical properties (wetting, oxidation behaviour...) and compared them with previous studies performed for instance on the isostructural Al_9Co_2 compound [144, 145].

Résumé en français

Introduction

Le développement d'alliages métalliques toujours plus performants est une discipline qui trouve un grand intérêt auprès de nombeux secteurs industriels tels que l'automobile, l'aéronautique, la catalyse, la biomédecine et bien d'autres encore. L'objectif de former un alliage est bien sûr d'obtenir un nouveau matériau présentant des propriétés physiques, mécaniques ou chimiques qui diffèrent des métaux qui le composent (matériau plus léger, plus performant, plus résistant aux contraintes, etc.). En tenant compte des multiples combinaisons d'éléments chimiques possibles pour former un alliage, on réalise que le développement et l'étude des propriétés de tels composés intermétalliques constituent un domaine de recherche très vaste, largement inépuisé, et qui ne cesse d'être étudié encore aujourd'hui. Alors que certains alliages sont conçus pour résister à des environnements contraignants (corrosion, fatigue, hautes températures etc.), d'autres sont développés pour leur propriétés magnétiques, électriques ou chimiques (semi-conducteur, supraconducteur, catalyseurs etc.). On parle de composé intermétallique lorsque l'alliage adopte une structure cristalline qui diffère de celle de ses constituants, en général pour une composition chimique bien particulière. Les alliages métalliques complexes (CMA) sont une classe particulière d'intermétalliques caractérisés par une maille élémentaire de grande dimension, contenant de quelques diisingines à plusieurs milliers d'atomes pouvant former des agrégats de haute symétrie. Il est possible de trouver parmi ces alliages des propriétés, ou des combinaisons de propriétés, qui ne se retrouvent pas dans des alliages de structures plus simples. Les alliages quasicristallins (QC) représentent un cas particulier de CMA. Ils possèdent une structure cristalline ordonnée mais apériodique, ainsi que des symétries interdites par les règles de la cristallographie classique (d'ordre 5, 8, 10, 12, etc.) [14]. Ainsi, aucune maille élémentaire ne peut être définie pour un QC parfait. Ces phases complexes apparaissent dans certains systèmes ternaires comme les Al-TM-TM' (TM= métal de transition), Ti-Ni-Zr, etc. et dans quelques binaires comme Cd-Yb, Cd-Ca, etc. En utilisant les règles de Hume-Rothery, Tsai *et al.* [9] ont découvert un grand nombre de nouvelles phases CMA en jouant sur des substitutions isoélectroniques, comme par exemple en substituant un métal de transition d'un système ternaire par un autre de la même colonne du Tableau Périodique. On connait aujourd'hui une centaine de phases quasicristallines stables, mais on ne sait pas prédire l'existence de phases complexes dans un système donné. Dubois *et. al* [3] ont cependant remarqué que parmi la centaine de phases QC connues, un grand nombre se trouve dans des systèmes ternaires ABC qualifiés de « push-pull ». Un système push-pull est un système pour lequel des composés intermétalliques existent dans les binaires A-B et A-C (c'est-à-dire que les interactions A-B et A-C sont attractives - Pull) alors que B et C sont immiscibles (le système B-C ne forme aucun composé et les interactions entre les constituants sont donc répulsives - Push). Les systèmes push-pull seraient donc propices à l'émergence de phases intermétalliques complexes. Les applications de cette nouvelle classe de matériaux sont pour l'instant limitées, principalement du fait de leur fragilité intrinsèque. En effet, les QC se comportent un peu comme des céramiques (ils sont durs et fragiles), et leur fragilité est donc un frein important pour des applications directes sous forme de matériau massif. Ils ont cependant déjà trouvé applications en tant que précipité sous forme de nanoparticules dans des aciers maraging [13] ou en tant que revêtement dans des poêles anti-adhésives [12] ou bien encore sous forme de composites métalliques ou à base polymère qui peuvent être mis en forme par des méthodes de fabrication additive [15]. Une autre application concerne la catalyse hétérogène. Le groupe de A.P. Tsai au Japon a rapporté des résultats encourageants concernant la production de H_2 par vapo-reformage de methanol sur un échantillon quasicristallin de Al-Cu-Fe ayant subi une attaque chimique [16]. De même, des approximants de type Al-TM ont été identifiés comme des matériaux prometteurs pour la semi-hydrogénation de l'acétylène [17]. Bien qu'une grande majorité des systèmes binaires ou ternaires ait été déjà étudiée, au moins partiellement, certains systèmes restent encore inexplorés et beaucoup sont encore incomplets aujourd'hui. C'est le cas par exemple du système Al-Ir, lequel a fait l'objet d'un certain nombre d'études mais dont le diagramme de phases présente encore quelques incertitudes. Ce système présente un intérêt certain. En effet, certains composés Al-Ir montrent de bonnes propriétés de dureté, de résistance à la fracture et à l'oxydation à haute température ainsi que de hauts points de fusion et pas de fragilité. On peut noter également la présence de deux phases CMA identifiées dans ce système, les composés $Al_{45}Ir_{13}$ [24] et $Al_{28}Ir_9$ [25]. Le travail présenté dans ce mémoire de thèse porte sur une réexamination en profondeur du système Al-Ir, en particulier dans sa partie riche en aluminium. Ce travail s'est poursuivi par une étude des systèmes push-pull Al-Au-Ir et Al-Ag-Ir qui n'avaient pas encore fait l'objet de publications dans la littérature, avec l'objectif d'identifier de nouvelles phases CMA. En effet, la présence de phases QC a déjà été rapportée dans le système Al-Cu-Ir et on peut donc raisonnablement espérer qu'une substitution isoélectronique de type Cu/Au ou Cu/Ag permette d'obtenir des composés similaires en suivant l'approche adoptée par Tsai *et. al*. Nous nous sommes également intéressés aux surfaces d'alliages Al-Ir, en essayant d'élaborer des composés de surface par dépôt d'iridium sur une surface monocristalline d'aluminium dans les conditions de l'ultra-vide. Dans la suite de résumé, on présente brièvement les méthodes expérimentales utilisées avant d'aborder les principaux résultats obtenus, tant en volume qu'en surface.

Méthodes expérimentales

Afin de préparer et de caractériser un échantillon d'alliage métallique massif, différentes techniques sont couramment utilisées en laboratoire. Dans le cadre de ce travail, les échantillons ont été préparés par fusion au four à arc. Les éléments purs sont déposés sur la sole d'un creuset refroidi par un circuit d'eau. L'enceinte est fermée et évacuée jusqu'à obtenir un vide secondaire, puis remplie d'argon. Un fort courant est appliqué entre une pointe en tungstène (cathode) et la sole du creuset (anode), générant un arc électrique intense. Celui-ci ionise les molécules d'argon environnantes et crée un plasma très chaud capable de fondre ensemble les éléments déposés. À cause du refroidissement rapide, l'échantillon obtenu n'est pas à l'équilibre thermodynamique et un traitement thermique est ainsi nécessaire. Pour ce faire, l'alliage est scellé sous vide dans une ampoule en quartz avant d'être placé dans un four à mouffles pour être recuit à haute température pendant plusieurs jours.

L'échantillon obtenu, polycristallin, est ensuite prêt à être étudié à l'aide de différentes techniques de caractérisations :

- **La diffraction des rayons X** sur poudre a été utilisée pour identifier les phases connues présentes dans les échantillons grâce à leur structure cristalline. En effet, chaque phase laisse une empreinte caractéristique sur le diagramme de diffraction et peut être ainsi identifiée via une base de donnée. La diffraction des rayons X sur poudre est une méthode qui permet également la résolution de structures cristallines. Cependant, cette méthode n'a été utilisée que pour l'identification de phases connues dans ces travaux. La diffraction des rayons X sur monocristaux permet d'établir la structure cristalline des phases inconnues. Lorsque les rayons X entrent en contact avec la matière, différents types d'interactions peuvent se produire. Parmi celles-ci, l'effet Rayleigh où le rayonnement est diffusé élastiquement est celui qui provoque le phénomène de diffraction. Si la matière est bien organisée, cet effet engendre alternativement des interférences constructives et destructives, caractéristiques de l'arrangement atomique de l'échantillon étudié. En résolvant le réseau d'ondes diffusées obtenu, il est donc possible de retrouver la structure cristalline du composé étudié. C'est précisément la tâche de la diffraction des rayons X sur monocristaux. L'échantillon polycristallin est broyé pour pouvoir collecter un monocristal de forme et d'aspect homogène. Celui-ci est monté sur un diffractomètre avant de l'irradier par des rayons X dans toutes les directions de l'espace. Un détecteur bidimensionnel récupère alors la position et l'intensité de tous les rayons diffractés. Ces données sont corrigées de plusieurs facteurs: de Lorentz, de polarisation, d'absorption et d'extinction, avant d'être traitées numériquement. Dans ces travaux, le programme SHELX-2013 [36] a été utilisé pour la résolution de ces données et pour l'établissement des structures cristallines.

- **La microscopie électronique à balayage** est une technique qui permet d'obtenir une image de la topographie de l'échantillon avec une résolution allant de quelques microns à quelques millimètres. L'échantillon est d'abord finement poli avant d'être placé dans le microscope. Alors qu'un microscope optique utilise les ondes lumineuses pour former une image, un microscope électronique utilise un faisceau d'électrons pour produire une image à l'aide d'un détecteur approprié. Ce faisceau est créé via un canon à électrons puis focalisé sur une zone de l'échantillon à l'aide d'un réseau de lentilles. Quand ce faisceau interagit avec la matière, il genère à la fois des électrons secondaires, des électrons rétrodiffusés ainsi qu'un rayonnement X. La détection des électrons secondaires (basse énergie), permet de former une image avec une bonne résolution en relief de la surface de l'échantillon. La détection des électrons rétrodiffusés (plus haute énergie), ne mène pas à une si bonne résolution mais permettra un meilleur contraste entre les phases présentes dans l'échantillon. La détection des rayons X apporte une information importante concernant la composition chimique de l'échantillon. En effet, chaque élément émet un rayonnement à des énergies caractéristiques. La détection de leur abondance en fonction de leur énergie apporte alors une information directe sur la stoechiométrie de la phase ciblée. Les rayons X pouvant sonder une profondeur non négligeable de l'échantillon (appelée la poire d'interaction), il faut donc être prudent sur les valeurs obtenues. Celles-ci pouvant être biaisées par la présence d'une autre phase en dessous de celle ciblée.

- **L'analyse thermique différentielle** est une technique qui consiste à suivre l'évolution de la différence de température entre l'échantillon et une référence inerte. L'échantillon est placé dans un creuset désigné pour l'appareil puis la chambre est pompée sous vide avant d'être remplie d'un gaz neutre. L'échantillon et la référence sont alors chauffés selon un programme où la vitesse de chauffe et de refroidissement ainsi que la température maximale de la mesure sont déterminées. Tout au long de l'analyse, la différence de signal entre le thermocouple de l'échantillon et celui de la référence est mesurée. Cette différence est appelée flux de chaleur et a la dimension d'une tension. Lorsque l'échantillon subit une réaction (décomposition d'une phase, fusion, recristallisation etc.), un pic sur le signal du flux de chaleur est détecté. Ainsi, les phases en présence dans l'échantillon peuvent être identifiées et leurs températures caractéristiques de réactions déterminées. Pour les nouvelles phases, ces températures peuvent être déterminées dans le but de reconstruire le diagramme de phases du système étudié. Si le principe de cette technique de caractérisation peut paraître simple, la compréhension et l'interprétation des pics dans le signal du flux de chaleur pour la construction d'un diagramme de phases peut devenir une tâche très délicate.

Le système binaire aluminium-iridium

Le système binaire Al-Ir est un système qui a déjà fait l'objet de nombreuses études dans la littérature. Les composés intermétalliques connus à ce jour pour ce système sont au nombre de six : Al_9Ir_2, $Al_{45}Ir_{13}$, $Al_{28}Ir_9$, Al_3Ir, $Al_{2.75}Ir$ et AlIr. Nombre d'auteurs sont venus apporter leur contribution au diagramme de phases de ce système tel qu'on le connait aujourd'hui. Malgré tout, quelques incertitudes planent toujours sur ce diagramme de phases. Parmi celles-ci, on peut noter le désaccord de certains auteurs concernant l'existence ou non du composé $Al_{13}Ir_4$. Egalement, d'autres auteurs semblent avoir identifié une variante superstructurale du composé $Al_{2.75}Ir$ sans donner plus de détails. En remarquant que la majorité des travaux se sont portés sur la partie riche en aluminium du système, il est également légitime de se demander si de nouvelles phases pourraient être découvertes du côté plus riche en iridium du diagramme de phases. Nos travaux se sont donc orientés une nouvelle fois sur l'étude du système Al-Ir avec pour objectif de lever ces incertitudes. Nous avons élaboré et caractérisé 47 échantillons binaires Al-Ir de différentes compositions. Trois principaux résultats sont résumés ci-après.

Le nouveau composé $Al_{2.4}Ir$

Dans plusieurs échantillons obtenus après recuit, un nouveau composé intermétallique qui n'avait alors jamais été rapporté dans la littérature a pu être identifié. Cette nouvelle phase a d'abord été identifiée sur les diagrammes de diffraction sur poudre. En effet, de nombreux pics de diffraction qui ne pouvaient être reliés à aucune phase binaire Al-Ir connue ont été observés. La diffraction sur monocristal a alors ensuite aidé à la résolution de la structure cristalline. Le composé de stoechiométrie $Al_{2.4}Ir$ cristallise dans une maille trigonale de paramètres a = 7.6089(3) et c = 30.177(1) (groupe d'espace $R32$, symbole de Pearson $hR102$). Les facteurs d'accord après affinement du modèle cristallographique montrent des valeurs acceptables : $R1$ ($I \geq 4\sigma$) = 0.0516, $wR2$ ($I \geq 4\sigma$) = 0.0944. Les données récoltées semblent cependant souffrir d'un important phénomène d'absorption et de meilleurs facteurs d'accord émergeront certainement d'une meilleure collection de données. Le modèle structural établi pour $Al_{2.4}Ir$ possède un certain désordre localisé autour d'une position d'iridium. A cet endroit, des positions atomiques d'aluminium partiellement occupées rompent localement la symétrie du groupe d'espace $R32$ en $R3$. Il a été déterminé que le polyhèdre formé par ces atomes d'aluminium autour de l'iridium pouvait s'orienter de deux manières différentes dans la maille. Ainsi, un modèle structural a alors été alternativement établi dans le groupe d'espace $R3$ afin de mieux décrire le système. En regardant dans la littérature, le diagramme de diffraction de ce composé $Al_{2.4}Ir$ ressemble totalement à celui de Al_7Rh_3 [74], composé dont la structure reste inconnue à ce jour. Il est fort probable que la phase Al_7Rh_3 adopte le même modèle structural que celui établi pour $Al_{2.4}Ir$.

La variante structurale de $Al_{28}Ir_9$

Un des échantillons préparés, ne contenant que la phase connue $Al_{28}Ir_9$, a été analysé par diffraction des rayons X sur poudre par rayonnement synchrotron. Le diagramme obtenu présentait alors un dédoublement systématique des pics de diffraction comparé au modèle de la littérature. Un tel phénomène n'a pu être observé qu'avec la diffraction synchrotron, permettant une très haute résolution des données. Une étude de diffraction *in situ* sur ce même échantillon a montré que la structure de $Al_{28}Ir_9$ variait légèrement en fonction de la température. Au delà de 790°C, le composé adopte le modèle structural de la littérature (a = 12.275(2) Å et c = 27.351(3) Å, groupe d'espace $P31c$, symbole de Pearson $hP222$). En dessous de 790°C, la structure de $Al_{28}Ir_9$ dévie légèrement de cette symétrie hexagonale pour former une maille orthorhombique de paramètres a = 12.2567(3) Å, b = 21.2785(5) Å et c = 27.3445(7) Å (groupe d'espace $Cmc2_1$, symbole de Pearson $oC444$). La transition directe entre les groupes d'espaces $P31c$ et $Cmc2_1$ étant impossible d'après les tables de cristallographie, la structure de $Al_{28}Ir_9$ a alors été décrite dans le groupe d'espace intermédiaire $P6_3mc$ pouvant lier les deux précédents. Les trois modèles ont été présentés et les liens entre les positions atomiques de chaque modèle ont été exposés.

La variante structurale de $Al_{2.75}Ir$

Le composé intermétallique $Al_{2.75}Ir$ a été stabilisé dans plusieurs échantillons bruts de synthèse et recuits. La diffraction des rayons X sur poudre de chacun de ces échantillons a révélé de faibles pics de diffraction supplémentaires à ceux du modèle connu de $Al_{2.75}Ir$ (paramètre a = 7.6656(2) Å). L'indexation de ces faibles pics avec ceux du modèle de la littérature a conduit à une maille cubique au paramètre de maille doublé, a = 15.3312(2) Å, suggérant ainsi l'existence d'une variante superstructurale (2x2x2) du composé $Al_{2.75}Ir$. De telles observations ont déjà été faites dans la littérature [28] mais aucune détermination structurale n'avait été réalisée jusqu'alors. Une collection de diagramme de diffraction sur poudre par rayonnement synchrotron a permis de mettre en évidence l'existence de deux variantes structurales de $Al_{2.75}Ir$ en fonction de la température. Au delà de 630°C, le composé adopte sa structure cubique désordonnée (occupations partielles d'aluminium) au paramètre a = 7.6656(2) Å (groupe d'espace $P23$, symbole de Pearson $cP60$), connue de la littérature. En dessous de cette température, une légère déviation de certaines positions d'aluminium fait passer $Al_{2.75}Ir$ dans une variante cubique plus ordonnée au paramètre doublé a = 15.3312(2) Å (groupe d'espace $F23$, symbole de Pearson $cF280$). Le modèle crsitallographique de cette variante superstructurale a été approché mais reste encore incomplet. Huit atomes d'aluminium, dont la position n'a pu être déterminée avec les données collectées, manquent toujours au système pour respecter la stoechiométrie $Al_{2.75}Ir$.

Systèmes ternaires à base de Al-Ir

Le système ternaire Al-Cu-Ir est connu pour présenter un certain nombre de phases quasicristallines dans le domaine riche en aluminium [77, 78]. En suivant la méthode utilisée par Tsai *et. al* telle qu'expliquée en introduction, ces travaux se sont orientés vers l'étude des systèmes ternaires Al-Au-Ir et Al-Ag-Ir, substituant ainsi le cuivre par deux autres élements de la même colonne. Ces deux systèmes n'ont encore fait l'objet d'aucun rapport dans la littérature, leur étude ayant donc pour but de mettre potientiellement en évidence des phases quasicristallines similaires à celles trouvées dans le système Al-Cu-Ir. Il est important de noter que l'iridium n'étant pas miscible avec les trois éléments Cu, Ag et Au, les trois systèmes Al-Cu-Ir, Al-Ag-Ir et Al-Au-Ir entrent donc la catégorie des systèmes push-pull. Les principaux résultats issus de l'exploration des systèmes Al-Au-Ir et Al-Ag-Ir sont résumés ci-après ainsi que la découverte d'une nouvelle phase dans le système Al-Si-Ir, cette dernière résultant d'une manipulation accidentelle.

Al-Au-Ir

Un total de 9 échantillons ternaires Al-Au-Ir, riches en Al, ont été préparés et caractérisés par des méthodes similaires à celles utilisées pour le système Al-Ir. Leur composition a été décidée de sorte à imiter la stoechiométrie des QC trouvés dans Al-Cu-Ir. La caractérisation de chacun de ces échantillons a pu mettre en évidence l'existence d'un nouveau composé intermétallique Al_3AuIr. Cette phase a une température de fusion de 990°C ainsi qu'une structure cristallographique non complexe cristallisant dans une maille trigonale isotype à Al_3Ni_2 de paramètres a = 4.2584(5) Å et c = 5.1991(7) Å (groupe d'espace $P\overline{3}m1$, symbole de Pearson $tP5$). Dans la maille élémentaire de Al_3AuIr se trouvent deux positions atomiques d'occupation mixte Au/Ir. Il a été déterminé que statistiquement, le ratio Au/Ir vaut 50/50. En fonction de l'encombrement généré par les différents environnements Au/Ir possibles autour des atomes d'aluminium, la position de ceux-ci peut légèrement dériver de leur position initiale. Ceci a pour conséquence directe de générer une position atomique partiellement occupée de Al, provoquant un certain désordre dans la maille élémenaire de Al_3AuIr. Un tel phénomène est également observé pour le composé isotructural $Al_3Cu_{1.5}Co_{0.5}$. Des calculs basés sur la théorie de la fonctionnelle de la densité (DFT) ont révélé que contrairement au système Al-Cu-Co, il est énergétiquement plus favorable pour le système Al-Au-Ir d'adopter un ratio Au/Ir de 1:1 (1:3 dans le cas de Cu et Co). Des calculs de densité d'états éléctroniques (DOS) sont venus confirmer ces résultats et d'autres observations ont montrées que Al_3AuIr était stabilisé par un mécanisme de Hume-Rothery. Des calculs de liaison chimique par approche ELI-D ont rélévé la présence de liaisons à deux centres et à multicentres dans la maille de Al_3AuIr. De par la distribution de ces liaisons, un clivage préférentiel du matériau est attendu le long des plans perpendiculaires à la direction [001].

En outre, un second composé intermétallique ternaire Al-Au-Ir a pu être identifié dans un échantillon recuit pauvre en or. La diffraction des rayons X sur monocristal a permis de résoudre la structure cristalline de ce composé. Avec 104 atomes dans la maille, la nouvelle phase possède une stoechiométrie $Al_{72}Au_{2.5}Ir_{29.5}$. Ce composé cristallise dans une maille tétragonale de paramètres a = 8.6339(2) Å et c = 21.8874(7) Å (groupe d'espace $I4_1/acd$, symbole de Pearson tI104). Cette phase est en effet relativement pauvre en or mais aucun composé binaire Al-Ir ne possède une structure similaire, témoignage que l'or joue un rôle déterminant dans la stabilisation de ce composé. $Al_{72}Au_{2.5}Ir_{29.5}$ possède une structure isotype de $BaMg_2[VO_4]_2$ où les atomes de Al prennent la place des Ba et O et les atomes de Au et Ir celles des Mg et V. Les facteurs d'accord obtenus après affinement de la structure montrent des valeurs optimales : $R1$ (I $\geq 4\sigma$) = 0.0165, $wR2$ (I $\geq 4\sigma$) = 0.0388. Parallèlement à la structure cristalline moyennement complexe de $Al_{72}Au_{2.5}Ir_{29.5}$, l'étude du système Al-Au-Ir n'a pas pu mettre en évidence l'existence de phases QC.

Al-Ag-Ir

Suivant la même procédure que pour le système Al-Au-Ir, 4 échantillons ternaires Al-Ag-Ir ont été préparés. Des problèmes d'évaporation ont alors rapidement été observés lors de la fusion à l'arc. En effet, après chaque synthèse, une fraction importante d'argent manquait systématiquement dans les échantillons. En conséquence, la composition chimique de chaque échantillon s'est vue fortement déviée de celle initialement ciblée. Ces alliages ont été analysés par diffraction des rayons X sur poudre et par microscopie électronique à balayage. Suite à ces analyses, aucune nouvelle phase ternaire n'a été observée. Les échantillons ont tous montré un mélange plutôt inhomogène de composés binaires Al-Ir et Ag-Ir connus. L'étude du système Al-Ag-Ir n'est pour le moment qu'à son commencement. Les problèmes d'évaporation et d'inhomogénéité encourus résultent probablement de la fusion un peu trop brutale des éléments par fusion à l'arc. Pour de futures préparations, une méthode plus douce, telle que la fusion par induction sera probablement envisagée.

Al-Si-Ir

Lors de l'étude du sytème binaire Al-Ir, un échantillon a été recuit dans un creuset en alumine ouvert placé dans un tube en quartz sous vide. La haute température du recuit a partiellement recristallisé le tube et des particules de quartz sont tombées dans le creuset, ajoutant involontairement du silicium à la composition. L'analyse de cet échantillon a révélé la stabilisation d'une phase ternaire Al-Si-Ir. Plusieurs échantillons ternaires Al-Si-Ir ont ainsi été subséquement préparés dans le but de caractériser entièrement ce nouveau composé. De composition $Al_{11}SiIr_6$, la phase cristallise dans une maille orthorhombique de paramètres a = 3.9573(1) Å, b = 12.8574(6) Å et c = 10.5989(9) Å (groupe d'espace $Cmcm$, symbole de Pearson oC36). Sa structure cristalline est isotype au composé Ga_2Ir [119] mais la position des Al et Si n'a pu être différenciée par diffraction des rayons X. Étant donné la composition chimique proche entre $Al_{11}SiIr_6$ et Al_2Ir, il n'est pas étonnant de découvrir une structure similaire à Ga_2Ir, Al et Ga appartenant à la même colonne du Tableau Périodique des éléments. Afin de mieux comprendre la stabilité du composé $Al_{11}SiIr_6$, des calculs d'enthalpie de formation basés sur la DFT ont été effectués. Il a été révélé que la teneur croissante en Si dans les composés $(Al_{1-x}Si_x)_2Ir$ avait pour conséquence de déstabiliser la phase. Ainsi, la faible teneur en Si dans $Al_{11}SiIr_6$ est favorable à la formation de ce composé. Des calculs de DOS sont venus appuyer ces observations.

Dépôt d'iridium sur la surface Al(100)

L'environnement d'un atome en surface diffère fortement de celui d'un atome en volume, influençant ainsi beaucoup les propriétés de surface. De plus, la surface d'un matériau peut présenter une structure différente de celle correspondant à une simple troncature du volume. Les structures atomiques des surfaces sont essentielles pour comprendre les propriétés qui en résultent, comme par exemple la catalyse. Nous avons donc réalisé les premières études de surface d'alliages Al-Ir. Les études de surfaces de composés intermétalliques nécessitent cependant l'exploitation d'échantillons monocristallins relativement conséquents, difficiles à obtenir et *a fortiori* coûteux. Une telle préparation d'échantillons n'ayant pu être réalisée, une méthode alternative a alors été envisagée. De l'iridium a ainsi été déposé sous ultra-vide par dépôt physique en phase vapeur sur une surface Al(100). Cette préparation a été réalisée à température ambiante ainsi qu'à 420°C. Le substrat Al(100) a été réutilisé pour chaque préparation, après avoir été nettoyé par de multiples cycles de bombardement ionique d'argon suivi d'un recuit à 510°C. L'échantillon Ir/Al(100) a été systématiquement analysé par diffraction d'éléctrons lents (LEED), spectroscopie de photoélectrons excités par rayons X (XPS) et microscopie à effet tunnel (STM).

Dépôt à 20°C

Pour les dépôts effectués à température ambiante, les diagrammes LEED montrent systématiquement une maille carrée de paramètre a = 2.86 Å avec un certain bruit de fond. L'aluminium pur est connu pour cristalliser dans une maille cfc au paramètre a = 4.05 Å. En observant uniquement la surface de l'aluminium pur, seul la face centrée est prise en compte. Ainsi, le paramètre de maille de surface de l'aluminium correspond à $4.05/\sqrt{2} = 2.86$ Å. Il s'agit donc de Al(100) qui est observé ici avec le LEED. Il a été révélé par des mesures STM que les taux de couverture étaient très inhomogènes en fonction de la région de la surface étudiée. En effet, alors que certains endroits montraient des terraces nues Al(100), d'autres montraient une forte couverture d'iridium désorganisé, expliquant la persistence du cliché de LEED de la surface Al(100) ainsi que le bruit de fond associé. L'iridium déposé a diffusé initialement le long des terraces Al(100). A faible couverture, les atomes d'iridium diffusent à travers les terraces pour décorer préférentiellement les bords de marche. Parallèlement, une germination de petits aggrégats d'atomes s'est poursuivie au milieu des terraces. A couverture plus élevée, ces aggrégats croissent sans coalescence, expliquant ainsi l'absence d'organisation autre que celle de Al(100) à la surface de l'échantillon. D'après les travaux précédents d'adsorption de Ir sur Cu(100) [133] et en tenant compte à la fois des calculs *ab initio* et des énergies de surface des différents éléments, un phénomène d'échange entre Al et Ir est envisagé. Les mesures XPS permettent de calculer la composition chimique en surface. Des dosages d'iridium ont été effectués sur une surface de Cu(110) afin de calibrer la concentration d'iridium déposée en surface. Ces valeurs ont été comparées à la littérature où un groupe d'auteurs a mesuré leur depôt d'iridium sur Cu(100) par microbalance. Ainsi dans nos expériences, il a pu être déterminé qu'un flux de 60 nA d'iridium maintenu pendant 90 min avait un pouvoir de couverture de 2 monocouches équivalentes (MLE). A titre indicatif, la composition calculée avec les données XPS après un dépôt de 2 MLE Ir sur Al(100) donne $Al_{80.7}Ir_{19.3}$. Cette valeur reste relativement élevée en Al car la XPS sonde l'échantillon sur une épaisseur de quelques nm.

Dépôt à 420°C

Pour des dépôts réalisés à 420°C, plusieurs structures de surface ont pu être identifiées. Les clichés LEED ont révélé la présence de deux domaines carrés, commensurés avec la maille du substrat, de paramètre $a' = a\sqrt{5}$ (6.40 Å) et orientés chacun de plus ou moins 26.6° par rapport à l'axe de la maille de surface Al(100). Les images STM ont confirmé la présence de ces deux domaines et leurs orientations. En étudiant le composé Al_9Ir_2 en terme d'empilement de plans corrugués d'atomes le long de l'axe c, il a été constaté que les structures de surface observées ici correspondent à certains plans de Al_9Ir_2. Comme on dépose une quantité restreinte d'iridium sur un large excès d'aluminium, il n'est pas étonnant de former le composé Al_9Ir_2, phase la plus riche en Al du système Al-Ir. De plus, la phase Al_9Ir_2 est la seule du système Al-Ir dont les paramètres de maille (a = 6.378(1) Å, b = 6.430(1) Å, c = 8.732(2) Å, β = 94.77(2)°) correspondent aux dimensions de 6.40 Å des deux domaines. Hormis ces deux domaines, les mesures STM ont également révélé la présence de deux autres phases de surface. La première s'apparente à une reconstruction (2×2) des domaines ($\sqrt{5}$x$\sqrt{5}$)R 26.6°. La seconde peut être associée à une couche incomplète de Al_9Ir_2. Ces deux différentes reconstructions n'apparaissent cependant pas sur les clichés LEED, suggérant que ces deux phases sont très minoritaires à la surface. Des calculs de LEED I(V) réalisés à l'université de Lappeenrenta en Finlande suggèrent la présence simultanée d'atomes d'iridium sous la surface de Al(100) ainsi que de la phase Al_9Ir_2. Ces résultats sont en adéquation avec les observations précédentes mais également avec des calculs *ab initio* réalisés dans l'équipe qui montrent que la présence d'iridium en sous-surface est favorisé par rapport à de l'iridium en surface. Les résultats expérimentaux décrits ci-dessus ont pu également être reproduits après dépôt à 320°C mais aussi à température ambiante suivi d'un recuit à 420°C. Après de multiples préparations, il a été remarqué que 5 à 7 cycles de bombardement/recuit ne suffisaient plus à nettoyer la surface Al(100). En effet, les pics de diffraction de la phase ($\sqrt{5}$x$\sqrt{5}$)R 26.6° s'estompaient mais restaient toujours visibles sur les clichés LEED. Ce fait témoigne d'une diffusion importante de l'iridium dans le volume ségrégeant à la surface lors des recuits. Maintenant que le composé Al_9Ir_2 a pu être obtenu en surface, il serait intéressant d'en étudier les propriétés physiques et chimiques (mouillage, oxydation...) et de les comparer avec celles du composé isostructural Al_9Co_2 [144, 145].

Conclusion

Le système binaire aluminium-iridium, connu pour pésenter de nombreux composés intermétalliques dont certains CMA, a fait l'objet d'un réexamen complet. Afin de lever certaines incertitudes concernant le diagramme de phases Al-Ir, l'étude approfondie de ce système a permi d'identifier une nouvelle phase binaire Al-Ir ainsi qu'une deuxième variante structurale pour deux des composés connus. Ces nouveaux résultats viendront prochainement compléter un rapport concernant la construction d'un diagramme de phases Al-Ir réactualisé. Un nouveau composé à également été découvert dans le système ternaire Al-Si-Ir et sa stabilité a été étudiée. Les sytèmes ternaires Al-Au-Ir et Al-Ag-Ir ont également été explorés. Deux nouveaux composés intermétalliques dont un CMA ont pu être mis en évidence dans le système Al-Au-Ir. L'étude du sytème Al-Ag-Ir n'en est pour le moment qu'à son commencement. Afin de palier aux problèmes rencontrés, une préparation des échantillons par four à induction sera préférée au four à arc pour la suite à donner à cette étude. Les surfaces des alliages métalliques est également un aspect intéressant à étudier, les propriétés qui en découlent différant de celles des matériaux massifs. Le système binaire Al-Ir a donc été aussi examiné en termes de surfaces. Quelques couches d'iridium ont ainsi été déposées sur une surface d'aluminium (100). A basse température, une croissance désordonnée d'aggrégats atomique a été révélé. A partir de 320°C en revanche, des couches successives de la phase Al_9Ir_2(001) se forment non pas seulement en surface, mais également dans une partie de la sous-surface. Une fois la croissance en surface de composé maitrisée, une étude concernant sa réactivité chimique pourra être envisagée. Ce sont les propriétés intéressantes des alliages métalliques complexes qui ont motivé l'exploration des systèmes précédemment mentionnés. Néanmoins, les études qui ont été menées dans cette thèse n'ont pour le moment concerné qu'un aspect purement fondamental. Par la suite, des études pourront être menées pour caractériser les propriétés physiques et chimiques de ces matériaux, en particulier celles des nouvelles phases que nous avons identifiées.

Publications, presentations and posters

Publications

1. **Joris Kadok**, Marie-Cécile de Weerd, Pascal Boulet, Émilie Gaudry, Y. Grin, V. Fournée and Julian Ledieu. Al_3AuIr: A New Compound in the Al–Au–Ir System. *Inorganic Chemistry* 54 (2015), pp. 7898–7905

Oral presentations

1. **Joris Kadok**, Vincent Fournée and Julian Ledieu. Dosing iridium on a Al(100) surface under UHV. Weekly meeting of the Max-Planck Institute CPfS, Dresden, Germany, 25 august 2015.
2. **Joris Kadok**, Marie-Cécile de Weerd, Pascal Boulet, Émilie Gaudry, Y. Grin, V. Fournée and Julian Ledieu. Al_3AuIr: A New Compound in the Al–Au–Ir System. C-MAC days 2015, Grenoble, France, 24 November - 25 November 2015.
3. **Joris Kadok**, Marie-Cécile de Weerd, Pascal Boulet, Émilie Gaudry, Y. Grin, V. Fournée and Julian Ledieu. Al_3AuIr: A New Compound in the Al–Au–Ir System. 20th International Conference on Solid Compounds of Transition Elements, isingragoising, Spain, 11 April - 15 April 2016.
4. **Joris Kadok**, Yurii Prots, Émilie Gaudry, Pascal Boulet, Juri Grin, Vincent Fournée and Julian Ledieu. Nouveau Composé dans le Système Al-Si-Ir. Congrès de l'association française de cristallographie, Marseille, France, 4 July - 7 July 2016.

Posters

1. **Joris Kadok**, Yurii Prots, Juri Grin, Marie-Cécile de Weerd, Pascal Boulet, Vincent Fournée and Julian Ledieu. The aluminium-iridium binary system and Al-Ir based ternary compounds. C-MAC days 2014, isinggreb, Croatia, 8 December - 11 December 2015.
2. **Joris Kadok**, Yurii Prots, Juri Grin, Marie-Cécile de Weerd, Pascal Boulet, Vincent Fournée and Julian Ledieu. The aluminium-iridium binary system and Al-Ir based ternary compounds. EMMA PhD school seminar, Metz, France, 7 May 2015.
3. **Joris Kadok**, Yurii Prots, Juri Grin, Marie-Cécile de Weerd, Pascal Boulet, Vincent Fournée and Julian Ledieu. The aluminium-iridium binary system and Al-Ir based ternary compounds. Euroschool C-MAC 2015, Bratislava, Slovakia, 1 June - 5 June 2015.

Appendix A

Tables of atomic coordinates for $Al_{28}Ir_9$

TABLE A.1: Atomic coordinates and isotropic displacement parameters for $Al_{28}Ir_9$ refined in the $Cmc2_1$ space group.

Atom	Site	x	y	z	U_{eq} (Å^2)	Occupancy
Ir1	4a	0	0	0	0.00958(15)	1
Ir2	4a	0	0.33373(18)	0.10472(8)	0.0125(5)	1
Ir3	4a	0	0.33367(19)	0.39343(8)	0.0116(5)	1
Ir4A	8b	0.3142(2)	0.22905(13)	0.16205(7)	0.0129(4)	1
Ir4B	4a	½	0.04244(15)	0.16171(10)	0.0107(6)	1
Ir5A	8b	-0.31646(19)	0.43875(13)	0.37896(6)	0.0137(5)	1
Ir5B	4a	½	0.62143(19)	0.37914(11)	0.0172(7)	1
Ir6A	8b	0.68975(18)	0.10249(11)	0.02944(6)	0.0115(4)	1
Ir6B	4a	0	0.79320(16)	0.02935(11)	0.0136(7)	1
Ir7A	8b	0.81961(17)	0.06065(14)	0.24976(8)	0.0157(4)	1
Ir7B	4a	0	0.87935(16)	0.24950(13)	0.0161(7)	1
Ir8A	8b	0.68904(18)	0.10386(12)	0.46967(6)	0.0113(4)	1
Ir8B	4a	0	0.79326(17)	0.46939(10)	0.0123(7)	1
Ir9A	8b	-0.15996(16)	0.38667(12)	0.24962(9)	0.0115(3)	1
Ir9B	4a	½	0.72576(15)	0.25042(14)	0.0129(7)	1
I10A	8b	0.3158(2)	0.22897(12)	0.33712(7)	0.0145(4)	1
I10B	4a	½	0.04295(16)	0.33723(10)	0.0116(6)	1
I11A	8b	-0.3182(2)	0.43865(13)	0.11993(7)	0.0145(4)	1
I11B	4a	½	0.62155(17)	0.11972(10)	0.0118(7)	1
Al1	4a	0	-0.0027(12)	0.2430(3)	0.000(14)	1
Al2	4a	0	0.3427(15)	0.0120(9)	0.043(7)	1
Al3	4a	0	0.3340(12)	0.6488(5)	0.008(3)	1
Al4	4a	0	0.3344(15)	0.8467(6)	0.019(4)	1
Al5	4a	0	0.0008(18)	0.0912(4)	0.032(3)	1
Al6	4a	0	0.3349(13)	0.2038(3)	0.018(2)	1
Al7	4a	0	0.3293(15)	0.4904(7)	0.023(4)	1
Al8A	8b	0.1806(12)	0.2690(9)	0.0903(4)	0.013(2)	1
Al8B	4a	0	0.4528(13)	0.1031(8)	0.027(6)	1
Al9A	8b	0.8847(10)	0.0366(7)	0.1620(4)	0.005(2)	1
Al9B	4a	0	0.9185(12)	0.1630(8)	0.010(5)	1

Al10A	8b	0.6716(14)	0.1021(7)	0.3075(5)	0.007(3)	1
Al10B	4a	0	0.7811(9)	0.3035(6)	0.004(3)	1
Al11A	8b	-0.1771(19)	0.3872(11)	0.0611(6)	0.035(4)	1
Al11B	4a	0	0.2142(10)	0.0601(6)	0.002(4)	1
Al12A	8b	-0.3387(12)	0.4384(6)	0.2182(4)	0.023(3)	1
Al12B	4a	0	0.1201(15)	0.2201(10)	0.041(8)	1
Al13A	8b	0.8581(9)	0.0508(7)	0.3383(3)	0.0036(16)	1
Al13B	4a	0	0.9172(10)	0.3371(7)	0.012(4)	1
Al14A	8b	0.3898(14)	0.2049(9)	0.0707(5)	0.017(3)	1
Al14B	4a	0	0.5875(9)	0.0707(6)	0.000(3)	1
Al15A	8b	0.3838(11)	0.2093(8)	0.4306(5)	0.017(3)	1
Al15B	4a	0	0.5922(14)	0.4292(10)	0.036(7)	1
Al16A	8b	0.3873(11)	0.2095(6)	0.2515(6)	0.018(3)	1
Al16B	4a	0	0.5861(8)	0.2490(8)	0.004(3)	1
Al17A	8b	0.1843(16)	0.2721(12)	0.4015(6)	0.026(4)	1
Al17B	4a	0	0.4476(7)	0.3879(5)	0.000(3)	1
Al18A	8b	0.6700(14)	0.0979(7)	0.1898(5)	0.024(3)	1
Al18B	4a	0	0.7877(12)	0.1876(7)	0.010(5)	1
Al19A	8b	0.1975(18)	0.2745(16)	0.2381(6)	0.063(5)	1
Al19B	4a	0	0.4520(6)	0.2218(4)	0.000(2)	1
Al20A	8b	0.8570(18)	0.0373(12)	0.4367(7)	0.072(6)	1
Al20B	4a	0	0.9262(10)	0.4303(7)	0.027(4)	1
Al21A	8b	-0.1738(16)	0.4003(9)	0.4395(7)	0.035(5)	1
Al21B	4a	0	0.2208(8)	0.4337(6)	0.000(3)	1
Al22A	8b	-0.1577(8)	0.3794(7)	0.3438(3)	0.0082(18)	1
Al22B	4a	0	0.3621(18)	0.3024(14)	0.131(16)	1
Al23A	8b	-0.3424(10)	0.4332(6)	0.4701(4)	0.022(3)	1
Al23B	4a	0	0.118(5)	0.460(4)	0.45(6)	1
Al24A	8b	-0.1913(14)	0.1929(8)	0.0037(5)	0.008(3)	1
Al24B	8b	0.3011(12)	0.3028(6)	0.0016(5)	0.002(2)	1
Al24C	8b	0.8875(15)	0.4981(8)	0.0015(7)	0.015(4)	1
Al25A	8b	0.3241(15)	0.0345(9)	0.1037(7)	0.030(4)	1
Al25B	8b	0.7974(12)	0.1454(8)	0.1030(5)	0.003(3)	1
Al25C	8b	0.896(2)	0.8284(10)	0.1021(8)	0.036(6)	1
Al26A	8b	0.3219(12)	0.0268(7)	0.3949(4)	0.002(3)	1
Al26B	8b	0.8021(12)	0.1499(7)	0.3953(5)	0.000(3)	1
Al26C	8b	0.8745(15)	0.8264(8)	0.3911(5)	0.018(4)	1
Al27A	8b	-0.1478(11)	0.1775(6)	0.3024(5)	0.022(3)	1
Al27B	8b	0.3274(8)	0.3654(5)	0.3019(3)	0.0039(19)	1
Al27C	8b	0.8121(12)	0.4855(7)	0.2970(5)	0.025(3)	1
Al28A	8b	-0.0472(14)	0.2307(8)	0.1569(5)	0.000(3)	0.5
Al28B	8b	0.2238(13)	0.3495(8)	0.1662(6)	0.050(4)	1
Al29A	8b	-0.107(3)	0.0842(17)	0.0396(11)	0.063(9)	0.5
Al29B	8b	0.3822(12)	0.4123(6)	0.0322(4)	0.026(3)	1

TABLE A.2: Atomic coordinates and isotropic displacement parameters for Al$_{28}$Ir$_9$ refined in the $P31c$ space group.

Atom	Site	x	y	z	U$_{eq}$ (Å^2)	Occupancy
Ir1	2a	0	0	0	0.0098(2)	1
Ir2	2b	⅓	⅔	0.10464(12)	0.0136(6)	1
Ir3	2b	⅓	⅔	0.39346(11)	0.0110(6)	1
Ir4	6c	0.5428(3)	0.4576(3)	0.16203(6)	0.0127(3)	1
Ir5	6c	0.1216(3)	0.8777(3)	0.37920(6)	0.0151(4)	1
Ir6	6c	0.7925(2)	0.2059(2)	0.02928(5)	0.0117(4)	1
Ir7	6c	0.8798(3)	0.1209(3)	0.24986(9)	0.01637(16)	1
Ir8	6c	0.7927(3)	0.2070(3)	0.46959(5)	0.0135(4)	1
Ir9	6c	0.2261(2)	0.7734(3)	0.24973(9)	0.01183(14)	1
Ir10	6c	0.5436(2)	0.4573(2)	0.33720(6)	0.0140(3)	1
Ir11	6c	0.1221(3)	0.8788(3)	0.12006(6)	0.0143(4)	1
Al1	2a	0	0	0.2429(4)	0.0016(19)	1
Al2	2b	⅓	⅔	0.0122(15)	0.062(11)	1
Al3	2b	⅓	⅔	0.6489(8)	0.011(5)	1
Al4	2b	⅓	⅔	0.8466(8)	0.015(5)	1
Al5	2a	0	0	0.0923(7)	0.034(4)	1
Al6	2b	⅓	⅔	0.2022(6)	0.022(3)	1
Al7	2b	⅓	⅔	0.4887(8)	0.018(5)	1
Al8	6c	0.4550(16)	0.5429(16)	0.0912(3)	0.0064(14)	1
Al9	6c	0.9226(18)	0.0752(18)	0.1626(3)	0.0088(16)	1
Al10	6c	0.784(2)	0.218(2)	0.3061(4)	0.014(3)	1
Al11	6c	0.210(2)	0.7788(19)	0.0598(6)	0.020(3)	1
Al12	6c	0.1213(17)	0.8955(17)	0.2184(4)	0.024(2)	1
Al13	6c	0.9036(16)	0.0884(15)	0.3377(3)	0.0075(17)	1
Al14	6c	0.5924(18)	0.4111(17)	0.0688(4)	0.006(2)	1
Al15	6c	0.589(2)	0.411(2)	0.4279(5)	0.022(3)	1
Al16	6c	0.5951(11)	0.4197(12)	0.2509(6)	0.0112(14)	1
Al17	6c	0.448(2)	0.546(2)	0.3913(4)	0.020(2)	1
Al18	6c	0.7694(13)	0.2000(13)	0.1897(5)	0.014(3)	1
Al19	6c	0.458(3)	0.544(3)	0.2295(5)	0.043(3)	1
Al20	6c	0.910(4)	0.077(4)	0.4339(7)	0.071(5)	1
Al21	6c	0.217(3)	0.780(3)	0.4348(7)	0.027(4)	1
Al22	6c	0.2517(10)	0.7872(11)	0.3434(4)	0.019(2)	1
Al23	6c	0.1346(14)	0.9116(15)	0.4707(5)	0.039(4)	1
Al24A	6c	0.0037(14)	0.3937(14)	0.0038(5)	0.009(3)	1
Al24B	6c	-0.0023(18)	-0.3899(15)	0.5007(7)	0.010(3)	1
Al25A	6c	0.3469(19)	0.0600(19)	0.1007(7)	0.025(4)	1
Al25B	6c	-0.3528(14)	-0.0613(14)	0.6068(6)	0.010(3)	1
Al26A	6c	0.3447(18)	0.0521(19)	0.3966(7)	0.017(4)	1
Al26B	6c	-0.3506(13)	-0.0508(13)	0.8941(5)	0.002(2)	1
Al27A	6c	0.0259(12)	0.3478(13)	0.3003(5)	0.024(3)	1
Al27B	6c	-0.0345(8)	-0.3079(9)	0.8006(3)	0.0065(17)	1
Al28A	6c	0.140(2)	0.435(2)	0.1637(8)	0.062(5)	1
Al29A	6c	-0.018(2)	-0.1978(19)	0.5327(7)	0.053(5)	1

TABLE A.3: Atomic coordinates and isotropic displacement parameters for Al$_{28}$Ir$_9$ refined in the $P6_3mc$ space group.

Atom	Site	x	y	z	U_{eq} (Å^2)	Occupancy
Ir1	2a	0	0	0	0.0098(3)	1
Ir2	2b	⅓	⅔	0.10381(12)	0.0126(6)	1
Ir3	2b	⅓	⅔	0.39260(12)	0.0114(6)	1
Ir4	6c	0.54237(10)	0.45763(10)	0.16206(6)	0.0136(4)	1
Ir5	6c	0.12256(10)	0.87744(10)	0.37916(6)	0.0146(4)	1
Ir6	6c	0.79371(9)	0.20629(9)	0.02949(6)	0.0116(4)	1
Ir7	6c	0.87942(4)	0.12058(4)	0.24986(10)	0.0166(2)	1
Ir8	6c	0.79245(9)	0.20755(9)	0.46976(6)	0.0130(4)	1
Ir9	6c	0.22636(4)	0.77364(4)	0.24962(9)	0.01180(18)	1
Ir10	6c	0.54348(10)	0.45652(10)	0.33734(6)	0.0130(4)	1
Ir11	6c	0.12105(10)	0.87895(10)	0.11996(7)	0.0142(4)	1
Al1	2a	0	0	0.2429(5)	0.005(3)	1
Al2	2b	⅓	⅔	0.0111(8)	0.012(4)	1
Al3	2b	⅓	⅔	0.6456(10)	0.027(6)	1
Al4	2b	⅓	⅔	0.8458(6)	0.000(3)	1
Al5	2a	0	0	0.0926(8)	0.025(4)	1
Al6	2b	⅓	⅔	0.2013(7)	0.016(3)	1
Al7	2b	⅓	⅔	0.488(2)	0.079(15)	1
Al8	6c	0.4558(4)	0.5442(4)	0.0913(4)	0.0072(17)	1
Al9	6c	0.9229(4)	0.0771(4)	0.1632(3)	0.0049(16)	1
Al10	6c	0.7831(7)	0.2169(7)	0.3068(5)	0.011(3)	1
Al11	6c	0.2160(7)	0.7840(7)	0.0613(6)	0.014(3)	1
Al12	6c	0.1126(6)	0.8874(6)	0.2182(5)	0.027(3)	1
Al13	6c	0.9062(6)	0.0938(6)	0.3391(4)	0.014(2)	1
Al14	6c	0.5910(5)	0.4090(5)	0.0685(4)	0.0033(19)	1
Al15	6c	0.5877(8)	0.4123(8)	0.4273(6)	0.023(3)	1
Al16	6c	0.5882(4)	0.4118(4)	0.2493(7)	0.0134(13)	1
Al17	6c	0.4513(6)	0.5487(6)	0.3912(5)	0.021(2)	1
Al18	6c	0.7856(11)	0.2144(11)	0.1901(8)	0.032(5)	1
Al19	6c	0.4572(7)	0.5428(7)	0.2289(5)	0.036(3)	1
Al20	6c	0.9172(10)	0.0828(10)	0.4332(7)	0.061(5)	1
Al21	6c	0.2187(12)	0.7813(12)	0.4365(9)	0.039(5)	1
Al22	6c	0.2318(8)	0.7682(8)	0.3436(6)	0.038(3)	1
Al23	6c	0.1130(11)	0.8870(11)	0.4711(8)	0.068(6)	1
Al24	12d	0.0050(10)	0.3932(6)	0.0024(4)	0.0107(10)	1
Al25	12d	0.3503(10)	0.0646(10)	0.1038(4)	0.021(2)	1
Al26	12d	0.3487(7)	0.0495(8)	0.3952(3)	0.0062(15)	1
Al27	12d	0.0329(10)	0.3204(10)	0.3001(4)	0.041(2)	1
Al28	12d	0.152(2)	0.443(2)	0.1623(8)	0.042(5)	0.5
Al29	12d	0.0276(19)	0.2044(18)	0.0326(7)	0.032(4)	0.5

Bibliography

[1] K. Kovnir et al. In: *Science and Technology of Advanced Materials* 8 (2007), pp. 420–427.

[2] C. Wolverton and V. Ozoliņš. In: *Physical Review Letters* 86 (2001), pp. 5518–5521.

[3] J.-M. Dubois, E. Belin-Ferré, and A. Tsai. *Quasicrystals and Complex Metallic Alloys*. Ed. by John Wiley and Sons. Encyclopedia of Chemical Technology, 2016. DOI: `10.1002/0471238961`.

[4] http://reference.iucr.org/dictionary/Crystal.

[5] T. Massalski. In: *Bulletin of Alloy Phase Diagrams* 1 (1980), pp. 27–33.

[6] U.R. Kattner and B.P. Burton. *Phase Diagrams of Binary Iron Alloys*. Ed. by OH Materials Park. ASM International, 1992.

[7] C.P. Wang et al. In: *Journal of Phase Equilibria and Diffusion* 5 (2004), pp. 320–328.

[8] J. Dshemuchadse et al. In: *Acta Crystallographica Section B* 69 (2013), pp. 238–248.

[9] A. Tsai, A. Inoue, and T. Masumoto. In: *Japanese Journal of Applied Physics* 27 (1988), pp. 1587–1590.

[10] A. Tsai. In: *Science and Technology of Advanced Materials* 9 (2008), p. 013008.

[11] Y. Ishii and T. Fujiwara. In: *Physical Review Letters* 87 (2001), p. 206408.

[12] D. Shechtman. Interviewed by Matthew Kalman. Oct. 2011.

[13] P. Liu and J.O. Nilsson. *New Horizons In Quasicrystals, Research and Applications*. Ed. by A.I. Goldman et al. World Scientific, Singapore, 1996.

[14] J.-M. Dubois and E. Belin-Ferré, eds. *Complex Metallic Alloys: Fundamentals and Applications*. Wiley-VCH Verlag GmbH & Co.: Weinheim, Germany, 2011.

[15] S. Kenzari et al. In: *Materials and Design* 35 (2012), pp. 691–695.

[16] S. Kameoka, T. Tanabe, and A. Tsai. In: *Catalysis Today* 93 (2004), pp. 23–26.

[17] M. Armbrüster et al. In: *Nature Materials* 11 (2012), pp. 690–693.

[18] M. Krajčí and J. Hafner. In: *Journal of Catalysis* 278 (2011), pp. 200–207.

[19] L. Piccolo and L. Kibis. In: *Journal of Catalysis* 332 (2015), pp. 112–118.

[20] G. Yao et al. In: *Journal of Alloys and Compounds* 581 (2013), pp. 109–114.

[21] L.A. Cornish P.J. Hill and and M.J. Witcomb. In: *Journal of Alloys and Compounds* 280 (1998), p. 240.

[22] K.N. Lee and W.L. Worrell. “Oxidation behaviour of iridium-aluminum and iridium-aluminum-silicon systems at very high temperatures”. In: *High-Temperature Oxidation and Sulphidation Processes*. Ed. by J.D. Embury. 1990, pp. 212–221.

[23] K.N. Lee and . W.L. Worrell. In: *Oxidation of Metals* 32 (1989), pp. 357–369.

[24] M. Boström et al. In: *Journal of Solid State Chemistry* 178 (2005), p. 339.

[25] S. Katrych, V. Gramlich, and W. Steurer. In: *Journal of Alloys and Compounds* 407 (2006), p. 132.

[26] J. Dshemuchadse, P. Kuczera, and W. Steurer. In: *Intermetallics* 32 (2013), pp. 337–343.

[27] S. Katrych et al. In: *Journal of Alloys and Compounds* 428 (2007), pp. 164–172.

[28] A. Oishi, K. Nishimoto, and R. Tamura. In: *Zeitschrift für Kristallographie* 224 (2009), pp. 115–118.

[29] Y. Yamabe mitarai et al. In: *Intermetallics* 15 (2007), pp. 479–488.

[30] L.A. Cornish P.J. Hill and and M.J. Witcomb. In: *Journal of Alloys and Compounds* 291 (199), pp. 130–144.

[31] http://www.eucmac.eu/.

[32] W.E. Wallace. In: *Annual Review of Physical Chemistry* 15 (1964), pp. 109–130.

[33] L. Pauling and J. Ewing. In: *Reviews of Modern Physics* 20 (1948), pp. 112–122.

[34] http://xray.chm.bris.ac.uk/research/facilities.html.

[35] Patrice Kenfack Tsobnang. PhD thesis. University of Lorraine, 2014.

[36] G.M. Sheldrick. In: *Acta Crystallographica Section A* 64 (2008), pp. 112–122.

[37] L.J. Farrugia. In: *Journal of Applied Crystallography* 32 (1999), pp. 837–838.

[38] L. Akselrud and Y. Grin. In: *Journal of Applied Crystallography* 47 (2014), pp. 803–805.

[39] http://pd.chem.ucl.ac.uk/pdnn/inst1/optics1.htm.

[40] https://icsd.fiz-karlsruhe.de/search/index.xhtml;jsessionid=75AD2CA0AE42841E9E00F0773A136194.

[41] P.E. Werner, L. Eriksson, and M. Westdahl. "TREOR, a Semi-Exhaustive Trial-and-Error Powder Indexing Program for All Symmetries". In: *Journal of Applied Crystallography* 18 (1985), pp. 367–370.

[42] J. Visser. "A Fully Automatic Program for Finding the Unit Cell from Powder Data". In: *Journal of Applied Crystallography* 2 (1969), pp. 89–95.

[43] A. Boultif and D. Louër. "Indexing of powder diffraction patterns for low-symmetry lattices by the successive dichotomy method". In: *Journal of Applied Crystallography* 24 (1991), pp. 987–993.

[44] W.J. Boettinger et al. *DTA and Heat-flux DSC Measurements of Alloy Melting and Freezing*. National Institute of Standards and Technology, 2006.

[45] https://www.webelements.com/.

[46] E. Gmelin and St.M. Sarge. In: *Pure and Apllied Chemistry* 67 (1995), pp. 1789–1800.

[47] E. Morîntale et al. In: *Physics AUC* 23 (2013), pp. 89–94.

[48] A. Tsai et al. In: *Materials Transactions - The Japan Institute of Metals and Materials* 31 (1990), p. 98.

[49] A. Tsai, A. Inoue, and T. Masumoto. In: *Japanese Journal of Applied Physics* 26 (1987), p. 1505.

[50] C. Chen and H.Chen. In: *Physical Review B* 33 (1986), p. 2814.

[51] P. Bancel and P. Heiney. In: *Physical Review B* 33 (1986), pp. 7917–7922.

[52] D. Shechtman et al. In: *Physical Review Letters* 53 (1984), p. 951.

[53] Paul Esslinger and Konrad Schubert. In: *Zeitschrift für Kristallographie* 48 (1957), p. 126.

[54] H. Schultz et al. In: *Zeitschrift für anorganische und allgemeine Chemie* 357 (1968), p. 299.

[55] K.M. Axler and R.B. Roof. In: *Advances in X-Ray Analysis* 29 (1986), p. 333.

[56] Lars-Eric Edshammar. In: *Acta Chemica Scandinavica* 21 (1967), p. 1104.

[57] Lars-Eric Edshammar. In: *Acta Chemica Scandinavica* 22 (1968), p. 2822.

[58] R. Ferro et al. In: *Atti della Accademia Nazionale dei Lincei. Classe di Scienze Fisiche, Matematiche e Naturali. Rendiconti Lincei. Scienze Fisiche e Naturali* 45 (1968), p. 556.

[59] K.M. Axler et al. In: *Journal of the Less Common Metals* 156 (1989), p. 213.

[60] Y. Grin and K. Peters. In: *Zeitschrift für Kristallographie* 212 (1997), p. 439.

[61] D. Pavlyuchkov, B. Grushko, and T.Ya. Velikanova. In: *Intermetallics* 16 (2008), p. 801.

[62] T. Abe et al. In: *Calphad* 32 (2008), p. 686.

[63] L. Kaufman and H. Bernstein. *Computer Calculation of Phase Diagrams*. Academic Press N Y. 1970.

[64] C. Jiang and B. Gleeson. In: *Acta Materialia* 54 (2006), pp. 4101–4110.

[65] C. Zhang et al. In: *Scripta Materialia* 59 (2008), pp. 403–406.

[66] M. Ode et al. In: *Intermetallics* 16 (2008), pp. 1171–1178.

[67] H. Okamoto. In: *Journal of Phase Equilibria and Diffusion* 30 (2009), p. 206.

[68] M. Mihalkovič and C. L. Henley. In: *Physical Review B* 88 (2013), p. 064201.

[69] M. Mihalkovič and C. L. Henley. In: *Physical Review B* 85 (2012), p. 092102.

[70] G. Kresse and J. Hafner. In: *Physical Review B - Condensed Matter and Materials Physics* 47 (1993), pp. 558–561.

[71] R. H. Swendsen and J.-S. Wang. In: *Physical Review Letters* 57 (1986), p. 2607.

[72] K. Hokushima and K. Nemoto. In: *Journal of the Physical Society of Japan* 65 (1996), p. 1604.

[73] E. Lyman, F. M. Ytreberg, and D. M. Zuckerman. In: *Physical Review Letters* 96 (2006), p. 028105.

[74] B. Grushko and M. Yurechko. In: *Zeitschrift für Kristallographie* 214 (1999), p. 313.

[75] B. Grushko and J. Gwóźdź. In: *Journal of Alloys and Compounds* 305 (2000), p. 219.

[76] Charles Day. In: *Physics Today* (2003), pp. 24–26.

[77] D. Kapush et al. In: *Chemistry of Metals and Alloys* 2 (2009), pp. 30–33.

[78] N. Athanasiou. In: *International Journal of Modern Physics B* 11 (1997), pp. 2443–2464.

[79] T. Ishimasa, Y. Tanaka, and S. Kashimoto. In: *Philosophical Magazine* 91 (2011), pp. 4218–4229.

[80] T. Seki and E. Abe. In: *Microscopy* 64 (2015), pp. 341–349.

[81] G.V. Voort. In: *ASM Handbook Series* 9 (2004).

[82] B. Slikson and T. Longo. In: *Proceedings of the IEEE* 52 (1964), pp. 1638–1641.

[83] M. Puselj and K. Schubert. In: *Journal of Less Common Metals* 35 (1974), pp. 259–266.

[84] J. Murray, H. Okamoto, and T. Massalski. In: *Bulletin of Alloy Phase Diagrams* 8 (1987), pp. 20–30.

[85] G. Kresse and J. Hafner. In: *Physical Review B - Condensed Matter and Materials Physics* 49 (1994), pp. 14251–14269.

[86] G. Kresse and J. Furthmüller. In: *Physical Review B - Condensed Matter and Materials Physics* 54 (1996), pp. 11169–11186.

[87] G. Kresse and J. Furthmüller. In: *Journal of Computational Materials Science* 6 (1996), pp. 15–50.

[88] P. Blöchl. In: *Physical Review B - Condensed Matter and Materials Physics* 50 (1994), pp. 17953–17979.

[89] G. Kresse and D. Joubert. In: *Physical Review B - Condensed Matter and Materials Physics* 59 (1999), pp. 1758–1775.

[90] J.P. Perdew, K. Burke, and M. Ernzerhof. In: *Physical Review Letters* 77 (1996), pp. 3865–3868.

[91] J.P. Perdew, K. Burke, and M. Ernzerhof. In: *Physical Review Letters* 78 (1997), pp. 1396–1396.

[92] A.J. Bradley and A. Taylor. In: *Philosophical Magazine Series 7* 23 (1937), pp. 1049–1067.

[93] B. Grushko, K. Urban, and C. Freiburg. In: *Scripta Metallurgica et Materialia* 25 (1991), pp. 2533–2536.

[94] R.V. Skolozdra, A.P. Prevarskii, and G.G Cherkashin. In: *Diagrammy Sostoyaniya Met. Sist.* 167 (1971).

[95] R. Sabiyranov, S. Bose, and S. Burkov. In: *Journal of Physics: Condensed Matter* 7 (1997), pp. 5437–5459.

[96] M. Ellner, U. Kattner, and B. Predel. In: *Journal of Less Common Metals* 87 (1982), pp. 305–325.

[97] M. Yurechko et al. In: *Journal of Alloys and Compounds* 329 (2001), pp. 173–181.

[98] T.B. Massalski and U. Mizutani. In: *Progress in Materials Science* 22 (1978), pp. 151–262.

[99] G. Trambly de Laissardière, D. Nguyen-Mahn, and D. Mayou. In: *Progress in Materials Science* 50 (2005), pp. 679–788.

[100] http://gurka.fysik.uu.se/ESP/.

[101] C. Ortiz, O. Eriksson, and M. Klintenberg. In: *Computational Materials Science* 44 (2009), pp. 1042–1049.

[102] O. Jepsen, A. Burkhardt, and K. Andersen. “The Program TB-LMTO-ASA 4.7”. In: Max-Planck-Institut für Festkörperforschung: Stuttgart ,Germany, 1999.

[103] U. von Barth and L. Hedin. In: *Journal of Physics C: Solid State Physics* 5 (1972), pp. 1629–1642.

[104] O. Andersen. In: *Physical Review B* 12 (1975), pp. 3060–3083.

[105] W. Lambrecht and O. Andersen. In: *Physical Review B: Consensed Matter and Materials Physics* 34 (1986), pp. 2439–2449.

[106] M. Kohout. In: *Faraday Discussions* 135 (2007), pp. 43–54.

[107] R. Bader. *Atoms in Molecules, A Quantum Theory*. Clarendron Press and Oxford University Press Inc., 1994.

[108] S. Raub and G. Jansen. In: *Theoretical Chemistry Accounts* 106 (2001), pp. 223–232.

[109] M. Kohout. "DGrid , version 4.6". In: Max-Planck-Institut: Leipzig, Germany, 2001.

[110] M. Kohout, F. Wagner, and Y. Grin. In: *Theoretical Chemistry Accounts* 108 (2007), pp. 150–156.

[111] F. Wagner et al. In: *Chemistry - A European Journal* 13 (2007), pp. 5724–5741.

[112] Y. Grin et al. In: *Journal of Solid State Chemistry* 179 (2006), pp. 1707–1719.

[113] A. Ormeci and Y. Grin. In: *Israel Journal of Chemistry* 51 (2011), pp. 1349–1354.

[114] H. Shin et al. In: *Physical Review B: Consensed Matter and Materials Physics* 84 (2011), p. 085411.

[115] M. Armbrüster et al. *Complex Metallic Alloys: Fundamentals and Applications*. Ed. by J.-M. Dubois and E. Belin-Ferré. Wiley-VCH Verlag GmbH & Co.: Weinheim, Germany, 2011.

[116] Y.A. Velikodyni et al. In: *Soviet Physics, Crystallography* 27 (1982), pp. 138–140.

[117] J. Murray and A. McAlister. In: *Bulletin of Alloy Phase Diagrams* 5 (1984), pp. 74–84.

[118] H. Okamoto. In: *Journal of Phase Equilibria and Diffusion* 28 (2007), p. 495.

[119] M. Boström, Y. Prots, and Y. Grin. In: *Solid State Sciences* 6 (2004), pp. 499–503.

[120] T.I. Yanson et al. In: *Acta Crystallographica Section C* 52 (1996), pp. 2963–2967.

[121] B. Aronssson. In: *Acta Chemica Scandinavica* 14 (1960), pp. 1414–1418.

[122] F. Weitzer and J.C. Schuster. In: *Journal of Solid State Chemistry* 70 (1987), pp. 178–184.

[123] U. Mizutani et al. In: *Philosophical Magazine* 93 (2013), pp. 3353–3390.

[124] H. Sato et al. In: *Philosophical Magazine* 93 (2013), pp. 3029–3061.

[125] A. McAlister. In: *Bulletin of Alloy Phase Diagrams* 8 (1987), pp. 526–533.

[126] I. Karakaya and W. Thomson. In: *Bulletin of Alloy Phase Diagrams* 7 (1986), pp. 359–360.

[127] N.R. Gall', E.V. Rut'kov, and A.Ya. Tontegode. In: *Physics of the Solid State* 48 (2006), pp. 369–376.

[128] H. Zhang et al. In: *Applied Surface Science* 254 (2008), pp. 7655–7658.

[129] J.D.R. Buchanan et al. In: *Physical Review B* 66 (2002), pp. 104427-1 104427-5.

[130] http://www.chem.qmul.ac.uk/surfaces/scc/scat5.htm.

[131] C. Julian Chen. *Introduction to Scanning Tunneling Microscopy*. Tech. rep. Oxford University Press, 2008.

[132] I. Horcas et al. In: *Review of Scientific Instruments* 78 (2007), p. 013705.

[133] G. Gilarowski and H. Niehus. In: *Surface Science* 436 (1999), pp. 107–120.

[134] N.R. Gall′, E.V. Rut′kov, and A.Ya. Tontegode. In: *Physics of the Solid State* 46 (2004), pp. 371–377.

[135] F. Weitzer et al. In: *Journal of Materials Research* 5 (1990), pp. 2152–2159.

[136] G. Ehrlich and F.G Hudda. In: *Journal of Chemical Physics* 44 (1966), pp. 1039–1049.

[137] R.L. Schwoebel. In: *Journal of Applied Physics* 37 (1966), pp. 3682–3686.

[138] L. Vitos et al. In: *Surface Science* 411 (1998), p. 186.

[139] J. Ledieu, E. Gaudry, and V. Fournée. In: *Science and Technology of Advanced Materials* 15 (2014), p. 034802.

[140] S. Alarcón-Villaseca et al. In: *The Journal of Physical Chemistry C* 115 (2011), pp. 14922–14932.

[141] M.A. Van Hove et al. In: *Surface Science Reports* 19 (1993), p. 191.

[142] A. Barbieri and M.A. Van Hove. In: *Private communication* ().

[143] J.B. Pendry. In: *Journal of Physics C: Solid State Physics* 13 (1980), p. 937.

[144] M. Wardé et al. In: *Applied Surface Science* 357 (2015), pp. 1666–1675.

[145] S. Nishimura et al. In: *Applied Catalysis* 76 (1991), pp. 19–29.

Le système binaire Al-Ir, du diagramme de phases aux surfaces atomiques

Un alliage métallique complexe (CMA) est un composé intermétallique dont la maille élémentaire est constituée d'un nombre important d'atomes formant bien souvent des agrégats de haute symétrie. De la complexité de ces composés peuvent découler des propriétés physico-chimiques intéressantes pour divers domaines d'application. Le système binaire aluminium-iridium est un système qui présente de nombreux composés intermétalliques dont la moitié sont des CMA. Malgré l'étude approfondie dont ce système a fait l'objet dans la littérature, certaines incertitudes demeuraient irrésolues, nous amenant ainsi à réexaminer le diagramme de phases Al-Ir. Nous avons également exploré les systèmes ternaires dits "push-pull" Al-Au-Ir et Al-Ag-Ir, propices à la formation de phases CMA selon certains auteurs. Au total, une centaine d'échantillons ont été préparés par fusion à l'arc puis analysés par diverses techniques de caractérisations: diffraction des rayons X (XRD), microscopie électronique à balayage (SEM), analyse dispersive en énergie (EDS) et analyse thermique différentielle (DTA). Quatre nouveaux composés intermétalliques ont ainsi été identifiés: $Al_{2.4}Ir$, $Al_{72}Au_{2.5}Ir_{29.5}$, Al_3AuIr et $Al_{11}SiIr_6$, ce dernier étant issu d'une manipulation accidentelle. La structure cristallographique de chacun de ces composés a été résolue, révélant $Al_{2.4}Ir$ et $Al_{72}Au_{2.5}Ir_{29.5}$ comme étant des CMA possédant une centaine d'atomes dans la maille. Des calculs basés sur la théorie de la fonctionnelle de la densité (DFT) sont venus apporter des précisions concernant la stabilité des composés Al_3AuIr et $Al_{11}SiIr_6$. Pour le système Al-Ir, une variante structurale de deux CMA déjà connus de la littérature a également pu être mise en évidence. Les structures cristallographiques de la variante de $Al_{2.75}Ir$ et de celle de $Al_{28}Ir_9$ ont ainsi été approchées, présentant 240 et 444 atomes dans leur maille respective. Les propriétés de surface comptent parmi les aspects les plus intéressants des CMA, par exemple pour la catalyse hétérogène. En l'absence de monocristaux de taille macroscopique, nous avons étudié la possibilité de former des composés de surface par dépôt de Ir sur une surface Al(100) suivi de recuits. Des caractérisations par diffraction d'électrons lents (LEED), spectroscopie de photoélectrons excités par rayons X (XPS) et microscopie à effet tunnel (STM) supportés par ces calculs *ab initio* ont révélé qu'à partir de 320°C, le composé Al_9Ir_2 se formait en surface mais également dans une partie du volume du substrat.

Mots-clés: Al-Ir, CMA, XRD, SEM, DTA, DFT, LEED, XPS, STM

The Al-Ir binary system, from the phase diagram to atomic surfaces

A complex metallic alloy (CMA) is an intermetallic compound whose unit cell contains a large number of atoms frequently forming highly-symmetric clusters. From the complexity of these compounds can arise physical and chemical properties interesting for various fields of application. The aluminium-iridium system exhibits numerous intermetallic compounds of which half of them are actually CMAs. Despite this system being extensively studied in the literature, some uncertainties remained unsolved, leading us to reinvestigate the Al-Ir phase diagram. In addition, the "push-pull" systems Al-Au-Ir and Al-Ag-Ir, favorable for the formation of CMA according to the literature, have been explored. Thus, near a hundred of samples have been prepared by arc-melting before being analysed with different characterisations techniques: X-ray diffraction (XRD), scanning electron microscopy (SEM), energy dispersive X-ray spectroscopy (EDS) and differential thermal analysis (DTA). From this study, 4 new intermetallic compounds could be identified: $Al_{2.4}Ir$, $Al_{72}Au_{2.5}Ir_{29.5}$, Al_3AuIr and $Al_{11}SiIr_6$, the latter being the result of a fortuitous manipulation. The crystallographic structure of each of these compounds has been solved, revealing $Al_{2.4}Ir$ and $Al_{72}Au_{2.5}Ir_{29.5}$ to be two CMAs with around one hundred of atoms in their unit cell. Calculations based on the density functional theory (DFT) brought further details about the stability of the two other Al_3AuIr and $Al_{11}SiIr_6$ compounds. In the Al-Ir system, a structural variant of two well-known CMAs has been also unveiled. The crystallographic structures of the $Al_{2.75}Ir$ and $Al_{28}Ir_9$ variant have been approached, revealing 240 and 444 atoms in their respective unit cell. The CMAs frequently exhibit interesting surface properties. In order to study the Al-Ir compound surfaces, iridium adsorption on Al(100) surface followed by annealing has been investigated. The characterisations by low-energy electrons diffraction (LEED), X-ray photoelectron spectroscopy (XPS) and scanning tunneling microscopy (STM) supported by *ab initio* calculations revealed that, from 320°C, the Al_9Ir_2 compound is formed at the surface but also in the substrate bulk.

Mots-clés: Al-Ir, CMA, XRD, SEM, DTA, DFT, LEED, XPS, STM